TOUGHNESS-DOMINATED HYDRAULIC FRACTURES IN COHESIONLESS PARTICULATE MATERIALS

A Dissertation
Presented to
The Academic Faculty

by

Robert S Hurt

In Partial Fulfillment
of the Requirements for the Degree of
Doctor of Philosophy in the
School of Civil and Environmental Engineering

Georgia Institute of Technology

May 2012

TOUGHNESS-DOMINATED HYDRAULIC FRACTURES IN COHESIONLESS PARTICULATE MATERIALS

Approved by:

Dr. Leonid Germanovich, Advisor
School of Civil and Environmental Engineering
Georgia Institute of Technology

Dr. Glen Rix
School of Civil and Environmental Engineering
Georgia Institute of Technology

Dr. Haiying Huang
School of Civil and Environmental Engineering
Georgia Institute of Technology

Dr. Robert Lowell
School of Earth and Atmospheric Sciences
Georgia Institute of Technology

Dr. Jose Adachi
Schlumberger

Dr. Peter Van Dyke
Weatherford International

Date Approved: October 4, 2011

To my wife

ACKNOWLEDGEMENTS

First and foremost I wish to thank my wife. Her support and encouragement has made this endeavor possible. I wish to express my sincere appreciation to my advisor, Dr. Leonid Germanovich, his guidance and encouragement was paramount in completing this work. He was gracious enough to allow my participation in many topics well beyond the scope of my dissertation. His expert tutelage will serve me well in the future.

I would like to thank my thesis committee: Dr. Glen Rix, Dr. Robert Lowell, Dr. Peter Van Dyke, Dr. Haiying Huang, and Dr. Jose Adachi. I and this work benefited significantly from their valuable comments and suggestions. I would like to especially thank Dr. Peter Van Dyke for his comments that significantly improved the text of this dissertation.

I greatly appreciate the assistance and encouragement from past and present graduate students of the Rock and Fracture Mechanics Group at Georgia Institute of Technology: Dr. Hong Chang, Dr. Jongwon Choi, Dr. Gence Genc, Charlie George, Devon Gwaba, Sihyun Kim, Dr. Cem Ozan, Dr. Pierre Ramondenc, Tahiru Mawia, and Chanin Ruangthaveekoon.

The nature of this work required extensive laboratory work. This was accomplished with the assistance of many undergraduate students working in the lab. I wish to thank Lucas Curry, Alexander Sitt, Robert Smith, Phillip Davis, Justin Cooner, Cameron Troxel, Warren Wade, Alex Berry, Christopher Arjona, Holli Jones, Mariam Yousuf, Christian Braneon, Andrew Schildmeyer, and Vivie Susanto.

I should also express my deep gratitude to my parents, John Hurt and Kim Guyer, for their continuous encouragement and support.

Finally, I appreciate the financial support provided by Schlumberger, Shell, National Science Foundation, and the Georgia Tech Foundation during the years of my Ph.D. study.

TABLE OF CONTENTS

LIST OF TABLES

LIST OF FIGURES

SUMMARY

In this work we argue that toughness (resistance) to fracture propagation is an inherent characteristic of cohesionless particulate materials. This is significant for understanding hydraulic fracturing in geotechnical, geological, and petroleum applications.

We developed experimental techniques to quantify the initiation and propagation of fluid-driven fractures in saturated particulate materials. The fracturing liquid is injected into particulate materials, where the fluid flow is localized in thin, self-propagating, crack-like conduits. By analogy, we call these conduits 'cracks' or 'hydraulic fractures.' The experiments were performed on three particulate materials – (1) fine sand, (2) silica flour, and (3) their mixtures. Based on the laboratory observations and scale and dimensional analyses, this work offers physical concepts to explain the observed phenomena. The goal of this study is to determine the controlling parameters of fracture behavior and to quantify their affects.

When a fracture propagates in a solid, new surfaces are created by breaking material bonds. Consequently the material is in tension at the fracture tip. In contrast, all parts of the cohesionless particulate material (including the tip zone of the hydraulic fracture) are likely to be in compression. In solid materials (with limited or no leakoff), the fluid lags behind the front of the propagating fracture. However, for fluid-driven fractures in cohesionless materials the lag zone is absent. The compressive stress state and the absence of the fluid lag are important characteristics of hydraulic fracturing in

particulate materials with low, or negligible, cohesion. At present, two kinematic mechanisms of fracture initiation and propagation, consistent with both the compressive stress regime and the absence of the fluid lag, can be offered. The first mechanism is based on shear bands propagating ahead of the tip of an open fracture. The second is based on the reduction of the effective stresses and material fluidization within the leakoff zone at the fracture tip.

Our experimental results show that the primary factor affecting peak (initiation) pressure and fracture aperture is the magnitude of the confining stresses. The morphology of the fracture (and fluid leakoff zone), however, changes significantly not only with stresses, but also with other parameters such as flow rate, fluid rheology, and permeability. Typical features of the observed fractures are multiple off-shoots (i.e., small branches, often seen on only one side of the fracture) and the bluntness of the fracture tip. The latter suggests the importance of inelastic deformation in the process of fracture propagation in cohesionless materials. Similar to solid materials, fractures propagate perpendicular to the least compressive stress.

Scaling indicates that, in experiments performed in the regime of limited leakoff (i.e., the thickness of the leakoff zone is much smaller than the fracture length), there is a high-pressure gradient in the leakoff zone, in the direction normal to the fracture. Fluid pressure does not decrease considerably along the fracture, however, due to the relatively wide fracture aperture. This suggests that hydraulic fractures in unconsolidated materials propagate within the toughness-dominated regime. Furthermore, the theoretical model of toughness-dominated hydraulic fracturing can be

matched to the experimental pressure-time dependences with only one fitting parameter. Scale analysis shows that large apertures at the fracture tip correspond to relatively large 'effective' fracture (surface) energy, which can be orders of magnitude greater than typical for hard rocks.

The main conclusion of our work is that fractures in cohesionless materials can be considered ‘thick.’ This implies that the pressure drop in the fracture is insignificant. Therefore, the fractures in our tests can be considered toughness-dominated. Further, the primary parameter in determining the peak injection pressure is that of confining stresses. In this work we present a comprehensive experimental development focusing on four main parameters: confining stresses, fluid rheology, injection rate, and permeability. We use dimensional analysis and scaling relationships and compare our experimental results to a toughness-dominated model of hydraulic fracturing in cohesionless saturated materials. Finally, we compare the developed model to field data.

1. INTRODUCTION

In this work we argue that toughness (resistance) to fracture propagation is an inherent characteristic of cohesionless particulate materials. This is significant for understanding hydraulic fracturing in geotechnical, geological, and petroleum applications.

We developed experimental techniques to quantify the initiation and propagation of fluid-driven fractures in saturated particulate materials. The fracturing liquid is injected into particulate materials, where the fluid flow is localized in thin, self-propagating, crack-like conduits. By analogy, we call these conduits 'cracks' or 'hydraulic fractures.' The experiments were performed on three particulate materials – (1) fine sand, (2) silica flour, and (3) their mixtures. Based on the laboratory observations and scale and dimensional analyses, this work offers physical concepts to explain the observed phenomena. The goal of this study is to determine the controlling parameters of fracture behavior and to quantify their affects.

When a fracture propagates in a solid, new surfaces are created by breaking material bonds. Consequently the material is in tension at the fracture tip. In contrast, all parts of the cohesionless particulate material (including the tip zone of the hydraulic fracture) are likely to be in compression. In solid materials (with limited or no leakoff), the fluid lags behind the front of the propagating fracture. However, for fluid-driven fractures in cohesionless materials the lag zone is absent. The compressive stress state

and the absence of the fluid lag are important characteristics of hydraulic fracturing in particulate materials with low, or negligible, cohesion. At present, two kinematic mechanisms of fracture initiation and propagation, consistent with both the compressive stress regime and the absence of the fluid lag, can be offered. The first mechanism is based on shear bands propagating ahead of the tip of an open fracture. The second is based on the reduction of the effective stresses and material fluidization within the leakoff zone at the fracture tip.

Our experimental results show that the primary factor affecting peak (initiation) pressure and fracture aperture is the magnitude of the confining stresses. The morphology of the fracture (and fluid leakoff zone), however, changes significantly not only with stresses, but also with other parameters such as flow rate, fluid rheology, and permeability. Typical features of the observed fractures are multiple off-shoots (i.e., small branches, often seen on only one side of the fracture) and the bluntness of the fracture tip. The latter suggests the importance of inelastic deformation in the process of fracture propagation in cohesionless materials. Similar to solid materials, fractures propagate perpendicular to the least compressive stress.

Scaling indicates that, in experiments performed in the regime of limited leakoff (i.e., the thickness of the leakoff zone is much smaller than the fracture length), there is a high-pressure gradient in the leakoff zone, in the direction normal to the fracture. Fluid pressure does not decrease considerably along the fracture, however, due to the relatively wide fracture aperture. This suggests that hydraulic fractures in

unconsolidated materials propagate within the toughness-dominated regime. Furthermore, the theoretical model of toughness-dominated hydraulic fracturing can be matched to the experimental pressure-time dependences with only one fitting parameter. Scale analysis shows that large apertures at the fracture tip correspond to relatively large 'effective' fracture (surface) energy, which can be orders of magnitude greater than typical for hard rocks.

The main conclusion of our work is that fractures in cohesionless materials can be considered ‘thick.’ This implies that the pressure drop in the fracture is insignificant. Therefore, the fractures in our tests can be considered toughness-dominated. Further, the primary parameter in determining the peak injection pressure is that of confining stresses. In this work we present a comprehensive experimental development focusing on four main parameters: confining stresses, fluid rheology, injection rate, and permeability. We use dimensional analysis and scaling relationships to compare our experimental results to a toughness-dominated model of hydraulic fracturing in cohesionless saturated materials. Finally, we compare the developed model to field data.

The thesis is organized as follows.

Chapter 1 “Introduction” summarizes work performed in this dissertation and introduces the structure of this document.

Chapter 2 “Fluid-driven fractures in particulate materials” presents a review of the

literature on hydraulic fracturing in unconsolidated materials.

Chapter 3 “Experimental approach for fluid-driven fractures of particulate materials” describes the experimental processes and procedures developed in this work for hydraulic fracturing in unconsolidated saturated materials.

Chapter 4 “Experimental results” presents the main experimental results, related dimensional analysis and description of the observed fracture morphology.

Chapter 5 “Features of fluid-driven fractures in particulate materials” analyzes the effect of parameters on fracture characteristics.

Chapter 6 “Toughness-dominated hydraulic fracture” presents the scaling relationships, based on the experimental observations and concludes that fluid-driven fractures in our laboratory experiments propagate in the toughness-dominated regime.

Chapter 7 “Fluid-driven fractures with industrial fluids” describes the experimental series utilizing an industrial fracturing fluid and culminating in a high-stress test in an industrial laboratory. In this chapter, we also describe the use of the developed model for the experimental design of the large-scale test.

Chapter 8 “Conclusions and future work” provides the main conclusions of this work and suggests recommendations for future work on hydraulic fracturing in unconsolidated materials.

2. FLUID-DRIVEN FRACTURES IN PARTICULATE MATERIALS

2.1. Introduction

Hydraulic fracturing of unconsolidated formations or "soft fracture" is an important consideration in petroleum and civil engineering disciplines. The application of hydraulic fracturing can be a useful technique or a troublesome result of pressurized fluids interacting with particulate materials. The work presented here focuses on hydraulic fluid-driven fractures in saturated cohesionless materials (mostly fine sand). During hydraulic fracturing of cohesionless materials, all material, even at the crack tip, is likely to be in compression [e.g., *Chang*, 2004; *Germanovich and Hurt*, 2007; *Hurt et al.*, 2005]. This presents even more complexities in that no tensile stresses, (considered in conventional fracture mechanics) can be present at the crack tip. It can be argued that the tip of a fracture in cohesionless particulate materials is not well defined, no new surfaces are created, and no material bonds are broken. There is more than ample evidence, however, of fracture-like formations within cohesionless materials due to hydraulic forces [*Chang*, 2004; *De Pater and Dong*, 2007; 2009; *Golovin et al.*, 2010; *Jasarevic et al.*, 2010; *Khodaverdian and Mcelfresh*, 2000]. Therefore, we consider what we present here as hydraulic fractures.

In civil engineering, the hydraulic fracturing phenomenon in soils can be problematic with earthen dams [*Talbot*, 1994; *Wang et al.*, 2007], horizontal directional drilling [*Elwood*, 2008; *Staheli*, 2010], and in-situ permeability testing [*Bjerrum et al.*,

1972]. Conversely, it can be a useful technique with remediation technologies [*Hocking*, 1996; 2004; *Murdoch*, 1993c; *Murdoch and Slack*, 2002; *Murdoch et al.*, 2006b], evaluating in-situ stresses [*Al-Shaikh-Ali et al.*, 1981; *Lefebvre et al.*, 1991; *Leroueil et al.*, 1983; *Lutenegger*, 1990; *Zhou et al.*, 2010b] and compensation grouting [*Au et al.*, 2006; *Gafar et al.*, 2009; *Soga et al.*, 2005; *Soga et al.*, 2006b].

In the petroleum industry, hydraulic fracturing is a frequently used technique (for over 50 years) in oil and gas reservoirs to enhance production [e.g. *Henderson et al.*, 1954]. Hydraulic fracturing in unconsolidated materials has increasingly been utilized as a sand control measure in unconsolidated reservoirs [*Ayoub et al., 1992*; *Hainey and Troncoso*, 1992; *Wedman et al.*, 1999], enhanced production by fracturing or water flooding [*Jones and Soler*, 1999; *Khodaverdian et al.*, 2010b] and cuttings reinjection [*Chin and Montgomery*, 2004; *Ji et al.*, 2009; *Van Den Hoek*, 1993]. There are also complications with shallow water flow [*Ostermeier et al.*, 2002; *Rohler et al.*, 2002].

Complications from hydraulic fracturing in cohesionless materials in industrial applications are primarily related to the initiation phenomenon. As an applied technique, the industry is concerned with the ability to effectively create and characterize fractures. As described below, there were attempts to capture initiation and propagation of hydraulic fractures in cohesionless materials. The complexities of this phenomenon have yet to be fully realized, however.

Thus, the thorough understanding of the processes and accurate modeling of unconsolidated hydraulic fracturing could lead to several advances in production of

energy resources such as petroleum, methane hydrate, and geothermal energy [*Alonso and Mingo*, 2010; *Holditch and Madani*, 2010; *Ito et al.*, 2008; *Jonk et al.*, 2003; *Nassir et al.*, 2010], design and maintenance of earthen dams [*Flores-Berrones et al.*, 2010], bioremediation [*Hocking*, 2004; *Murdoch*, 1995b; *Murdoch and Chen*, 1997; *Murdoch et al.*, 2006a], rehabilitation of foundations [*Soga et al.*, 2005; *Soga et al.*, 2006a], in-situ characterization of stress states [*Guo et al.*, 2006]. Recently, subsidence mitigation has been suggested as a possible application of hydraulic fracturing in cohesionless materials [*Germanovich and Murdoch*, 2010]. This chapter gives a brief review of the literature on hydraulic fracturing in unconsolidated materials.

2.2. Experimental Observations

Within the last two decades, there were a number of physical experimental studies that focused on determining mechanisms and/or improving modeling aspects of hydraulic fractures in unconsolidated material [e.g., *De Pater and Dong*, 2007; *Dong*, 2010; *Germanovich and Hurt*, 2007; *Huang et al.*, 2011; *Ito et al.*, 2009; *Jasarevic et al.*, 2010; *Khodaverdian and Mcelfresh*, 2000; *Khodaverdian et al.*, 2009; *Lullo et al.*, 2004; *Shin and Santamarina*, 2010]. The most common laboratory experimental technique consists of an unconsolidated sample (fine or coarse grain), loaded to a certain defined boundary conditions (either stress or displacement controlled). A fracturing fluid is applied under a controlled rate through a borehole and the pressure signature is monitored over time. The sample is then mined and any evidence of fracturing is noted.

Most studies consider that fracture initiation corresponds to the significant reduction of fracturing fluid pressure (under constant fluid flow rates).

2.2.1. *Murdoch* [1993]

One of the first comprehensive experimental and theoretical analyses of hydraulic fracture propagation in soils was published by *Murdoch* [1993a; 1993b; 1993c]. He used a rectangular sample (with a volume of $10\ \text{cm} \times 10\ \text{cm} \times 39\ \text{cm}$) with stress-controlled boundaries. Five sides of the sample were constrained by neoprene air bladders. One side consisted of a transparent loading plate. The boundary conditions were limited to pressures less than $105\ \text{kPa}$ ($15\ \text{psi}$). The samples consisted of partially saturated clayey silt (cohesive particulate material). The fracture fluid was glycerin with a rhodamine dye.

The author found that the magnitude of the water content in the samples influenced the value of the effective fracture toughness (**Figure 2.1** (a)). Interestingly, Murdoch noted the existence of a fluid lag zone at the fracture tip (**Figure 2.1** (b)). This is likely analogous to the lag zone that exists in fluid-driven fractures in brittle materials, with negligible leakoff, and suggests that tensile strength is present. *Murdoch et al.* [1991] concluded that, based on the numerical analysis of *Nilson and Griffiths* [1986], *Nilson* [1986], and *Geertsma and Klerk* [1969], the pressure gradient due to fluid flow in the fracture is small and the pressure distribution is nearly uniform. In other words, the pressure drop required to drive fluid flow within the fracture is small compared to the pressure required to drive the fracture itself. Uniform pressure in the fracture

corresponds to the toughness-dominated regime of hydraulic fracture propagation [*Detournay*, 2004]. Toughness-dominated hydraulic fractures in fully saturated cohesionless materials are also considered in this work.

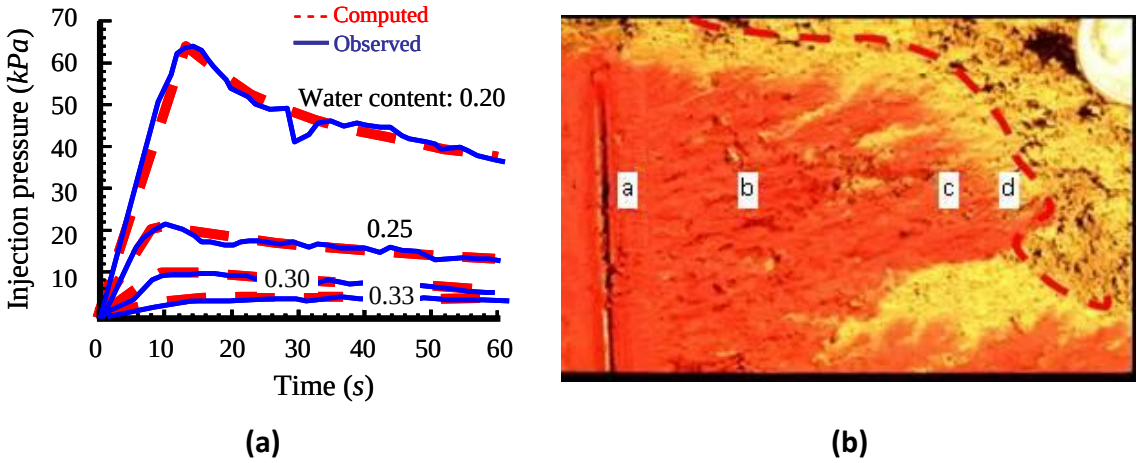

Figure 2.1. (a) Pressure versus time record for injection tests on partially saturated materials [*Murdoch*, 1993c]. (b) Hydraulic fracture with fluid lag letters a, b, c, and d indicate starter slot, parent fracture, "lobes", and leading edge of the fracture, respectively [*Murdoch*, 1993a].

2.2.2. Khodaverdian et al. [2000] and [2009]

Khodaverdian and Mcelfresh [2000] performed hydraulic fracturing injection experiments in a radial flow cell. The sample consisted of 200 mesh sand with confining stresses up to 5000 psi. Fracture fluid was primarily a guar based cross-linked polymer (**Figure 2.2** (a)). They argued that the primary failure mechanism was shear failure within the process zone. This failure process was attributed to significant plasticity and pore pressure increase (and thus reduction of effective stress) at the tip of the fracture. In this case, the process zone of the fracture is considered to be within the leakoff zone.

In general, they found that net fracture pressures increased with decreasing fluid efficiency or increasing leakoff. The fractures generated were complex with multiple branching or segmented fractures.

Khodaverdian et al. [2009] utilized a polyaxial cell, with a volume of $45\ \mathrm{cm}^2$. Boundary stresses were applied by flat jacks. They attempted to mimic field conditions utilizing similar sand properties and by saturating with oil. They scaled the boundary stresses down from field values due to the scale of the experiments (i.e., proximity of boundary to borehole). A shear thinning polymer was used as the fracture fluid. The authors mention that the lower net pressures in their tests compared to those in the literature may be associated with scale issues from early tests. The main conclusion is that mechanisms for stimulation are due to shear induced dilation and effective stress reduction at the tip of the invaded zone.

However, there was no direct observation of fractures in the post mortem excavation of the samples. The authors do conceptualize two regimes of fracture propagation in unconsolidated materials mobility driven and formation damage driven (Figure 2.2 (b & c))[*Khodaverdian et al.*, 2010a]. The two regimes represent the significance of shear failure in the leakoff zone surrounding the propagating fracture. In the mobility driven case the fluid leakoff zone penetrates farther into the formation from the fracture face, increasing the instances of shear failures in this zone. In the formation damage regime the presence of an internal and external filtercake limits the leakoff zone size decreasing shear failure in the leakoff zone.

In these experiments, the fracturing fluid leaked off into the sample obscuring any possibility to directly observe fracture formation. This could be a different phenomenon than what we are describing in this work. The process presented by *Khodaverdian et al.* [2009] is leakoff dominated, perhaps defined as water flooding. In what we present in this work, the control of leakoff is an important experimental technique.

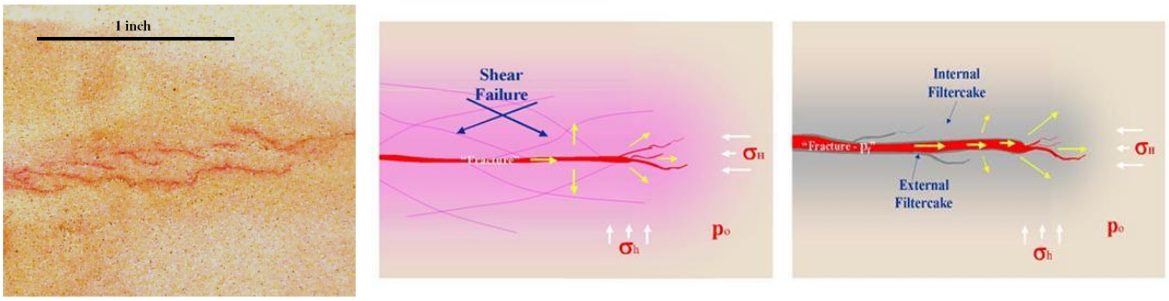

Figure 2.2. (a) Image of a cross-section of a fracture from an injection test [*Khodaverdian and Mcelfresh*, 2000]. (b) and (c) Conceptual schematics for two different regimes; (b) mobility driven, (c) formation damage driven [*Khodaverdian et al.*, 2010a].

2.2.3. Delft Group

One of the most comprehensive experimental programs focusing on hydraulic fracturing in cohesionless soils has been accomplished by a group at Delft University of Technology or the "Delft Group" [*Bohloli and Depater*, 2006; *De Pater and Dong*, 2007; 2009; *Dong*, 2010; *Dong and De Pater*, 2008]. They utilized a number of different sample chambers, in a number of different configurations.

Bohloli and Depater [2006] utilized a pressure controlled axisymmetric sample with a volume of $0.4\ \mathrm{m}\ \mathrm{x}\ 0.51\ \mathrm{m}$. The sample consisted of fine sand, with a mean particle diameter of 110 μm. The maximum confining stresses were $40\ \mathrm{MPa}$. They used a variety of fracturing fluids: viscous Newtonian fluid ($50{,}000\ \mathrm{cP}$), bentonite slurry, and a borate cross-linked gel. The boreholes were orientated both horizontally and vertically. They found a considerable influence on fracture development due to fluid rheology. Also they found that a good wall building fluid is important for generating fractures.

A wall building fluid can be described as a polymer fluid suspension. The long chains of the polymers collect on the fracture face, building an external filter cake (external to the host material). The solvent portion of the fluid (water in guar cross-linked gels) continues to leakoff into the formation, further dehydrating the remaining polymer on the fracture walls. This wall of polymer chains creates additional restriction to fluid mobilizing out of the fracture and into the formation. Therefore, the greater the wall building capabilities the less leakoff is present.

The authors noted that with a viscous Newtonian fluid very high-pressures were obtained without visible fractures. Further, in their tests borehole orientation may play an important role in the initiation of fractures. Finally, in most cases of fracture development “the stress dependence of the maximum pressure agrees better with cavity expansion theory than with conventional fracturing theory.”

De Pater and Dong [2009] and *Dong* [2010] describe a similar axisymmetric cell with a smaller sample size (i.e., a diameter of $152\ \mathrm{mm}$, and a length of $217\ \mathrm{mm}$). This cell is advantageous in that fractures can be directly observed by a CT scanning machine during the tests. They found that the larger scale tests showed qualitatively the same results as the smaller scale tests. The authors observed that fractures tend to propagate in less permeable formations. Further, the significance of permeability on fracture propagation is much stronger than for strength contrasts in unconsolidated materials.

The real time CT scanning also allowed for an analysis of fracture closure pressures [*Dong*, 2010; *Dong and De Pater*, 2007b]. The closure pressures of fractures in samples of fine sand were found to be much lower than the confinement pressures. The post injection pressure analysis using conventional methods (G-function and square-root plot) also overestimated the closure pressure. The closure pressure, determined by observing fracture closure through CT scanning, varied from 44% to 24% of the confining pressure.

The work presented by the Delft University group is the most comprehensive yet. Several scales, fluids, and boundary conditions were utilized. However, the stress ratio (i.e., minimum to maximum) varies significantly. Further, many injection tests resulted in little evidence of fracture, and they are considered to be pure infiltration tests. Nevertheless, the injection pressures are found to be much greater than the confinement. In low stress samples, they found that injection pressures could be up to an order of magnitude greater than the confining stress. At greater confinements, they

found that injection pressures were greater by a factor of 2. Additionally, although the stress ratio was not equal across the test conditions, the maximum injection pressure was greater than even the maximum stress when fractures were observed. Finally, the authors suggest a dependence on maximum injection pressures with confinement. Our results support this and also fit with the data shown in **Figure 2.3** (see Chapter 8 for comparison with our results).

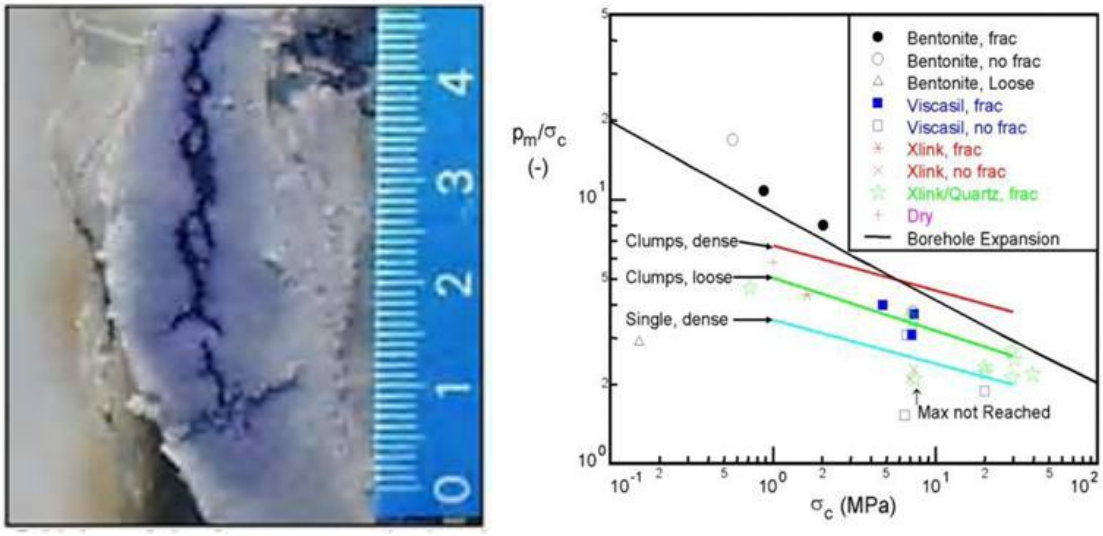

(a) **(b)**

Figure 2.3. (a) and (b) from *De Pater and Dong* [2007]. (a) Cross-section of an excavated fracture created by injecting a cross-linked gel with quartz powder additive the degree of saturation was not measured. (b) Shows the dependence on normalized peak pressure versus confinement.

2.2.4. Georgia Tech Group

Chang [2004] utilized similar tests as described in this work. The work she presented was in dry materials. The samples were primarily dry silica flour (with a mean particle diameter of 19 μm). However, other samples were also used (**Figure 2.4**).

Multiple fracturing fluids were utilized (e.g., silicone adhesives, joint compound). These experiments allowed for excavation and preservation of the fracture after the fracturing process. *Chang* found an increase in fracture thickness with increasing stress [*Chang*, 2004]. This assumed that the leakoff in her experiments was negligible. The work we present here suggests that fracture aperture decreases with confinement while leakoff increases. Therefore her tests may have contained significant leakoff volumes.

Chang's experiments showed peak pressures that were orders of magnitude greater than the applied boundary conditions. She presented three main fracture tip geometries: (1) beveled, (2) fingered, and (3) rounded. The tip geometry was attributed to three mechanisms: (1) cavity expansion for the tip-rounded front, (2) shear bands for beveled front, and (3) leakoff and liquid cavitation for the fingering front. The most important conclusion of her work was that all parts of the material, including at the fracture tip, are likely to be in compression [*Chang et al.*, 2003]. The main results from the work of *Chang* were extended to saturated materials by *Germanovich and Hurt* [2007] and *Hurt et al.* [2005].

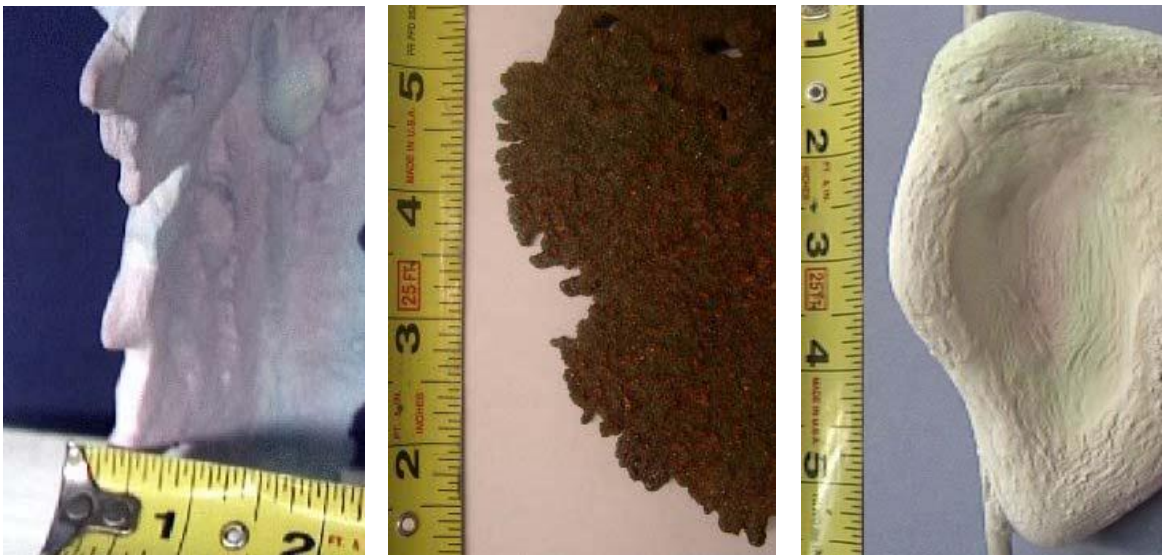

(a) **(b)** **(c)**

Figure 2.4. Three typical fracture fronts of hydraulic fractures observed in dry particulate material [*Chang*, 2004]: (a) beveled front (in silica flour); (b) fingered front (in Georgia Red Clay); and (c) round front (in silica flour).

2.2.5. *Golovin et al.* [2010] and *Jasarevic et al.* [2010]

Golovin et al. [2010] and *Jasarevic et al.* [2010] utilized a stiff cell with a volume of 2 ft^3. They applied boundary stresses mechanically, and then monitored the stress change during the fracture experiment. A low viscosity gel with a variable concentration of solids was injected that solidified after the injection event. The authors cross-sectioned the resulting fracture impression and evaluated the fracture morphology. The authors mention that the fracture plane is generally perpendicular to the minimum principle stress. They found that increasing the injection rate or lowering the solids concentration transitioned fractures from planar to more arbitrary with multiple branching forms. The effects from parameter changes are described as “matrix flooding,

cavity formation, single fracture formation or multiple branching stochastic fracturing" [*Golovin et al.,* 2010]. The authors attribute the arbitrary multiple branching fracture morphology to higher injection rate [*Golovin et al.,* 2010]. That is, the change of injection rates from low to high transitions the fracture form from a single planar fracture to a multiple branching less planar form. They also observe that the net pressure increases with minimum confining stress, similar to our results [*Golovin et al.*, 2010].

Figure 2.5. Image of fracture cross-section from [*Jasarevic et al.*, 2010]. The red injection trace shows the first injection stage; the blue trace was a second independent injection stage. This sample was fine sand, partially saturated with a 30w oil.

2.2.6. Huang et al. [2011]

The experiments mentioned above tend to follow a particular pattern of a three dimensional sample, loaded to some boundary condition, and injected with a fracturing fluid. A different approach has been implemented by *Huang et al*. [2011]. These experiments were conducted utilizing a Hele-Shaw cell with transparent sides as a radial flow device. This allowed for real time visualization of a 2D injection into porous media.

The authors identify four propagation regimes: (1) radial flow regime, (2) leakoff dominated regime, (3) grain displacement regime, and (4) viscosity fingering-dominated regime (**Figure 2.6**). They attribute these regimes to three energy dissipation mechanisms: (1) viscous losses due to leakoff, (2) grain deformation, and (3) fluid flow within the fracture. Following *Chang* [2004] and *Hurt et al.* [2005], the authors conclude that "the mixture of the sand grains and the fluid may have an induced apparent cohesion or apparent toughness". They indicate, however, that "such an apparent toughness may depend on parameters such as the characteristic length scales of the problem". This concept was observed in the super-dislocation model presented by *Wu* [2006].

The analogy between viscous fingering and fractures generated in cohesionless material implies that the fracturing process can be viewed as a viscous fluid invading another viscous fluid [*Chin and Montgomery*, 2004; *Germanovich and Hurt*, 2007; *Huang et al.*, 2011]. The work by *Huang et al.* [2011], however, may be the first physical experiments which verify this fluid-like behavior. Although these experiments do not allow for the evaluation of the impact of boundary stresses, they provide an important insight into the interplay of competing forces on the fracturing process in unconsolidated materials.

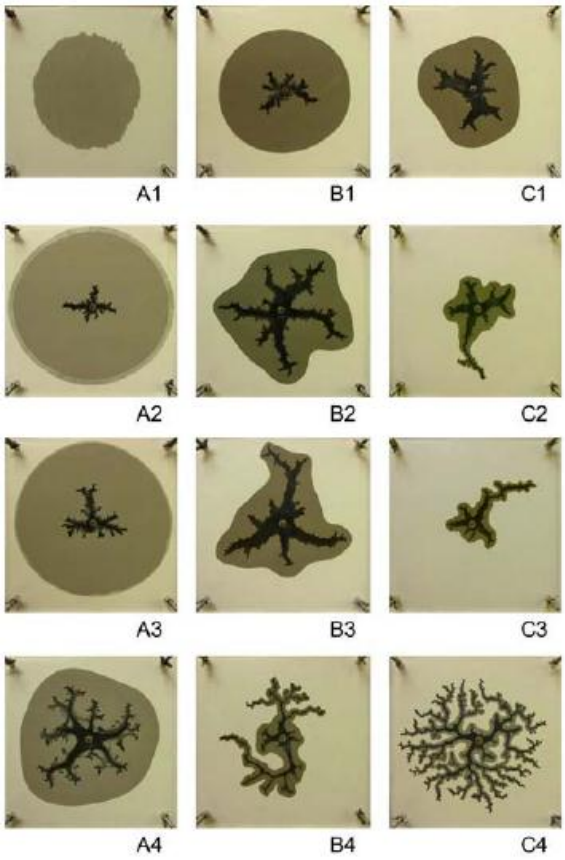

Figure 2.6. Experimental results from [*Huang et al.*, 2011]. The authors inject glycerin into fine sand and record results. They identify four primary flow regimes: (A1), radial flow regime; (A2, A3 and B1), the infiltration- (or leakoff-) dominated regime; (A4, B2, B3 and C1), grain displacement-dominated regime; (C4) viscous fingering-dominated regime.

2.2.7. Summary of literature on experimental modeling

The literature listed above contains the main developments in physical modeling of hydraulic fracturing of unconsolidated fine sand. However, it is certainly not an exhaustive treatment of the subject. There are several authors that performed physical experimental modeling addressing issues of fluid-driven fractures in unconsolidated materials [*Au et al.*, 2006; *Elwood*, 2008; *Ito et al.*, 2009; *Lullo et al.*, 2004; *Shin and*

Santamarina, 2010]. Many utilize significantly different experimental techniques that make comparison to the material presented above (and in this work) somewhat difficult. For example, *Shin and Santamarina* [2010] used an unusual experimental apparatus with a fine grain soil sample. The generated fractures did not initiate from a borehole, but from the soil surface.

In general, most physical experimental observations presented in the literature include a fairly narrow range of experimental parameters, or they may look at only a few parameters. Many attempt to model in-situ conditions for field applications. While this provides a wealth of knowledge for current techniques and processes, the fundamentals of hydraulic fracturing in cohesionless materials still is an open question. Further, fracturing is not sufficiently visualized in 3D. For example, the fracture aperture may prove to be an important and necessary experimental observation to analyze fluid flow in the fracture, or whether traditional fracture mechanics approaches (e.g. apparent fracture toughness) are attempted.

In our own experimental development, we found that trying to discern differences in the fracture morphology might require changes in multiple parameters over several orders of magnitude. In what we present here, we change each of our chosen parameters (i.e., stress, flow rate, viscosity and permeability) by three orders of magnitude. In Section 5.2, we show that some parameters generate an insignificant effect on peak pressure, but significantly affect fracture morphology. Further, we compensate for our limited capabilities by employing dimensional analysis (Section 4.2)

and by varying more readily variable parameters. Nevertheless, it is possible that other parameters can affect fracture morphologies and peak pressures significantly; yet they are not addressed fully here. Finally, our experimental program is unique in that the fracture aperture is preserved after many of our tests. This allows for analysis of parameter changes on fracture aperture.

2.3. Theoretical Modeling

In traditional linear elastic fracture mechanics (LEFM), the process zone is introduced to alleviate the stress singularities at the fracture tip. This process zone harbors inelastic deformation ahead of the crack tip and allows for finite stresses at the crack tip. In LEFM this process zone is small compared to the fracture itself [e.g., *Anderson*, 1995]. In contrast, in unconsolidated materials, the plastic zone may be large in comparison to the fracture, especially for those fractures generated in the laboratory. However, the consequences of a large plastic zone ahead of the crack tip on the modeling aspect are not yet fully quantified.

Several models were introduced to account for crack tip plasticity in soft rock such as tensile failure, continuum damage mechanics, apparent fracture toughness, and crack layer concept [*Martin*, 2000; *Gil*, 2003]. However, the ability to extend LEFM or any of the other proposed models incorporating tip plasticity has yet to be generally accepted as sufficiently accurate for hydraulic fracturing of unconsolidated material. Many authors argue that traditional methods are ill-suited for modeling fractures in unconsolidated cohesionless materials [*Chin and Montgomery*, 2004; *Lullo et al.*, 2004;

Zhai and Sharma, 2005; *Bohloli and Depater*, 2006; *Shin and Santamarina*, 2010; *Xu et al.*, 2010].

From a traditional LEFM standpoint the process (plastic) zone exists in real materials, however, we are not so concerned with physical failure processes at the crack tip. The physical deformation mechanisms within the process zone are not the primary concern, but how to account for the energy lost within the process zone is important. However, due to the complex coupling of fluid flow and matrix deformation many authors chose to develop models that attempt to capture particular deformation characteristics [*Chin and Montgomery*, 2004; *Lullo et al.*, 2004; *Zhai and Sharma*, 2005; *Prodanovic et al.*, 2009; *Shin and Santamarina*, 2010]. For example *Zhai and Sharma*, [2005] and *Khodaverdian et al.* [2009] argue that permeability and porosity evolves with the deformation ahead of the crack tip. Here we consider several of such models.

2.3.1. LEFM-based models

Currently, the common wisdom suggests that traditional hydraulic fracturing models (based on LEFM) are limited in their ability to adequately describe fractures in unconsolidated materials [*Hurt et al.*, 2005; *Bohloli and Depater*, 2006; *Germanovich et al.*, 2007; *De Pater and Dong*, 2007; 2009; *Dong and De Pater*, 2008; *Khodaverdian and Mcelfresh*, 2000; *Khodaverdian et al.*, 2010a; *Zhai and Sharma*, 2005]. Although we agree that the mechanisms that are involved at the crack tip in propagating soft fractures are likely different than in hard rock, it may be that these differences are primarily confined to the process zone at the crack tip. If this hypothesis proves valid,

then perhaps a more traditional approach to fracture modeling could be useful, in some conditions. The literature provides several approaches to modeling soft fracture that follow a more traditional linear elastic fracture mechanics approach, which is essentially based on the concept of effective fracture toughness.

For example, *Murdoch* [1993c] utilized a LEFM approach and an effective fracture toughness concept to model his physical experiments [1993a, 1993b] on hydraulic fracturing in fine-grained partially-saturated particulate materials . Therefore, the host material did possess tensile strength, as indicated by the fluid lag zone (**Figure 2.1** b). This complicates the extension of his work to cohesionless coarse grain materials, as the lag zone is not expected to be present. Murdoch [1993a,b,c] also reports that experiments with various degrees of water saturation. The interpreted fracture toughness was smaller for increasing values of saturation. Nevertheless, even in fully saturated materials he was able to employ the concept of effective fracture toughness to simulate his experimental results.

2.3.2. Fracture tip scale modeling

Tip-scale models are utilized due to the significant difference in deformation characteristics of brittle and unconsolidated materials [e.g., *Settari A.*, 1989; *Franquet*, 1999; *Gil*, 2003; *Chin and Montgomery*, 2004; *Zhai and Sharma*, 2005; *Prodanovic et al.*, 2009; *Wu et al.*, 2009; *Xu et al.*, 2010]. For soft rock, *Papanastasiou* [1997] developed a cohesive zone model in an attempt to explain the discrepancy of much greater in-situ fracture toughness when compared to laboratory values. This was attributed to the

effects of significant plastic deformation at the crack tip. *Papanastasiou* [1997] used a cohesive zone model with effective fracture toughness. This model was specifically designed for soft rocks such as poorly consolidated sandstones and clays. In essence, his propagation criterion is based on critical crack tip opening displacement. That is, when the crack opening opens to a critical value, the crack propagates. The author used a combined finite difference and finite element model to solve the coupled nonlinear fluid flow, rock deformation, and fracture process in an impermeable solid. The result was able to explain the high in-situ fracture toughness due to the shielding of the crack tip by the plastic yielding ahead of the crack tip. He found that due to elasto-plastic deformation, the effective fracture toughness could be more than an order of magnitude greater than that needed for fracture propagation in LEFM. Accordingly, hydraulic fractures were much wider than in LEFM.

Originally developed for nonlinear deformation, *Dong and De Pater* [2008], *De Pater and Dong* [2009] and *Dong* [2010], extended the cohesive zone model to unconsolidated material by reducing the tensile strength within the cohesive zone to a small but non-zero value. The lack of tensile strength in unconsolidated material may complicate the extension of traditional fracture mechanics models.

Zhai and Sharma [2005; 2006] considered that the in-situ stress anisotropy combined with shear failure characteristics is important in determining the size of the fracture zone. The resulting permeability anisotropy is their primary mechanism behind the localized fluid flow. That is, they use the propagation of pore pressure coupled to

the effective stress impact on porosity and permeability. In their model, the fracture is represented by a narrow, highly permeable zone that develops perpendicular to the minimum in-situ stress, just as in traditional fractures.

Shin and Santamarina [2010] argue the shear failure mechanism at the crack tip of cohesionless granular materials [e.g., *Chang*, 2004; *Wu*, 2006] is inconsistent with their observations. Similar to *Zhai and Sharma* [2005; 2006], they consider that inter-particle forces (i.e., skeletal, weight, fluid capillary and fluid drag) increase porosity due to strains normal to the propagation direction. In particular they argue that opening mode fractures do not develop from shear displacements at or near the crack tip as suggested by *Chang* [2004] and *Wu* [2006] for particulate media and for solid materials [e.g., *Newman* 1974]. *Shin and Santamarina* [2010] support their qualitative particle-scale arguments with finite difference numerical modeling showing that "observations categorically imply that previous hypotheses for hydraulic fracture are not compatible with the fundamental behavior of uncemented granular materials."

Wu [2006] presented two mechanisms of fracture propagation. First, utilizing discrete element numerical simulations of injection into particulate materials, the initiation of hydraulic fractures was found to be due to fluidization of the particulate material due to fluid flow. This confirmed several other possibilities on mechanisms of hydraulic fracturing in unconsolidated materials [*Chang*, 2004; *Hurt et al.*, 2005] such as fluidization of the particle matrix ahead of the crack tip. Further developments found that three flow patterns can be identified: (1) fixed bed flow, (2) formation of a stable

cavity and (3) propagation of an unstable cavity [*Wu,* 2006; *Huang and Wu*, 2008]. The second mechanisms applied to hydraulic fractures with limited (or negligible) leakoff. A super dislocation based model of shear banding, [e.g., *Lin and Thomson*, 1986; *Cherepanov et al.*, 1995; *Sadananda and Ramaswamy*, 2001], applied to cohesionless materials, demonstrates a possible non-locality of the fracture criterion [*Wu*, 2006].

A coupled DEM-CFD modeling of fluid flow media focused on the critical injection velocity during the injection process [*Zhang and Huang*, 2011]. The results indicate shear failure due to well bore expansion. They mimic those shown in the literature on physical [*Alsiny et al.*, 1992; 1994; *Chang*, 2004; *Bohloli and Depater*, 2006] and numerical experiments based on a continuum approach [e.g., Wu, 2006; Kim, 2012]. Physical experiments showed similar shear banding by fluid injection events [*Chang*, 2004; *Bohloli and Depater*, 2006] and by mechanically induced borehole expansion [*Alsiny et al.*, 1992; 1994]. These shear failure events could be an important consequence to preferential fluid flow during the cavity expansion process [*Chang*, 2004; *Germanovich et al.*, 2007; *Zhang and Huang*, 2011].

2.4. Summary

Existing experimental results suggest that hydraulic fractures in unconsolidated particulate materials tend to develop primarily in the direction of least principle stress [*Murdoch*, 1993a; 1993b; 1993c; *Khodaverdian and Mcelfresh*, 2000; *Hong* 2004; *Hurt et al.*, 2005; *Bohloli and Depater*, 2006; *Murdoch et al.*, 2006; *De Pater and Dong*, 2007; 2009; *Germanovich et al.*, 2007; *Dong and De Pater*, 2008; *Golovin et al.*, 2010]. Further,

the required pressures to initiate and propagate hydraulic fractures in cohesionless materials often require injection pressures significantly greater than the least principle stress, as others have shown [*Khodaverdian and Mcelfresh*, 2000; *Hong* 2004; *Hurt et al.*, 2005; *Bohloli and Depater*, 2006; *Murdoch et al.*, 2006; *De Pater and Dong*, 2007; 2009; *Germanovich et al.*, 2007; *Murdoch et al.*, 2006b; *De Pater and Dong*, 2007; *Dong and De Pater*, 2008; *Golovin et al.*, 2010].

The modeling of hydraulic fracturing in cohesionless materials can benefit from quantification of the propagating fracture apertures. However the measurement of fracture width is typically not attempted. Techniques in the literature to verify the existence of fracture are: images from CT scanning [*De Pater and Dong*, 2009], traces of colored fracturing fluid infiltration in a host material [*Murdoch*, 1993a; 1993b; 1993c; *Khodaverdian and Mcelfresh*, 2000; *Bohloli and Depater*, 2006; *Golovin et al.*, 2010], the use of colored proppant [*Jasarevic et al.*, 2010], interpretation of fluid flow conditions or measurables [*Khodaverdian et al.*, 2009], or direct visualization [*Huang et al.*, 2011]. These techniques determine fracture orientation and general shape. However, these results cannot (yet) reliably determine fracture aperture and leakoff thickness under known stress conditions. Observation of fracture aperture may be the one experimental result that allows us to reliably extend existing fracture models to soft fractures with an unknown and undeterminable fracture aperture. The experimental technique we developed is an important factor in developing the basis for our modeling. In particular,

our tests allow for the preservation of fracture aperture during excavation and cross sectioning of the solidified fracture.

3. EXPERIMENTAL APPROACH FOR FLUID-DRIVEN FRACTURES OF PARTICULATE MATERIALS

3.1. Introduction

In our tests, the general governing parameters important for propagating fractures are fluid rheology, injection flow rate, confining stresses and permeability of the formation. An important feature of our experimental technique is the preservation of fracture aperture. The number of studies that measured fracture aperture are limited [*De Pater and Dong*, 2007; *Dong and De Pater*, 2008; *Dong*, 2010].

A schematic of the general test procedure is shown in **Figure 3.1.** By utilizing the silicone injection fluid the post-fracture leakoff was constrained. This allowed for preservation of the fracture aperture for post-experiment evaluation. The main experimental result is the characterization of the fracture form (leakoff thickness, fracture aperture and overall fracture geometry). During the test, we record injection pressure (that must be calibrated for fracture pressure), flow rate (if not constant), global sample response (pore fluid and sample volume expansion or contraction). Typically, we prescribe the injected volume (less than $625\ \mathrm{ml}$) at a fixed injection rate. Keeping in mind industrial applications and observations in nature (e.g., magmatic and sand dikes) we designed our experiments to limit leakoff and promote efficient fracture. Other experimental work in cohesion less materials typically exhibit low fracture efficiencies with high-leakoff [*e.g., Khodaverdian and Mcelfresh*, 2000; *Bohloli and*

Depater, 2006; *De Pater and Dong*, 2007; *Dong and De Pater*, 2007b; *Golovin et al.*, 2010; *Jasarevic et al.*, 2010; *Khodaverdian et al.*, 2010a].

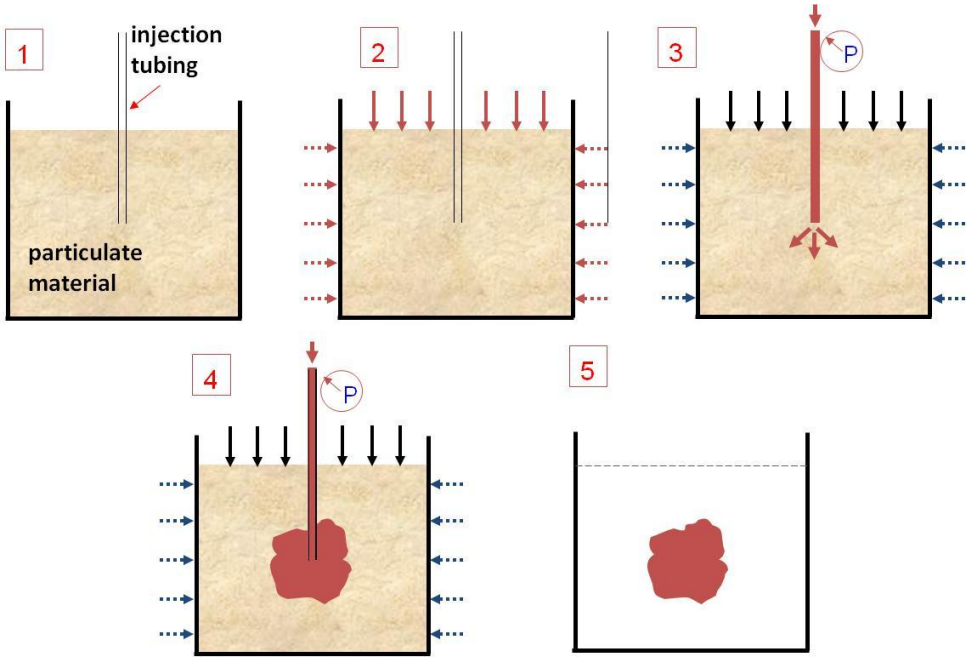

Figure 3.1. General procedure of laboratory experiments: (1) preparation of sample with injection tubing placed in particulate material, (2) loading of sample, (3) initial injection of fracturing liquid, (4) monitoring of injection pressure during hydraulic fracturing, and (5) solidification and excavation of hydraulic fracture.

In this chapter, we describe our experimental processes and procedures. First, we describe the equipment including loading frames, pressure cells, and injection systems. The following section describes the fluid rheological properties and such sample properties as permeability, strengths, and deformation characteristics. Then a description of the techniques of preparing samples and conducting the injections tests are presented. Finally, we present the calibration of measured quantities and test

results. The results and analysis of our injection tests are described in Chapters 4 and 5 for silicone injection tests and Chapter 7 for cross linked guar injection tests.

3.2. Equipment

Our experimental procedures were developed around a number of different experimental cells. The results presented here are primarily tests that were conducted in two pressure controlled cells, described in detail below. However, a number of other cells were utilized to refine procedures and develop techniques. A description of the auxiliary cells and some results are described in Appendix D.

3.2.1. Experimental cells

The pressure cells are similar in form and operation to "triaxial" cells used for material testing in geotechnical engineering disciplines. The sample is contained within a cylindrical, flexible, and impermeable membrane. The sample is constrained vertically by two rigid end platens, one mounted to the fixed base plate. The injection source is passed through the lower platen and base plate, mounted and sealed prior to creating the sample. The top platen is free floating and only supported by the sample. A loading ram passes through the top of the assembled cell to apply the vertical load to the top platen. A general schematic of the apparatus is shown in **Figure 3.2**. In this section the various cells are described in greater detail.

3.2.1.1. Large Triaxial Cell

The “large” scale triaxial cell (LTC) shown in **Figure 3.2** contains a cylindrical sample (with a diameter of 12 in and a height of 22 in). The maximum hydrostatic load applied to the sample was 80 psi. The cell itself is mounted in a large steel loading frame.

The loading frame (**Figure 3.2**) consists of two steel plates with a thickness of 1 in supported by four steel tubes with a diameter of 3 in that contain stainless steel treaded rod with a diameter of 1 in to support the frame under loading. The top plate has a pneumatic cylinder bolted to it between the frame and the cell. This pneumatic cylinder applies the vertical load to the sample. The top of the frame lifts off the frame base plate allowing free access to the cell during sample preparation, post experiment excavation, and cell assembly and disassembly.

The base plate of the LTC is shown in **Figure 3.3**. This illustrates the injection source configuration just prior to affixing the membrane and creating the sample. The tubing for the injection source passes completely through the base plate of the LTC. A compression fitting is affixed to the base plate to seal the sample at the location where the injection tube passes through the base plate. The injection source outlet is centered within the soil sample (**Figure 3.3**). Many different configurations of injection sources were utilized. However, the general configuration remained the same. A more thorough discussion of the injection source is available in Appendix E.

The pore fluid within the sample is controlled through the upper and lower platens. The lower platen is fixed to the cell base plate. The upper platen is free to move. The platens have two holes to provide pore fluid in and out of the sample. Each of the platens has a polycarbonate plate with numerous large holes drilled in it. A number of plastic wire mesh layers are affixed to the plate. This wire mesh is arranged from coarse to fine to assist in distributing the pore fluid while restraining the mobilization of particles out of the sample space. Finally, a piece of filter paper is placed between the sample and plastic mesh layers. The upper platen is connected by two flexible tubes that pass outside the sample, inside the cell, to the lower base plate. The membrane that provides the lateral confinement is sealed around the top and bottom platens.

The membrane used to provide the lateral confinement was a gum rubber tube with a diameter of $12\ \text{in}$, with a wall thickness of $0.125\ \text{in}$. Originally the cell utilized a latex membrane with $0.06\ \text{in}$ wall. These proved to be fragile, however, and were often damaged during the testing process. Therefore, we sourced the gum rubber tube that was much more robust. There is a considerable difference in the stiffness of the two different membranes, but there is no evidence of differences in experimental results.

3.2.1.2. High-pressure Triaxial Cell

The High-pressure Triaxial Cell (HPTC) is constructed from a traditional rock triaxial cell. The sample size has a diameter of $4\ \text{in}$ and a height of $8\ \text{in}$. A new base plate and top platen were fabricated to facilitate an unconsolidated sample (**Figure 3.4**

and **Figure 3.5**). Originally, a latex membrane with a thickness of 0.03 in was used for lateral confinement. This proved unstable at confinement pressures above 500 psi. Therefore, a gum rubber membrane, similar to one in the LTC, was used. The injection source was of the same configuration as the one from the LTC. Every attempt was made to create the same experimental conditions in the HPTC as in the LTC with the obvious exception of confining stresses and sample size.

3.2.2. Injection systems

The injection system consists of an injection source, displacement chambers, pressure gauge, injection pump and the associate tubing. These components are described in more detail below.

3.2.2.1. Injection Source

The geometry of the injection source had a significant impact on fracture geometry. In our experiments, it was apparent that the size of the injection source must be orders of magnitude larger than the scale of the inhomogeneity of the sample. There was a considerable development in the configuration of the injection source from a single outlet hole, to a linear slit, to the cylindrical configuration used on a majority of the tests. A complete description of the different source geometry and its effects on experimental results is available in Appendix E.

Cylindrical source geometry was utilized for the majority of the results presented in this work. This is manufactured by drilling a series of holes into the injection tubing

(typically with 90 degree phasing) along a length of tubing. The holes are then covered with a 250 micron stainless steel mesh soldered in place then covered with a small piece of filter paper; this eliminated the infiltration of the unconsolidated material during compaction and saturating processes.

Typical injection source construction is shown below in **Figure 3.6.** A drilled piece of stainless steel tubing is shown illustrating the spacing and phasing of the perforations along with the crimped tube with stainless steel mesh silver soldered in place over the perforations. A number of various tubing sizes were used from 0.25 in to 0.5 in. For comparison tests between the LTC and HPTC a tubing of 0.375 in was used. This provided the best compromise in viscous losses and overall tubing size.

3.2.2.2. Injection Pumps

Three pumps were utilized in the injection test, a small triplex plunger pump, a single diaphragm plunger pump and a large triplex plunger pump. The specifications of each pump are shown in **Table 3.1**. Our tests were conducted at a constant injection rates, with a prescribed injection amount.

The small triplex pump allowed for precise control of the flow rate. However, the flow rate was not adequate to produce fractures with some of the experimental parameters (i.e., low viscosity fluids, in high-permeability samples, at high stresses). The single diaphragm pump provided a necessary increase in flow rate but there were significant pressure fluctuations that made interpretation of the pressure curves difficult. For example, the pressure curves in **Figure 3.7** show the pressure signature

recorded from the diaphragm pump (a) and the large triplex pump (b). The large triplex pump proved useful at high rates for producing smooth pressure signatures.

3.2.2.3. Pressure Gauge, Displacement Chamber and Associated Tubing

The tubing connecting the injection source to the displacement chamber consists of only a ½ in NPT elbow and union. This limited the viscous losses due to fluid flow of our fracturing fluid, within the injection tubing. The connecting elbow was drilled and tapped for connection of the pressure gauge/transducer.

The pressure gauge was connected to the elbow with a short length of high-pressure nylon tube. The tube was filled with oil to limit the volume of fracturing fluid that entered the nylon tubing. The nylon tubing became important when the two large pumps were operated due to electrical interference with the pressure transducers. The pressure gauge was connected to a data acquisition system to monitor and record injection pressures.

The pumps were not designed for pumping high-viscosity fluids. Therefore, the displacement chamber separated the pump fluid from the fracturing fluid. It consisted of a stainless steel cylinder with two removable end caps. Inside was a piston with a double O-ring seal to separate the pumping fluid from the fracturing fluid. The displacement chamber allowed for exact volumes of injection at a constant rate. The pump side of the displacement chamber was filled with water or oil, the opposite what was being pumped. This allowed for an additional check of the injected volume. The

displacement chambers were connected to the various pumps by a flexible high-pressure hydraulic line.

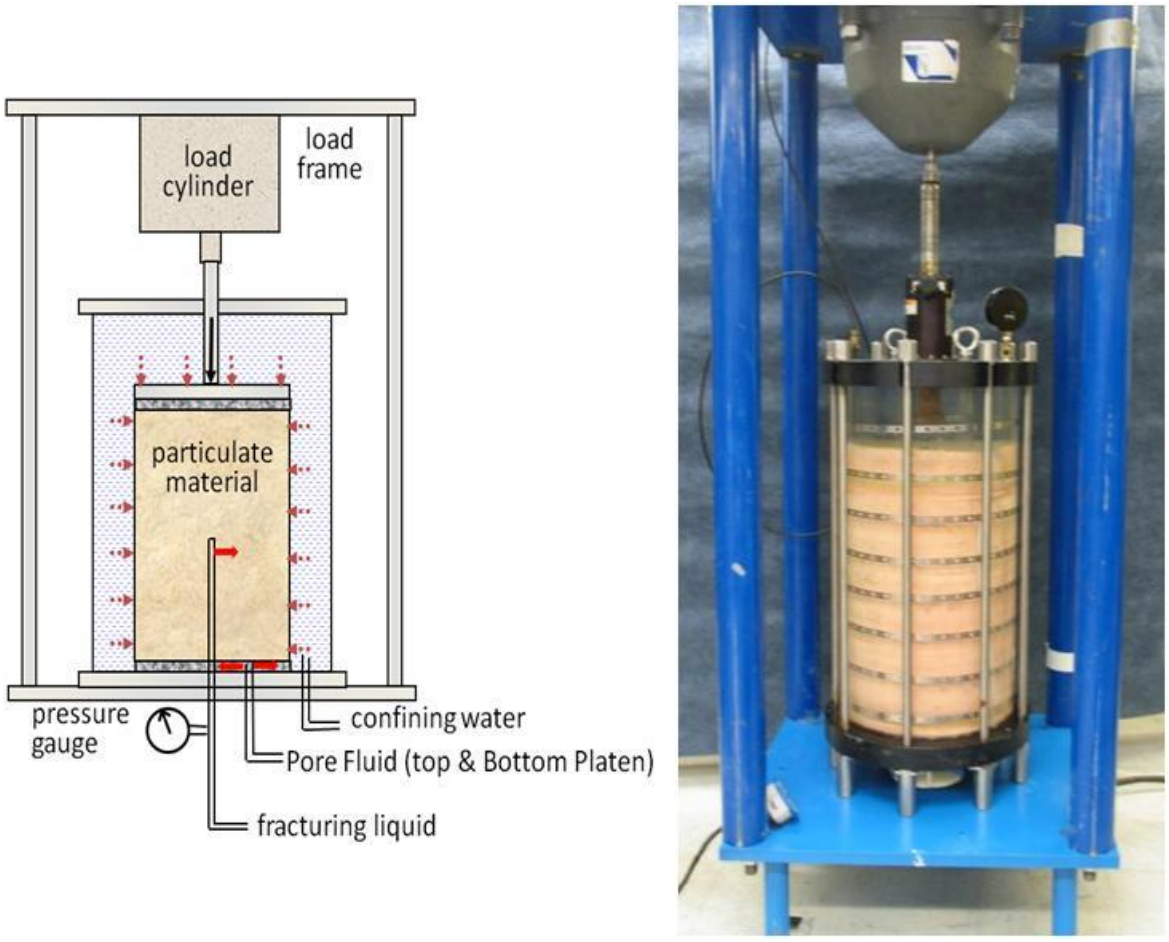

(a) **(b)**

Figure 3.2. (a) Schematic of general experimental apparatus and (b) large triaxial cell.

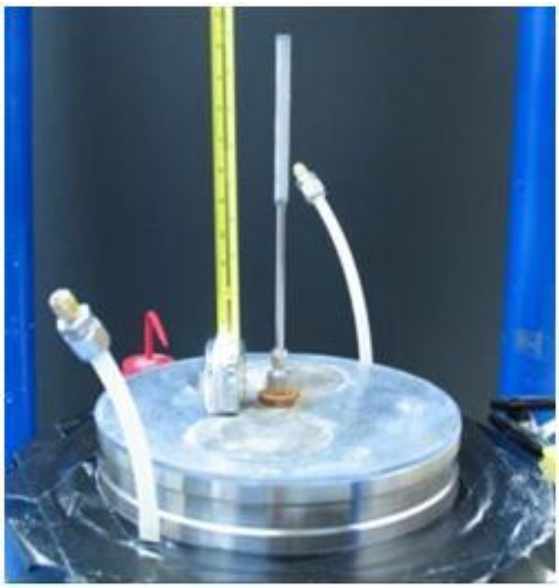

Figure 3.3. Base plate of the large triaxial cell. The diameter of the sample base plate is 12 inches.

(a) **(b)**

Figure 3.4. (a) Assembled high-pressure cell and loading frame. (b) Sample after outer cell is removed. The sample diameter is 4 inches.

Figure 3.5. High-pressure cell base plate and injection source.

Figure 3.6. Injection source construction. Tubing diameter is 0.375 inches.

Table 3.1. Specifications for injection pumps.

Pump	Maximum Flow Rate	Maximum Pressure
Small Triplex	50 ml/min	5000 psi
Single Diaphragm	1700 ml/min	5000 psi
Large Triplex	15000 ml/min	5000 psi

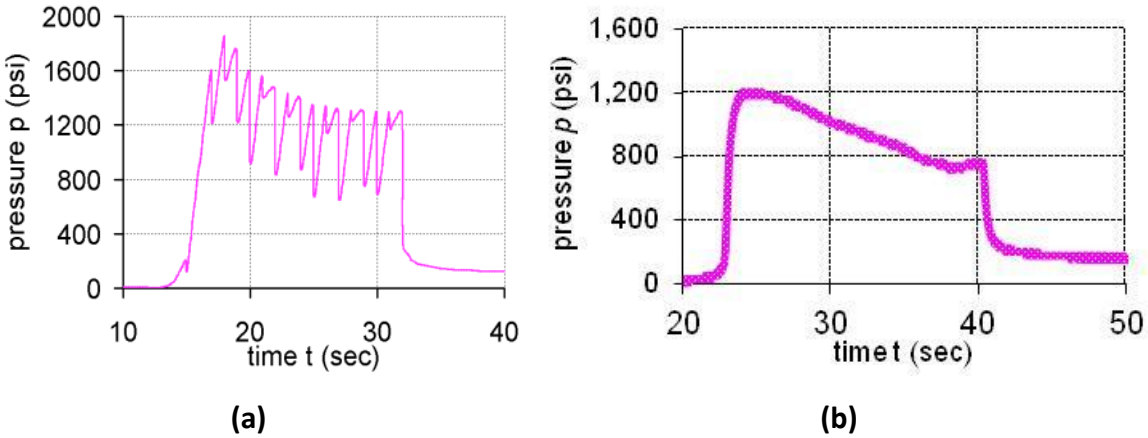

Figure 3.7. Plots from two different pumps: (a) diaphram and (b) triplex. The diaphram pump causes significant fluctuations in the injection pressure. While such data are still useful, the triplex pumps provide a smooth pressure-time curve.

3.3. Fracturing Fluids

The fracturing fluids were chosen due to a number of various requirements. First, a high-viscosity was needed to reduce the volume of leakoff. Second, the fluid must solidify in a saturated environment. Third, the fluid must be able to be purged of the injection system, so the system can be reused. Finally, the fluid must be immiscible with the pore fluid. All of these properties were necessary to adequately define the fracture geometry and post experiment inspection of the fracture aperture and leakoff thickness.

3.3.1. Silicone adhesive

We used silicone adhesive for the fracturing fluid in tests when fracture aperture was preserved. This fluid is a high-viscosity Herschel-Bulkley fluid [*Herschel and Bulkley*, 1926]. The high-viscosity is beneficial in that the fracture does not close after the experiment is complete, even though confining stresses are maintained until the fluid is fully solidified (typically two days). Other benefits include a moisture cure process that readily solidifies in submerged conditions (when utilizing water as pore fluid). The high-viscosity allows for a more moderate fluid injection rate. Injection rate does reach a maximum realistic value due to the limited sample size. For example, typically tests in our large cell at injection rates of $5000\ \mathrm{ml/min}$ had a duration of $2\ \mathrm{s}$. Utilizing the high-viscosity fluids, we were able to propagate fractures at much lesser rates. We utilized three different silicone adhesives. The specifications from the manufacturer (Dow Corning, http://www3.dowcorning.com/) are listed in **Table 3.2**. All of the silicone

adhesives are a one part RTV silicone rubber. The RTV cures by the release of acetic acid when exposed to moisture. The use of pore fluids other than water (e.g., oil, glycerin) impeded the solidification of the silicone adhesive.

There were several tests conducted with glycerin as the pore fluid. The test results in both peak pressures and fracture morphologies were identical to tests with water as the pore fluid. This indicates that the solidification process of silicone adhesive does not significantly hinder or alter the fracturing or leakoff process at our time scales.

The rheology of the silicone adhesive allowed for a qualitative analysis timing of the injection sequence. This is illustrated in **Figure 3.8**. The high-viscosity fluid, if placed carefully in the displacement chamber, maintains a fairly distinct boundary between the different fluid colors. The fracture cross section shown in **Figure 3.8** shows the result. The white fluid was first to be injected into the formation. The black fluid follows. This is accomplished by way of a single injection event. The viscous nature of the silicone adhesive allows the fluid in the displacement chamber to act as a plug, thus a limited degree of fluid mixing occurs. A thorough description of the leakoff and aspects of fracture growth due to the colored injections are presented in Chapter 4.

Given the polymer nature of the silicone adhesive there may be two distinct types of leakoff processes, the formation of an internal or external filter cake. First internal filter cake is the flow of whole injection fluid into the formation or pore space [*Economides and Nolte*, 2000]. This is due to fluid displacement from the pressure gradient between the injection fluid and pore fluid. The external filter cake is due to the

inability of the polymer chains to invade the pore space. The solvent separates from the invading fluid and leaks off into the formation, due existence of high-pressure gradients. The polymer chains build up on the fracture walls and act as an additional porous matrix. The consolidated polymer chains absent of the formation matrix are considered the external filter cake. These processes are not mutually exclusive and typically are observed together, if the polymer is impeded from free flowing into the formation.

The leakoff characteristic of the silicone adhesives were analyzed through post sample cross-section. As shown in **Figure 3.8** the leakoff surface is fairly stable especially in the proximity to the borehole (tan colored region). The tan color comes from the mixing of white silicone and the F110 quartz sand. The black region is pure silicone adhesive, there is no evidence that leakoff has occurred with the black fluid. The locations of leakoff with the black fluid are primarily at the tips of the fracture. If the leakoff process was constant rate of fluid mobilization into the sample matrix (perpendicular to fracture growth), then we would expect a gradation in the color of the leakoff zone along the length of the fracture. It appears the majority of the leakoff process is confined to the tip region of the propagating fracture, thus during fracture extension the fluid flow is primarily parallel to the fracture face. There may be a small region of external filter cake, however, the analysis of it is not considered in this work. There was no further attempt to characterize the possible development of the internal or external leakoff. In this work, we consider the leakoff of the fracturing fluid as a singular process.

3.3.2. Guar-based fracturing fluids

The guar-based fluids were an attempt to utilize an industrial fracturing fluid in our tests. The fluid is a proprietary mixture that was provided by Schlumberger (SLB). It can be described as a guar cross-linked gel with a resin component that allows for solidification of the leakoff region. For simplicity we call this fluid a guar gel. A picture of the mixed fluid is shown in **Figure 3.9.**

Table 3.2. Silicone adhesive specifications (http://www3.dowcorning.com/). The term "skin over time" is defined as the time when the skin starts to appear on the surface of the fluid, when exposed to ambient humidity.

Silicone	Skin over time	Cure Time	Viscosity
732	10 min	24 hrs	55000 cP
734	10 min	24 hrs	43000 cP
739	20-30 min	24 hrs	155000 cP

Figure 3.8. Crossection of injection test with silicone. The white fluid was the first fluid injected followed by the black. Other than the color there is no diferance in the fluid properties. This is acomplished by a single injection event. Scale bar represents 1 inch.

Figure 3.9. Guar based fracturing fluid. The fluid was poured out of the glass beaker and remains on a flat surface in a single form.

3.4. Rheological properties of fracturing fluids

The rheological properties of the fracturing fluids were measured with two separate testing procedures. For high fluid shear strain rates, flow tests were conducted with lengths of tubing of various diameters. For characterizing the fluid viscosity at low shear strain rates a viscometer with a cone (4^{o}) and plate (40 mm) geometry was utilized [e.g., *Macosko*, 1994]. We first describe the fluid flow tests, and then incorporate the rheometer data to characterize the fluid for the range of shear rates of interest.

The fluid flow tests were conducted using a constant flow rate and monitoring the pressure drop. The pressure gauge is placed at one end of the tubing with the

displacement chamber in a similar configuration as used in our tests. The other end of the tubing is placed in an open container. The pump is set to maintain a specific flow rate. The pressure is recorded over time and when flow is established and then the steady state pressure is noted. To calculate the rheological parameters from our tests we use a number of constitutive fluid flow models.

Among different constitutive models of polymer-based fluids [e.g., *Bird et al*., 1987], the Herschel-Bulkley law [e.g., *Herschel and Bulkley*, 1926]

$$\tau = \tau_o + K\dot{\gamma}^n \tag{3.1}$$

represents an important generalization of models typically used to characterize rheology of many petroleum fluids [e.g., *Hemphill et al.*, 1993]. Here τ_o is the yield stress, K is the consistency index, and n is the power law exponent (also called the fluid flow behavior index). The power law fluid flow model

$$\tau = K\dot{\gamma}^n \tag{3.2}$$

is a special case of (3.1) when $\tau_o = 0$. If $n = 1$, eq. (3.1) is reduced to the Bingham plastic model

$$\tau = \tau_o + K\dot{\gamma} \tag{3.3}$$

Models (3.1) – (3.3) are used below to characterize rheology of the silicone and guar-based fluids used as a fracturing fluid in our experiments.

3.4.1. SILICONE FLUID

3.4.1.1. 732 Silicone fluid ("medium" viscosity)

We first start by estimating the pressure drop utilizing the fluid flow parameters measured by SLB along with the power law fluid model. The values of the consistency index, K, were measured, with the SLB cone-and-plate rheometer [e.g., *Macosko*, 1994], between 500 to 600 $Pa\ sec^n$. The fluid flow behavior index, n, was measured to be 0.16 to 0.20. Due to complexities of the fluid (e.g., high viscosity and curing process) the strain rates achievable with the cone and plate rheometer are low in comparison to the pipe flow experiments. To test the application of the derived fluid flow parameters, we calculate the expected pressure loss within the pipe utilizing the power-law model and the parameters measured with the SLB rheometer. If we use the standard model for flow of a power-law fluid (3.2) in a circular pipe, the pressure drop in the pipe that corresponds to these parameters is given by [e.g., *Chilton and Stainsby,* 1998]

$$\Delta P = \left(\frac{Q(3+1/n)}{\pi R^3} \right)^n \frac{2KL}{R} \tag{3.4}$$

where Q is the flow rate, R is the tube radius, and L is the tube length. The pressure drop for each flow rate was measured for at least three separate experiments and the average is listed (**Table 3.3**). The comparison of results from calculating the pressure drop using (3.4) and the measured pressure drop is presented in **Table 3.4**. We can see a reasonable estimation of the pressure drop at the lowest flow rate of 50 ml/min. However, there is a significant underestimation of the pressure drop at higher flow

rates. The considerable difference between the calculated and measured pressure drop suggests that the rheological parameters, K and n, may be inconsistent at shear rates exhibited in our fluid flow tests. It may also indicate that, if the same fluid flow parameters are utilized, the power law model (3.2) is not representative of the fluid flow across the range of shear rates we are interested in ($0.1\ \text{sec}^{-1}$ to $1000\ \text{sec}^{-1}$).

Table 3.3. Pipe flow experimental parameters and data for 732 silicone fluid.

TEST	Flow rate		Inner Diameter		Length	Pressure	
	m^3/sec	cm^3/min	cm	in	m	Pa	psi
1	8.33E-07	50	1.0	0.402	1.83	8.76E+05	127
2	8.33E-06	500	1.0	0.402	1.83	2.76E+06	400
3	1.67E-05	1000	1.0	0.402	1.83	4.48E+06	650
4	2.50E-05	1500	1.0	0.402	1.83	5.58E+06	809
5	8.33E-05	5000	1.0	0.402	1.83	1.45E+07	2103

Table 3.4. Pipe flow calculated versus measured pressure drop for 732 silicone fluid.

TEST	Measured Pressure		Calculated Pressure	
	Pa	psi	Pa	psi
1	8.76E+05	127	6.57E+05	95
2	2.76E+06	400	9.94E+05	144
3	4.48E+06	650	1.13E+06	163
4	5.58E+06	810	1.21E+06	176
5	1.45E+07	2100	1.50E+06	218

Because of this disagreement, we then estimated the rheological properties of the fluid directly from our data. We utilize the pressure drop solution (3.4) for the pipe flow of the power law fluid (3.2). Using the least square method (LSM), we determined the values of K and n required to obtain the best fit. The solid (red) curve in **Figure 3.10** shows the results of fitting equation (3.4) to the experimental data (blue triangles). The dashed (green) lines represents the flow rate computed based on eq. (3.4) and the SLB parameters generated though the analysis of rheometer data. As can be seen, the SLB parameters do not provide a good fit at strain rates exhibited during our pipe flow tests. Furthermore, the fluid flow parameters derived using our experimental results do not match the rheometer results at low shear strain rates.

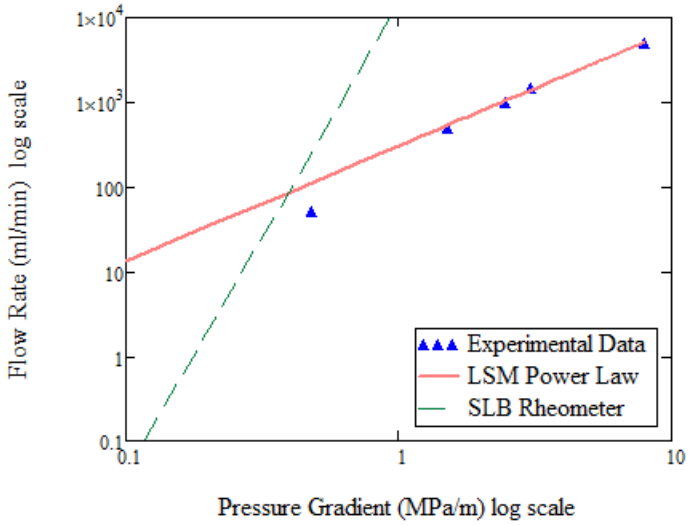

Figure 3.10 Power-law fluid flow model comparison to experimental results in log scale. Fitted model parameters (red line) are $K = 137\ Pa\ sec^n$, $n = 0.74$, the rheometer parameters (green dashed line) are $K = 550\ Pa\ sec^n$, $n = 0.18$

Given the non-slumping nature of the silicone fluid, one may expect that some magnitude of yield stress would be a characteristic of this fluid. Therefore, we also used a solution for pressure drop in the circular pipe with the Herschel-Bulkley fluid [e.g., *Chilton and Stainsby,* 1998]

$$\frac{\Delta P}{L} = \left(\frac{Q(3+1/n)}{\pi R^3} \right)^n \frac{2K}{R} \frac{1}{(1-\mathrm{X})\left(1-a_1\mathrm{X}-a_2\mathrm{X}^2-a_3\mathrm{X}^3\right)^n} \qquad (3.5)$$

where

$$\mathrm{X} = \frac{2\tau_o L}{R\Delta P}, \quad a_1 = \frac{1}{2n+1}, \quad a_2 = \frac{2n}{(n+1)(2n+1)}, \quad a_3 = \frac{2n^2}{(n+1)(2n+1)} \qquad (3.6)$$

Using again the least square method, we determined K, n and τ_o that provide the best fit of (3.5) to our pipe flow data. The fitting results are shown in **Figure 3.11** (solid line), where we also plotted (dashed line) the fitting results for the power law fluid shown in **Figure 3.10**. The Herschel-Bulkley model appears to provide the best fit (**Figure 3.11**) of both data sets, across the full range of shear strain rates. At low shear rates, the derived H-B parameters fit the data generated by the SLB rheometer. At high shear rates, the H-B model fits well with the data from the flow tests.

Figure 3.12 shows the shear stress calculated based on the rheological parameters obtained from our test results (red and blue curves) and based on the parameters measured with the rheometer (green curve). Finally, **Figure 3.13** shows the effective viscosity of the fluid calculated by,

$$\mu_{eff} = \frac{\tau}{\dot{\gamma}} \tag{3.7}$$

The resulting model parameters are listed in **Table 3.5**.

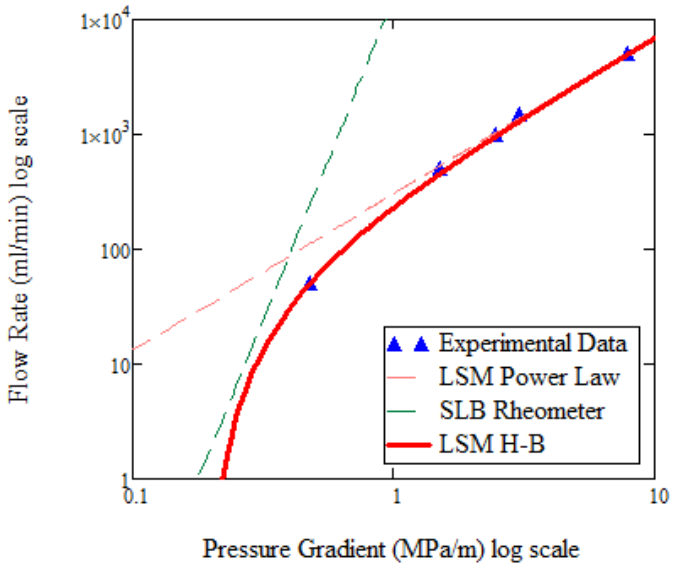

Figure 3.11. Herschel-Bulkley fluid flow model comparison to experimental results in log scale. Fitted model parameters (red line) are $K = 123\ Pa\ sec^n$, $n = 0.75$, and $\tau_o = 475\ Pa$. The blue triangles represent the experimental data points.

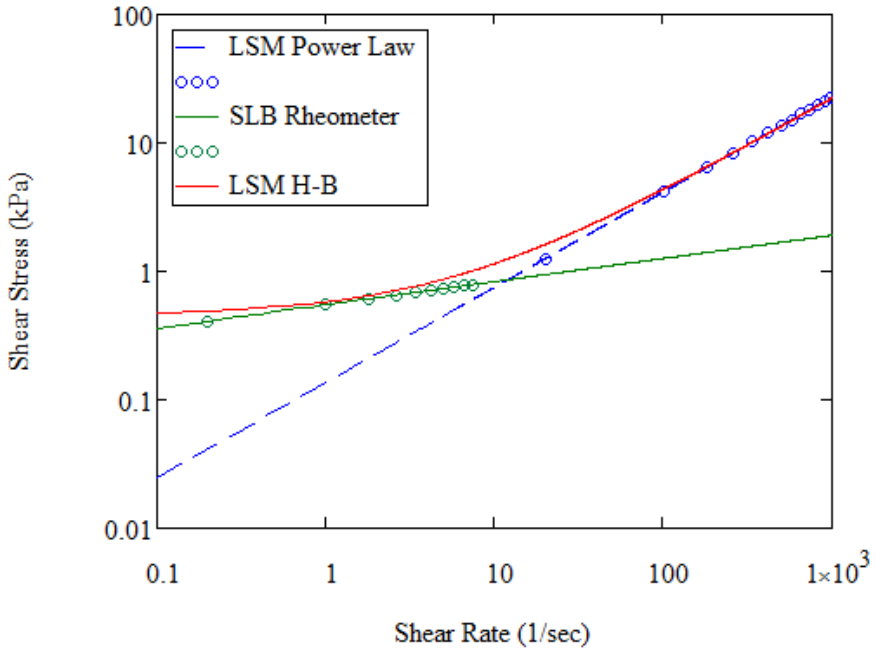

Figure 3.12. Shear stress versus shear rate for two power-law models for low and high shear rates of 732 silicone along with the HB model for both ranges of shear rates. The dots represent the valid shear rates for the respective power-law models.

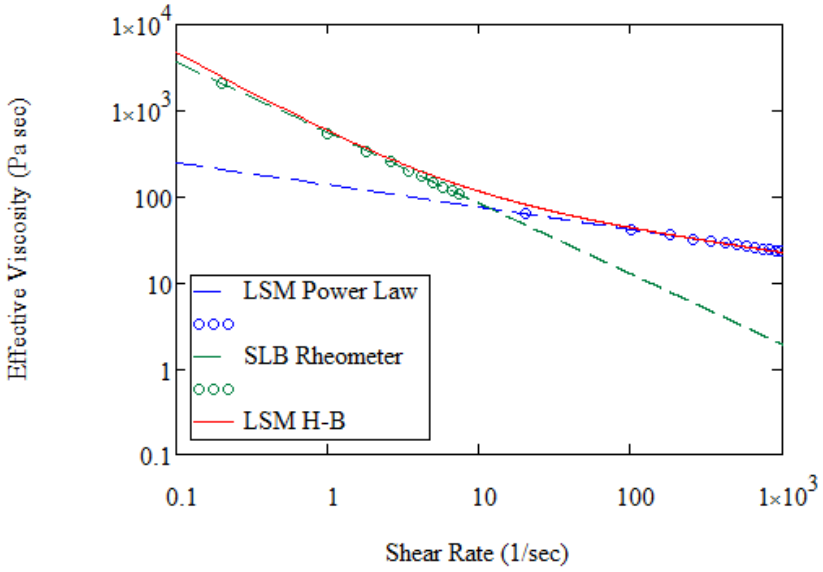

Figure 3.13 Effective viscosity (3.7) versus shear rate for the 732 silicone fluid for the experimental and rheometer parameters (**Table 3.5**). The dots represent the valid shear rates for the respective power-law models.

Table 3.5. Table of K and n parameters for silicone and guar.

MATERIAL	MODEL	K	n	τ_o
		Pa sec^n		Pa
732 Silicone	LSM H-B	123	0.75	457
	LSM Flow Test Power Law	137	0.74	0
	SLB Rheometer Power Law	550	0.18	0
739 Silicone	LSM H-B	603	0.60	485
	LSM Dow Corning Power Law	971	0.51	0
	SLB Rheometer Power Law	1190	0.19	0
Guar-based	LSM Power Law	11	0.41	0
	SLB Rheometer	50	0.33	0

3.4.1.2. 739 Silicone fluid (high viscosity)

A similar exercise was accomplished for the high viscosity silicone fluid (739)**.** The high viscosity fluid is similar to the medium viscosity fluid; the curing process is the same. To increase the viscosity there is a reduction in the amount of solvent. For the high viscosity silicone, we have data from the manufacturer (Dow Corning) of viscosity at three shear rates (**Table 3.6**). We have completed a limited number of flow tests with the high viscosity silicone fluid (739) and our results agree with this data. Similar to above, at low shear strain rates, we use the rheometer derived parameters of the

power-law model, provided by Schlumberger. For high strain rates, we utilize the data provided by Dow Corning and compute the fluid low parameters utilizing a power-law model. **Figure 3.16** shows the power-law model from the rheometer, and the power-law fitting of the data from **Table 3.6**. We take these results and use the Herschel-Bulkley fluid flow model to characterize the fluid across the entire range of shear rates. The shear stress versus shear strain rate is shown in **Figure 3.14**. **Figure 3.15** shows the effective fluid viscosity versus shear rate. The final H-B model parameters are listed in **Table 3.5**.

Table 3.6. Data from Dow Corning (personal communication)

Viscosity, *cP*	**Shear rate [sec^{-1}]**
200,000	25
150,000	50
70,000	200

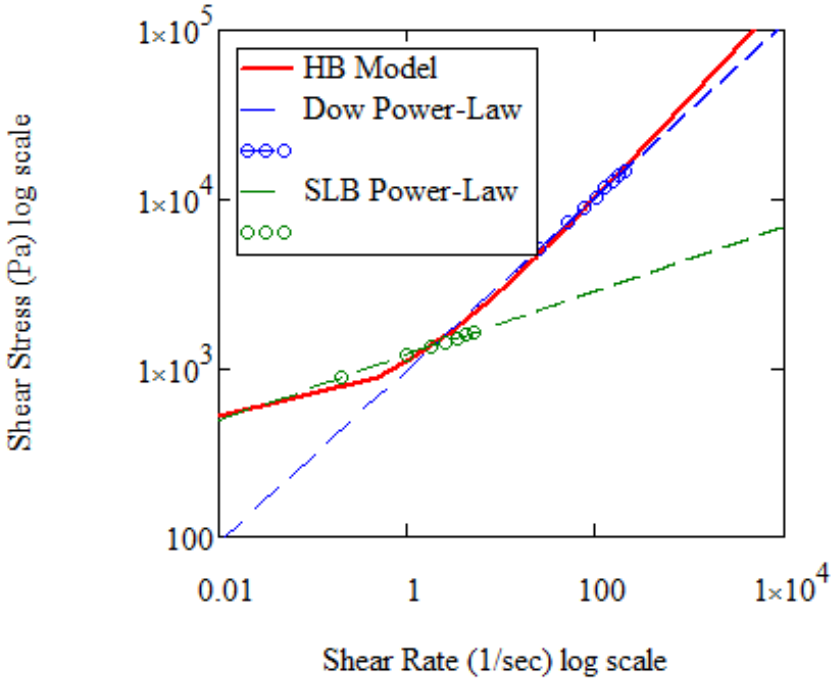

Figure 3.14. The H-B model fit to the data. Fitted model parameters (blue line) are $K = 603\ Pa\ sec^n$, $n = 0.60$, and $\tau_o = 485\ Pa$. The dots represent the valid shear rates for the respective power-law models.

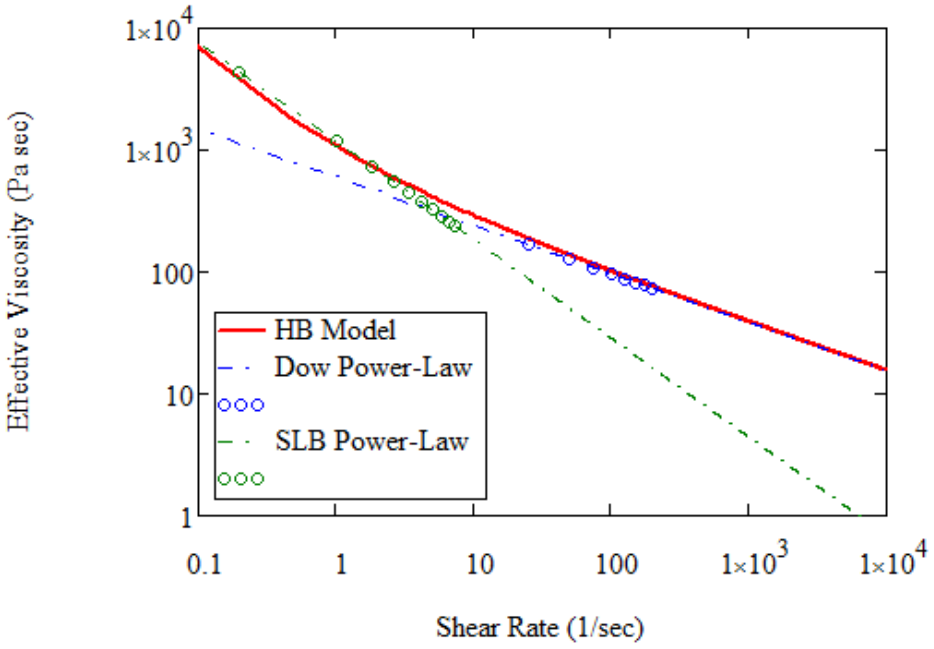

Figure 3.15. The effective viscosity versus shear rate from the H-B model. Fitted model parameters (blue line) are $K = 603\ Pa\ sec^n$, $n = 0.60$, and $\tau_o = 485\ Pa$. The dots represent the valid shear rates for the respective power-law models.

3.4.1.3. GUAR FLUID

We accomplish a similar exercise as above with the guar data (**Table 3.7**). The data from calculating the pressure drop using equation (3.4) and comparing with the measured pressure drop is presented in **Table 3.8**. **Table 3.8** clearly shows a consistent over-prediction of the calculated pressure drop for all the fluid flow rates. This over estimation of the pressure drop is roughly two to three times the measured value. This suggests that the power law fluid model may adequately represent the fluid behavior. There may be a slight over estimation of the consistency index by the rheometer, however. Consequently, we only utilize the power law model in this section, and not the Herschel-Bulkley.

Table 3.7. Pipe flow experimental parameters and data for guar fluid.

TEST	flow rate		Inner Diameter		length	Pressure	
	m^3/sec	ml/min	cm	in	m	Pa	psi
1	5.83E-07	35	0.46	0.18	1.83	1.03E+05	15
2	8.33E-06	500	0.46	0.18	1.83	3.20E+05	46
3	8.33E-05	5000	0.46	0.18	1.83	7.93E+05	115
4	1.67E-05	1000	0.46	0.18	1.83	3.59E+05	52
5	4.17E-05	2500	0.46	0.18	1.83	5.17E+05	75
6	8.33E-05	5000	0.46	0.18	1.83	7.72E+05	112

Table 3.8. Pipe flow calculated (equation (3.4)) versus measured pressure drop for guar fluid.

TEST	Measured Pressure		Calculated Pressure	
	Pa	psi	Pa	psi
1	1.03E+05	15	3.44E+05	50
2	3.20E+05	46	8.05E+05	117
3	7.93E+05	115	1.68E+06	244
4	3.59E+05	52	1.00E+06	146
5	5.17E+05	75	1.35E+06	195
6	7.72E+05	112	1.68E+06	244

We complete the same LSM fitting exercise with the guar fluid (**Figure 3.16**). Figure 3.17 indicates that the power-law exponent provided by the rheometer is consistent with our data. The consistency index provided by the rheometer is higher than the value indicated by our tests, however. In the case of the Herschel-Bulkley model, there was no increase in fit quality and estimated yield stresses were negligible.

In Figure 3.17, we show the calculated shear stress from parameters generated by our test results, along with the parameters measured with the rheometer. Similar to Figure 3.14 for the silicone test, the comparison of the calculated shear stress versus shear strain rate shows an increase in discrepancy between the parameters with increasing strain rate (albeit less so). Finally, **Figure 3.18** is the effective viscosity plot. Similar to above, the effective fluid viscosity may be better approximated by utilizing the parameters estimated by our flow tests. A summary of the fluid flow parameters chosen for this work is provided in **Table 3.9**.

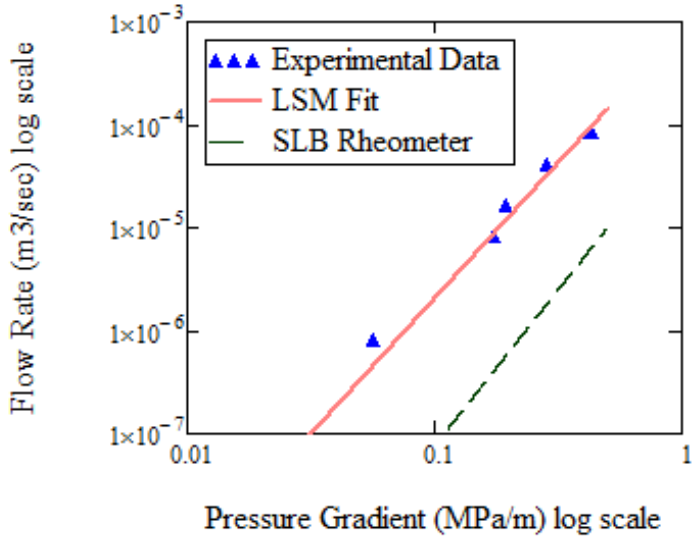

Figure 3.16. Power-law fluid flow model comparison to experimental results in log scale. Fitted model parameters (red line) are $K = 11\ Pa\ \text{sec}^n$, $n = 0.41$, the rheometer parameters (green dashed line) are $K = 50\ Pa\ sec^n$, $n = 0.33$.

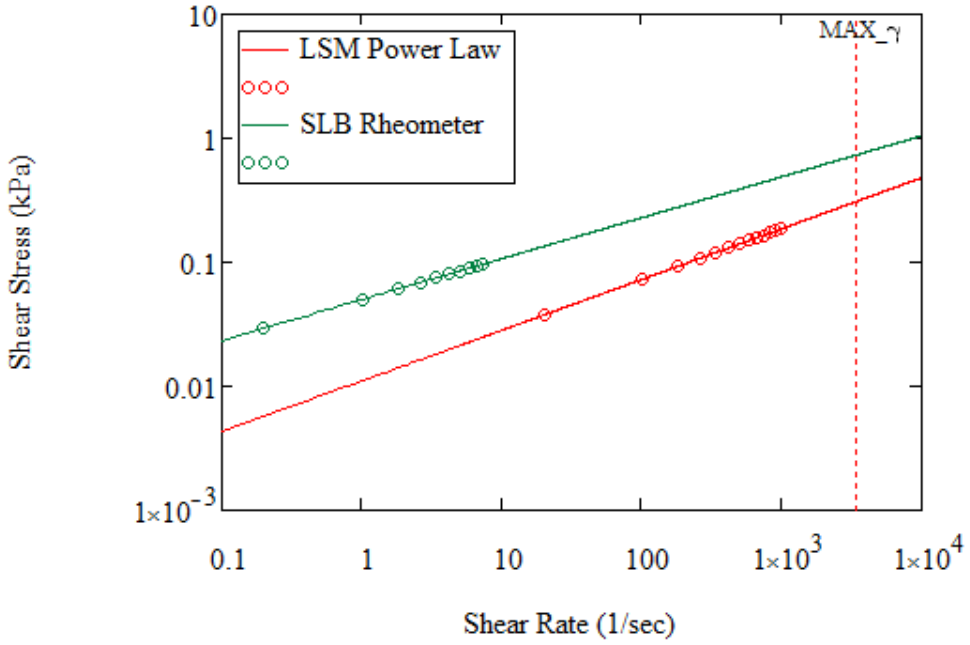

Figure 3.17. Comparison of shear stress versus shear rate for the power law model with experimental and rheometer parameter sets. The parameter set from SLB overestimates the shear stress in the tubing (assumed to be largest shear stress during a fracture test). The dots represent the valid shear rates for the respective power-law models. MAX_γ represents the largest expected shear rates expected in our tests.

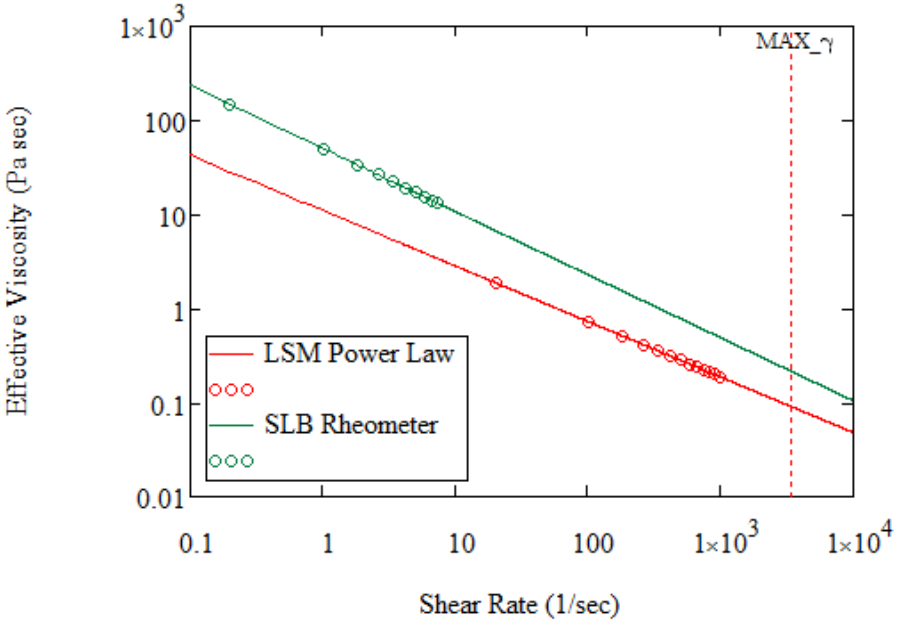

Figure 3.18. Effective viscosity versus shear rate for guar fluid for the experimental and rheometer parameters. The dots represent the valid shear rates for the respective power-law models. MAX_γ represents the largest expected shear rates expected in our tests.

Table 3.9. Table of K and n parameters for silicone and guar.

MATERIAL	MODEL	K	n	τ_o
		Pa sec^n		Pa
732 Silicone	LSM H-B	123	0.75	457
739 Silicone	LSM H-B	603	0.60	485
Guar-based	LSM Power Law	11	0.41	0

3.5. Properties of Unconsolidated Materials

The sample utilized for our fracture tests consisted of fine sand, silica flour (silt), and mixtures of the two. The silica flour provided low permeability (~ 20 mD) but proved to be problematic when attempting to saturate. The ability to modify the permeability proved useful in generating fractures with fluids that exhibit high-leakoff in pure clean sands. Below, we describe the mechanical properties and permeability of the samples in detail.

3.5.1. Quartz sand F110

The sand utilized in these experiments is fine poorly graded quartz sand, chosen based on a number of criterions. First, it was one of the smallest spherical particle sizes readily available (Scanning Electron Microscope (SEM) image of the particles is in **Figure 3.11**(c)). Second, the sand was well processed and had relatively small volumes of fines, ensuring uniformity across samples. Finally, it was readily available and consistent across batches acquired from the manufacturer.

The grain size distributions (GSD) of all the samples are available in **Figure 3.12**. These tests were conducted in accordance with ASTM D 422 – 63. Additionally the minimum and maximum densities and porosities are listed in **Table 3.10**. The samples for the injection test were all prepared at maximum density. Our preparation technique (rodding) provided ~ 100 % relative densities. In most instances, the relative density was greater than 100 %; however we do not report relative densities greater than 100%. This indicates the increased efficiency of our sample preparation technique

compared to the technique utilized in the ASTM D 4254 – 91 standard. The average maximum measured porosity and density during the test preparation are also listed in **Table 3.10**.

High initial densities were chosen to limit the degree of compaction during the cavity expansion process, either at initiation or during fracture propagation. This also ensured that samples are uniform with respect to densities, both individually and over the entire experimental series. Creating uniform samples of a specific relative density can be difficult in such a large sample size. In addition, initial density was not chosen as an experimental parameter in this work. Finally, the maximum relative density will lead to the lowest possible permeability decreasing the fracturing fluid leakoff.

The mechanical properties of F110 are tested by a consolidated drained triaxial test as described by *Lambe* [1951]. The deformation characteristic follow what is typically expected of fine sands [*Lambe and Whitman*, 1979]. Representative deformation cures of the sand and sand/flour mixture are shown in **Figure 3.21**. The friction angle and stiffness (values listed in **Table 3.10**) were measured using confinements of 10 psi and 80 psi representing a majority of testing conditions of our injection tests. Our injection test confinements ranged from 8 to 2000 psi. The highest confinement properties were not tested, due to testing equipment limitations However, it is expected that greater confinements will tend to reduce dilation (limiting the softening behavior) and increase stiffness with limited effect on critical state friction angles [*Lambe and Whitman*, 1979; *Mitchell et al.*, 2005].

The permeability tests were conducted as prescribed in ASTM D5084-03 method C-Falling Head Test. A sample with a diameter of 2 in and a length of 5 in was created using the same densification technique that we utilize in our injection tests. The prescribed confinements and deviatoric stresses were also similar to the injection tests (8 psi to 80 psi confinements). To measure permeability, a pressure gradient is applied across the sample and the resulting flow rate is recorded. Multiple pressure gradients are utilized for each sample. Over twenty samples were tested for each sample combination (F110, silica flour and mixtures). The permeability of F110 at maximum density and 80 psi confinement was 1.3 Darcy. The value of permeability as a function of silica powder content is shown in **Figure 3.22**.

3.5.2. Silica powder

The silica flour powder used in our experiments was SIL-CO-SIL 106 from ITC Minerals and Chemicals. It is produced from high purity silica which is precision ground to microcrystalline sizes. The mean particle size was measured to be 22 μm. The particle shape is angular as shown in **Figure 3.19** (a) and (b). Silica flour proved difficult to saturate using our sample preparation technique (high initial densities). There are a number of techniques to mitigate the difficulties and achieve a saturated sample. However, these techniques cannot be applied to our experimental apparatus without significant modification. For example, a slurry of silica flour could be compacted to achieve a dense state. To accomplish a slurry compaction technique would require a significant modification of the loading frame and triaxial cell. Further, it is doubtful that

the magnitude of density, due to static loading, would approach the density achieved by rodding, without extremely high surcharge loads.

Silica flour may complicate the assumption of a cohesionless sample. Ignoring confining stresses, the boundary of cohesionless versus cohesive samples is when the fraction of silt or clay material exceeds $50\ \%$ [*Mitchell et al.*, 2005]. Strictly speaking, the silica flour sample can be interpreted as a cohesive soil using the USCS classification. With no clay content silts tend to go from sand-like to clay-like mechanical behavior as particle size decreases [*Mitchell et al.*, 2005]. Due to the inert nature of silica, electrostatic forces between the particles can be considered of limited importance. Finally, the importance of capillary and electrical forces are limited with increasing skeletal forces [e.g., *Santamarina et al.*, 2001]. Given the large confining stresses on the tests with silica flour, we would not expect any cohesive properties of the particular materials used in our experiments to dominate the fracturing process. The upper limit of the capillary pressure in the silica powder can be estimated (using Laplace formula, surface tension of fluid ~10^2 dynes/cm, and a pore radius $\sim 10\mu\mathrm{m}$) as < $10\ \mathrm{kPa}$, which is less than half of the lowest confinement utilized in our tests ($55\ \mathrm{kPa}$). Therefore, in our tests we consider the silica flour cohesionless.

Only a limited number of fracturing tests were performed with pure silica flour due, in part, to the complications of saturating. We were unable to fully saturate the silica flour without excessive sample disturbance due to the high pressure gradients required to drive the pore fluid. The results of the pure silica flour fracturing tests are

presented in Chapter 4. The silicone injection tests exhibited significantly different fracture morphologies when compared to fine sand and mixtures.

The small size of the sample for the permeability tests allowed for adequate saturation levels and characterization of the permeability of pure silica flour. The tests were conducted in the same manner as described above for quartz sand. As shown in **Figure 3.22** the average permeability measured was $25\ \mathrm{mD}$.

3.5.3. Sand-flour mixtures

A number of different mixtures of fine sand and silica flour were tested as possible candidates for injection test. The fraction of silica flour exhibited a measurable effect on both the permeability and deformation characteristics of the sample. The permeability of sand and silica flour mixtures were tested as described above (falling head test), under the same confining stresses as the fracture tests ($8\ \mathrm{psi}/16\ \mathrm{psi}$, $80\ \mathrm{psi}/160\ \mathrm{psi}$). The results are shown in **Figure 3.22**. An issue with the migration of fines through the sample became apparent with mixtures lower than 15% silica flour. The fines migration manifested itself as a gradual reduction of permeability with increasing test duration. This reduction reached a minimum value of permeability similar in magnitude to that of pure silica flour. Tests with sample mixtures containing greater than 15% silica flour measured permeability values remained consistent through the entire test cycle. Therefore, we attribute it to fines migration due to the fluid flow. The values for mixture fractions lower than 15% shown in **Figure 3.22** are those measured during the initial tests of permeability. Therefore they are an estimation.

The deformation characteristics of the 20% silica flour mixture exhibited greater degrees of softening behavior and stiffness when compared to fine sand **Figure 3.21**. Given the results of the above analysis, the chosen particle mixture was 20% silica flour for the reduced permeability sample. This provides an order of magnitude decrease in the sample permeability while not affecting the cohesionless nature of the particulate material.

Table 3.10. Sample properties. The properties listed with ASTM were measured using the ASTM standards listed above. Those listed with EXP are values measured or calculated during preparation of our experiments.

	D_{10}	D_{30}	D_{60}	D_{50}	Cu	Cc	ϕ_{peak}	ϕ_{min}
	μm	μm	μm	μm	D_{60}/D_{10}	$D_{30}^2/(D_{10}D_{60})$	@ 0.5 MPa	
Sand F110	110	165	210	195	1.90	1.18	29	26
Silica Flour	6	15	30	22	5.0	1.25	44	38
20% Silica	25	140	180	150	7.2	4.35	37	28.5
	ρ_{min} ASTM	ρ_{max} ASTM	ρ_{max} EXP.	η_{max}	η_{min} ASTM	η_{min} EXP	E @ 0.5 MPa	
	g/cm^3	g/cm^3	g/cm^3				MPa	
Sand F110	1.43	1.73	1.83	0.46	0.35	0.30	70	
Silica Flour	1.04	1.71	1.87	0.61	0.39	0.29	110	
20% Silica	1.25	1.73	1.90	0.53	0.35	0.28	90	

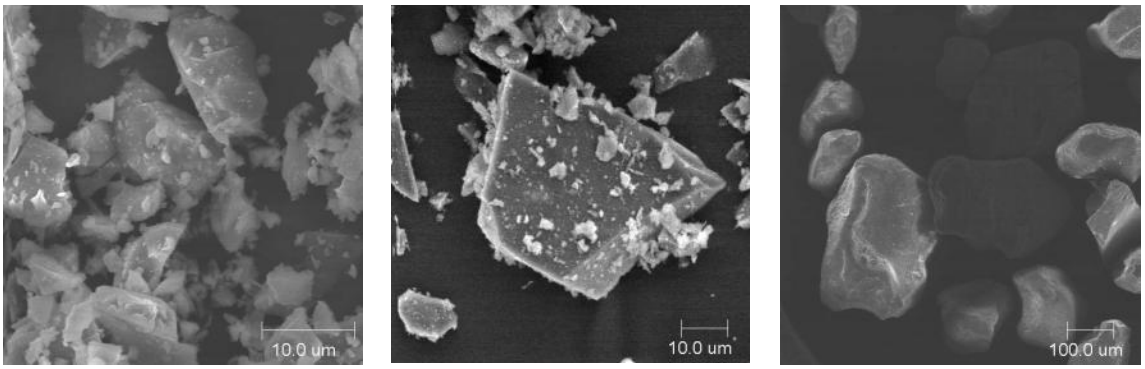

Figure 3.19. Scanning Electron Microscope images of particles: (a) and (b) silica flour (c) fine sand [*Chang*, 2004].

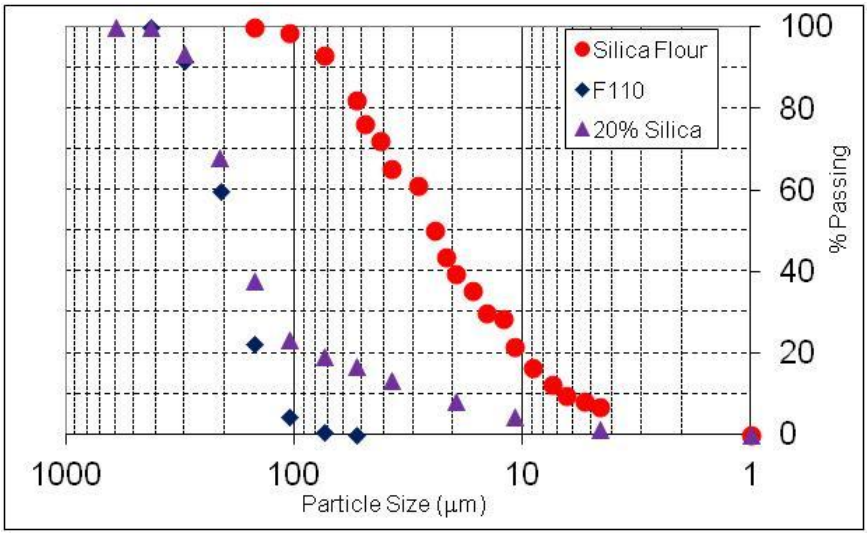

Figure 3.20. Grain size distribution for F110 sand, silica flour, and their mixture (with 20% of flour).

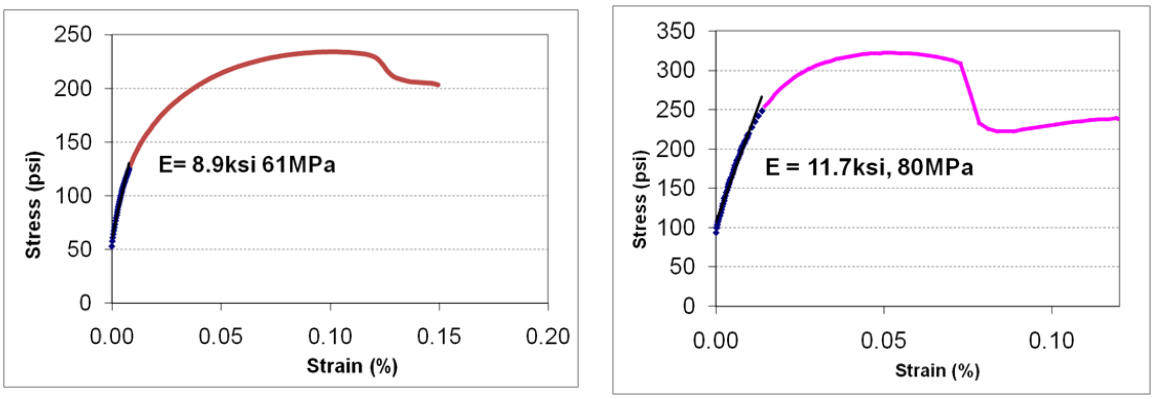

(a) (b)

Figure 3.21. Strength curves for (a) silica sand (b) sand/flour mixture. Triaxial tests were at 80 psi confinment with drained pore pressure. The sand flour mixture has a greater stiffness with more softening behaviour.

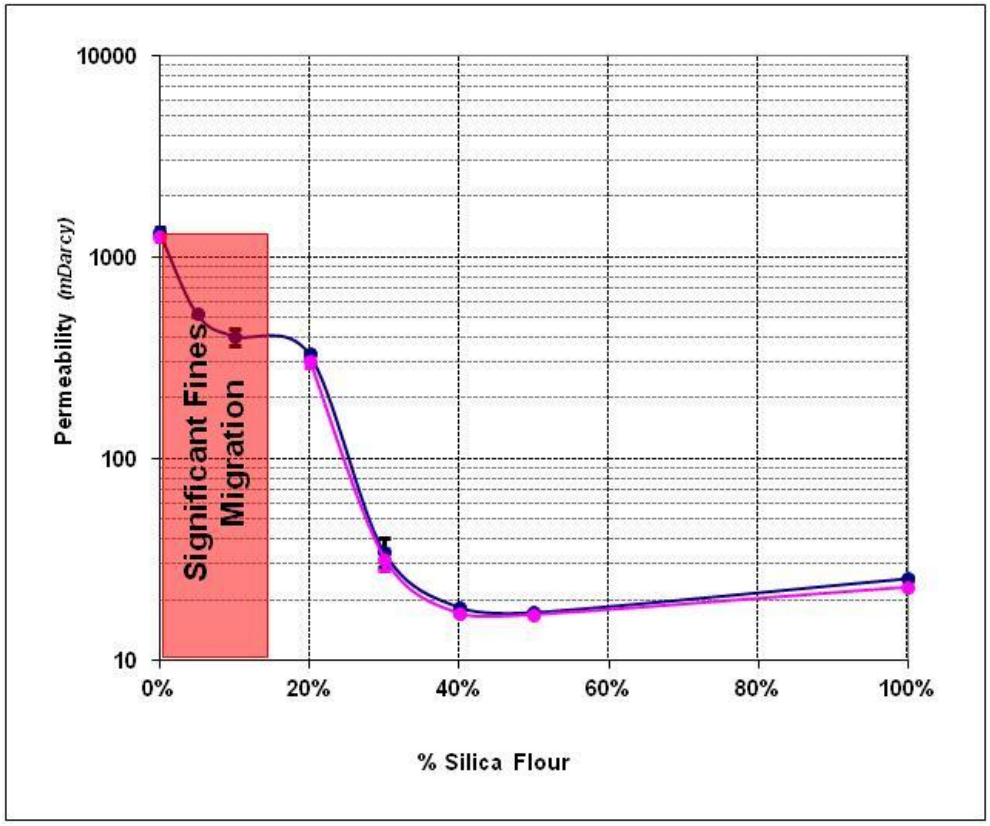

Figure 3.22. Permeability of samples with percenatge of silica flour flour**.**

3.6. Experimental Techniques

A significant effort went into ensuring that the LTC and HPTC were as similar as possible with regards to the preparation, geometry and injection events. In general, the techniques utilized in sample preparation were the same for all the experimental apparatuses, just scaled due to sample size.

3.6.1. Sample preparation

A hard shell split mold is placed around a flexible and impermeable membrane that serves as the outer radial boundary of the sample. Soil (oven dried) is placed in lifts and compacted with a rod. Each sample is completed with eight lifts ensuring a uniform sample density.

During rodding the top of layer being compacted remains loose. In our experience, significant compaction only takes place in the lower third of a given layer (plus lower layer, if any). Tamping can be utilized to compact the loose upper section of a layer, however, the density would not approach the value of a rodded sample. Therefore, a temporary mold is placed above the top boundary of the sample and several additional layers are rodded to compact the top section of the sample. Finally, the extra layers are carefully removed and the top of the sample remains in a compacted state. The initial density remained constant during the entire experimental series. For example, 20% silica flour mixtures created measured densities ranging from 1.88 to 1.90 g/cm^3 for over twenty tests.

Once the sample preparation is complete, the top platen is placed and the membrane is sealed around it. A vacuum is then applied to the closed sample. The split mold is removed and the cell and loading frame are completely assembled. The cell is filled with water to provide confinement of the sample.

After a small confinement pressure is applied, the sample is flushed with CO_2. Following the CO_2 flushing, vacuum is then again applied to the closed system and allowed to draw down the sample again. There were typically three CO_2 flushing sequences. The final stage involves flushing the pore fluid in. The vacuum source is allowed to draw down the sample one last time then closed off and under a low flow rate pore fluid is flushed into the sample, this continues until the sample is completely saturated. On the large-scale cell the saturation time was typically around four hours. Once the vacuum pressure was relieved, the pore fluid was continually flushed through the sample for a number of pore volumes. This technique was developed to ensure the best possible saturation and uniformity of the samples. Utilizing this technique typically gained saturation levels above 85% (measured by Skempton's coefficient).

It should be noted that there was no observable difference in the results of fracturing tests in saturated or dry tests conducted in fine sand and silica flour mixtures. However, the utilization of incompressible pore fluid allowed for qualitative tracking of the sample pore volume during an injection event (More details are given in Section 5.2.5).

3.6.2. Injection procedure

All tests are conducted under constant pressure-controlled boundary conditions. Further, the samples are under drained pore pressure conditions. Once the sample was constructed and saturated, preparations for the injection test began. The sample was first loaded hydrostatically up to the prescribed test value. This loading was typically done in 10 psi stages to allow the sample to respond accordingly. Once the maximum hydrostatic load was applied the deviatoric load was applied in a similar stepwise fashion.

The stress ratio (σ_v/σ_h) was kept constant at 2 to 1. We wanted to provide a high-stress ratio to ensure the highest probability of generating vertical fractures. However, we want to ensure that global sample failure is not an issue. Our sample characterization test results suggest stress ratios of 3 to 1 for global failure of our dense F110 (weakest sample). Further, samples still remained fairly elastic at stress ratios of 2 to 1. Therefore, all pressure controlled triaxial tests were conducted under stress ratios of 2 to 1.

The change in volume of the sample pore fluid and cell confinement was monitored during loading and injection events. This allowed for monitoring change in sample volume and pore fluid response. The change in volume during hydrostatic loading gave a qualitative measure of the quality of sample preparation. The samples of similar material showed a similar pattern of sample compaction, indicating the initial conditions are the same.

Once the loading of the sample was complete, the assembly of the displacement chamber and associated tubing was initiated. The displacement chamber was filled first with the chosen fracturing fluid. Every precaution was taken to ensure that no air bubbles were entrained within the fracturing fluid while filling the displacement chamber. This was a challenge with the silicone fluids.

The volume of prescribed injection fluid, plus additional fluid to account for system volume, was added to the displacement chamber. The end cap of the displacement chamber plus associated fittings and elbow for direct injection source connection was then installed. The air was purged from the displacement chamber and the compression fitting to attach to the injection source was sealed when the injection fluid reached the fitting.

Once the sample side of the displacement chamber was filled and sealed, the pump side was completed. On the pump side of the chamber the fluid chosen was opposite (water or oil) of what was being pumped. Similar to the fracturing fluid, every effort was made to purge air from the system on the pump side of the displacement chamber. The fracturing fluid delivery system was not attached to the sample until the sample was ready for the injection. Due to the nature of the solidification process of the silicone adhesives, the time from filling the displacement chamber to running a test was kept as short as possible. Typically, it was within $10\ \mathrm{min}$.

There was no attempt to pre-fill the injection source with fracturing fluid prior to the start of the injection event. Initially, we attempted to pre-fill to ensure that the

fracturing fluid was at the injection source once the pump was turned on. This proved unnecessarily difficult. Technically, because water is the fluid first out of the injection source there may be an initiation event prior to the fracturing fluid reaching the sample. This does not appear to be an issue for two reasons. First, the volume of fluid injected prior to the peak pressure is typically much greater than the volume of water displaced. Second, we tested the injection of water at the maximum rate ($15\ \mathrm{L/min}$) and found no evidence of fracture initiation or sample volume response due to any cavity expansion.

The pump was prefilled, and tested at the set injection rate. The fracturing fluid delivery system was then attached to the injection source and to pump. The pressure transducer was attached to the elbow attached to the base of the injection source tubing. The data acquisition was initiated and after $10\ \mathrm{sec}$ the pump was started.

The pump ran until the displacement chamber was depleted, the piston bottomed out and the pump pressure relief valve was activated. The pump was then shut down. The pressure decline in the injection tubing was monitored until it reached a fairly constant value (typically below confinement).

Once the experiment was complete, the fracturing fluid delivery system was disconnected from the injection source, the source was capped, and the displacement chamber and fittings were thoroughly cleaned. The sample was left undisturbed and under pressure for at least $24\ \mathrm{hrs}$ to allow for solidification of the injected fluid. During this time pore fluid volume and cell confinement volume were monitored to ensure sample stability. After the solidification of the fracture, the sample was unloaded. The

loading frame and confinement cell disassembled, and then the sample was carefully excavated. The solidified fracture was then removed from the cell cleaned, cataloged and cross-sectioned.

3.7. Calibration

This section describes the calibration techniques used to analyze and verify the experimental results. All of the pumps were calibrated and checked for consistent flow rates at multiple times. All loading frames were also calibrated to ensure the applied load resulted in the desired stress conditions. The pressure transducers were calibrated once a year using a dead-weight calibrating machine. The samples were utilized over and over so the GSD and permeability of the sample materials were tested multiple times throughout to verify the constancy of the samples. The most important calibration came in estimating the pressure drop due to the fluid flow in the injection source.

The calibration of injection pressure due to fluid flow in the injection delivery system was the most important task in analyzing the experimental results. Initial tests in the LTC had a relatively complex fracturing fluid delivery system. This proved adequate with the low flow rate experiments. However, the increased capabilities of the flow rate required modifications to the experimental apparatus, due to increased frictional losses. The resulting fracturing fluid delivery system was modified to what is described in Section 3.2.2. The pressure gauge was essentially recording the injection pressure at the base of the injection source. Therefore, the viscous losses were due to $22\ \text{in}$ of tubing and the pressure drop across the perforations.

The pressure loss due to fluid flow within the injection source was estimated by two separate methods. First, the fracturing fluid delivery system was assembled with an injection source. This assembly was simply left in the open air and fracturing fluid was injected through the system. The pressure generated due to the prescribed flow rate was recorded. Second, an analysis of the pressure curve after shut-in allows for an additional estimate of the pressure loss due to fluid flow. The fluid flow maintains a constant rate until the piston reaches the end of the displacement chamber, signaling the end of the test. Fluid flow then stops immediately (ignoring any inertial effects). The displacement chamber remains connected and pressurized so there is no reversal of flow. Therefore, the instantaneous drop in pressure after shut-in should be the same order as the pressure drop in the system. As an example, the pressure curve in **Figure 3.23.** This test exhibited the highest pressure drop observed at 1500 psi. This example is an extreme case; most of our tests exhibited an order of magnitude less pressure drop. The pressure time history analysis is the technique typically utilized.

The pressure drop due to the flow of the guar fluid was negligible, even at rates up to 15 L/min (less than 24% of the peak pressure at 15 L/min). For most silicone fluid injection tests the pressure loss in the system was less than 20% (for flow rate less than 1000 ml/min). For tests with greatest injection rates (5 L/min) utilizing silicone fracturing fluid the pressure drop could be over 50%. These high-pressure drops have a significant effect on the interpretation of the pressure curve. However, for the results presented here we consider it a secondary issue.

The pressure curves were simply reduced by the value of the estimated pressure drop in injection source. Technically, the pressure drop should be calculated for the unsteady flow rate at the initial stage and final stage of the test. Peak and propagation pressures, however, are our main concern so a more thorough analysis of the non-steady state fluid flow is not considered.

High viscous losses in the injection tubing (> 50% of peak pressure) were noted on a number of tests with silicone adhesive. These tests exhibited two distinct issues. First, due to variances in manufacturing the fine mesh inconstancies in the fine screen selected for injection source construction created abnormally high-pressure gradients. A coarse mesh ($250\ \mu m$) combined with filter paper was selected to eliminate this issue. Second, in some instances the wrong diameter of tubing was selected during high-rate tests or clogging of the screen was observed. This condition created a peculiar pressure signature (**Figure 3.24**), and thus not used, for the experimental observations presented in Chapter 4. Nonetheless, the fracture morphology did follow similar patterns as the successful tests.

3.7.1. Boundary effect

Often interaction of fractures with the pressure-controlled boundary during our tests was noticeable. The geometry of these interactions was varied depending on the fracture shape. There were three distinct changes in the pressure curve that signified boundary interaction. If the pressure remained constant, increased, or the curvature of the pressure curve became negative, then this usually signified some boundary

interactions. We then measured the solidified fluid that formed on the boundary. Back calculating using the flow rate and estimated volume, the time of the perturbation corresponded to the volume of fluid on the boundary. Three examples of pressure curves and fracture forms are shown below in **Figure 3.25**. There was not a detectable pattern in the reaction of the pressure curve and the geometry of the fracture at the boundary. Though, it is likely due to the geometry of the fluid link between the boundary and the parent fracture.

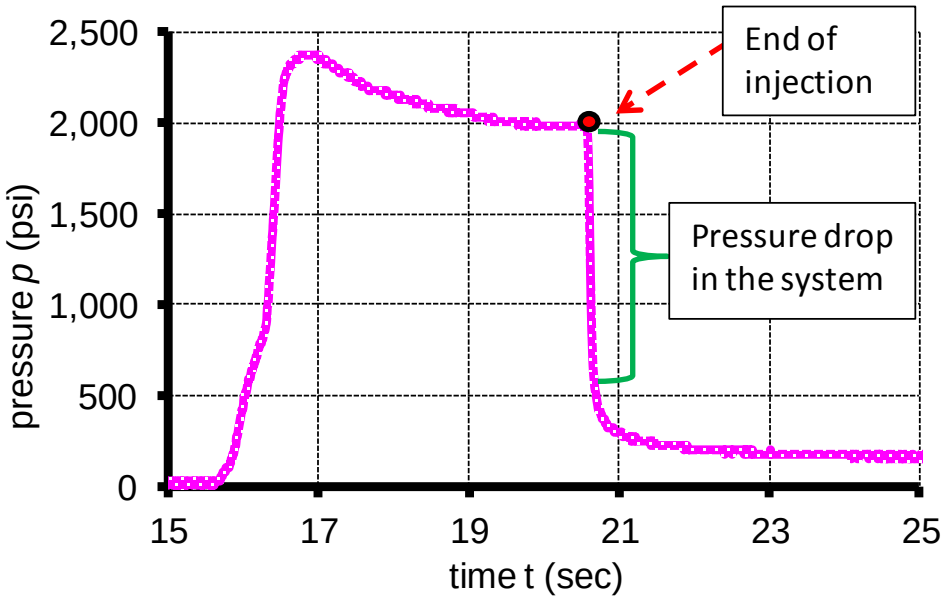

Figure 3.23. Example of the estimation of pressure drop in the system by analysis of the pressure curve. Taken from Test 01-31-11 with 5000 ml/min injection rate, 20% silica flour mixture, and silicone adhesive.

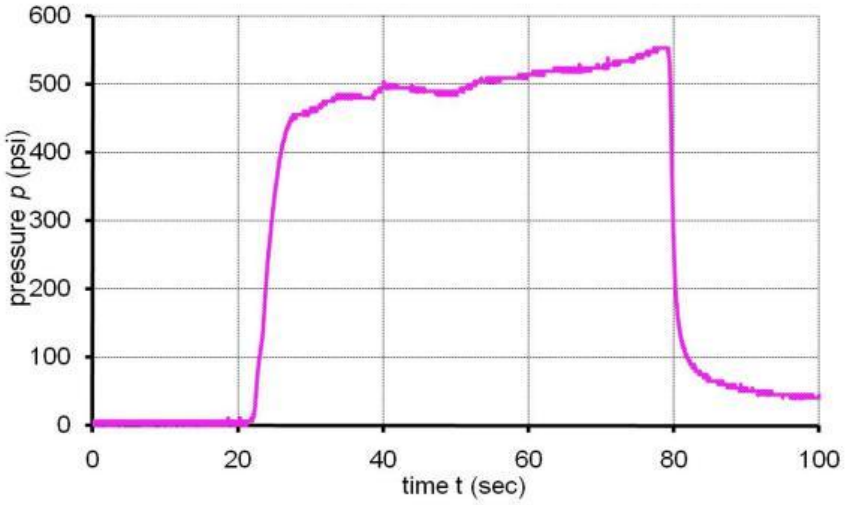

Figure 3.24. The characteristic pressure curve for inadequate tubing size or clogged screen. The estimated pressure drop would be the same as the "initiation" pressure.

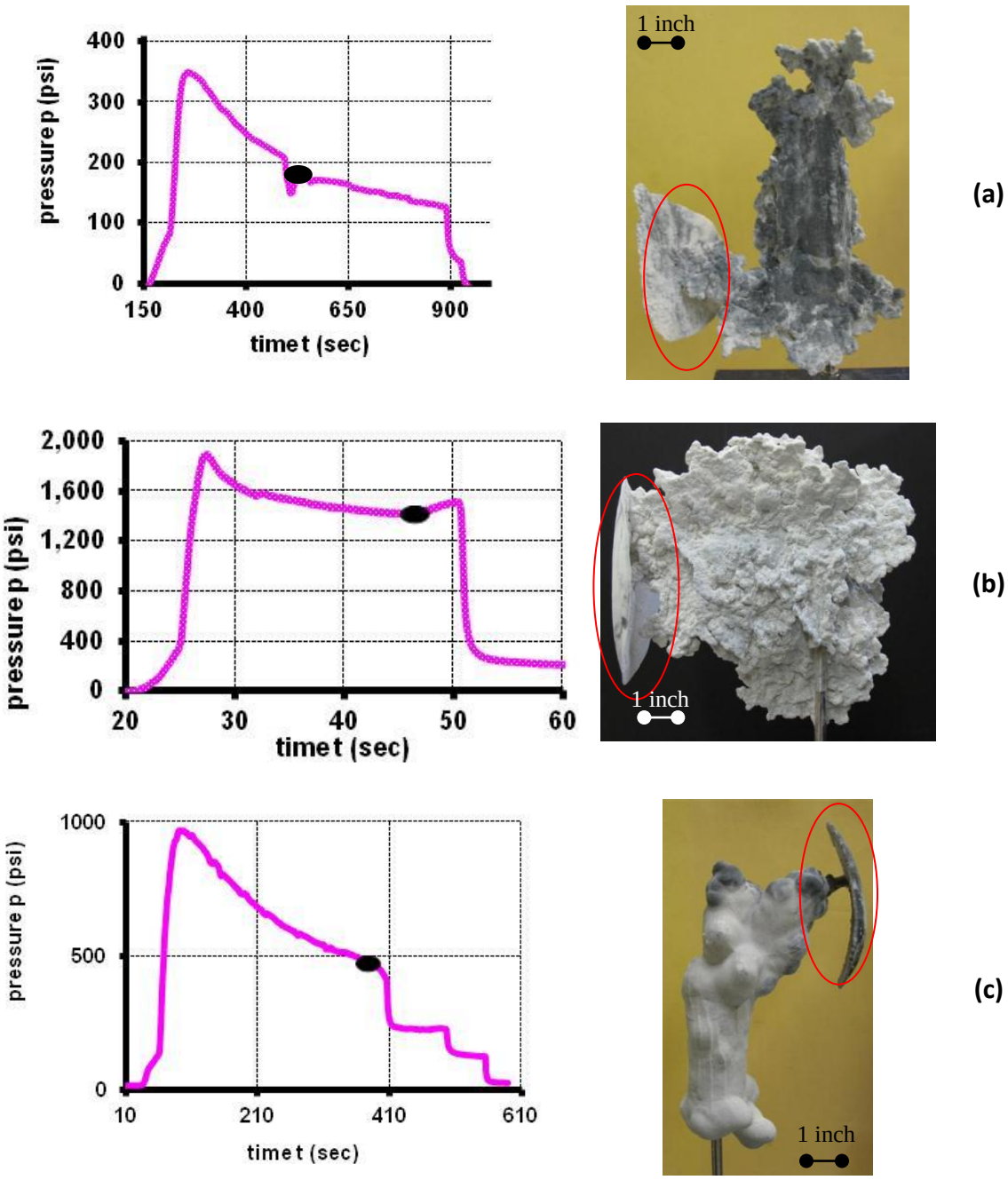

Figure 3.25. Examples of pressure curve indicators of boundary interactions. Black dots on pressure curve indicate the start of the boundary volume injection shown in the red circles. (a) and (c) show a decreasing pressure when the boundary is reached. (b) Shows an increase in pressure with contact.

3.8. Conclusions

In this section we presented our various experimental pressure cells. We also characterized the sample materials and fracturing fluids. We described the processes and procedures developed to successfully initiate and propagate fractures in saturated cohesionless particulate materials. Finally, we discussed the necessary calibration of the experimental techniques. The following are the main points of this chapter:

1. The tests are conducted under pressure controlled boundaries and under drained pore pressure conditions.
2. The stress ratio (σ_v/σ_h) is held constant at 2.
3. The injection source is of cylindrical geometry, typically with a length of 3 in to 5 in.
4. The fracturing fluid (guar and silicone) exhibit shear thinning fluid and Herschel-Bulkley rheologies.
5. Two positive displacement triplex plunger pumps and a diaphragm pump are utilized at a constant injection rate.
6. Injection rates varied from 50 to 15000 ml/min.
7. Samples of fine quartz sand (F110), crushed silica flour, and a mixture of 20% silica flour and 80% F110 are used for the injection tests.
8. Permeability values are measured to be 1000 mD, 25 mD and 350 mD, respectively.

4. EXPERIMENTAL RESULTS

4.1. Introduction

The results of an extensive experimental series, conducted utilizing silicone adhesive (RTV) fracturing fluids, are presented in this chapter and Chapter 5. Chapter 4 focuses on the pressure signatures, global sample response and external fracture observations. Chapter 5 is primarily confined to the description of parameter effects on, and a description of, the internal fracture characteristics. In this chapter, we start with the dimensional analysis that we developed to help guide the experimental process. Then, we detail the pressure curves and what pressure signatures are characteristic of our tests. Next, we describe the various observed fracture morphologies with the silicone injection tests. We look at the sample response and how fractures can exhibit various dilation regimes (global, internal etc.). Finally, we show an example of global shear band development of the sample in the large triaxial cell due to an injection test. Parameter affects and fracture cross-sections are discussed in more detail in Chapter 5. Initially, we describe the typical results generated in our tests.

The fractures presented in **Figure 4.1** are three examples of our typical experimental results. In this series the same confining stress, source geometry, soil properties and injection fluid properties were utilized. Qualitatively the first sample illustrates the initiation process. In contrast, the others show the propagation of the fracture. We observe clear evidence of cavity expansion in all three samples. The main or primary cavity expansion is seen in all three, but in the largest sample there is

evidence of local cavity expansion along the length of the fracture. The remaining fracture aperture is also quite thick, suggesting that there is significant plasticity present during the fracturing process. Further, the leakoff surface is characteristic of many of our experiments in saturated quartz sands. **Figure 4.1** and **Figure 4.2** illustrate the reproducibility of both the general fracture morphology and pressure curve properties of these experiments.

The ability to cross-section the fractures is an important contribution of this work. We measured the leakoff thickness and aperture of our silicone adhesive tests and analyzed the results. The cross-section in **Figure 4.3** (a) is from an experiment conducted using a clear silicone adhesive. This thin section clearly indicates the distinct leakoff zone. In addition, the fracture aperture is void of sample material. We measure fracture aperture as the region of the cross-section that is void of any particulate material. The leakoff thickness measured and presented here is the thickness of one side a distance of $2\ \mathrm{in}$ away from the borehole. These cross-sections are taken from the largest lateral extent of the fracture. Many samples were injected with two different colors of the same fluid; a cross-section is shown in **Figure 4.3** (b). The injection event started with the white fluid followed by black. The majority of "newly" injected fracturing fluid is invading the tip region of the fracture and not contributing to the leakoff surface measurably.

The fractures (experiments) presented here are categorized by date for cross-referencing. The code is *mm-dy-year.* This allows for referencing in the main text to

experimental data available in Appendix A, B, and C. For brevity, only pertinent experimental data is included within the text. The full experimental parameters (Appendix A) and results (Appendix B and C) are available. In addition, time zero in most pressure-time histories presented below does not indicate the moment when the injection begins. In some cases (primarily Chapter 6) when necessary, the curves are adjusted. However, most are not and the injection event starts when any positive register of pressure is recorded (typically 20 sec) For example: **Figure 3.25**.

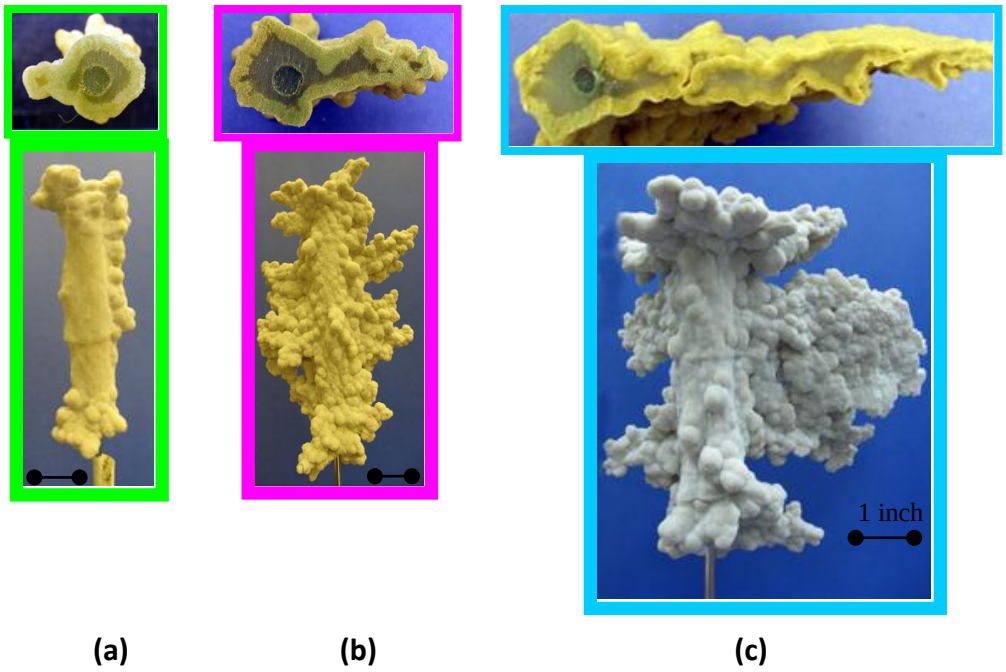

Figure 4.1. Fractures observed in experiments with different volume injections (a) Test 09-02-05 (100 ml), (b) Test 09-21-05 (200 ml), and (c) Test 06-17-05 (400 ml).

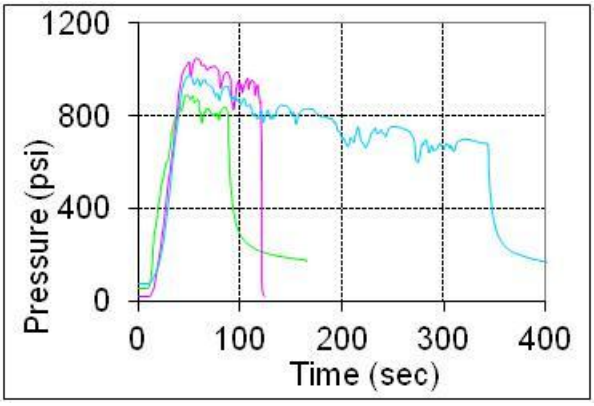

Figure 4.2. Experimental pressure-time histories corresponding to fractures shown in Figure 4-1. The colors represent: green 100 ml injection, pink 200 ml injection, and blue 400 ml injection

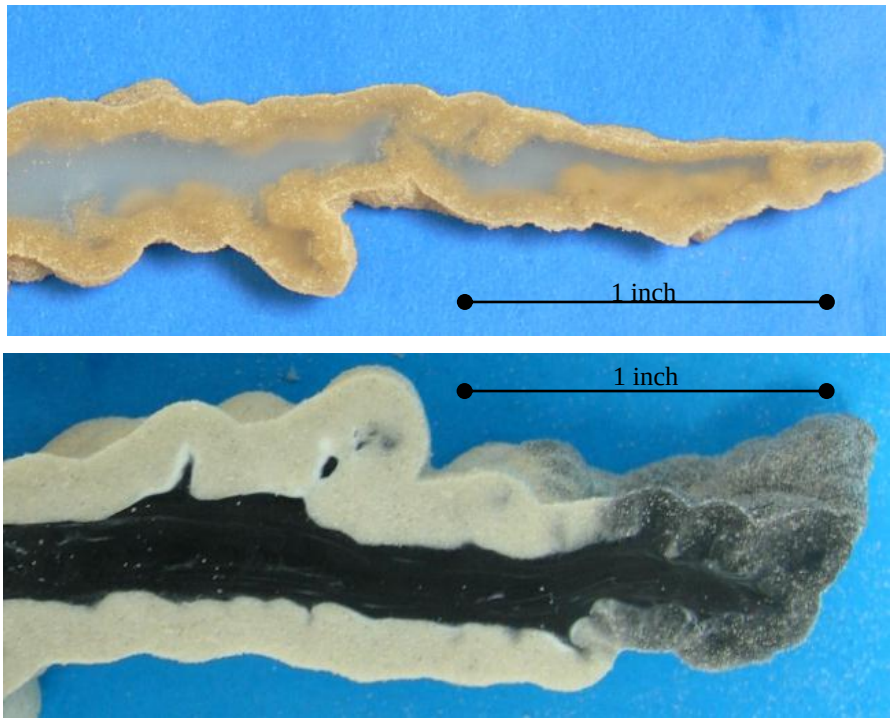

(a)

(b)

Figure 4.3. Examples of fracture cross-sections (a) Test 06-17-05 Injected with clear silicone (b) Test 09-27-07 injected with white, then black silicone.

4.2. Dimensional Analysis

To aid the experimental process of hydraulic fracturing in saturated materials, we utilized dimensional analysis of the obtained results [e.g., *Barenblatt*, 2003]. In general, the number of parameters describing hydraulic fracturing in saturated cohesionless materials may be rather large. In fact, it is probably not practical to vary all the parameters in one experimental program, such as presented in this work. Therefore we vary the injection rate, Q, fluid parameters or more accurately, consistency index, K, and n fluid flow behavior index, material permeability, k, and confining stress, σ_o. As described below, other parameters vary much less in our experiments or they are not independent. For example, confining stresses, σ_1 and σ_3, constitute two independent parameters, in general. In our tests, however, their ratio was constant at 2. Hence, in the dimensional analysis of our experimental results, we include only one parameter of $\sigma_o = \sigma_3$ to characterize the effect of confining stresses. The only independent parameters that we consider to significantly change in our experiments are Q, K, n, k, and σ_o.

Consider first fracture initiation, which occurs at or near (e.g., (a)) the peak, P_{peak}, of the injection pressure. Per the above discussion,

$$P_{peak} = f(K, n, E, \nu, k, c, \tan\phi, Q, \sigma_{\max}, \sigma_{\min}) \qquad (4.1)$$

this analysis gives 11 parameters with 3 basic dimensions. This requires 8 dimensionless groups. By incorporating the assumptions and simplifications given above, eq. (4.1) reduces to,

$$P_{peak} = f(Q, K, n, k, \sigma_0) \tag{4.2}$$

where the dimensions of the parameters are

$$\begin{aligned} [Q] &= \frac{\mathrm{m}^3}{\mathrm{sec}} = \frac{\mathrm{L}^3}{\mathrm{T}} \\ [K] &= \mathrm{Pa} \cdot \mathrm{sec}^{\mathrm{n}} = \frac{\mathrm{MT}^{n-2}}{\mathrm{L}} \\ [k] &= \mathrm{m}^2 = \mathrm{L}^2 \\ [\sigma_o] &= \mathrm{Pa} = \frac{\mathrm{M}}{\mathrm{LT}^2} \\ [n] &= 1 \end{aligned} \tag{4.3}$$

Therefore, we obtain six parameters, with three basic units. Choosing *Q, K, and k* as independent dimensions we identify the relevant dimensionless combinations

$$\Pi = \frac{P_{peak}}{K}\left(\frac{k^{3/2}}{Q}\right)^n, \Pi_1 = \frac{\sigma_o}{K}\left(\frac{k^{3/2}}{Q}\right)^n, \Pi_2 = n \tag{4.4}$$

applying the Π-theorem [e.g., *Barenblatt*, 2003] results in

$$\frac{P_{peak}}{K}\left(\frac{k^{3/2}}{Q}\right)^n = f\left[\frac{\sigma_o}{K}\left(\frac{k^{3/2}}{Q}\right)^n, n\right] \tag{4.5}$$

Our experimental results for the two primary dimensionless groups are shown in **Figure 4.4** and **Figure 4.5**. We plotted over 45 experimental data points from our silicone injected fracture tests. It is important to note, although the fluid flow behavior

index does vary slightly with the various silicone fracturing fluids, it is not apparent in the trends indicated in **Figure 4.4** or **Figure 4.5**. Furthermore, in Chapter 7 we include the guar fluid in the same dimensional analysis and find that in our data, the results of the dimensional analysis is not sensitive to the value on n, regardless of fluid type (silicone or guar). Therefore we only consider the two primary dimensional groups a dimensionless peak injection pressure and a dimensionless confining stress.

Values of the dimensionless groups plotted in **Figure 4.4** vary by five orders of magnitude, yet we still obtained a reasonable fit with a simple power law curve fitting. Although plotting on a log scale limits the fit accuracy, having a simple dimensionless relationship between confining stress and the peak of the injection pressure is useful for determining governing relationships of hydraulic fracturing in particulate materials. In fact, this result may be one of the most important developments of this work, because our scaling indicates the existence of a process which determines the scaling of peak injection pressures of hydraulic fractures in unconsolidated materials.

For comparison, a more traditional way of plotting peak injection pressures resembles **Figure 4.6**. On the one hand, **Figure 4.6** shows a relationship between the confining stress and the peak of the injection pressure. On the other hand, the effects from other experimental parameters are ignored. For example**,** our peak injection pressure data for experiments conducted at confinements of 80 psi vary significantly. The data form a single vertical line that represents over 30 experiments (**Figure 4.6**). If

we incorporate our developed dimensionless groups the impact of the combination of experimental parameters is more evident.

Peak pressure is not solely dependent on confining stresses. Our results suggest that other experimental parameters are important in controlling leakoff. Without adequate leakoff control, fractures cannot be generated in cohesionless materials. Changes in permeability, fluid rheology, and flow rate do not exhibit significant effect on the injection pressures. Nevertheless, they are important for leakoff control. **Figure 4.6** shows the same data from our tests but in different axes. There is an apparent increase with peak pressure as the confining stresses are increased. However, the other parameters cannot be ignored, and by adopting appropriate dimensionless terms we observe the data collapsing to a power law dependence shown in **Figure 4.4**. If we approximate dependence in (4.4) by a power law then we obtain,

$$\frac{P_{peak}}{K}\left(\frac{k^{3/2}}{Q}\right)^{n} = A\left[\frac{\sigma_o}{K}\left(\frac{k^{3/2}}{Q}\right)^{n}\right]^{\alpha} \tag{4.6}$$

this can also be expressed as

$$P_{peak} = A\sigma_o{}^{\alpha}K^{1-\alpha}\left(\frac{k^{3/2}}{Q}\right)^{(\alpha-1)(n)} \tag{4.7}$$

here α=1.05, A=1.05, (**Figure 4.4**) and n=0.75 is value of the fluid behavior index of the medium viscosity silicone adhesive (732) used in the majority of our experiments (**Table 3.9).** Substituting these values in (4.6), we finally obtain

$$P_{peak} = A\sigma_o^{\alpha} K^{\beta} k^{\gamma} Q^{\delta} \tag{4.8}$$

where A=30, α=1.05, β=-0.05, γ=0.06, and δ=-0.04 for the medium viscosity silicone adhesive (732). The slightly smaller value of n for the high viscosity silicone does not change the exponents representing the fluid flow parameters significantly (γ=0.05, and δ=-0.03). The value of α close to unity implies nearly linear dependence of the peak pressures on confining stresses. Conversely, small values of exponents β, γ, and δ suggest the peak pressure in (4.8) only weekly depends on permeability, flow rate and fluid viscosity. This quantifies what we noted in the experiments. Changes in confining stresses exhibit a significant effect on the initiation pressures. In contrast, changes in the other experimental parameters are less evident.

The positive exponent for the permeability in (4.8) indicates an increase in peak injection pressures for an increase in permeability. Several experimental studies in the literature found that increases in permeability tend to increase the fracture pressure [*De Pater and Dong*, 2009; *Khodaverdian and Mcelfresh*, 2000]. Moreover, some (but not all) of our results also indicate similar trends (Chapter 5). The discussion of experimental parameters and their effects on our test results is presented in Chapter 5.

Plotting our data along with that which is available in the literature [*Bohloli and Depater*, 2006; *De Pater and Dong*, 2007; *Dong and De Pater*, 2008] we observe similar results, the threshold normalized peak pressures decrease to ~3 with increasing confinement (**Figure 4.6**). This may indicate a change in governing parameters. In low stress states, the fluid pressure required to drive fluid flow within the fracture and the

leakoff zone dominates. Therefore, our peak pressures are much greater than confining stresses. Under greater stress conditions the required fluid pressure to open the fracture is much greater. We may expect an upper bound of normalized initiation pressure for very high confining stresses. *Zhou et al.* suggested that peak pressures must be 2.5 times the confinement to hydraulically fracture sands at high-confinement [*Zhou et al.*, 2010]. Our results indicate that the ratio is likely lower than 3.0, supporting this finding.

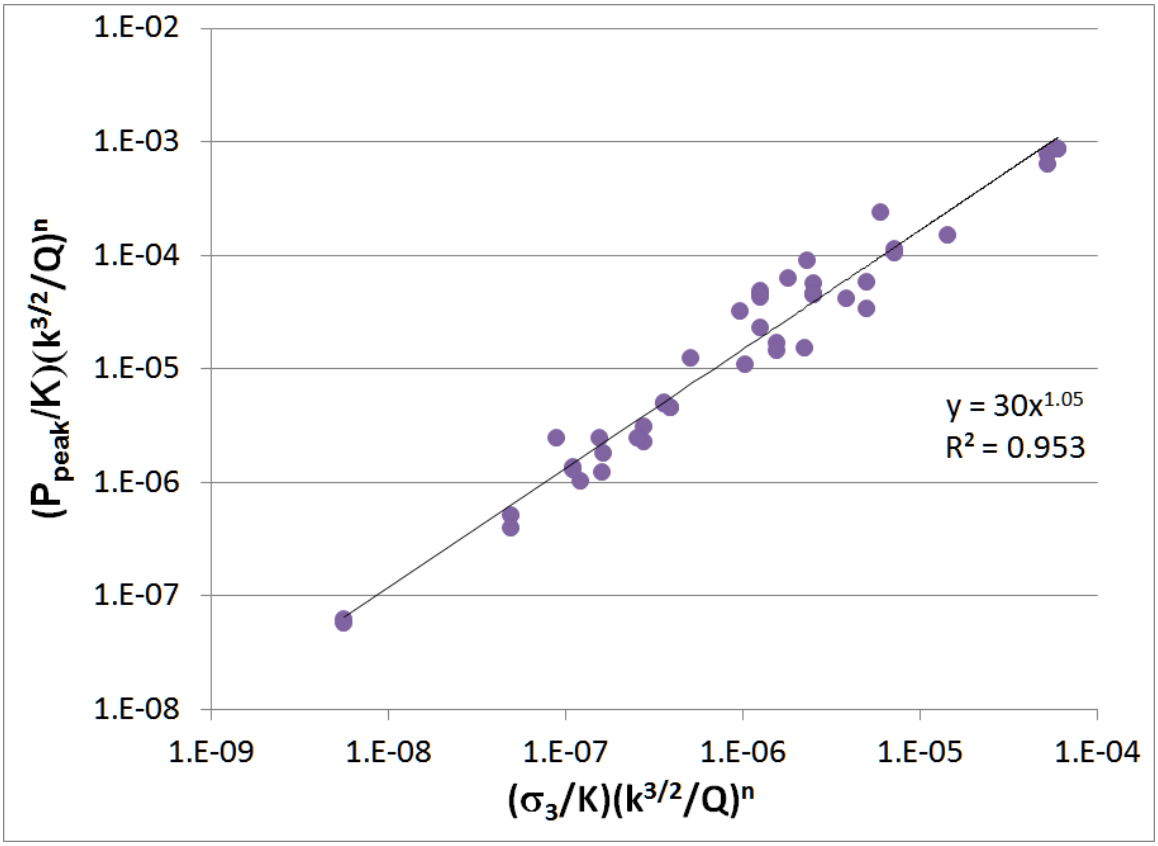

Figure 4.4. Dependence of dimensionless peak injection pressure versus dimensionless confining stress (plot based on 45 test results). For only tests injected with silicone fracturing fluids.

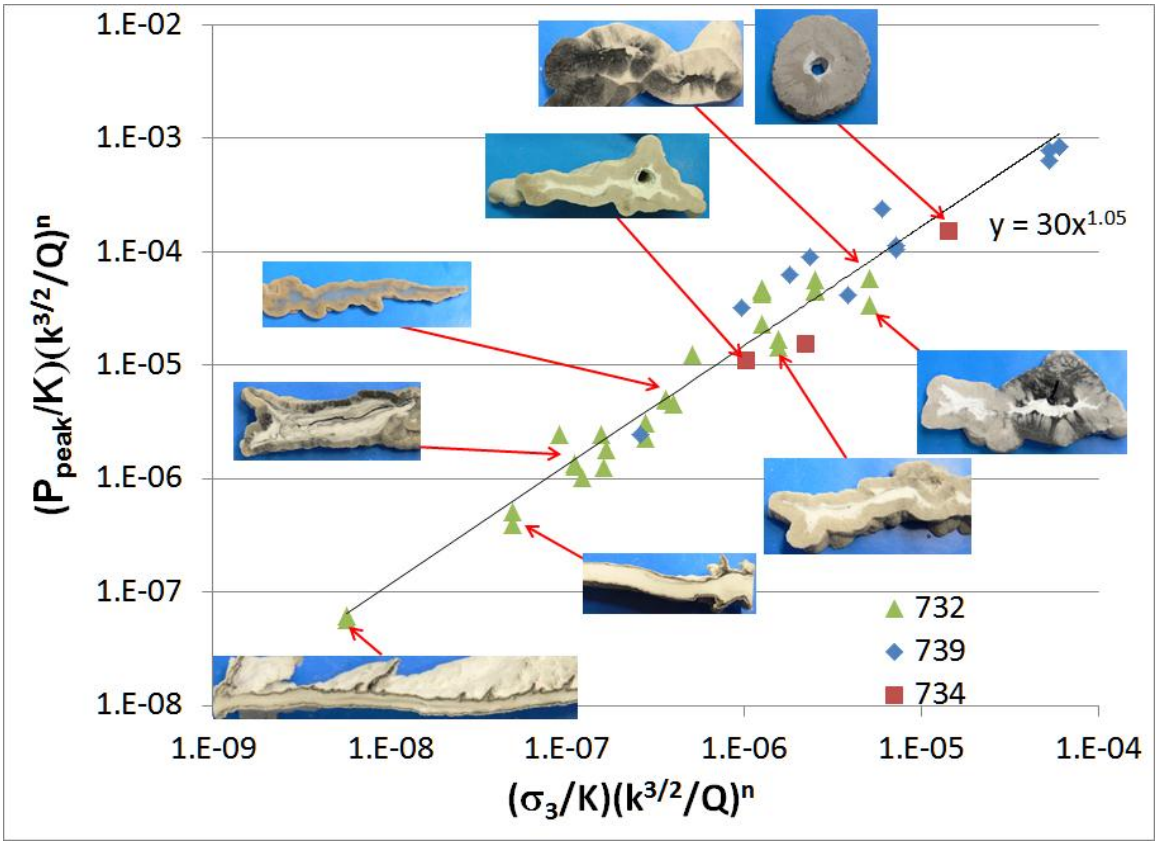

Figure 4.5. Same plot as Figure 4-4 with fracture cross-sections. This shows a general trend of increasing leakoff with increasing dimensionless parameters. The data points are listed in groups of silicone fluid type. Table 3-3 gives the n and K values for the silicone fluids (medium viscosity silicone (732) K = 123 Pa sec^n, n= 0.75; high viscosity silicone (739) K = 603 Pa sec^n, n= 0.60). The 734 data points are limited, so the characterization is not included here. The viscosity of the 734 is lowest of the silicone fluids (K = 43 Pa sec^n, n= 0.60).

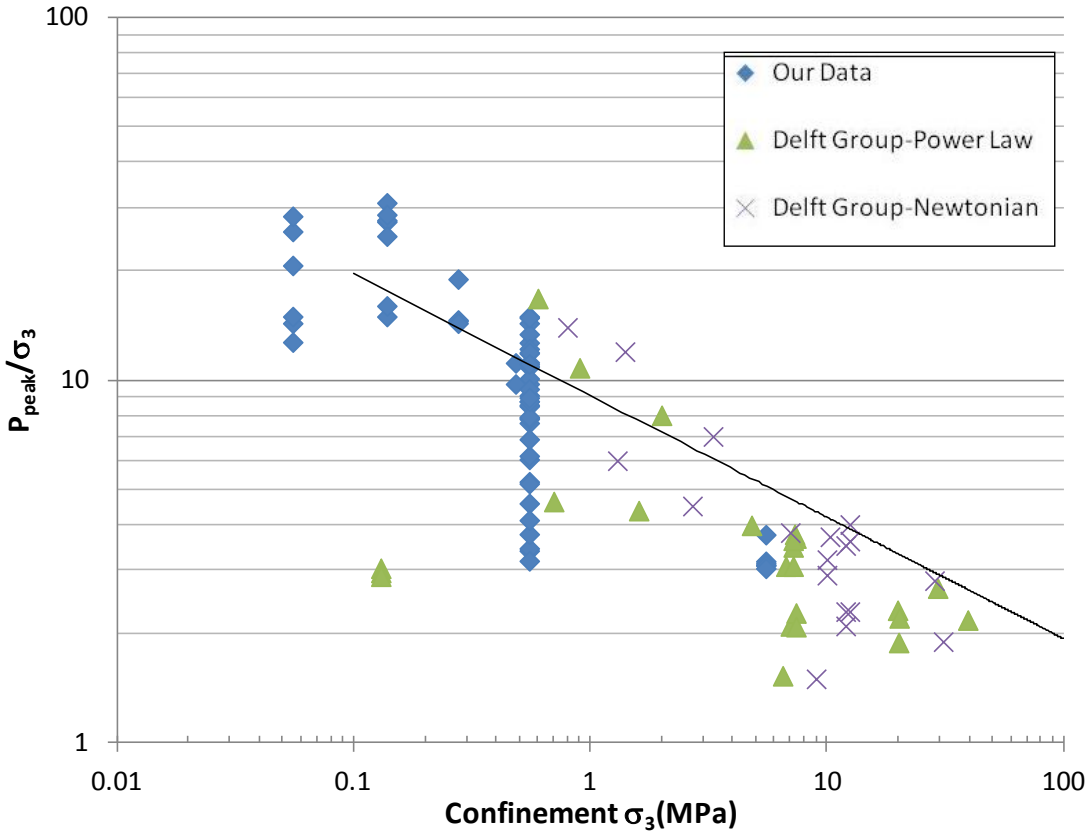

Figure 4.6. Normalized peak pressure versus confinement taken from *Bohloli and Depater*, [2006], *Dong* [2010] and *Dong and De Pater* [2007a] with our data added. The straight line represents the peak pressure from cavity expansion tests in dry sand from *Alsiny et al.* [1992] as presented by *Bohloli and De Pater* [2006].

4.2.1. Dimensional analysis of fracture propagation

Dimensional analysis may be applied to fracture propagation in a similar fashion. We utilize our measured fracture aperture and leakoff thickness along with the recorded injection pressure at the end of the fracture injection. In our tests the final pressure measured at the end of the injection sequence is the minimum pressure. Therefore, we can utilize a similar dimensional analysis as above, with P_{min} replacing P_{peak} and incorporating experimental time.

$$P_{\min} = f(Q, K, n, k, \sigma_0, t) \tag{4.9}$$

We can consider fracture efficiency instead of the aperture and leakoff thickness as separate independent terms. We calculate the efficiency as

$$e = \frac{w}{w + w_{leak}} \tag{4.10}$$

where w is fracture aperture an w_{leak} is the thickness of the leakoff zone. It gives a quantitative evaluation of the ratio between injected volume and fracture volume. This definition is similar to the fracture efficiency used in the oil and gas industry (though not a volume formulation). Fracture efficiency is a function of the experimental parameters and conditions and experimental time,

$$e = f(Q, K, n, k, \sigma_0, t) \tag{4.11}$$

If we consider that fracture efficiency changes monotonically with time, we can replace t in equation 4.9 with efficiency e and obtain $P_{\min} = f(Q, K, n, k, \sigma_0, e)$. This results in six parameters, with three basic units. The parameters with independent dimensions are again chosen to be, Q, K, and k. The resulting Π terms are

$$\Pi_1 = \frac{P_{\min}}{K}\left(\frac{k^{3/2}}{Q}\right)^n, \ \Pi_2 = \frac{\sigma_o}{K}\left(\frac{k^{3/2}}{Q}\right)^n, \ \Pi_3 = e \tag{4.12}$$

so that

$$\frac{P_{\min}}{K}\left(\frac{k^{3/2}}{Q}\right)^{n} = F\left[\frac{\sigma_o}{K}\left(\frac{k^{3/2}}{Q}\right)^{n}, e\right] \tag{4.13}$$

The dimensionless groups are plotted by fracture efficiencies in **Figure 4.7**. We observe decreasing efficiency with an increase of dimensionless pressure versus dimensionless stress. The data set is not conclusive, however. If we plot fracture aperture instead of fracture efficiency, as shown in **Figure 4.8**, then there is no detectable pattern within the dimensionless parameter plot.

The lack of correlation between the dimensionless groups and fracture aperture suggests that there may be one or several missing parameters. The most likely parameter, from a LEFM stand point, is material stiffness. If we consider an elliptical shaped hydraulic fracture, the maximum fracture width (w_{max}) can be shown as [e.g., *Economides and Nolte*, 2000]

$$w_{\max} = \frac{2 p_{net} d}{E'} \tag{4.14}$$

where p_{net} is the net hydraulic pressure (internal fluid pressure minus the fracture closure pressure), d is the minimum extent of the fracture (either height or width), and E' is the plain strain elastic modulus. The plain strain elastic modulus is related to the Young's modulus by the Poisson's ratio $E'=E/(1-\nu^2)$. A significant dependence on the confining stress exists for the Young's modulus, in our unconsolidated particulate materials. Nonetheless, as shown in Chapter 3, our stiffness is identical for all our samples at similar confinement stresses. Therefore, the interpretation of **Figure 4.8** is

not that the material stiffness is missing from our dimensional analysis, but that it is important. In this work, we specifically chose our materials to maintain similar Young's modulus. An extension of this work, however, would likely benefit from the inclusion of material stiffness as a varied parameter.

If we exchange fracture aperture thickness with leakoff thickness (as shown in **Figure 4.9**), then there is a trend of increasing leakoff thickness with increasing dimensionless parameters. This is likely the reason that a small trend is shown in **Figure 4.7**. This indicates that fracture aperture is not characterized by our scaling analysis. Leakoff thickness may be, however. This is reinforced by the experimental observations in that the confining stress plays a significant role in determining the magnitude of leakoff thickness. Below we utilize an additional dimensionless analysis to further characterize our observed leakoff thickness.

The cross-sectioning of our fractures, coupled with the two color phase fluid injection allows for a qualitative analysis of the leakoff process. In a majority of our tests, as described fully in Chapter 5, the leakoff appears to be mainly confined to the tip region of the propagating fracture (**Figure 4.10**). To facilitate this analysis, we define two length scales: (1) the thickness of the leakoff in the vicinity of the fracture tip, d, and (2) the thickness of the leakoff layer at a distance far away from the tip, h. If we consider that $h \simeq d$ then they are both independent of time. Following a similar process as above we obtain

$$h = f\left[Q, K, n, k, \sigma\right] \tag{4.15}$$

Choosing Q, K, and k as independent dimensions we identify the relevant dimensionless combinations

$$\Pi = \frac{h}{Q^{1/3}}\left(\frac{\sigma}{K}\right)^{1/(3n)},\ \Pi_1 = \frac{\sigma_o}{K}\left(\frac{k^{3/2}}{Q}\right)^{n},\ \Pi_2 = n \tag{4.16}$$

applying the Π-theorem [e.g., *Barenblatt*, 2003] results in

$$\frac{h}{Q^{1/3}}\left(\frac{\sigma}{K}\right)^{1/(3n)} = \mathrm{F}\left[\frac{\sigma_o}{\mathrm{K}}\left(\frac{\mathrm{k}^{3/2}}{\mathrm{Q}}\right)^{\mathrm{n}}, n\right] \tag{4.17}$$

The data are plotted in **Figure 4.11**. If we approximate dependence in (4.17) by a power law and group fluids with similar fluid flow behavior indices *n* then we obtain,

$$\frac{h}{Q^{1/3}}\left(\frac{\sigma}{K}\right)^{1/(3n)} = \mathrm{A}\left[\frac{\sigma_o}{\mathrm{K}}\left(\frac{\mathrm{k}^{3/2}}{\mathrm{Q}}\right)^{\mathrm{n}}\right]^{\alpha} \tag{4.18}$$

this can also be expressed as

$$h = A\sigma_o^{\ \alpha - 1/3n} K^{1/3n - \alpha} k^{3n\alpha/2} Q^{1/3 - n\alpha} \tag{4.19}$$

where α=0.5, A=11,000 (**Figure 4.11**) and n=0.75 (value of the fluid behavior index of the medium viscosity silicone adhesive (732) Substituting these values in (4.18), we finally obtain

$$P_{peak} = A\sigma_o^{\ a} K^b k^c Q^d \tag{4.20}$$

where A=11,000, a=0.06, b=-0.06, c=0.56, and d=-0.05 for the medium viscosity silicone adhesive (732). For the high viscosity (739) silicone the values of the exponents are A=11,000, a=0.06, b=-0.06, c=0.56, and d=-0.05. For both fluids, the dimensional analysis shows the importance of permeability on the leakoff thickness. The other parameters have smaller magnitudes of exponents.

The dimensional analysis has been shown as an important tool for evaluating parameter effects on peak fracture injection pressures. Further, it appears that leakoff thickness can also be characterized through dimensional analysis, independent of time. This time independence is due to the relatively uniform leakoff thickness along the length of the cross-sectioned fracture. Clearly, longer experimental time scales should be implemented to verify the scalability of this result.

This may be the first direct experimental observation of the dominance of the leakoff process in the tip region of a propagating fracture in cohesionless materials. This is an important consequence of this work. Further, the experimental observations of the leakoff processes predominantly at the tip are reinforced through the dimensional analysis of the measured leakoff thickness.

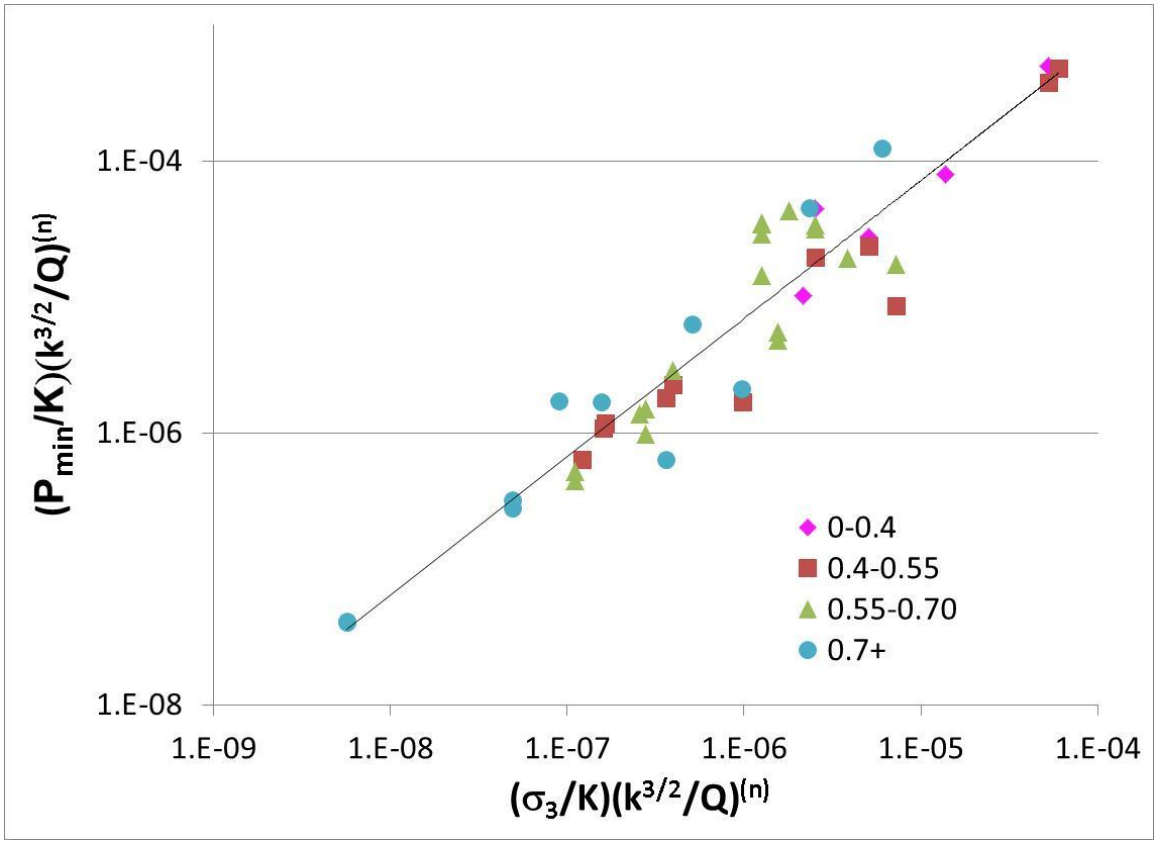

Figure 4.7. Dimensionless minimum pressure versus dimensionless confining stress. This is a similar plot as shown in **Figure 4.4** but with fracture efficiencies are explicitly shown in the legend. On can see a small trend of decreasing efficiencies with increasing dimensionless parameters.

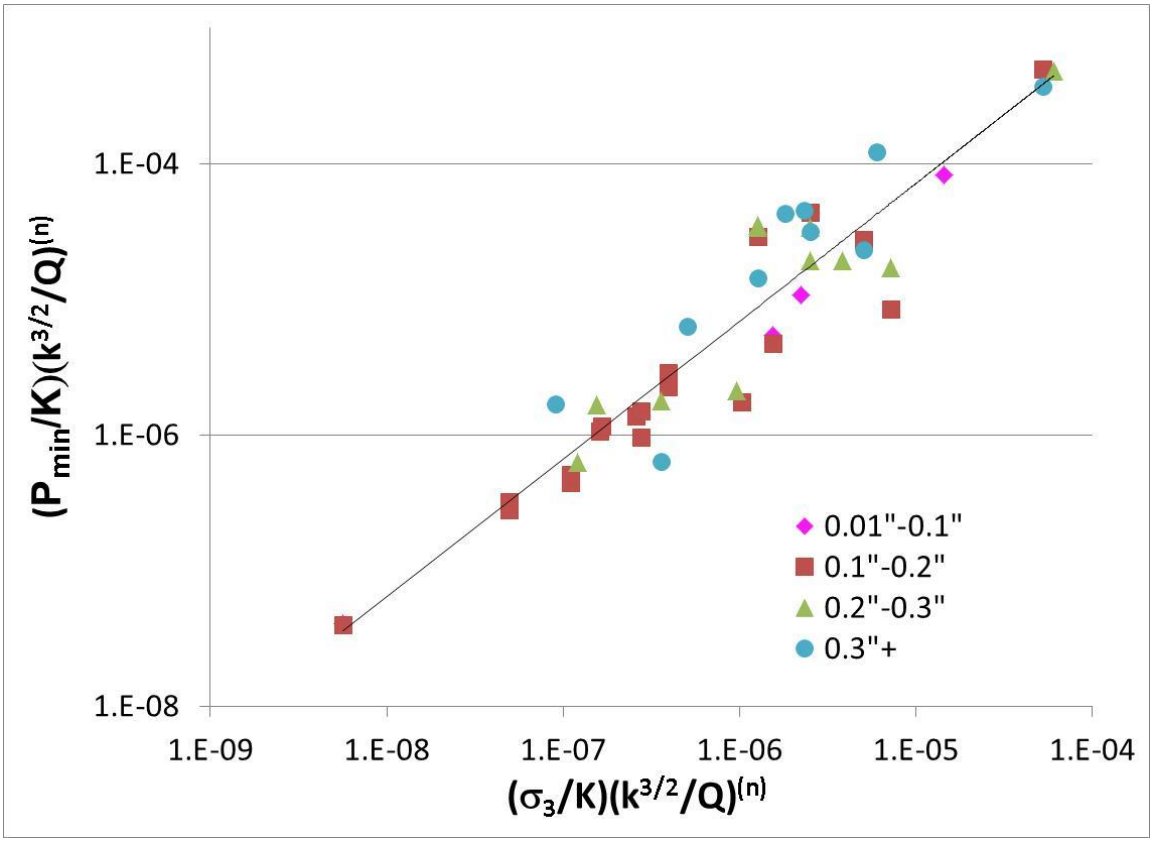

Figure 4.8. Dimensionless minimum injection pressure versus dimensionless stress. This is a similar plot as shown in **Figure 4.4** but with thickness of aperture in the legend. No apparent trend in fracture aperture with the dimensional parameters.

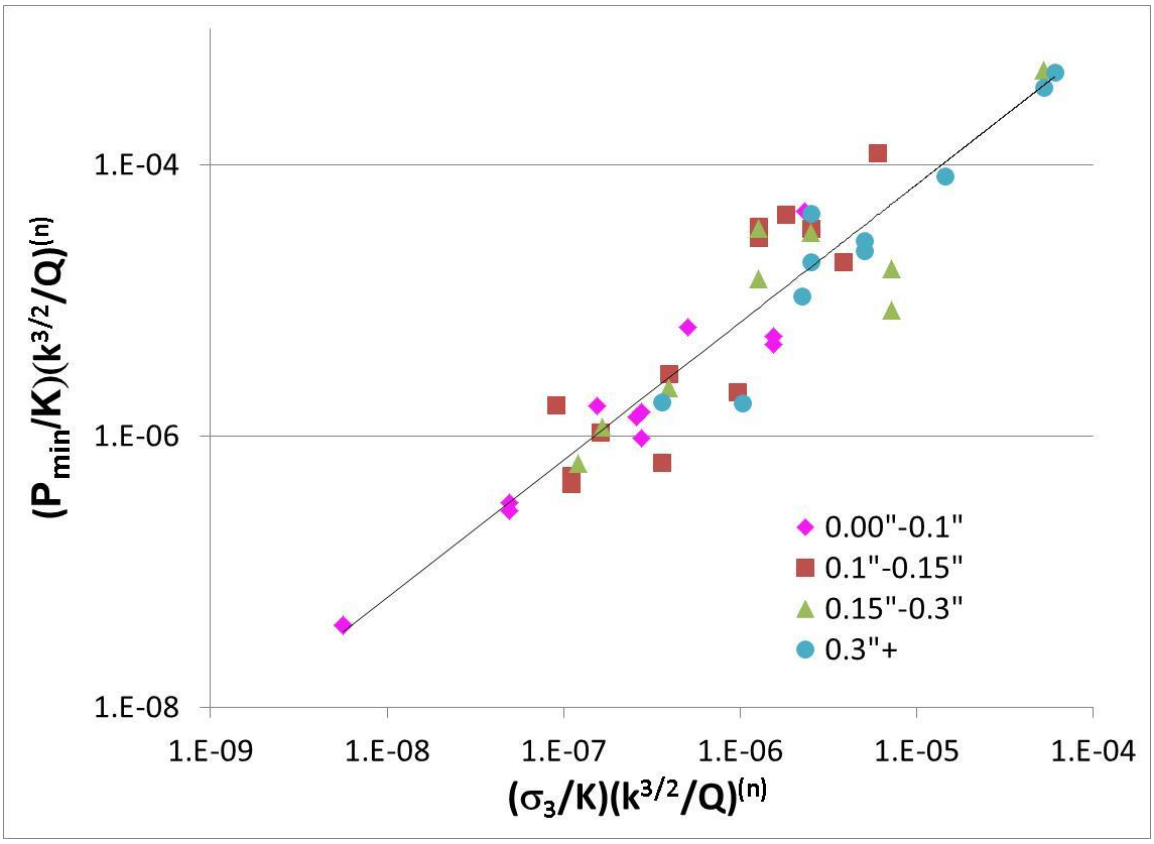

Figure 4.9. Dimensionless minimum pressure versus dimensionless stress for various leakoff thicknesses in *inches*. This is a similar plot as shown in **Figure 4.4**, but with leakoff thickness in the legend. Leakoff thickness does appear to increase with increasing dimensionless parameters.

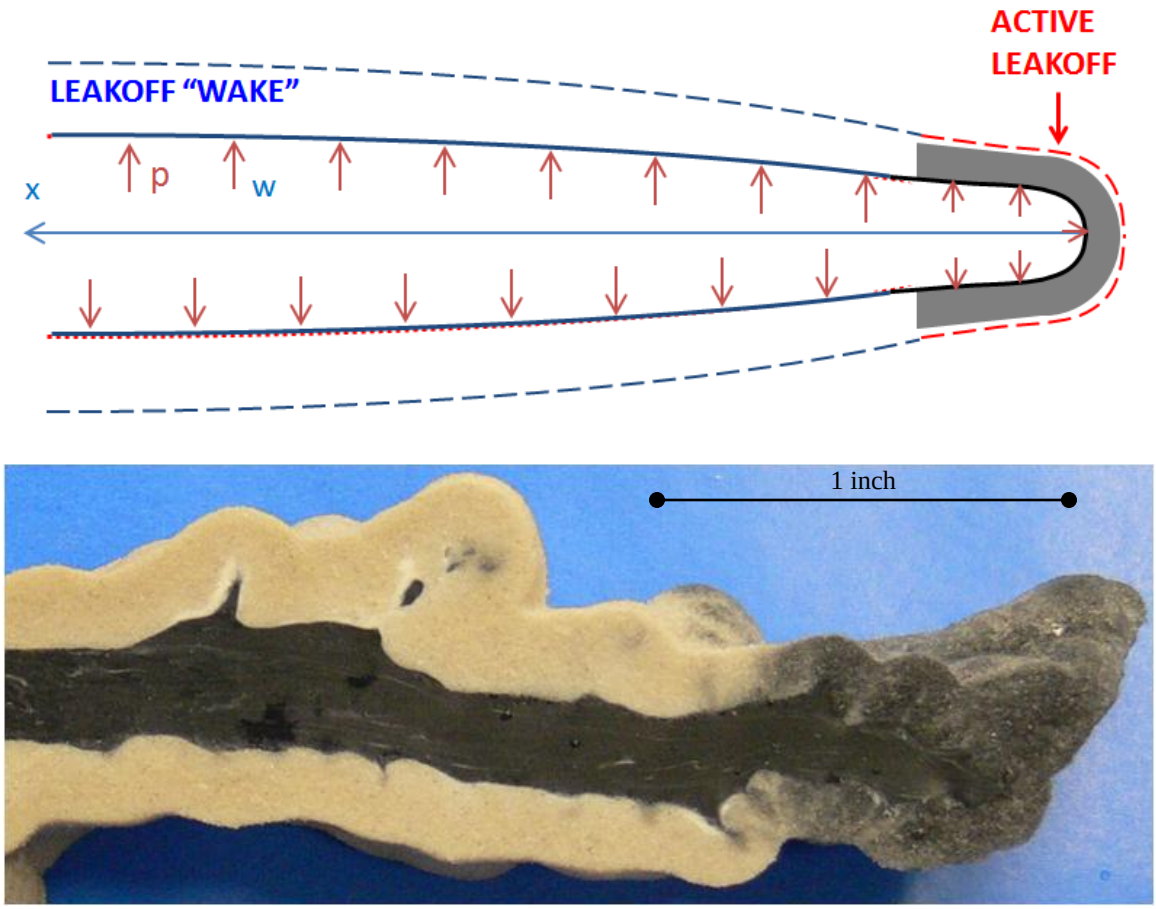

Figure 4.10. Picture of fracture cross-section with schematic of leakoff progress. The majority of the black colored fluid is primarily leaking off at the tip of the fracture. Further, there is an abrupt change in the leakoff color perpendicular to the fracture propagation direction. This suggests that a majority of the leakoff thickness occurs at the tip of the fracture. A more thorough discussion of the leakoff layer is in Chapter 5.

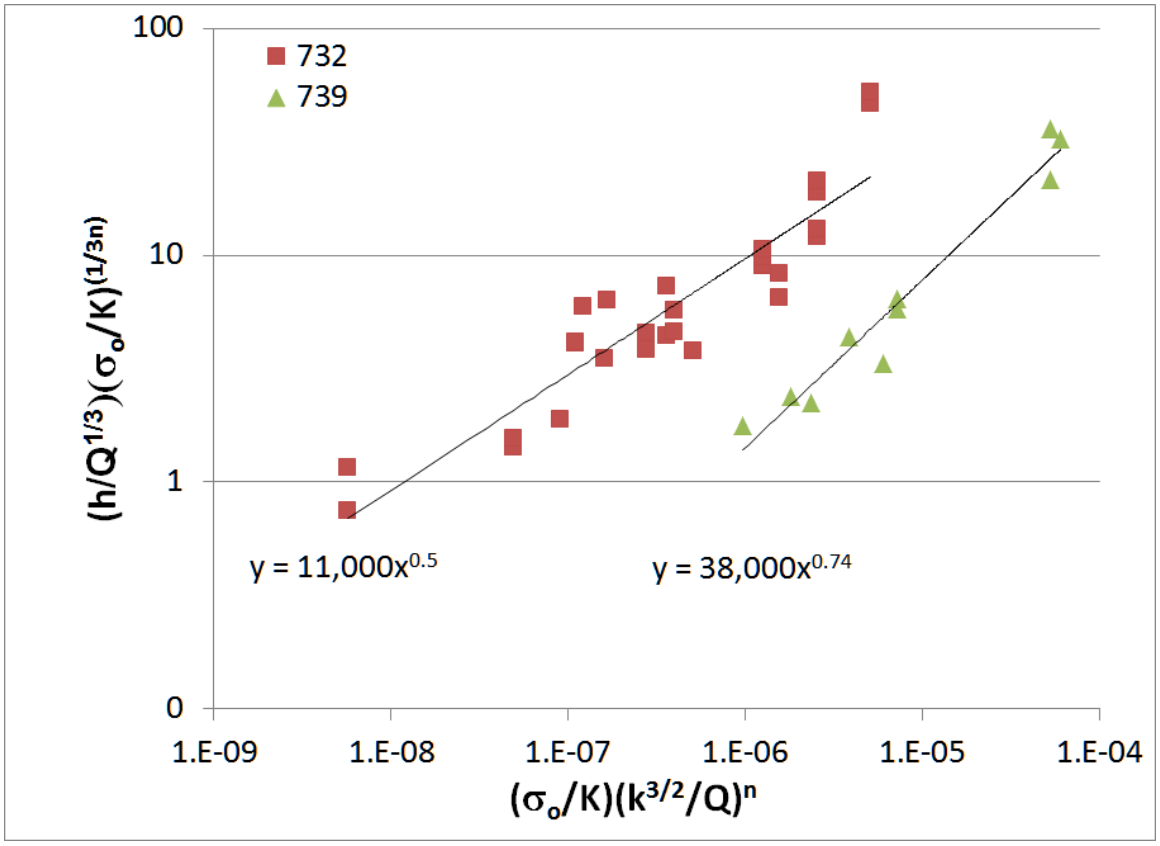

Figure 4.11. Plot of dimensionless leakoff thickness versus dimensionless confinement. The colored dots represent the measured leakoff thickness for the fracture tests utilizing silicone adhesive injection fluid.

4.3. Injection Pressure Signatures

The recorded fracture injection pressure is an important result from our tests. The use of the single diaphragm pump did not produce pressure curves that were particularly useful in interpreting the generated pressure versus time data. We are able to estimate peak pressures from these pressure curves and when verified with results generated from other pumps, pressures are theoretically the same. The pressure curves presented here are only from the triplex pumps. These pumps produced smooth pressure curves when no other issues arose (e.g., clogging of injection tubing or screens).

4.3.1. Characteristic Pressure Curve

Pressure curves generated in our tests were primarily smooth with a gradual pressure decline (**Figure 4.12**). A defined peak exists with smooth curvature down to a constant pressure that signifies fracture interaction with the interface of the lateral boundary. The pressure signature fluctuations due to boundary interactions are discussed further in Section 3.7.1.

We found no discernible pattern of pressure signature with fracture shape. As an example, **Figure 4.13** shows a high-leakoff test along with a low leakoff test, the normalized adjusted pressure curves are similar and peak pressures are identical, yet geometries are very different. In general, the resulting pressure signatures of our tests were as varied as the created fracture shapes (**Figure 4.13** and **Figure 4.14**). In **Figure 4.14** there are two tests under the same conditions, the peak pressures were similar, yet

propagation pressures were not. Only the peak injection pressures of our tests showed any significant trends.

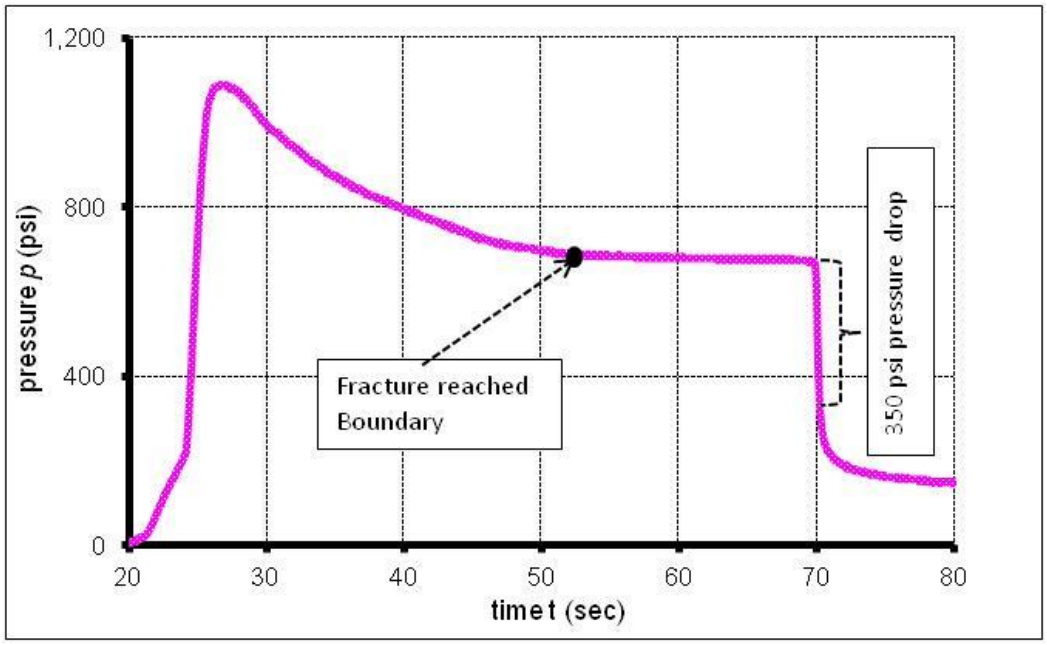

Figure 4.12. An example of expected pressure-time curve, raw data and unadjusted pressures shown for Test 04-05-11.

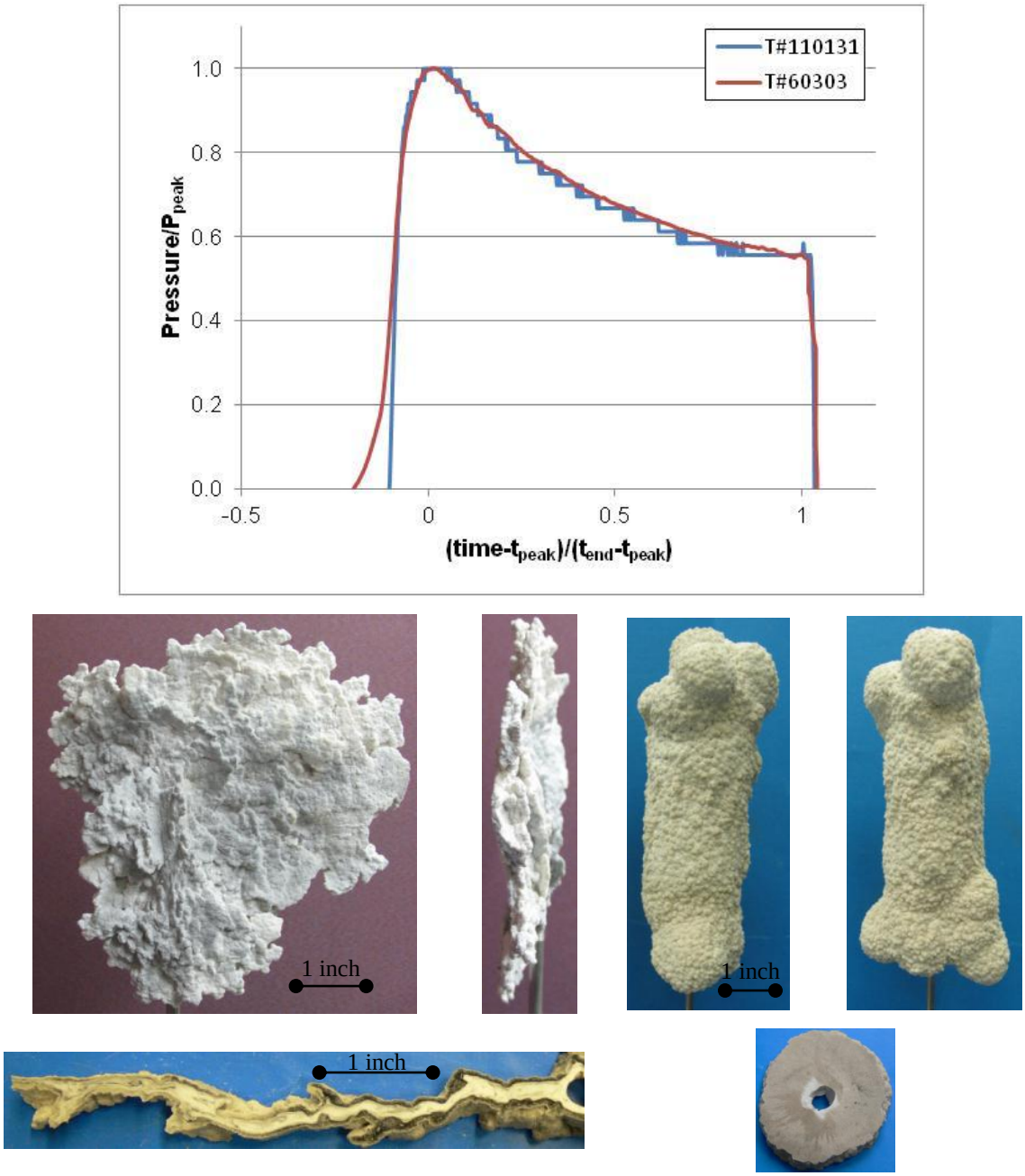

Figure 4.13. Normalized Pressure (adjusted pressures) versus normalized time and fractures created in (a) Test 01-31-11 (b) test 03-03-06. Two very different geometries yet same normalized pressure-time histories.

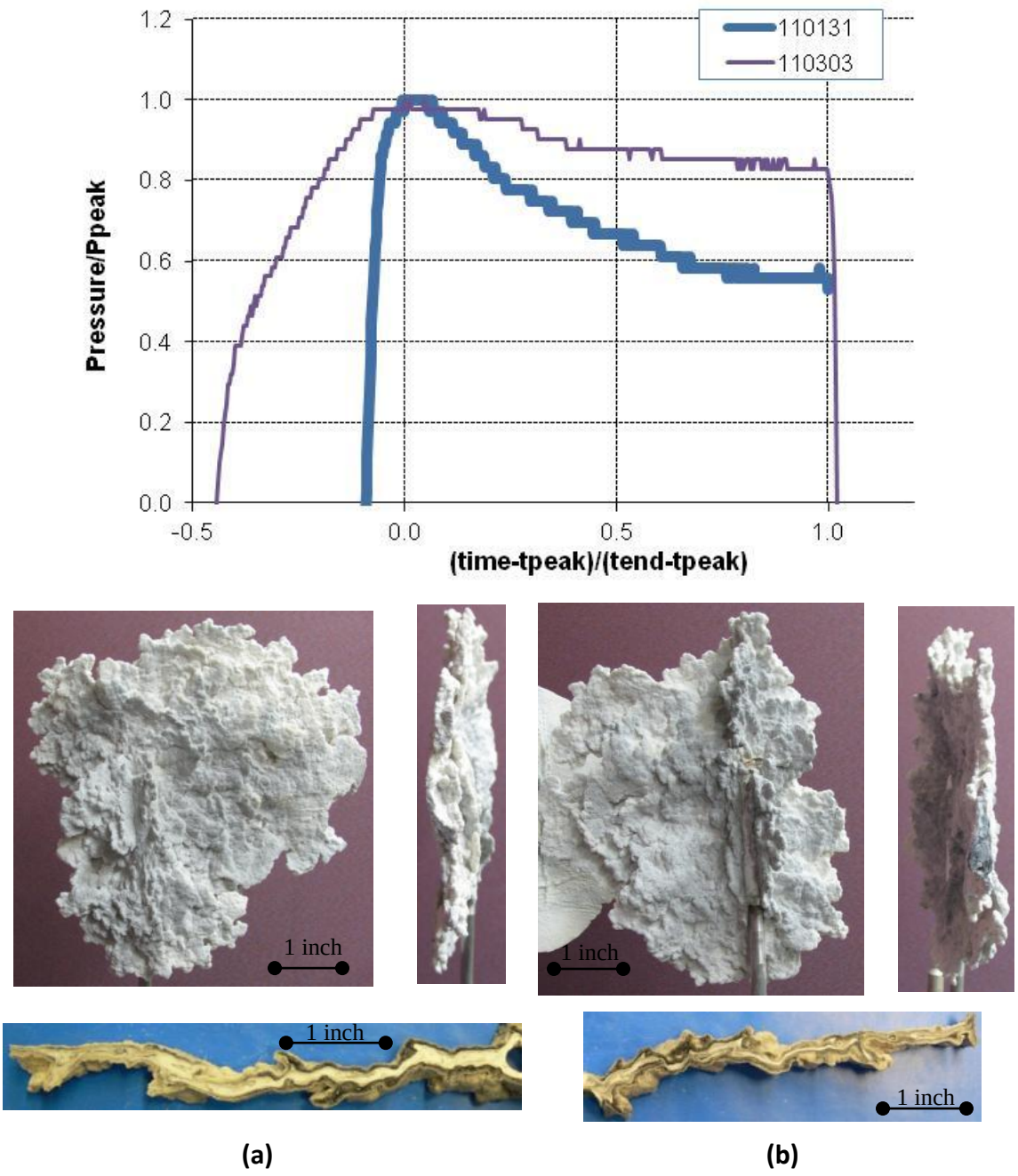

Figure 4.14. Normalized pressure-time curves from two identical Tests. Although peak pressures in the tests were simililar, presure-time histories during fracture propagation varried considerably. (a) Test 01-31-11 (b) Test 03-03-11.

4.4. Fracture Morphology

We use the term fracture morphology to describe both the fracture shape and the leakoff surface. In high-leakoff tests, the morphology we describe is primarily the leakoff surface (as shown in **Figure 4.16** (a)) the actual fracture morphology is obscured due to the leakoff. However, the fracture geometry becomes much more apparent as we manipulate the experimental parameters to limit leakoff. Nevertheless, in most tests, the leakoff surface does illustrate basic fracture geometry. In this section, we describe in detail the leakoff surfaces and cross-sections of our experiments.

4.4.1. Leakoff features

The features that dominate the surface of fractures in highly permeable saturated sands appear as a point-source infiltration phenomenon. We call these "spheroids" and their size decreases with increased resistance to fluid invasion. These features are not unique to our tests, three examples from the literature are shown in **Figure 4.15**.

We found that the spheroids can be significantly reduced by reducing the confining stresses and/or permeability, or increasing the viscosity and/or flow rate or any combination thereof (basically increase fluid flow resistance in the matrix). **Figure 4.16** shows a decrease in spheroids with decrease in confining stress (all other parameters remaining the same).

If we decrease the resistance to fluid flow in the host material, then these features become progressively larger until the formation does not 'fracture' and only

fluid invasion takes place. The fracture in **Figure 4.17**(b) shows the boundary of the leakoff thickness we considered useful. There is very little evidence of fracture development for such an experiment.

The characteristic fracture shape appears dependent on the magnitude of the leakoff. Large volumes of leakoff lead to significant tortuosity as the spheroid development dominates. The fractures become less tortuous and more planar, as the spheroid development becomes less dominate. However, fractures appear as a collection of these features whenever present on the fracture surface. This indicates that the leakoff process dominates the fracture development.

4.4.2. Silica flour experiments

In an attempt to reduce the size of the spheroid features we conducted several tests in $100\ \%$ silica flour samples. These tests resulted in a dramatic change in the nature of the fracture morphology. The images in **Figure 4.19** show the result of one such experiment. The feature is less planar and has multiple wings. These wings are orientated vertically and there appears to be three main branches. The three wing feature has not been as prevalent in our experiments described above. However, the results presented by *Chang* [2004] presented numerous instances of three winged fracture development in dry silica flour samples injected with joint compound.

Saturation of pore fluid was not possible due to the size of the LTC and the low permeability of the dense silica flour. Therefore, we limited the silica flour experiments to dry samples. The silica flour experiments contain many unique features. The leakoff

thickness is quite thin compared to greater permeability experiments. Multiple offshoots emanate from the primary fracture. These offshoots are typically at distinct acute angles to the propagation direction. In instances where curvature of the facture is observed, the majority of angular protrusions are on the fracture face positioned to the outside of the curve. We have measured several of these angular offshoots. There was no detectible pattern with any of the experimental parameters; typically these angles were between 40^{o} to 70^{o}. These offshoots suggest a manifestation of a localized shear failure mechanism at the crack tip.

4.4.3. Transition of features

The leakoff features are consistent with a majority of our experimental results. However, there is a transition as the spheroid feature decreases to a limiting value (as shown in **Figure 4.21**). Once the leakoff surface becomes thin enough the spheroids are no longer apparent and the fracture morphology changes significantly. Our silicone fracturing tests feature these spheroids for all fine sand and silica flour mixtures for all our parameters, except for two "transition" fractures described later in this section. There was only a dramatic change in fracture morphology when the sample consisted of dry silica flour.

The prevalence of the bubbly features described above is a direct consequence of our particular experimental parameters. A significant question arises from observing our spheroids. That is, what happens when the spheroids reduce to past a minimum size? The sizes of the spheroids continue to decrease as the matrix fluid flow resisting

forces increase. The reduction in the size continues until the spherical nature of the localized leakoff became less rounded and more a flat petal-like feature. In our tests, these pedal features are typically oriented in a vertical direction (**Figure 4.21**).

These experiments also show a transition away from the localized leakoff feature (small individual petals) to a more uniform brittle-like fracture surface (shown in **Figure 4.22**). The brittle-like features (shown in **Figure 4.22**) exhibit similar leakoff surface characteristics as the fractures described in Chapter 7 (comparison pictures in **Figure 4.224**). The brittle-like features are relatively smooth and appear as one continuous feature, unlike the leakoff-dominated features mentioned above. Brittle-like in particulate materials is different from solids, because in solids, fractures can be brittle for any leakoff, large or small. In particulate materials brittle-like corresponds to small leakoff. The existence of the single planar feature suggests that fracturing fluid was delivered by a fracture process and subsequently the leakoff process initiated. Contrast this with the spheroids that indicate the local leakoff process precedes the fracturing process.

(a) (b) (c)

Figure 4.15. Three examples of bubbly surface features: from the works of (a) *Chang* [2004], (b) *Dong* [2010], and (c) *Jasarevic et al.* [2010].

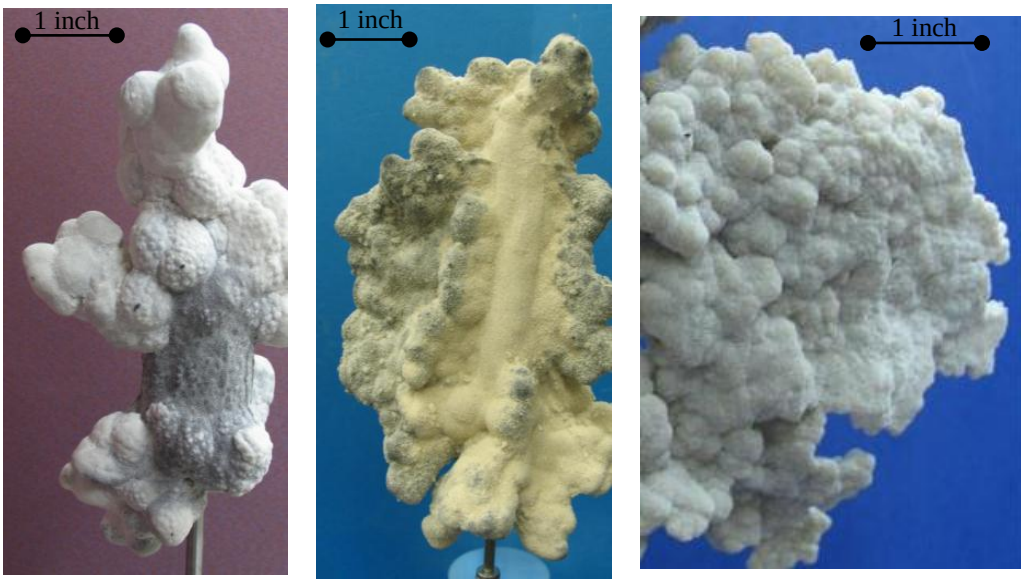

(a) (b) (c)

Figure 4.16. Bubbly features in the leakoff layer observed in: (a) Test 02-10-11 (80 psi), (b) Test 11-22-06 (40 psi), and (c) Test 09-28-05 (20 psi). Leakoff thickness decreases from (a) to (c) due to a reduction in confinement stress.

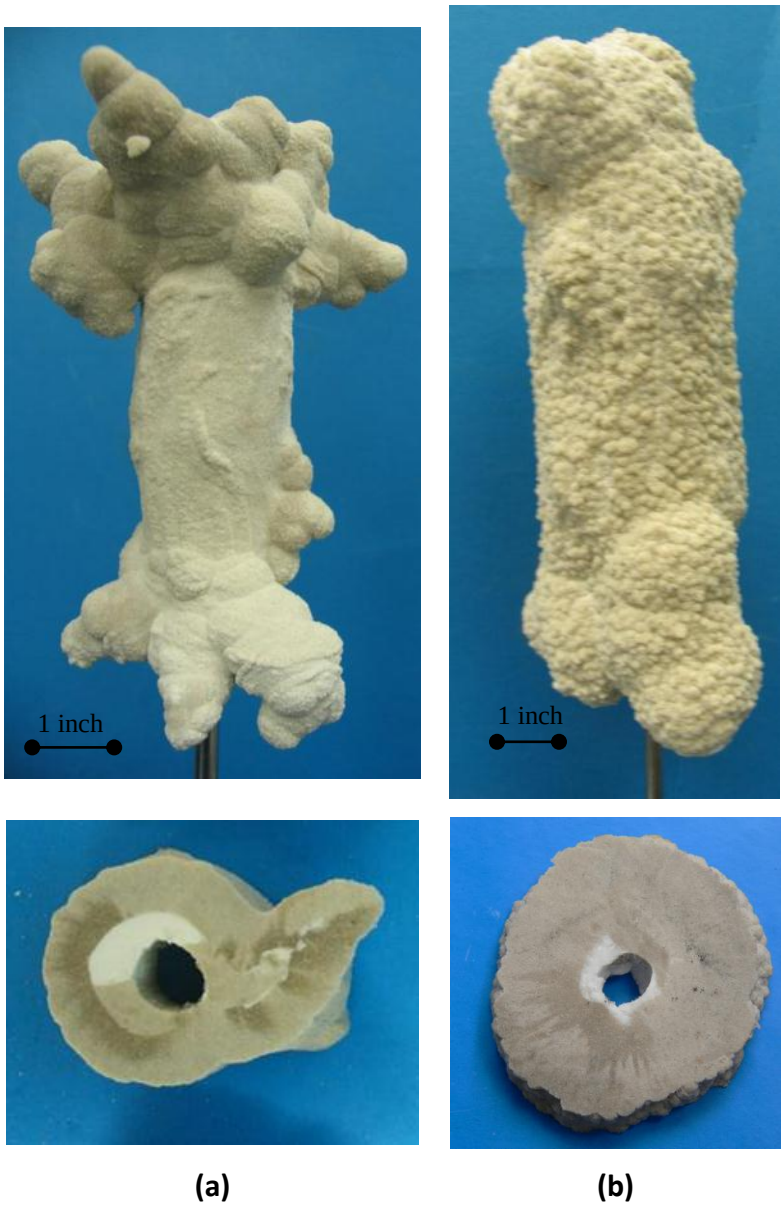

Figure 4.17. Large leakoff tests: (a) Test 08-11-07 (600 ml/min) and (b) Test 03-03-06 (50 ml/min) (b) Fracturing parameter combinations resulting in the large leakoff tests are not the primary goal of this work. Leakoff is increased from (a) to (b) by only the reduction of flow rate.

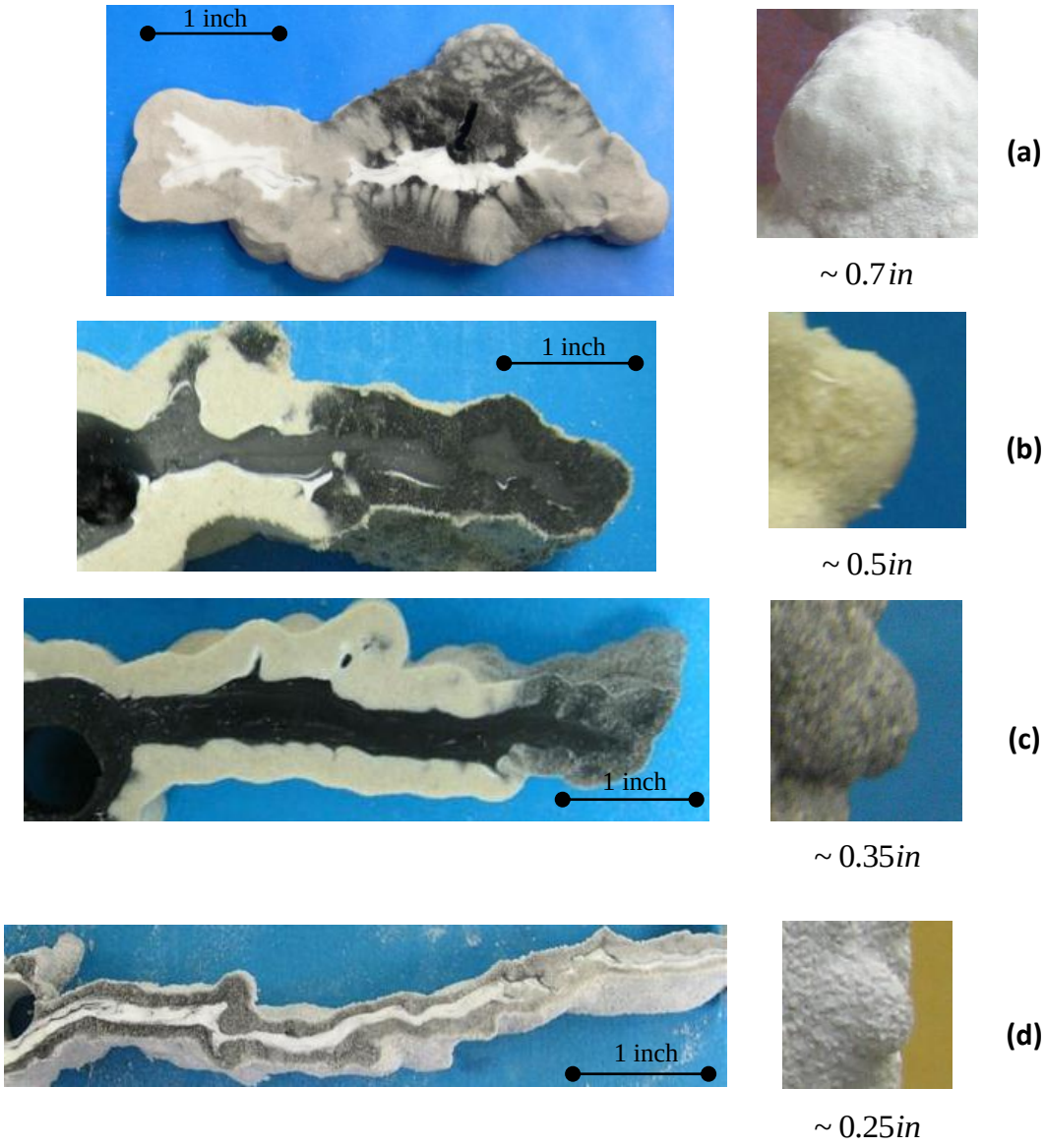

Figure 4.18. Cross-sections of fractures with decreasing bubbly features: (a) Test 02-10-11, (b) Test 11-22-06, (c) Test 09-27-07 and (d) Test 11-06-08. Approximate size of spheroids is shown on the left. The width of leakoff decreases from (a) to (d). Fracture aperture also decreases, but less so.

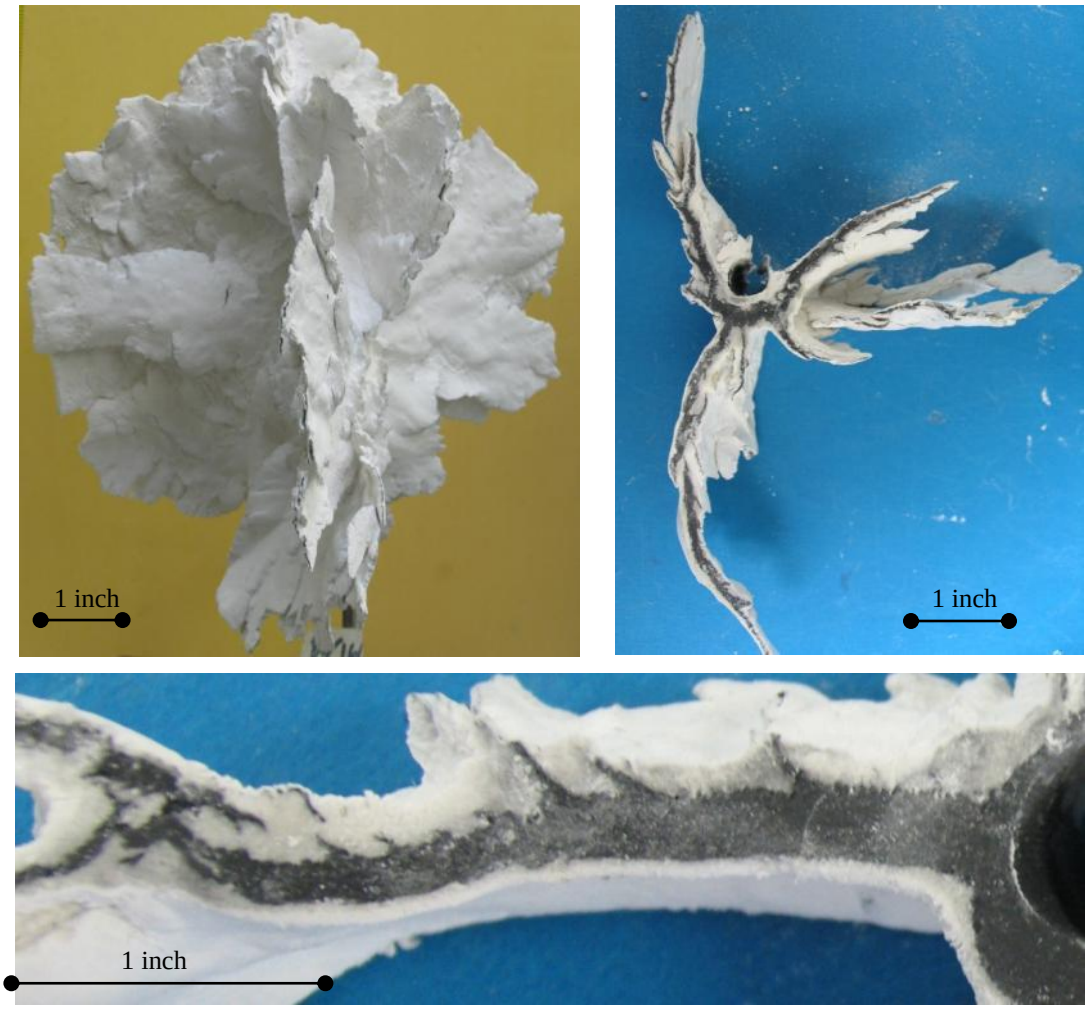

Figure 4.19. Fracture morphology observed in Test 09-22-08 fracturing of 100% silica flour. The offshoots typically are smaller than the fracture aperture and are only on one side of the fracture face (typically on the outside face of the curved surface of the fracure). Offshoots are at acute angles to the propagation direction.

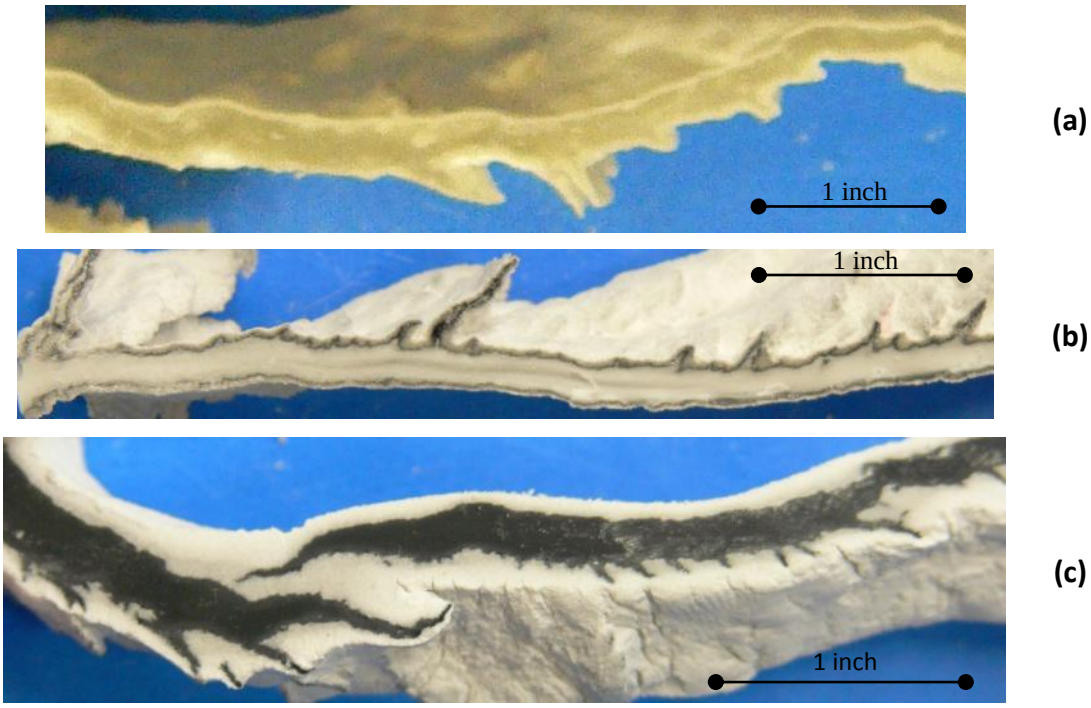

Figure 4.20. Multiple silica flour injection test cross sections showing acute angular offshoots fracture propagation from left to right in images. Notice offshoots are on one side of the fracture face. (a) Test 08-14-08 (b) Test 09-15-08 and (c) Test 09-22-08.

Figure 4.21. Decrease of spheroid size to a pedal-like feature. Red circles indicate the size of localized leakoff features, the pedal feature has an aspect ratio ~3/1.

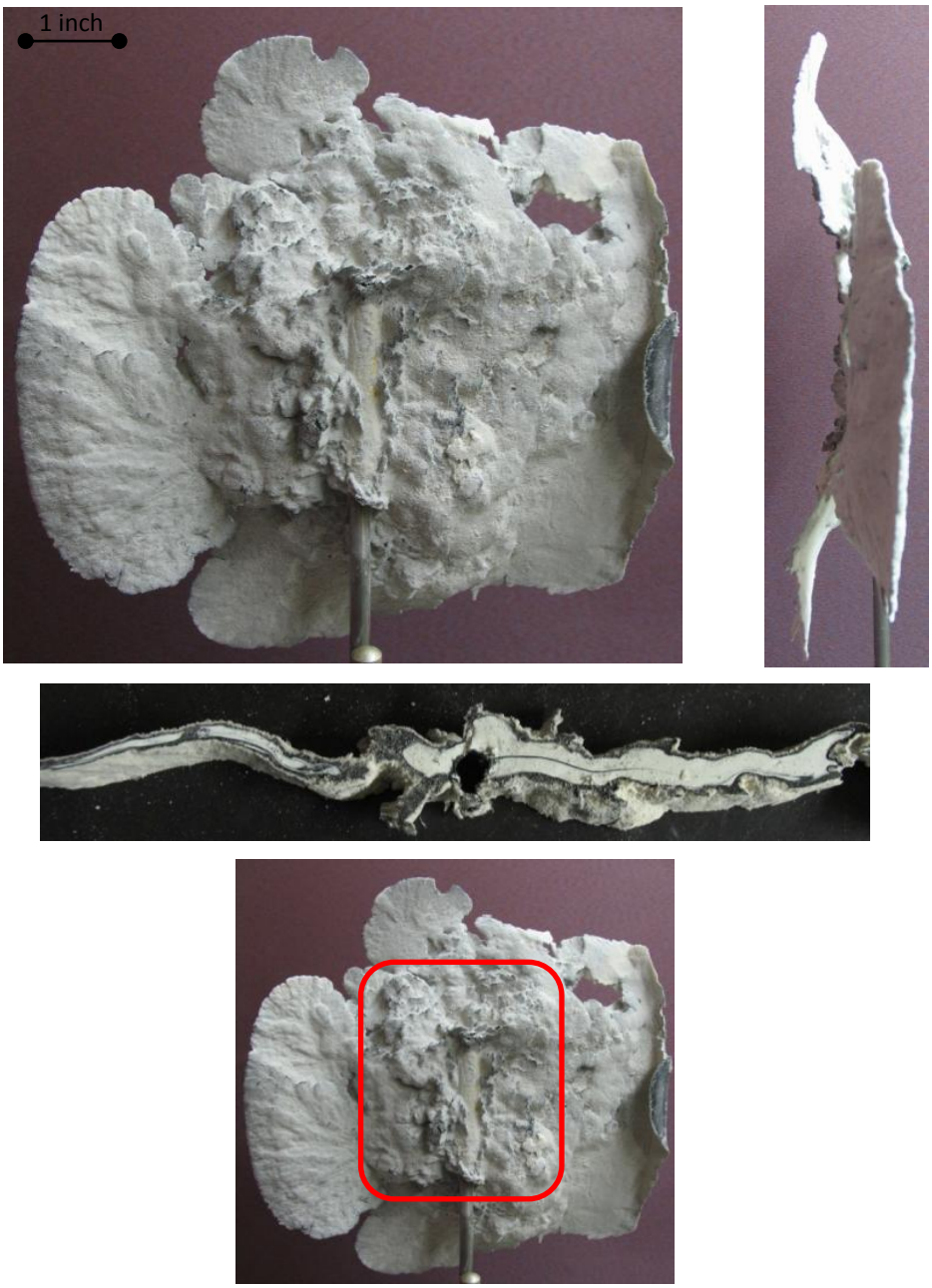

Figure 4.22. Example of the transition away from localized leakoff to more brittle-like fracture morphology (Test 03-17-11). The cross-section of the fracture shows a thick region where the leakoff is localized, the brittle-like region is quite thin in comparison. The regions outside the red square in the lower image are brittle-like features.

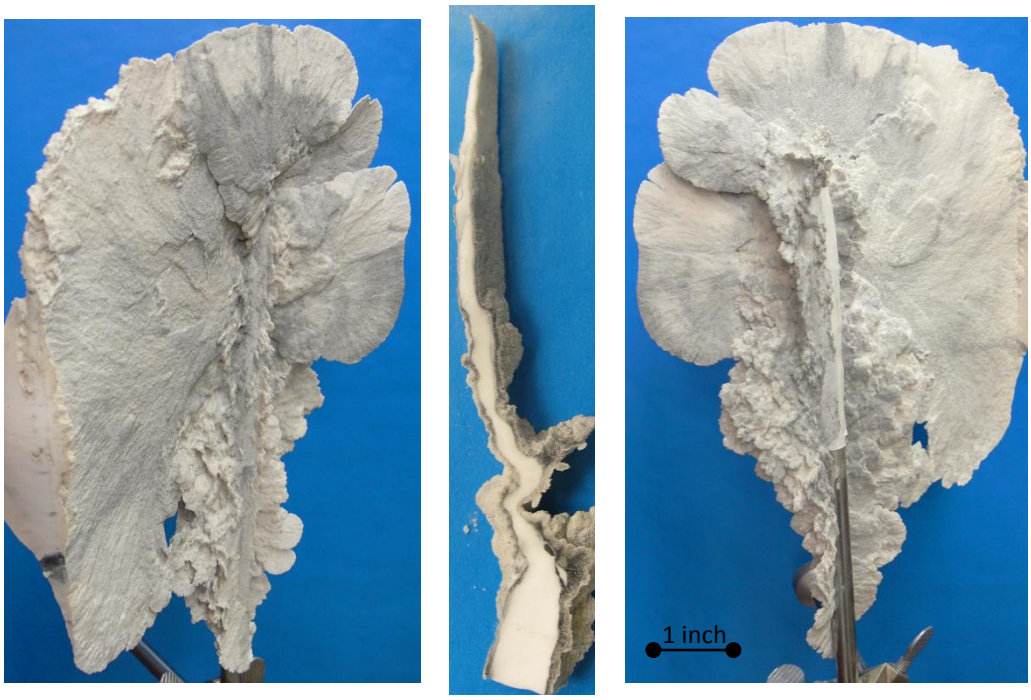

Figure 4.23. Silicone injection Test 11-05-12 showing transition in fracture morphology. The brittle region shown in the cross-section (top of image (b)) has limited offshoots and very thin leakoff layer.

Figure 4.24. Brittle-like features of fractures generated by three different fluids: (a) guar fluid Test 10-14-10, (b) medium viscosity silicone Test 05-12-11 and (c) high-viscosity silicone Test 03-17-11.

4.5. Sample Response During Fracture Tests

We recorded the cell and pore fluid volume during the injection tests. This allowed for monitoring sample response during the injection test, and after. In general, under the highest injection rates ($5000\ \mathrm{ml/min}$) the sample continued to respond for a significant time after the pumping was complete. Low injection rates exhibited no significant response after the injection event stopped. In addition, the resolution of the volume tracking was not sufficient to accurately monitor the volume change for the time scale of the experiments with high injection rates (**Figure 4.26**). We present two examples of the volume response in **Figure 4.24**.

The low stress, low rate experiments often experience significant dilation that results in pore fluid being drawn into the sample during the injection event (**Figure 4.24** (a)). This is registered as a negative volume response of monitored pore fluid volume. The leakoff process contributes to an increase in the measurement of pore fluid volume. Consequently, the exact magnitude of the dilation cannot be adequately quantified with our measurement technique.

In moderate stress, low rate tests, there is limited evidence of sample dilation. However, the confinement volume response exceeds injected volume for all experiments. This indicates that some sample dilation occurs in all tests.

If a sample exhibits an initial negative dilating pore fluid response **Figure 4.24** (a) the change in confinement volume showed a significantly greater volume expansion, than the volume of fluid injected. The excessive confinement response suggests a

significant degree of dilation. The presence of sample dilation suggests significant shear banding, perhaps from the fracture extension processes.

The reduction in pore volume is not seen in the high-stress experiments. Further significant change occurs in both the cell and pore fluid after the injection event has ceased. This is true for both high and low permeability samples. Finally, the confinement response is typically similar in volume, or slightly less than the injected volume. However, there is significantly greater pore fluid volume response than in the low flow rate tests.

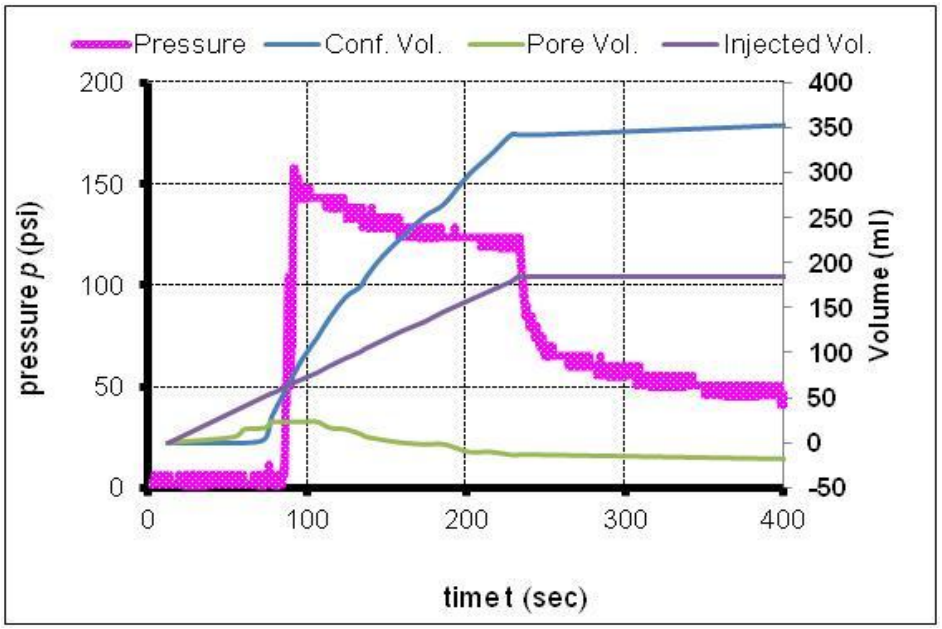

(a)

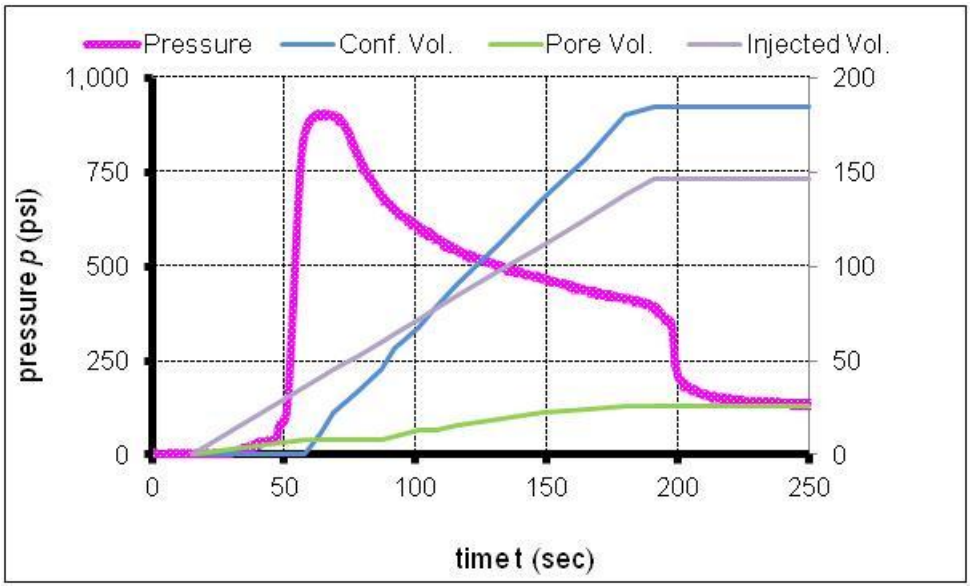

(b)

Figure 4.25. Unadjusted pressure-time and volume-time records from (a) Test 05-12-11 8 psi confinement (b) Test 04-22-11 80 psi confinement. Note the different pore fluid responses. Both tests were conducted in samples of fine sand silica flour mixture. The tests were injected with medium viscosity silicone (K=123 cP sec^n, n=0.75) at the same flow rate 50 ml/min.

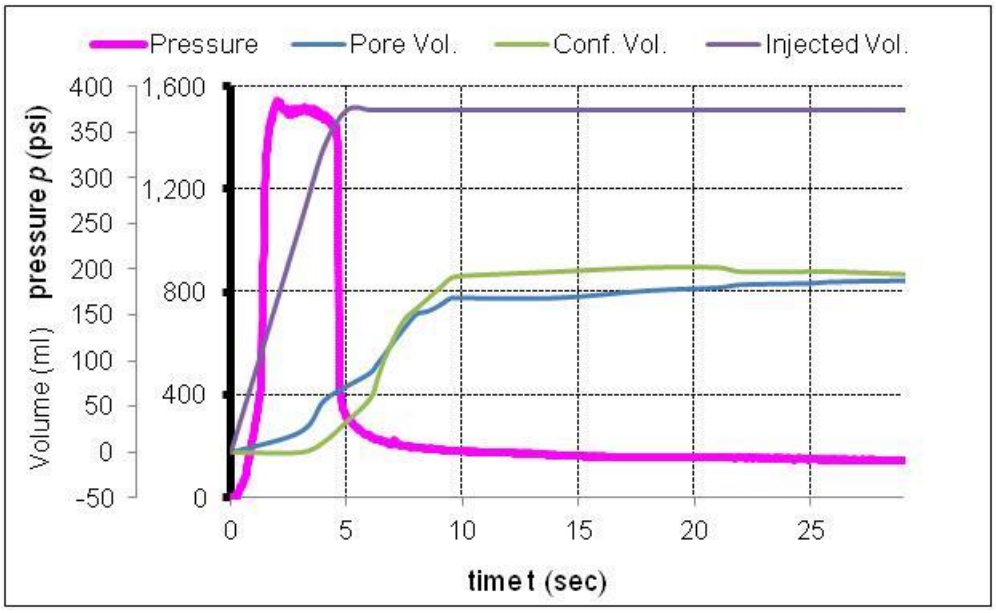

Figure 4.26. Example of the pressure record and volume response of a high flow rate Test 05-19-11. Sample of fine sand at 80 psi confinement was injected with medium viscosity silicone (K=123 cP sec^n, n=0.75) at 5000 ml/min.

4.6. Observed Shear Failure

The scale of our sample size is an important consideration in our work. In the large triaxial cell, there were several instances when a shear band was visible during the injection event. The band manifested as a distinct trace on the outer surface of a sample (**Figure 4.27** (a)). This was primarily visible during high-stress experiments in the LTC with low flow rates and high-viscosity fluids. These shear bands are visible on the surface of the sample. These are considered global shear bands and are likely due to limited sample size. Additionally, they are likely different than shear bands attributed to the extension of the fracture mentioned in Section 4.5.

The fracture shape is still quasi-planar with multiple off-shoots that are orientated in the general direction of the shear band. The development of a global shear band may be attributed to the limited lateral extent of the sample. The experiments in the small triaxial cell developed global shear bands regularly (Appendix D). However, the limited boundary does not necessarily invalidate our results. The resulting fracture shapes do not change materially, compared to other samples with no evidence of shear bands. It appears that while the shear band does provide a preferential pathway for fracture development the trends of parameter changes are consistent across the entire experimental series. That is, the trends shown in the scaling relationships hold whether there is evidence of shear band development or not.

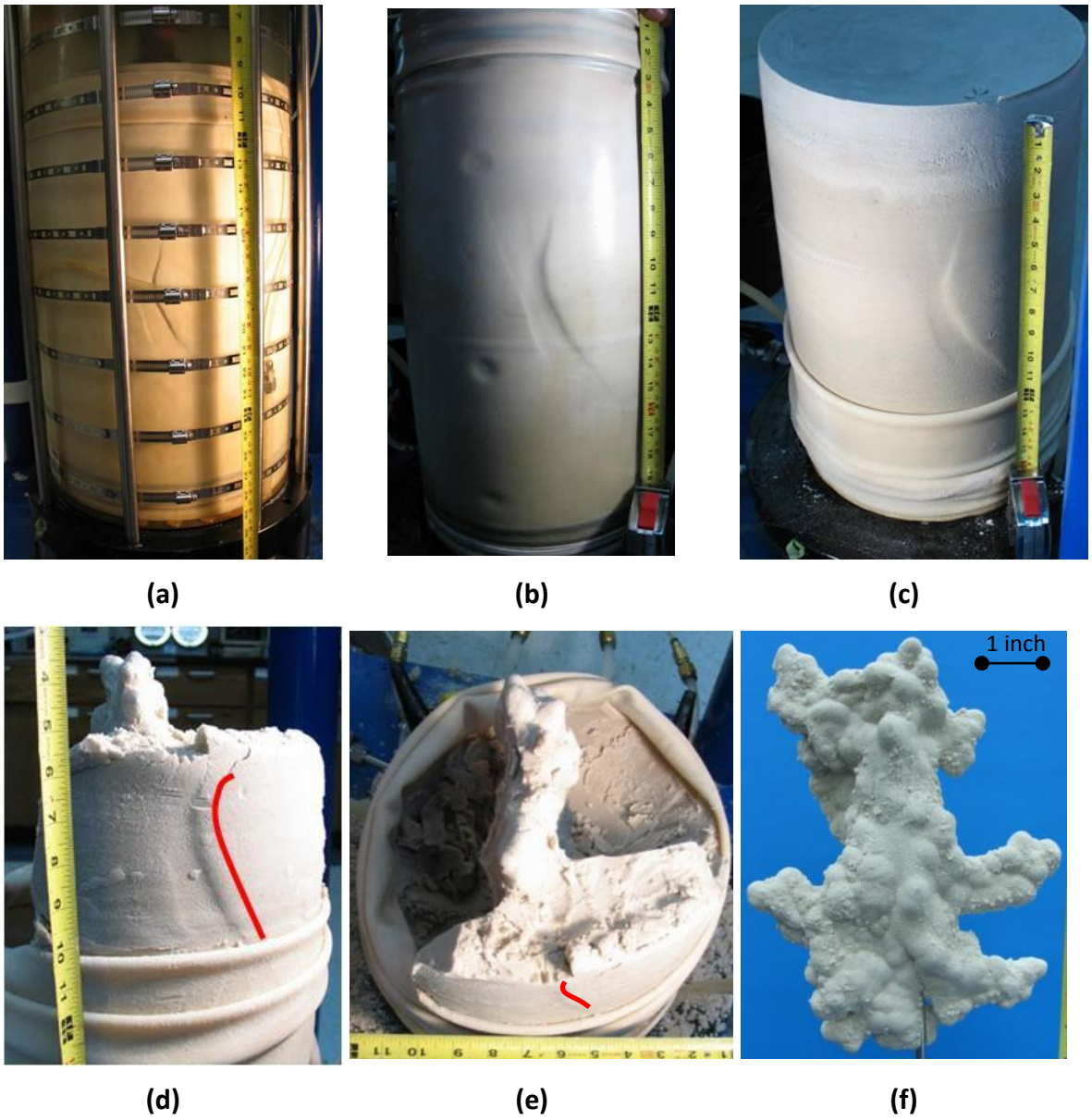

Figure 4.27. Test 02-01-06 with shear band: (a) The shear band is visible on the boundary of the sample while under confinement. (b) Unloaded sample and cell disassembled. (c) Outer membrane removed. (d) Sample during excavation. (e) Image showing the fracture orientation with respect to shear band. (f) The excavated fracture.

4.7. Conclusions

In this chapter, we presented a dimensional analysis of the initiation pressures for fractures in cohesionless particulate materials. We presented the various fracture morphologies and how experimental parameters affect these features. Further we analyzed sample response and characteristic pressure-time histories due to injection events. Shear band propagation was shown to exist in some of our LTC tests, depending on parameter selection. The main points of this chapter can be summarized by:

1. The dimensional analysis of our experimental results suggests a power-law dependence of peak injection pressure versus confining stress.
2. Other parameters such as fluid rheology, permeability, and injection flow rate are less significant for peak pressures yet important for controlling leakoff.
3. Peak injection pressures are not a reliable indicator of fracture morphology in our test conditions.
4. If peak pressures are normalized by confinement stress, then they vary significantly (12 to 28) at low confinements (<0.5 MPa) while at high-confinements (~ 5 MPa) they exhibit less variability (3.0 to 3.5).
5. Normalized injection pressure-time curves can be similar for very different fracture morphologies.
6. In high-leakoff tests, leakoff appears as a collection of multiple spheroidal point-source events that form the general fracture shape. Thus leakoff appears to affect fracture development.

7. As leakoff is controlled, the size of these spheroids decreases, and then the fracture transitions to a brittle-like feature.
8. Brittle-like fracture appears as one continuous feature. This suggests that the fracture may not be driven by the localized leakoff feature.
9. Brittle-like in particulate materials is different from solids, because in solids, fractures can be brittle for any leakoff, large or small. In particulate materials brittle-like corresponds to small leakoff.
10. Fractures in silica flour samples display significant differences in their morphology compared to fractures in sand and sand mixtures.
11. The scale of the sample may still be significant because global shear bands were observed.
12. There appears to be significant localized dilation of all samples because the volume of the confinement response during an injection event is typically larger than the injected volume of fracturing fluid.

5. COMPLEXITIES OF FLUID-DRIVEN FRACTURES IN PARTICULATE MATERIALS

5.1. Introduction

In this chapter, we present the analysis of fracture cross-sections observed in our experiments. We describe in detail how specific parameter changes affect the fracture morphology and pressure signature. In addition, we look at other parameters that provide insight to the complexity of hydraulic fracturing in cohesionless materials. Subsequently, we describe the fracture tip, and other observations of the fracture and leakoff surfaces. The majority of the experiments presented in this section were conducted with the Large Triaxial Cell (LTC) as described in Chapter 3.

5.2. Effects of Parameter Variations

In this section, we describe the effects of parameter variations on the fracture initiation pressures, leakoff thickness and fracture aperture. Each parameter is presented independently and the peak pressures are presented versus the magnitude of the single parameter. Then cross-sections of some example tests are shown. The groups presented are similar in all other experimental parameters, except the one of interest.

5.2.1. Boundary conditions

We found that the magnitude of the confining stresses was a primary factor in determining the fracture initiation pressure. As the confining stresses were increased, the thickness of leakoff and injection pressure increased while fracture aperture decreased. Recall, as described in Chapter 3, the vertical stress is always twice the

horizontal in our tests. A series of tests, where the only experimental parameter that was varied was the confinement, are shown below in **Figure 5.1**. The peak pressure versus confinement plot is shown in **Figure 5.2**. The results of plotting peak pressures versus confinement confirm the results of the dimensional analysis (Chapter 4). In general, an increase of an order of magnitude in confinement pressure results in a less than an order of magnitude increase in the relative peak pressure (for our test conditions).

Confinement = 8 psi

Peak = 193 psi

Test 05-12-11

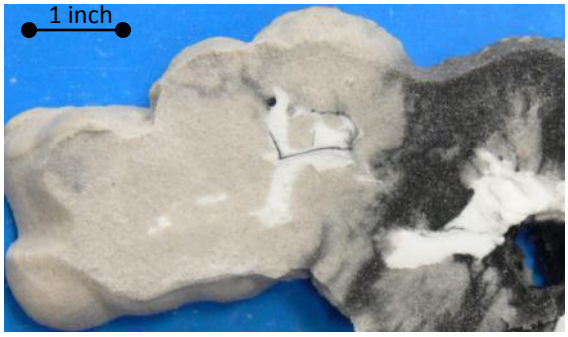

Confinement = 80 psi

Peak= 916 psi

Test 02-10-11

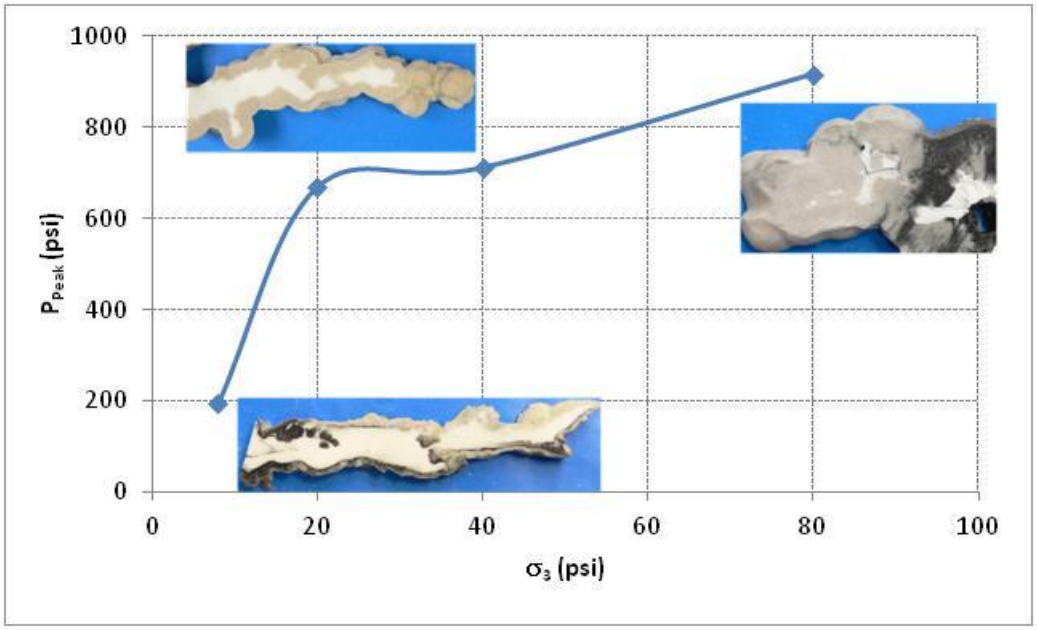

Figure 5.1. Three experiments, with cross-sections, comparing peak injection pressures to confinement. Series of samples illustrate the effect from the change of boundary conditions. The injection tests were conducted in fine sand by injecting with medium viscosity silicone at an injection rate of 50 ml/min. Notice significant leakoff thickness in the 80 psi confinement tests, yet limited leakoff with larger fracture aperture with 8 psi confinement.

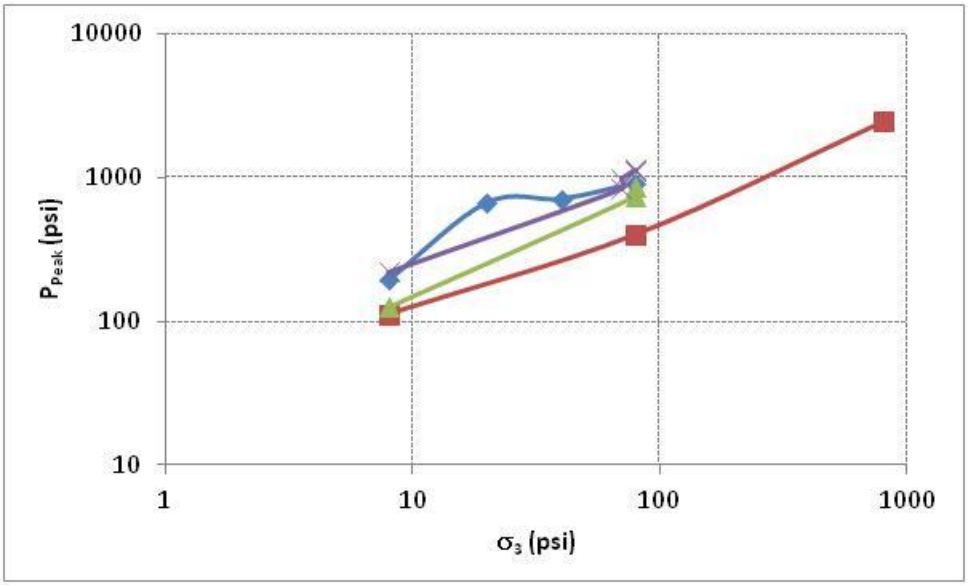

Figure 5.2. Confinement stresses versus peak pressure. Markers are grouped to indicate separate experimental series that all parameters except stress are held constant. Significant changes in peak pressures are observed with increasing confinement.

5.2.2. Effects of fluid rheology

A thicker fracture with less leakoff was a result of the increase of fluid viscosity. It is important to mention that there was no attempt to analyze differences in fluid rheology beyond the effective fluid viscosity. Although both the silicone and guar fluids are shear thinning, it must be considered that the wall building characteristics are probably vastly different. For example, the guar based fluid exhibited more leakoff, when compared to the silicone fluids, in the high permeability fine sand samples,. Conversely, the guar fluid exhibited comparatively lower leakoff in the lower permeability formations. In addition, the existence of the yield stress for the silicone fluid likely contributes to the preservation of leakoff. Fluid wall building characteristics must be quantified for a more thorough analysis. Peak pressure and minimum pressure showed a slight increase with an increase of viscosity. However, it was within experimental error. The fluid pressures remained within the same order of magnitude with an increase of three orders of magnitude of viscosity.

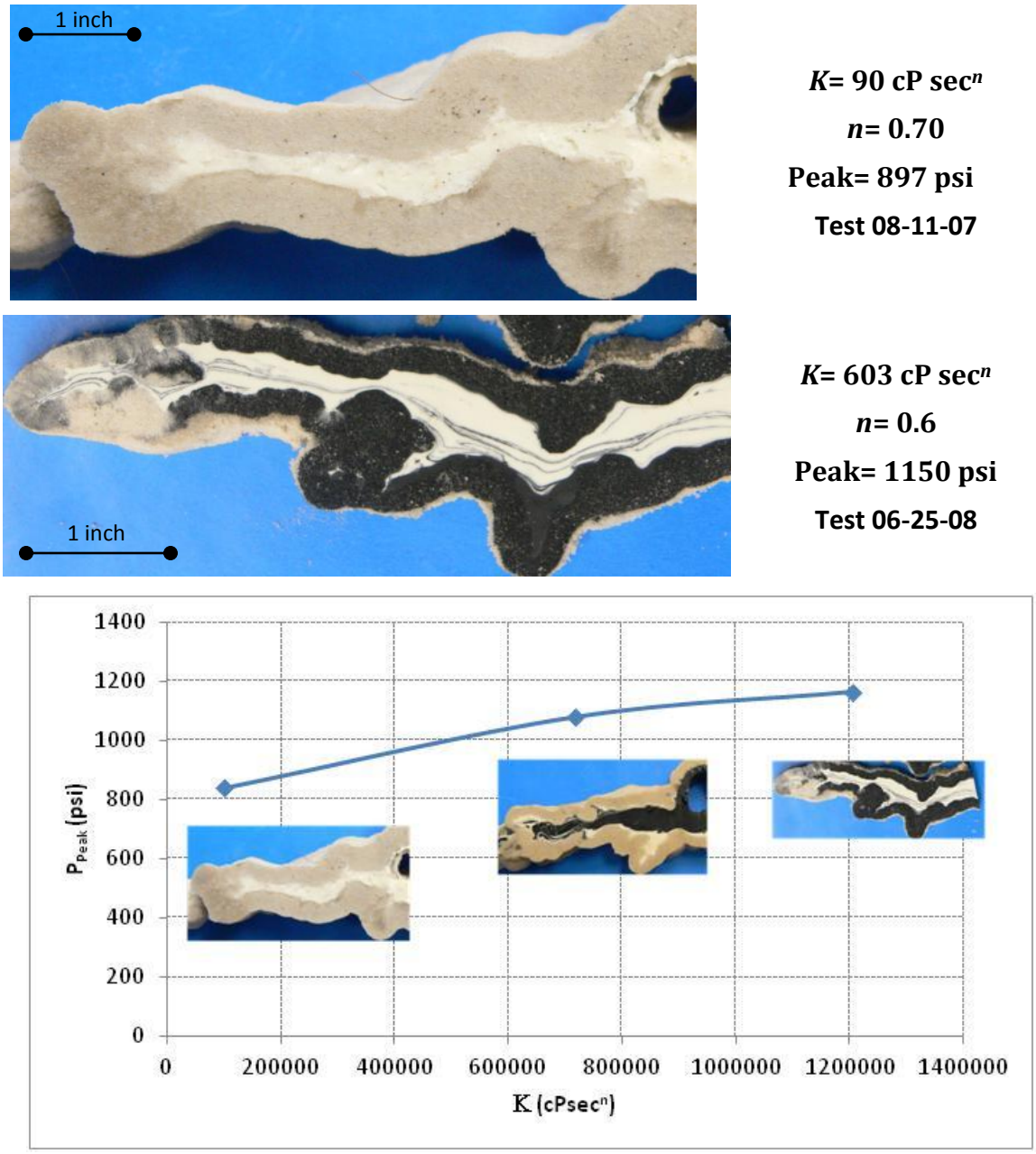

Figure 5.3. Three experiments, with cross-sections, comparing peak injection pressures to fluid consistency indexes (viscosity). Slight decrease in peak injection pressures with decreasing viscosity. Illustrates the changes fracture morphology due to the viscosity of the silicone adhesive. The samples were fine sand at 80 psi confinement injected at a rate of 1700 ml/min.

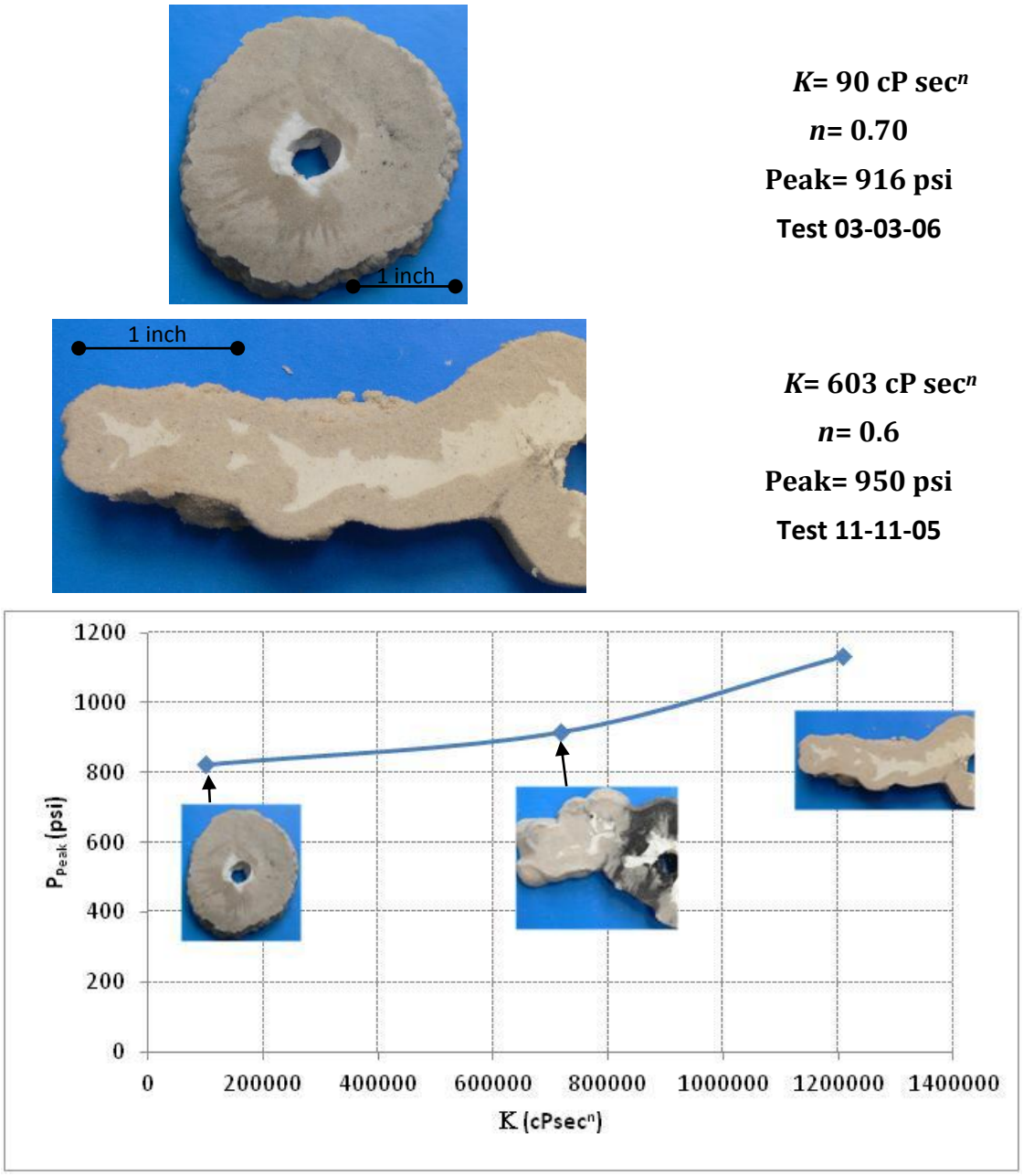

Figure 5.4. Three experiments, with cross-sections, comparing peak injection pressures to fluid consistency indexes (viscosity). Slight decrease in peak injection pressures with decreasing viscosity. There is a significant shift in leakoff thickness with increasing rate. The samples were fine sand at 80 psi confinement injected at a rate of 50 ml/min.

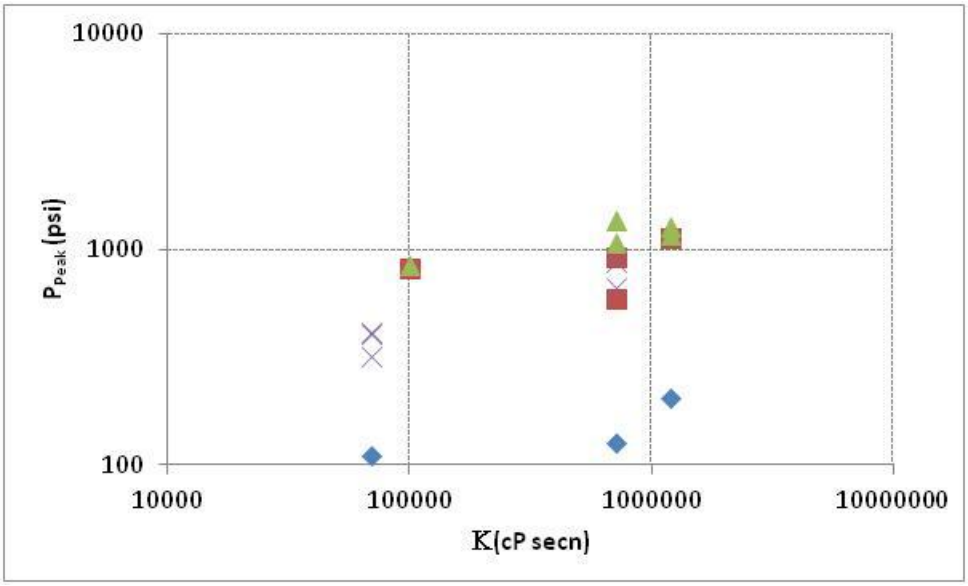

Figure 5.5. Peak pressures for test series at different viscosities (guar tests are included). Markers are grouped to indicate separate experimental series that all parameters except viscosity are held constant. There appears to be a slight increase in peak pressure with increasing viscosity.

5.2.3. Effects of fluid flow rate

Fluid flow rate showed no quantifiable effect on injection pressures. Our data suggests that even with three orders of magnitude change in the flow rate, there was no significant increase in injection pressures. However, flow rate can be instrumental in generating fractures. There is a number of test series were the fracture process was enhanced due only to an increase in injection rate (**Figure 5.6)**. In **Figure 5.7** the impact of the reduction in leakoff due to the increase in flow rate is still noticeable. **Figure 5.8** shows very little change in leakoff with three orders of magnitude change in flow rate. There is no evidence of a change in peak pressure due to increases in flow rate. This is significantly different than field applications. Typically, there is an increase in injection pressures with increases in flow rate in the field. However, the fractures described here can be considered thick; therefore the viscous losses due to fluid flow within the fracture are negligible. In field applications the viscous losses may become significant as the fracture increase in length.

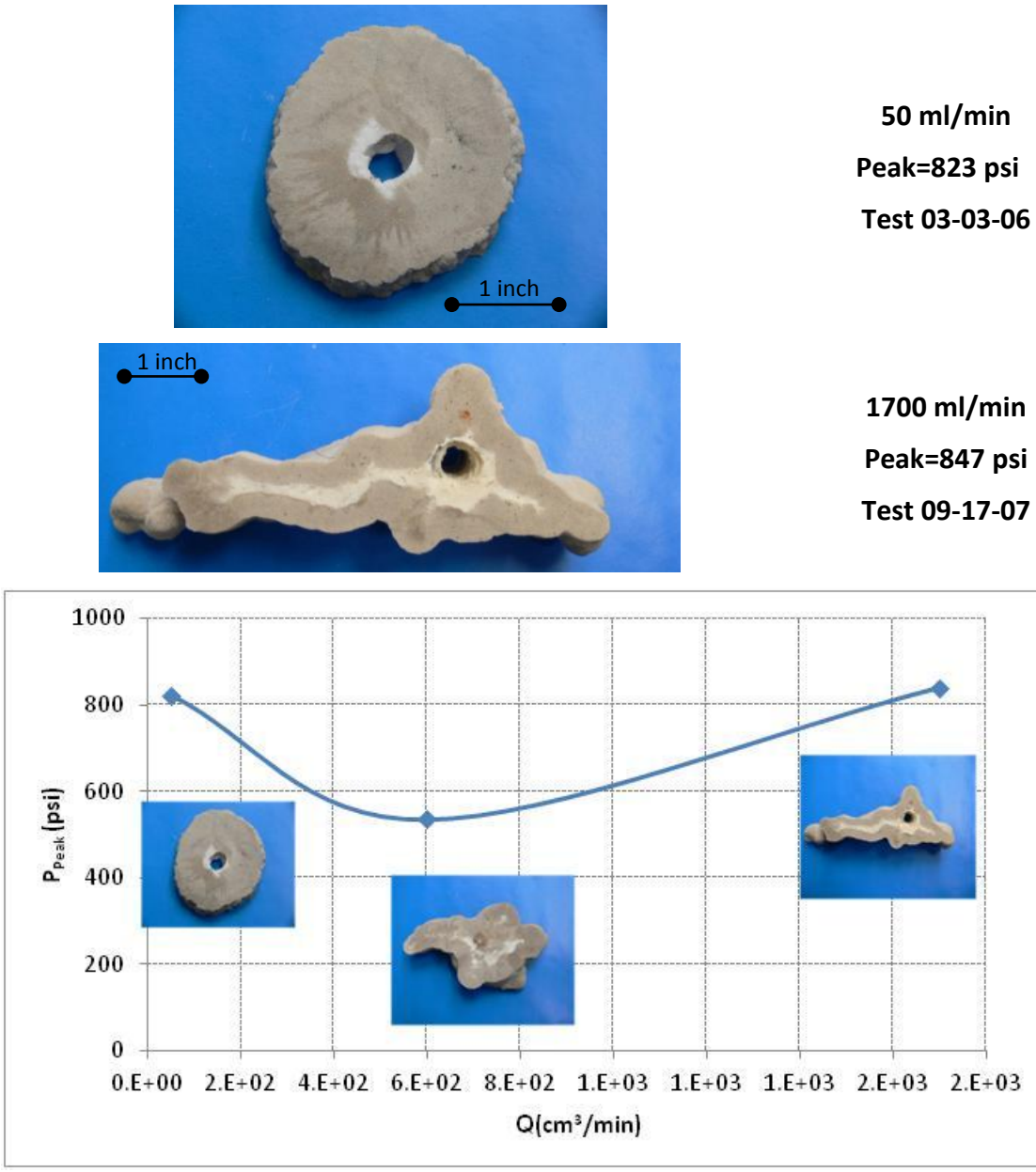

Figure 5.6. Three experiments, with cross-sections, comparing peak injection pressures to different flow rates. An example of the transition from mainly leakoff, to fracture due only to an increase in flow rate. The samples were 1000 mD fine sand at 80 psi confinement fractured with the low viscosity silicone adhesive.

50 ml/min
Peak=587 psi
Test 02-10-11

5000 ml/min
Peak=618 psi
Test 05-19-11

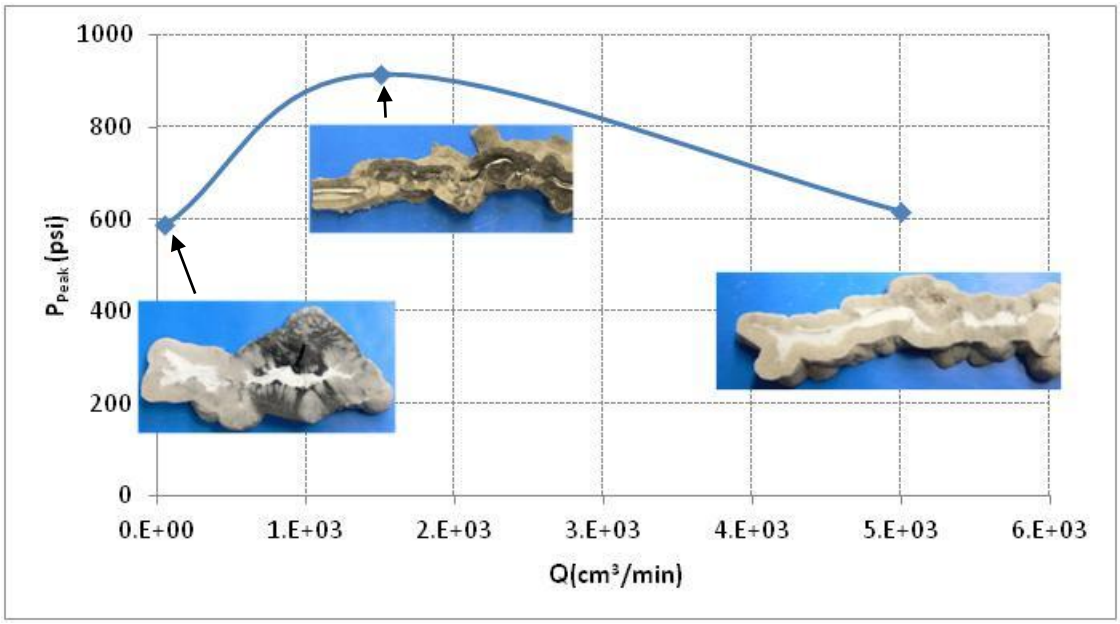

Figure 5.7. Three experiments, with cross-sections, comparing peak injection pressures to different flow rates. The flow rate did have significant impact on leakoff thickness, peak pressures are within our experimental error. The samples were 1000 mD fine sand at 80 psi confinement fractured with the medium viscosity silicone adhesive.

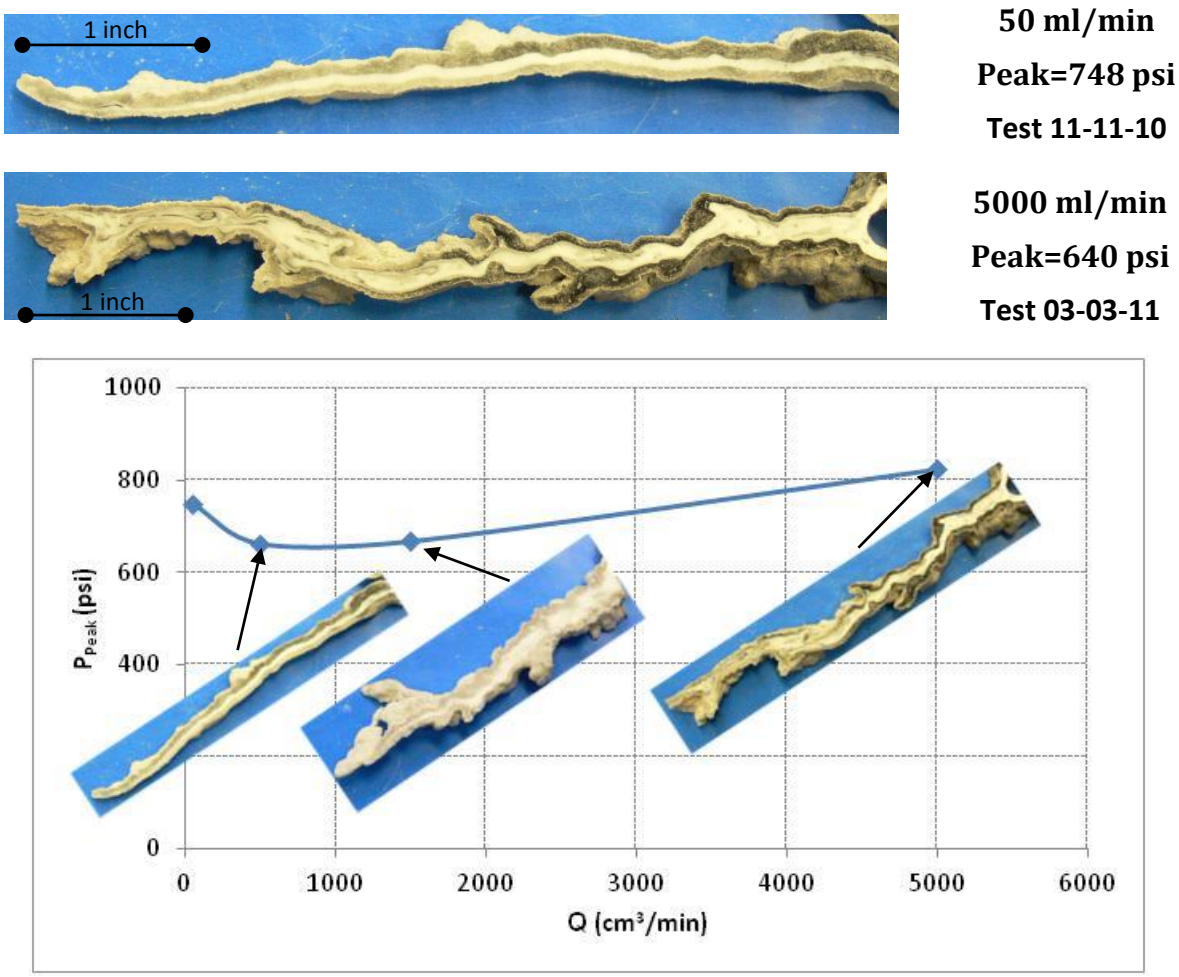

Figure 5.8. Three experiments, with cross-sections, comparing peak injection pressures to different flow rates. Less noticeable change of fracture aperture and leakoff thickness as the flow rate was increased, due to lower permeability. The samples were 350 mD sand/silica flour mixture at 80 psi confinement fractured with the medium viscosity silicone adhesive.

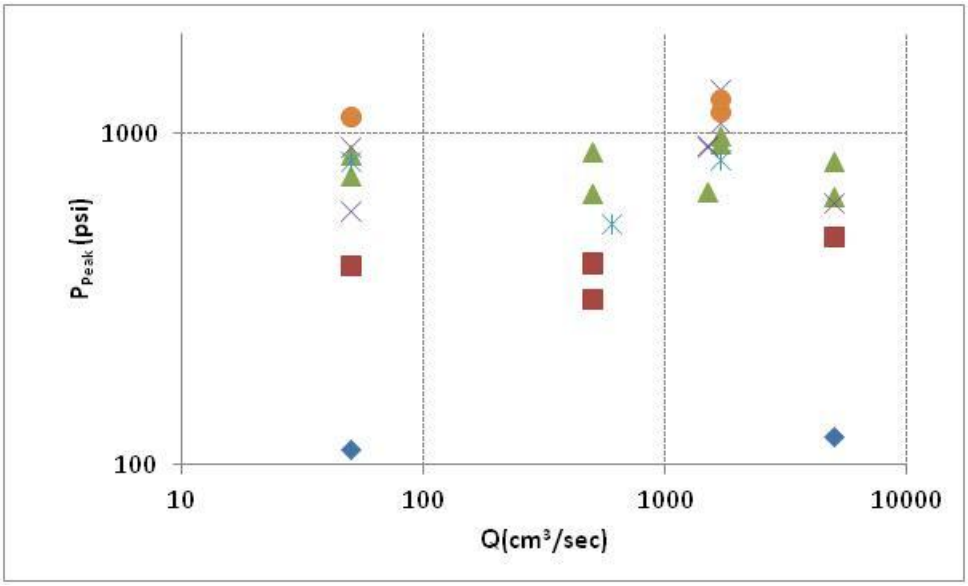

Figure 5.9. Peak pressures for tests at various flow rates (only silicone tests are shown). Markers are grouped to indicate separate experimental series that all parameters except flow rate are held constant, and then peak pressures are compared. There appears to be no change in peak pressures with changes in injection rate.

5.2.4. Importance of sample permeability

Reducing the permeability reduced the leakoff of the fracture. There is evidence of slight correlation in permeability with fracture pressures, in our tests. This is primarily confined to the comparison of injection pressures in samples of pure silica flour to those of fine sand and fine sand/silica flour mixtures. Comparing samples of fine sand to those with mixtures there is no correlation in permeability and injection pressures. **Figure 5-10** and **Figure 5-11** show two experimental series in which the reduction of permeability one order of magnitude reduces the leakoff significantly, yet the peak pressures do not appear to be affected.

350 mD

Peak=937 psi

Test 11-06-08

1000 mD

Peak=1079 psi

Test 09-27-07

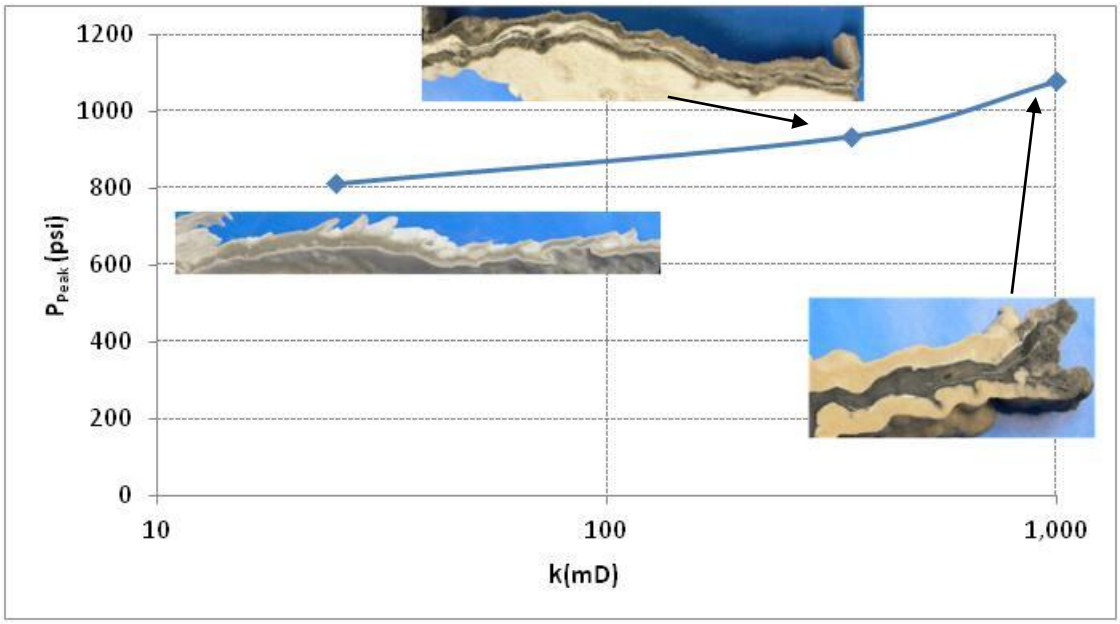

Figure 5.10. Three experiments comparing peak injection pressures to different values of permeability. Comparison to dry silica flour experiments exhibited the only significant decrease in peak pressures. The decrease in permeability had a significant impact on leakoff thickness while little effect on peak pressures and slight impact on fracture apertures.

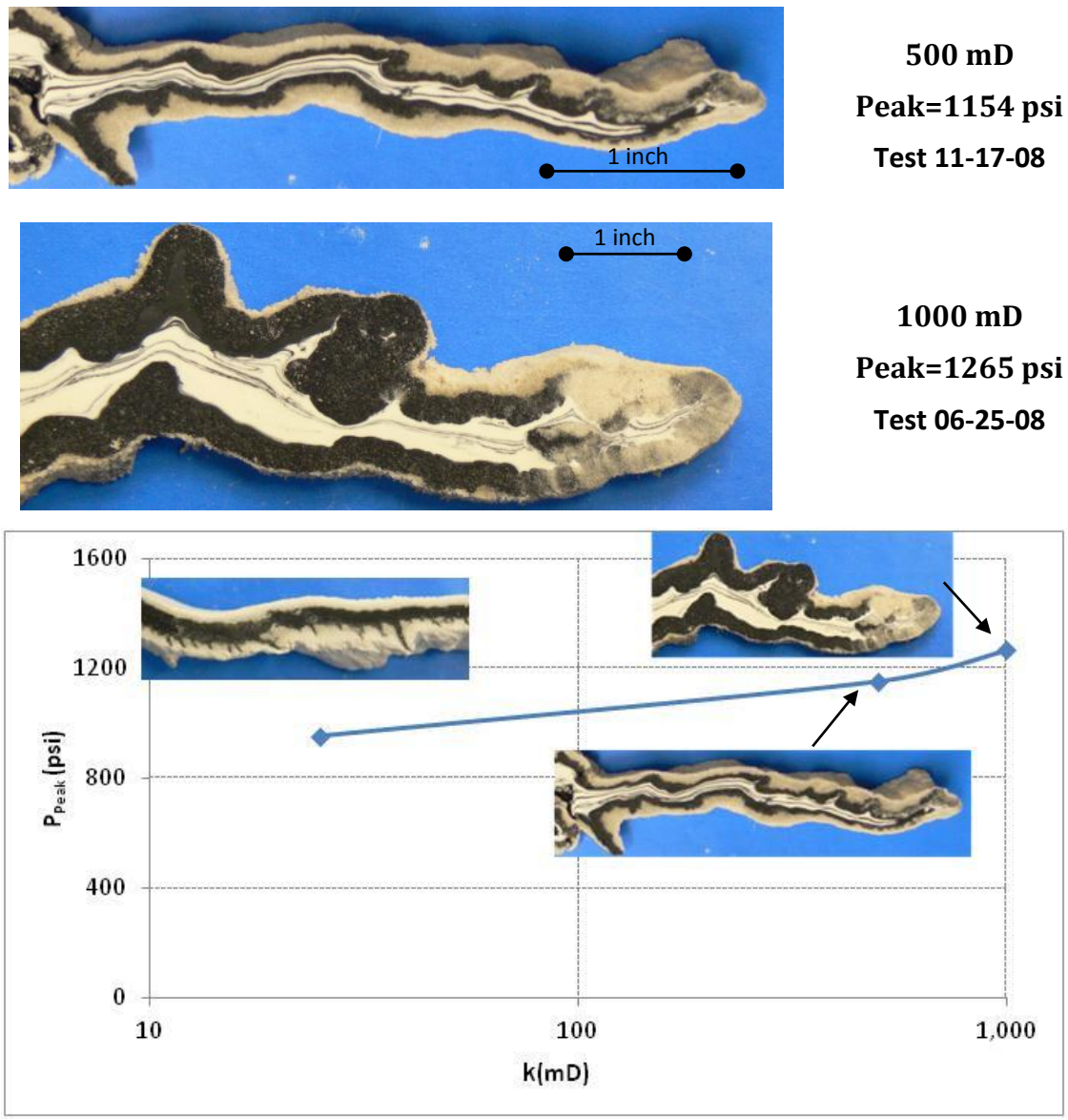

Figure 5.11. Three experiments comparing peak injection pressures to different values of permeability. Comparison to dry silica flour experiments exhibited the only significant decrease in peak pressures. Leakoff thickness is reduced with decreasing permeability. The injection tests were at 80 psi confinement injected with High viscosity silicone at a rate of 1700 ml/min.

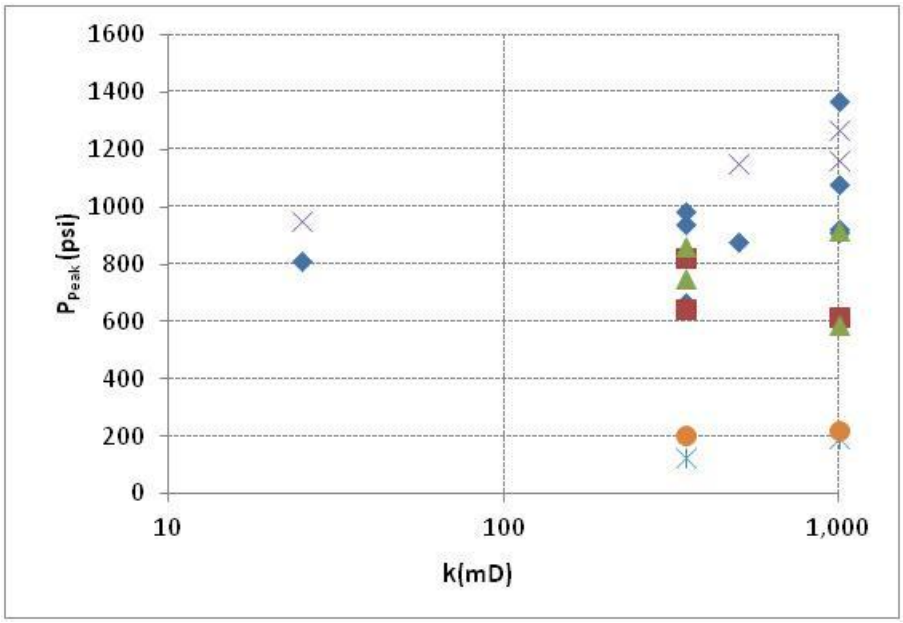

Figure 5.12. Injection peak pressure versus permeability data. Markers are grouped to indicate separate experimental series that all parameters except permeability are held constant, and then peak injection pressures are compared. There appears to be a slight increase in pressure for certain data series, but it is not conclusive.

5.2.5. Summary of parameter effects

In this section, we presented a qualitative analysis of our results. Here we summarize the effects of parameter changes on the fracture geometry and pressure signature. In general, we find that boundary conditions have the most significant impact on peak pressures. This supports the dimensional analysis presented in Chapter 4. **Figure 5.13** shows a dependence of fracture and leakoff morphology (aperture and leakoff characteristics) on the variation of main parameters (not in dimensionless form). Our independent (controlling) experimental parameters Q, K, k and σ suggest the existence of two characteristic times

$$t_1 = k^{3/2}/Q, \text{ and } \quad t_2 = \left(K/\sigma\right)^{1/n} \tag{5.1}$$

the ratio t_1/t_2 is equivalent to $\Pi_1{}^{1/n}$, where Π_1 is the dimensionless parameter equation (4.3) used in Chapter 4 for analyzing our test results.

Leaving aside the physical meaning of times t_1 and t_2, they are both related to the magnitude of leakoff. Indeed, the level of leakoff, generally increases with permeability k and decreases with flow rate Q. Therefore, we expect leakoff to be more pronounced as t_1 grows. Similarly, leakoff is greater for thinner fluids, so that leakoff increases with K. It decreases with σ, however, because increasing confining stresses generally corresponds to increasing fluid pressure in the fracture. Hence, opposite to t_1, we expect leakoff to be less pronounced as t_2 becomes greater. This effect is illustrated in **Figure 5.13**. This shows characteristic times t_1 and t_2 as well as the fracture morphology for a number of representative experiments. These two characteristic times

describe quantitatively the range of parameters in our tests. For the silicone tests the characteristic times range in value

$$10^{-16}\,sec \lesssim t_1 \lesssim 10^{-12}\,sec$$
$$10^{-6}\,sec \lesssim t_2 \lesssim 10^{-4}\,sec \qquad (5.2)$$

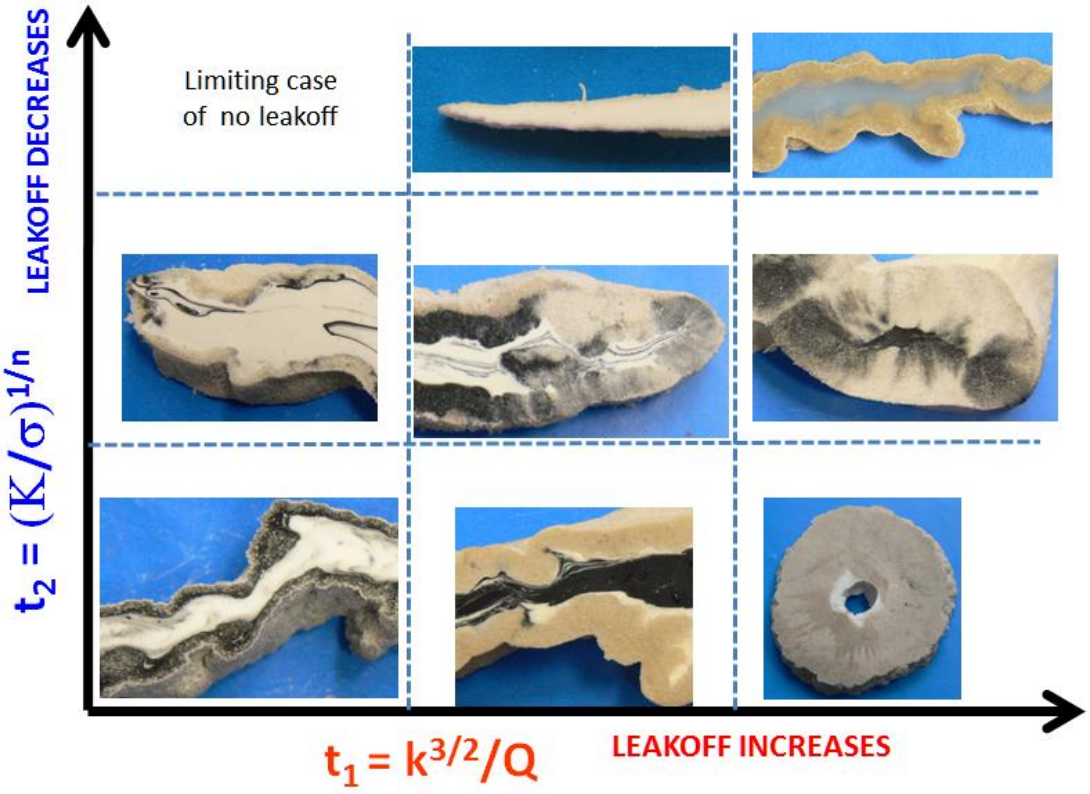

Figure 5.13. Quantitative dependence of fracture and leakoff morphology (aperture and leakoff characteristics) on the variation of two characteristic times. The leakoff thickness decreases with increasing characteristic time, parameters t_2 and/or t_2. The fracture aperture is less definitive, but in general we find aperture increases with characteristic time parameter t_2.

5.3. Other observations

5.3.1. Changes in pore fluid

To determine the impact of pore fluid on the resulting fracture morphology and peak pressures several tests were performed with various pore fluids. These tests were conducted in the STC (Appendix E). The test series also allowed for an analysis of the impact of the solidification process of the silicone adhesives on the experimental results. In this section, we describe those results.

Comparing dry versus saturated samples in fine sand we observed no change in peak pressures or fracture morphology for sample injected with silicone adhesive. It may be that the ratio of the pore and injection fluid viscosities is important, as we expect in immiscible porous media fluid flow (**Figure 5.14**). Given the high viscosity of the silicone adhesive, we would expect that the difference between the viscosity of air and water to be negligible as the ratio of the invading fluid viscosity and pore fluid is still very high. Therefore, we would expect stable viscous flow in the porous matrix (ignoring deformation of the matrix).

We also conducted several tests utilizing glycerin as the pore fluid. These tests were completed in the STC in samples of fine sand, at moderate confinements (20 psi to 40 psi). Similar to the conditions of the tests above, the invading fluid viscosity is still orders of magnitude greater than that of glycerin. Therefore, we would expect stable viscous flow. There was not a perceivable difference in fractures conducted with water or glycerin as the pore fluid.

We analyzed the effect of the solidification process of the silicone adhesive by utilizing glycerin as the pore fluid. The silicone adhesive would not solidify when submerged in pure glycerin due to its cure process. When injection tests were conducted with glycerin pore fluid the samples would not solidify until excavated. The created fractures were still competent, and excavation was possible without damaging the fracture. There was no perceivable difference in morphology or injection pressures between experiments with air, water, or glycerin as the pore fluid.

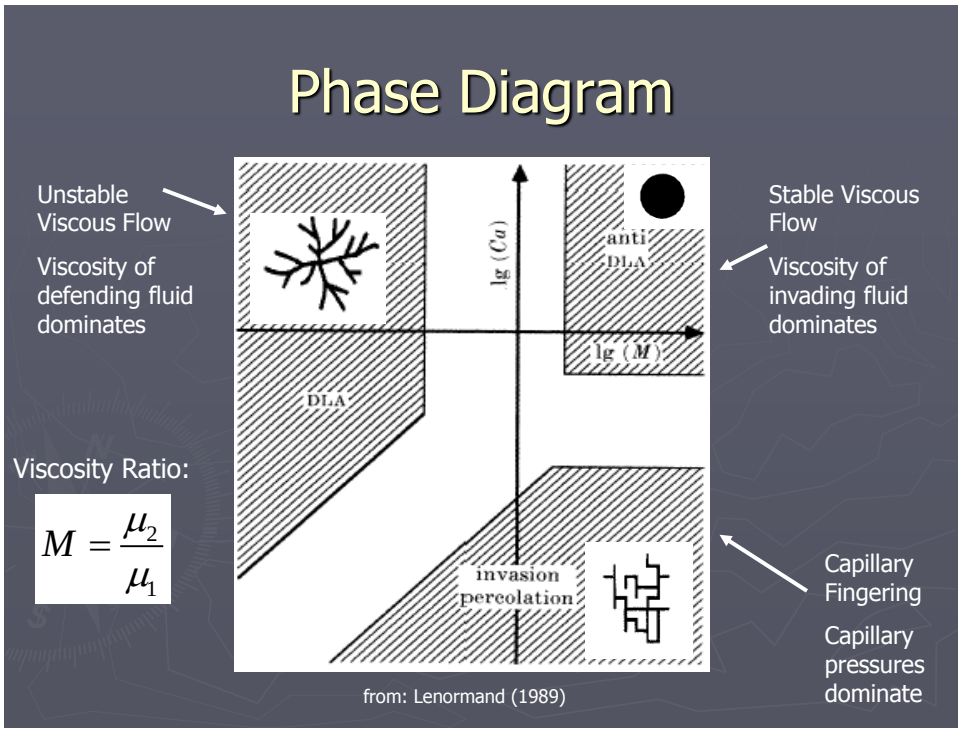

Figure 5.14. Patterns of immiscible fluid flow in porus media from modified after [*Lenormand*, 1989]. There are no grain displacements in this figure. The viscosity of our injection indicates we would reside within the stable viscous flow regime, with pore fluids of air, water and glycerin.

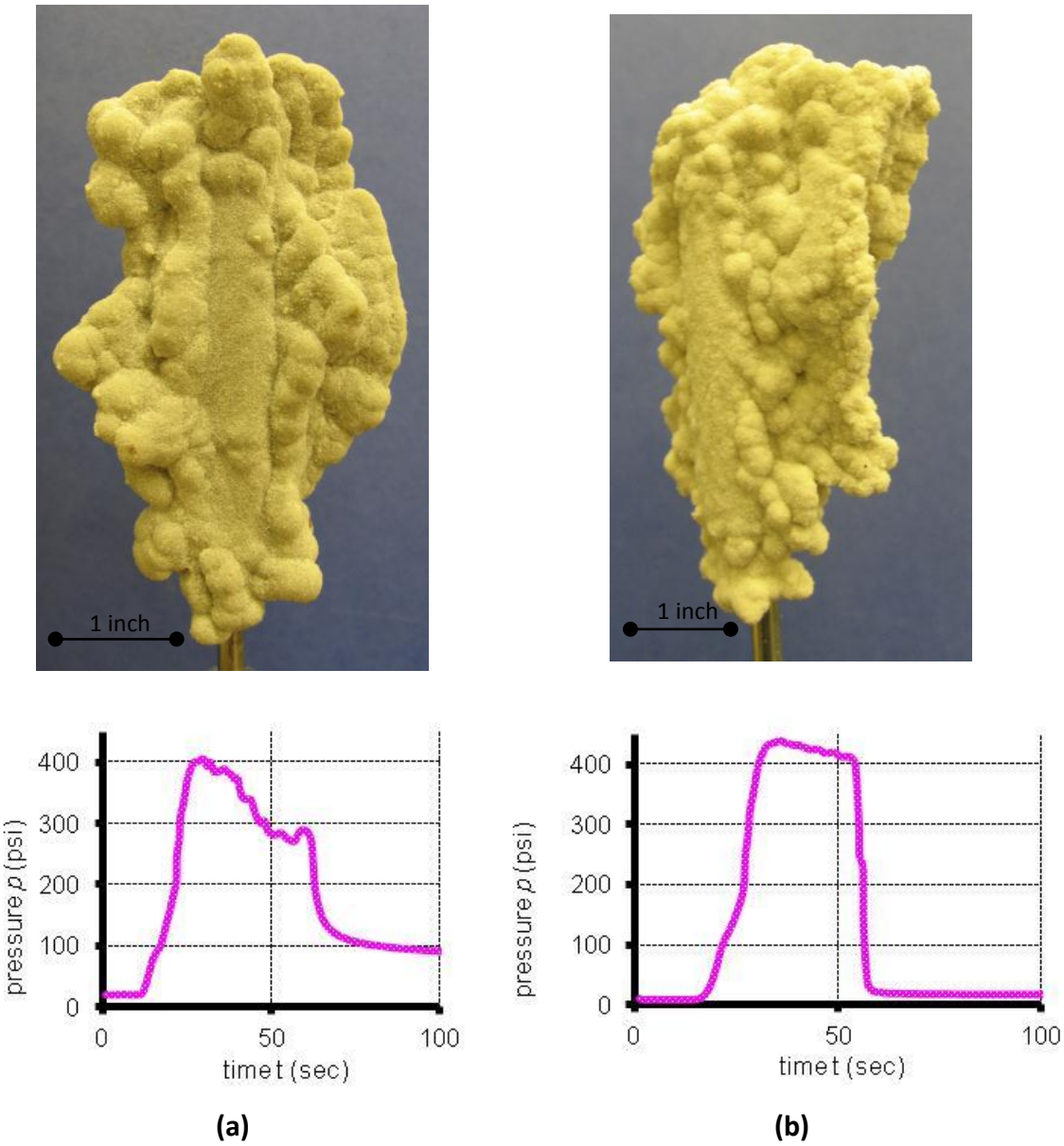

Figure 5.15. Two STC experiments conducted with water (a) and glycerin (b) as the pore fluid. The injection tests were conducted in fine sand, at a confinement of 40 psi, with medium viscosity silicone at an injection rate of 50 ml/min.

5.3.2. Unsymmetrical growth

Unsymmetrical growth is directly observed through the colored fluid injections. Various color schemes were utilized to enhance the contrast between injection timing events. The best combination was white and black colored fluids. Two examples are given below in **Figure 5.16**. A qualitative analysis would describe the growth patterns as somewhat radial. However, the pattern of the first color injected is not fully mimicked by the pattern of the second fluid. Therefore, the growth of these fractures is probably quite erratic and not constant on any one leading edge. The sample size limits the ability to determine whether the fractures will continue in such a quasi-radial fashion. In addition, the effect of boundary interaction is not well known. For example, **Figure 5.17** shows an experiment with a significant change in both leakoff thickness and aperture when close to the boundary.

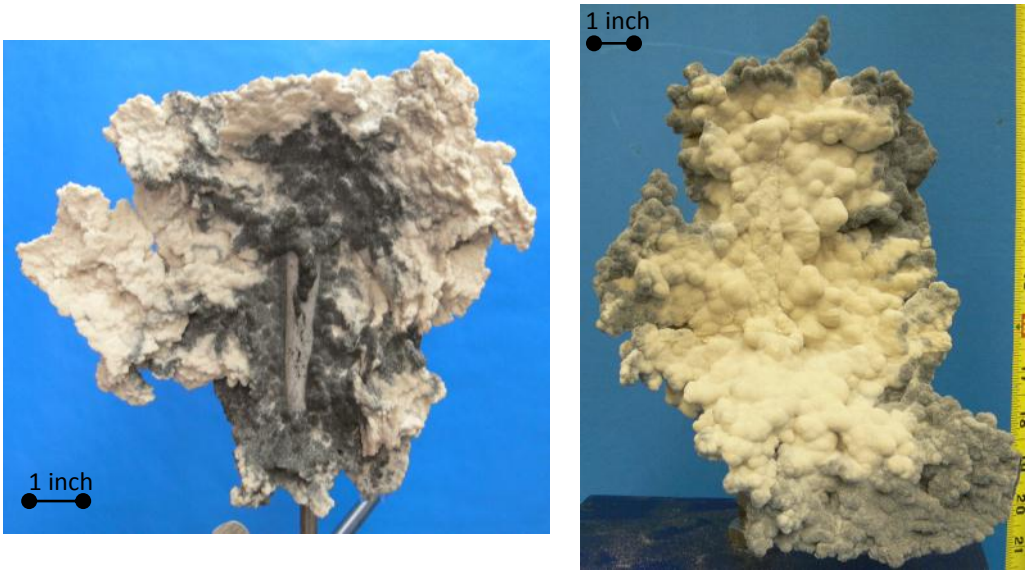

(a) **(b)**

Figure 5.16. (a) Injection test with black fluid preceding white fluid. Note the variable nature of the colored boundary. The white material surrounding the injection source is filter paper used as a part of the injection source. (b) an injection test with white fluid preceding black. The lower right extent of the fracture reached the boundary. (a) Test 03-30-11 (b) Test 09-27-07.

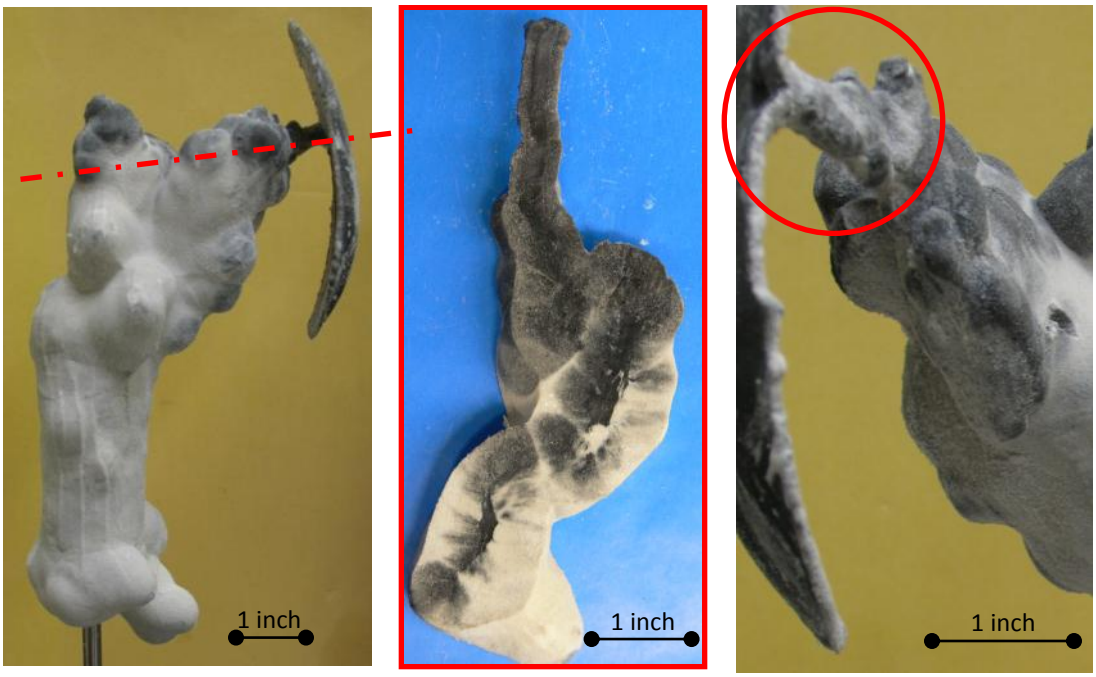

Figure 5.17. (b) Cross-section of Test 09-11-09 that interacted with the boundary (at dashed line (a)). The curved solidified form (c) is from fracturing fluid propagating on the interface between the sample and membrane. The red circle on the left indicates that this form is tubular. Note the reduced leakoff and increased aperture indicating a significant change propagation regime.

5.3.3. Interface experiments

Several tests were conducted using samples with mixed layers of materials. This served two purposes; (1) to examine whether fractures propagate preferentially in a given permeability, and (2) to examine whether the leakoff characteristic varies significantly for a given sample.

The first series were conducted in a large constrained boundary mold (**Figure 5.18**). The injection source and injection system are the same as used in the other work presented here (described in Chapter 3). The samples were compacted through static loading from the top, along with vibration under load. This did create a less dense sample in the lower layer. However, the interface remained a defined plane within the sample. The samples were injected at a rate of $50\ \mathrm{ml/min}$, with medium viscosity silicone. The peak pressures were similar to those from the LTC tests with a confinement of $20\ \mathrm{psi}$.

The tests demonstrate a significant change in the leakoff between the two layers. The coarse sand exhibited distinct horizontal striations near the borehole. Along the propagated fracture, the bubbly features (spheroids) in the coarse sand are significantly larger than the spheroids in the fine sand. The leakoff surface of the fine sand portion looked identical to samples in the triaxial cells with $20\ \mathrm{psi}$ confinements. Further, the fracture propagation did not exhibit a preference for a particular sample, in each test the fractures propagated in the lower layer. We attribute this to differences in the layer densities.

We conducted a single interface test in the (LTC). In this test, the sample was prepared in a similar fashion as the other LTC tests. The sample consisted of a lower layer of silica flour, a middle layer of fine sand and a top layer of silica flour. The injection source was centered in the sand layer. The samples were compacted to maximum density using the rodding technique. There was no saturation due to the inability to saturate large samples of high-density silica flour with our equipment.

The result of the interface LTC test is shown in **Figure 5.19**. The fracture was contained within the top and bottom layers. There was no fracture propagation in the sand layer, only leakoff. The fracture reached the boundary in the lower layer. The results of the pressure record are identical to samples of only silica flour.

The interface experiments illustrate the complex nature of the leakoff surface. There can be significant difference in the leakoff characteristic depending on the physical properties of the sample. There is evidence in the literature that unconsolidated fractures tend to propagate in lower permeability samples [*De Pater and Dong*, 2007; *Dong and De Pater*, 2008; *Khodaverdian and Mcelfresh*, 2000]. Our results indicate that this is true when comparing silica flour to fine sand samples. In sand materials, however, there may be other significant factors that need to be resolved (e.g., density).

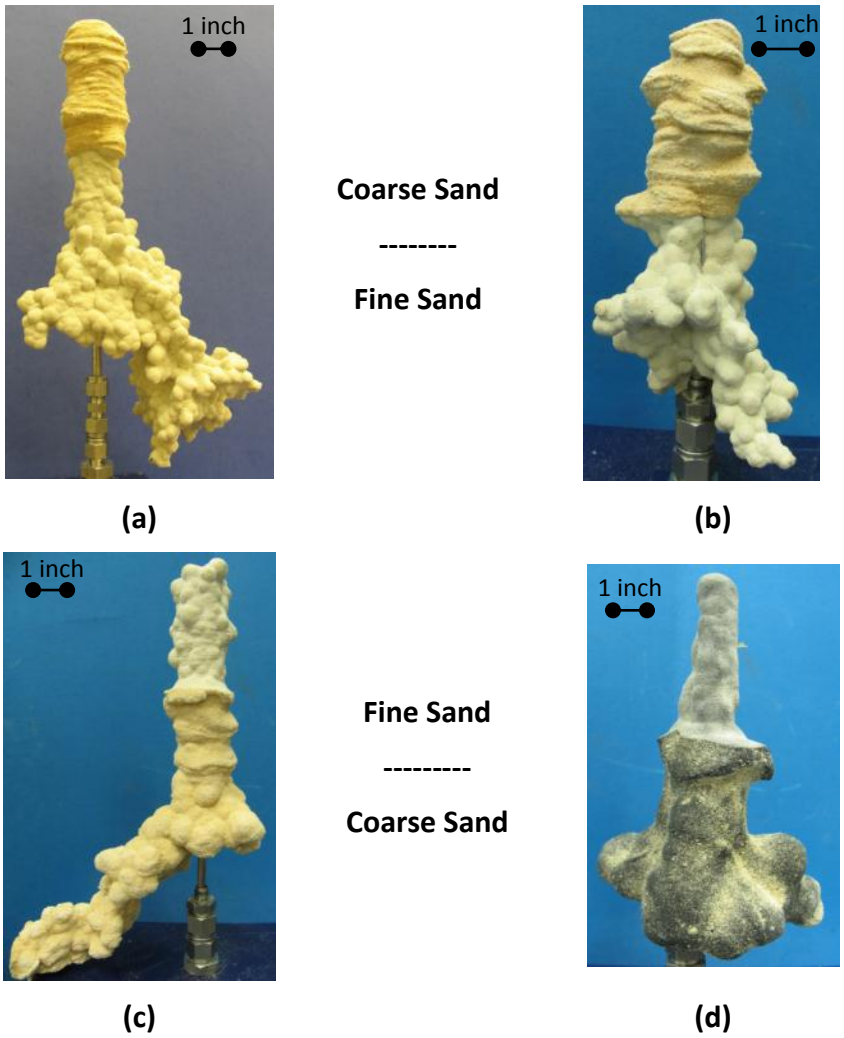

Figure 5.18. Interface experiments conducted in a constrained boundary mold (Appendix D for description). The samples were dry and loaded vertically to 80 psi. The samples were layered with fine sand and coarse sand. The fracturing fluid was medium viscosity silicone injected at a rate of 50 ml/min (a),(b), and(c) were injected with white fluid, (d) was black.

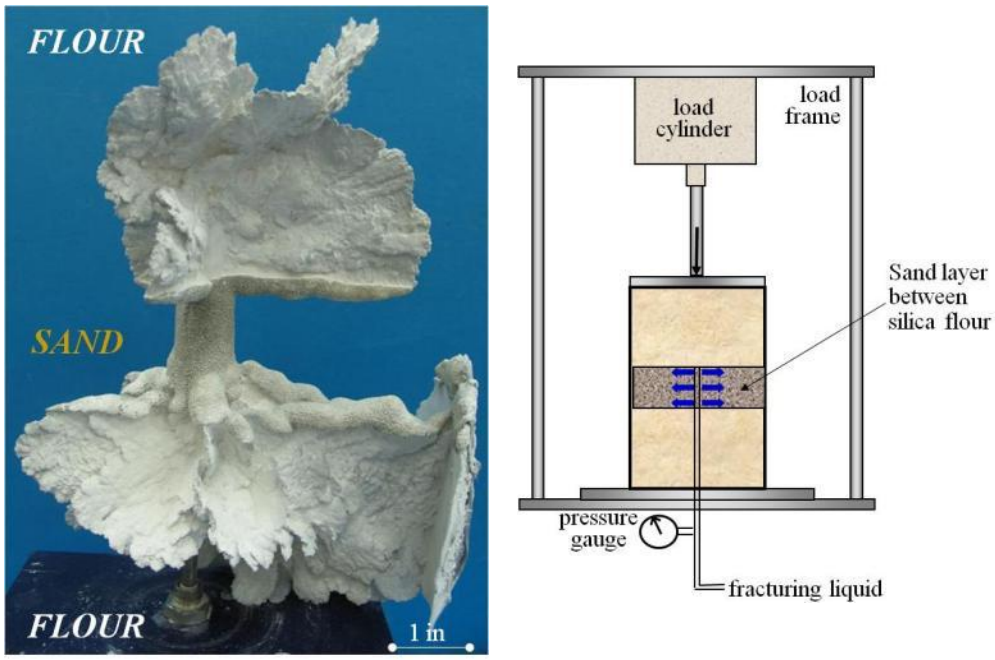

(a) **(b)**

Figure 5.19. LTC interface Test 09-15-08 conducted at 80 psi confinement. A layer of fine sand with a thickness of 3 in between two layers of silica flour. There is no fracture in the sand layer; it is confined to the top and bottom silica layer.

5.4. Tip and Fracture Surface Characteristics

The results of our injection test show a complicated geometry that typically opens perpendicular to the least principle stress. Aside from the observations mentioned above that are directly related to changes in parameters, there are other general observations that may indicate tip or initiation processes. We found four basic experimental observations that can be made with respect to the fracture initiation and tip:

1. Continued cavity expansion after initiation.
2. Splitting tips, offshoots are at acute angles to fracture propagation direction.
3. Leakoff ahead of the fracture tip.
4. Observations of fluidization

Each of these observations is discussed below in more detail.

5.4.1. Cavity expansion and shear failure

In our injection tests, the initial cavity expansion process is readily apparent. As can be seen in **Figure 5.21** (d) there was consistently a layer of fracturing fluid, with no suspended sample material, around the injection source. In addition, tests with sections of the leakoff zone present around the borehole (undisturbed by the fracturing process) vertical features (striations) are present that indicate shear failure (**Figure 5.20**). Further, in some tests similar features (striations) indicating a similar process are along the fracture and at the tip (**Figure 5.20** (d)).

There are several numerical and experimental models of this shear band process available in the literature. **Figure 5.21** (a) shows a FLAC model described by [*Chang*, 2004] originally by [*Kim*, 2011] illustrating the shear band development due to cavity expansion; the model solution is mesh dependent but qualitatively the model and experimental feature are similar. Examples of the cavity expansion process utilizing a discrete element code (PFC-3D) with coupled fluid dynamics DEM-CCFD were also presented [*Zhang and Huang*, 2011]. The DEM model shows similar shear band development when the maximum shear strain rate is plotted (**Figure 5,22** (b)). Further, other experimental results from injection tests that were CT scanned during the injection event (**Figure 5.22** (c)); show similar borehole expansion results as our tests [*Dong*, 2010].

Shear bands due to the process of fracture propagation in cohesionless materials may be a different scale from the shear bands that develop due to the cavity expansion that progresses around the injection source. Shear bands as a mechanism of fracture propagation in cohesionless materials were hypothesized by *Chang* [2004] and *Chang et al.* [2003]. There are characteristics that exist at the crack tip that were attributed to shear bands [*Chang*, 2004; *Chang et al.*, 2003; *Germanovich and Hurt*, 2007; *Hurt et al.*, 2005]. Numerical simulations have also shown shear band development [*Wu*, 2006]. However, there is little direct evidence of shear bad development ahead of the crack tip. *Dong* [2010] shows shear band development ahead of a crack tip through CT scanning during an injection event (**Figure 5.23**) [*Dong and De Pater*, 2008]. Two cross-sections of

low stress experiments presented in this work are identical to the CT images. The fracture cross-sections exhibit blunt tips, suggesting propagation due to shear bands at the crack tip. The comparisons of the experimental results are shown in **Figure 5.23**. The fracture tips are remarkably similar. The experiments by *Dong* [2010] utilized high leakoff fluids. Our experiments show very low levels of leakoff. This is important as most of the available literature considers that the failure ahead of the crack tip is due to the reduction of effective stresses and shear failure within the leakoff zone [*Dong*, 2010; *Dong and De Pater*, 2008; *Khodaverdian and Mcelfresh*, 2000; *Khodaverdian et al.*, 2009]. However, our experiments have a very limited volume of leakoff, yet still appear to propagate in a similar fashion. This indicates that the shear events may be larger than the leakoff zone. Thus, the presence of sufficient fracturing fluid ahead of the crack tip to harbor these shear bands is may not be essential.

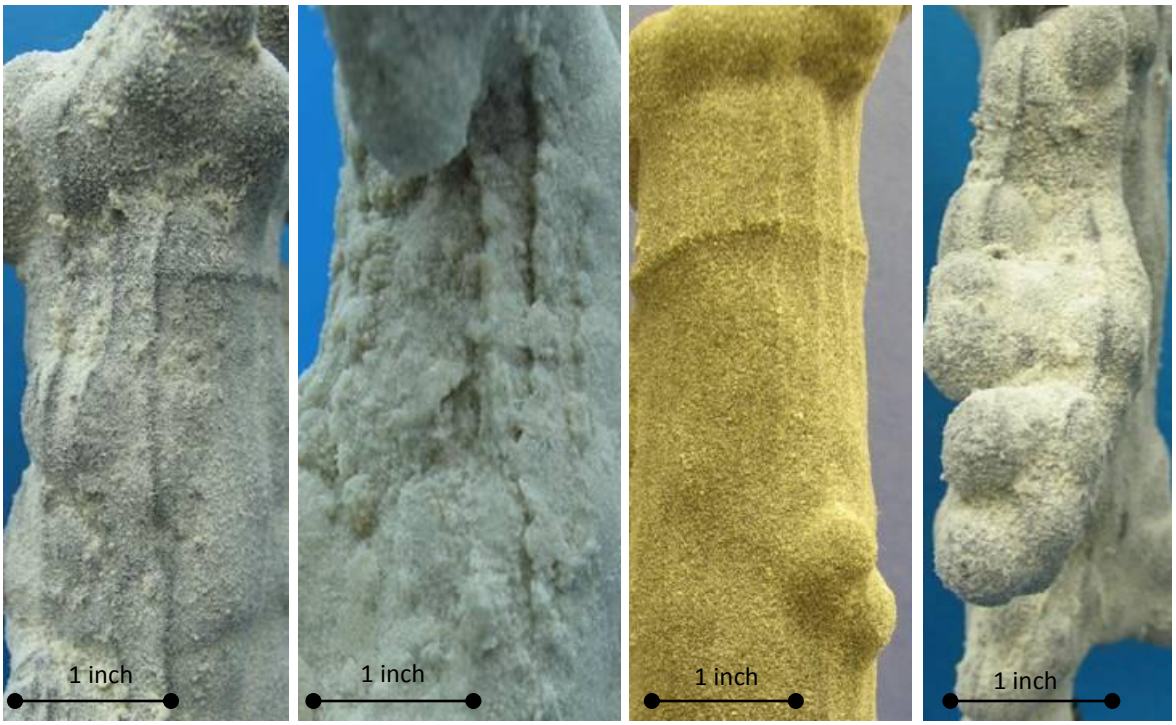

Figure 5.20. Images of vertical striations indicating shear failure. (a) Test 04-14-06, (b) Test 02-01-06 and (c) Test 09-14-05 Vertical features remain in the leakoff zone from the cavity expansion around the borehole. (d) Test 04-14-06 Similar features along the fracture extent.

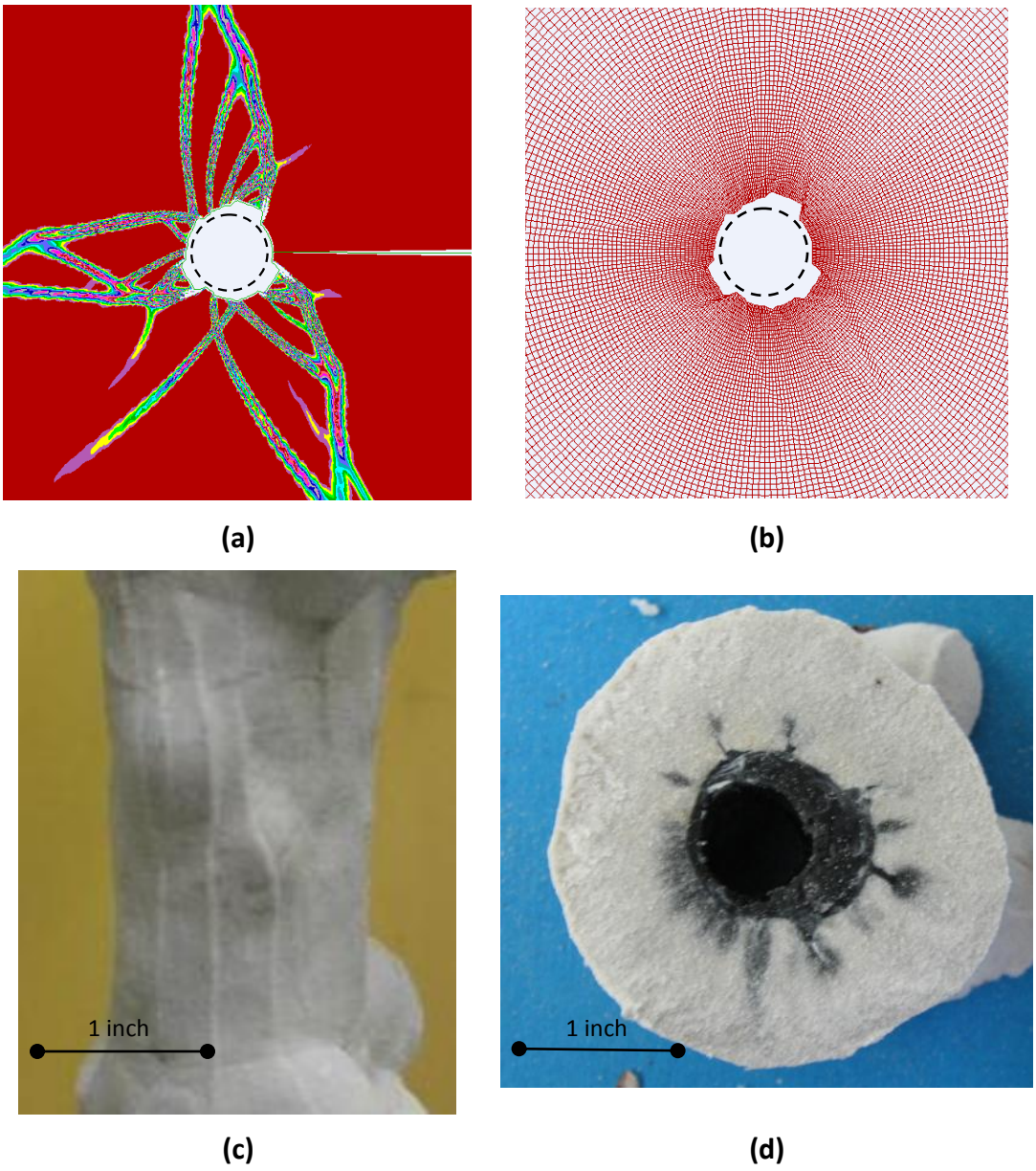

Figure 5.21. Cavity expansion in strain-softening material simulated with FLAC model from [*Chang*, 2004; *Kim*, 2011]: (a) shear strain increments and (b) the corresponding deformed mesh. Shear strain increments represent the developed shear bands. Although the solution is mesh dependent, it represents the physical process. The vertical lines in (c) are from one of our injection Test 09-11-09 cross-section shown in (d).

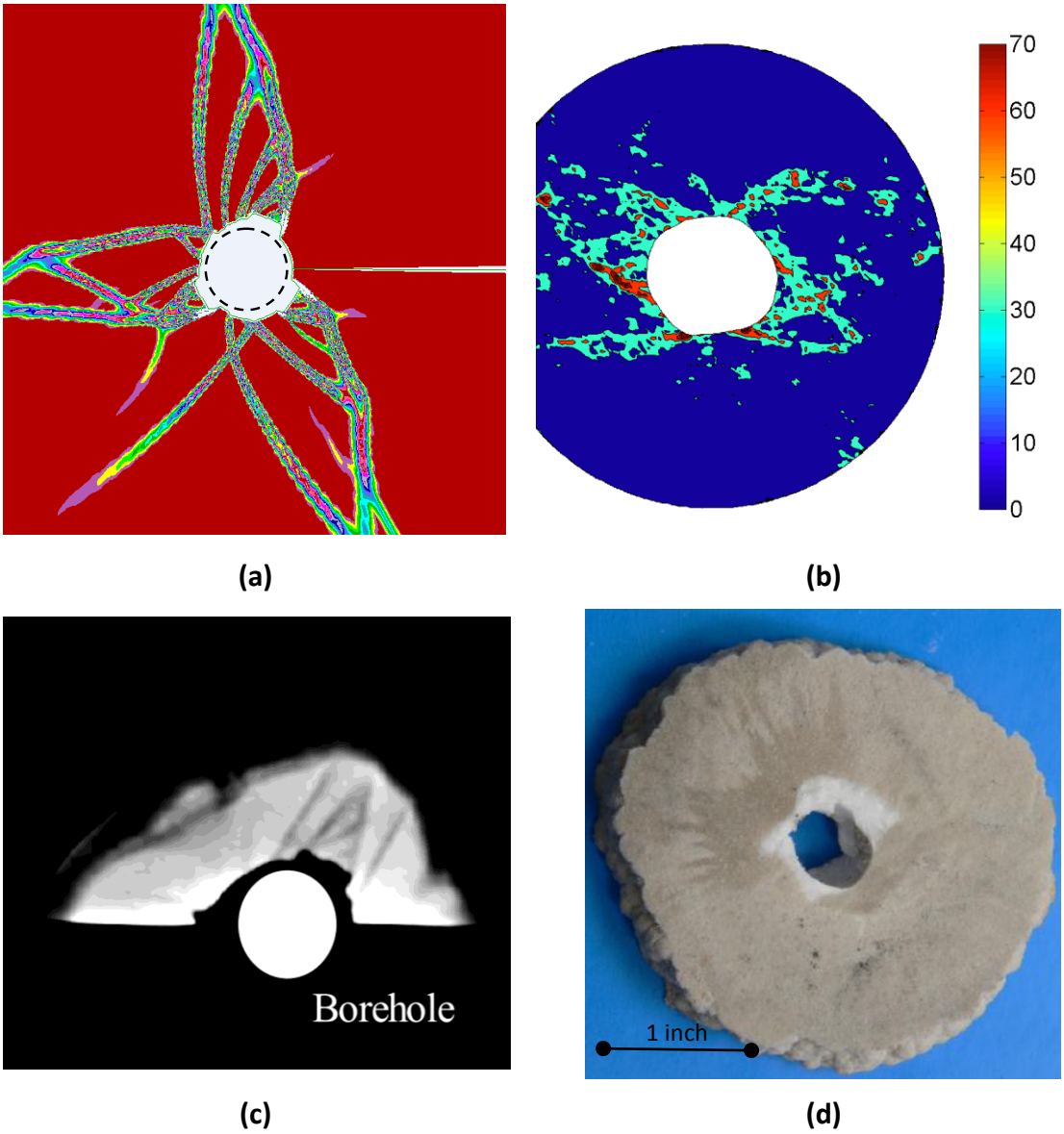

Figure 5.22. More examples of models of borehole expansion from the literature (a) FLAC model [*Chang*, 2004; *Kim*, 2011] (b) Maximum shear strain rate from DEM-CCFD model [*Zhang and Huang*, 2011] (c) CT scans during injection experiments in saturated sands [*Bohloli and De Pater*, 2006] (d) a cross section from Test 03-03-06.

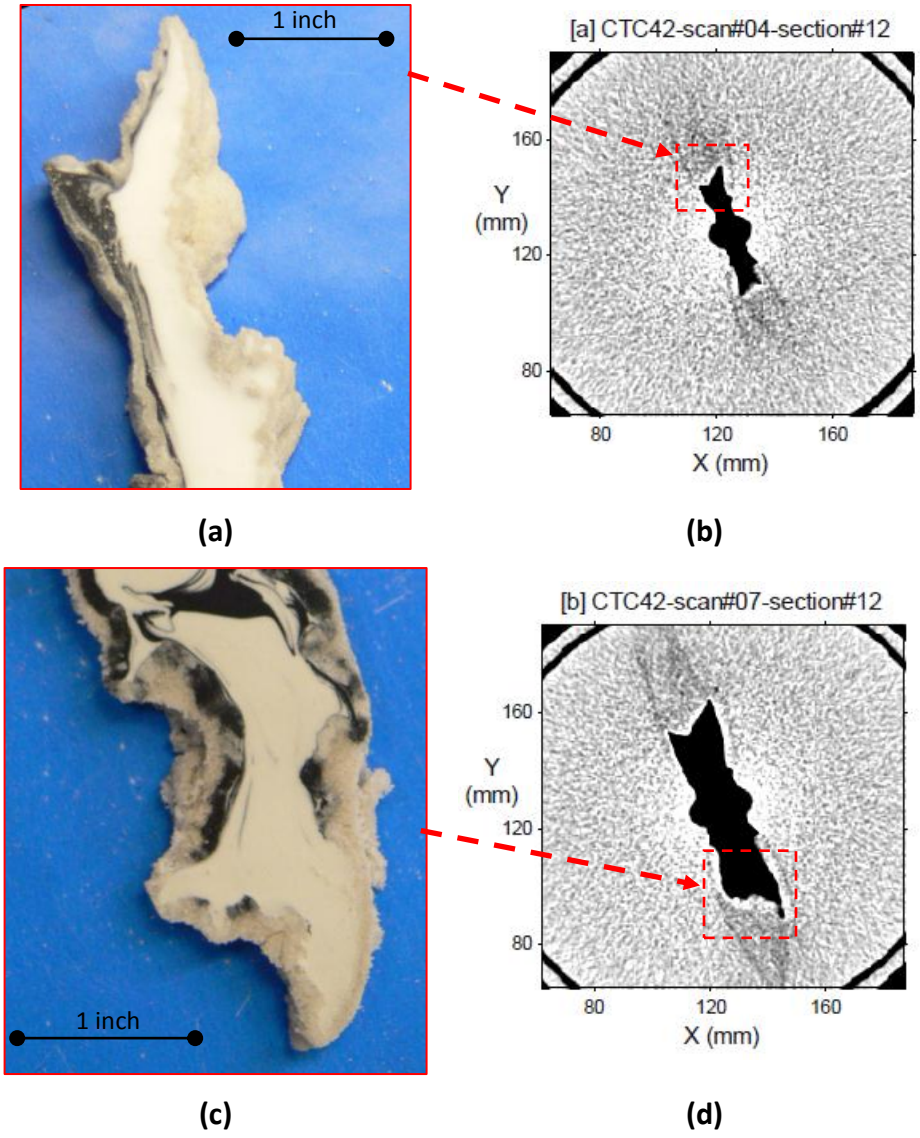

Figure 5.23. Cross sections of two of our tests with CT scan images from *Dong* [2010] tip morphologies are similar, notice the large shear bands emanating from the tips in the CT images. (a) Cross-section from a low leakoff experiment. (b) Shear bands do not appear to extend to boundary. (c) Cross-section from another low leakoff experiment. (d) Shear bands extend to boundary and along the walls of the fracture. *Dong's* tests were samples of fine sand at 1 MPa confinement with a bentonite / grout slurry (high leakoff fluid). Our samples were fine sand at 0.05 MPa confinement injected with medium (a)Test 03-30-11 and (c) Test 03-10-11 high viscosity silicone (low leakoff fluid) at 50 ml/min.

5.4.2. Splitting tips and offshoots

The splitting tip feature is a common occurrence in cross-sections of our injection tests. **Figure 5.24**, **Figure 5.25**, and **Figure 5.26** illustrate the complicated geometry at the fracture tip. Further, there is evidence of splitting tips in the leakoff surface (**Figure 5.26**) along the fracture extent. These features are consistently orientated at acute angles with the direction of fracture propagation.

There are often tri-splitting tips in our experiments (as shown in **Figure 5.25**). These show two acute offshoots on both fracture faces, with a third tip orientated along the fracture propagation direction. These features are much more apparent in experiments when the leakoff thickness is comparable to the fracture aperture, or much smaller. In experiments with significantly more leakoff there appears to be a smoothing effect on the fracture walls. The high leakoff experiments also show diffuse flow at the tip of many of the offshoots, both at the fracture tip and along the fracture walls (**Figure 5.27**) illustrating the leakoff process ahead of the crack tip.

5.4.3. Leakoff ahead of the tip

In **Figure 5.27** are several examples of fluid leakoff into regions at the tip of the fracture or other offshoots. These regions indicate a highly permeable zone in the leakoff zone ahead of the crack tip. The nature of this phenomenon appears to be leakoff thickness dependent. The high-permeability, fine sand features exhibit a much more diffuse invasion pattern ahead of the crack tip. The pattern of leakoff in the lower

permeability mixture is much more focused with angular offshoots that are more prevalent.

The close up view in **Figure 5.28** shows a feature emanating from the initial cavity. The tip of the fracture shows many branches and a complex evolution (white fluid invaded prior to black). This appears similar to the leakoff-dominated regime presented by *Huang et al.* [2011].

In a few of our tests, we observed regions of nearly pure silicone on the leakoff surface (**Figure 5.29**). This indicates a localized failure of the leakoff layer due to over-pressurization. It must be stressed that these features are not planar, these nearly pure silicone offshoots illustrate the three dimensional nature of the point source geometry of the invasion fluid.

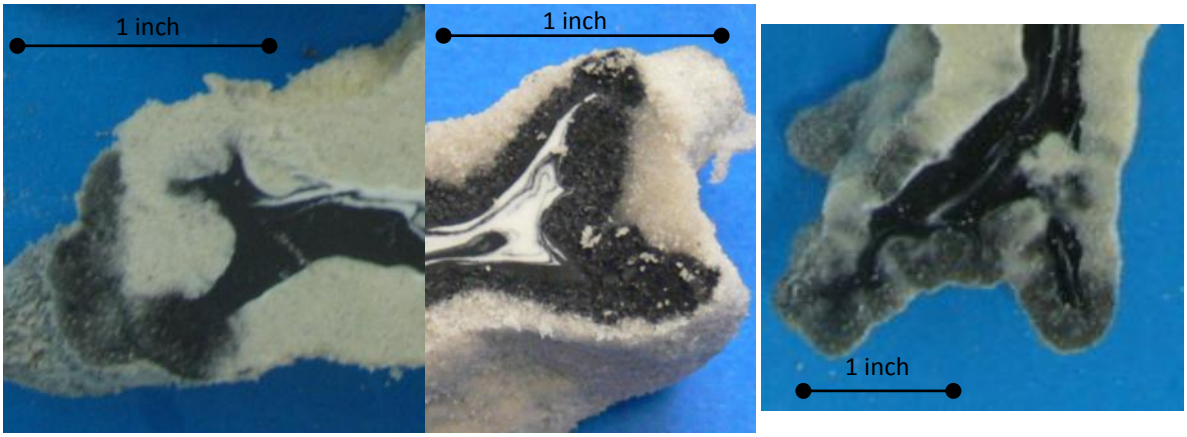

Figure 5.24. Splitting tips features of three different tests.

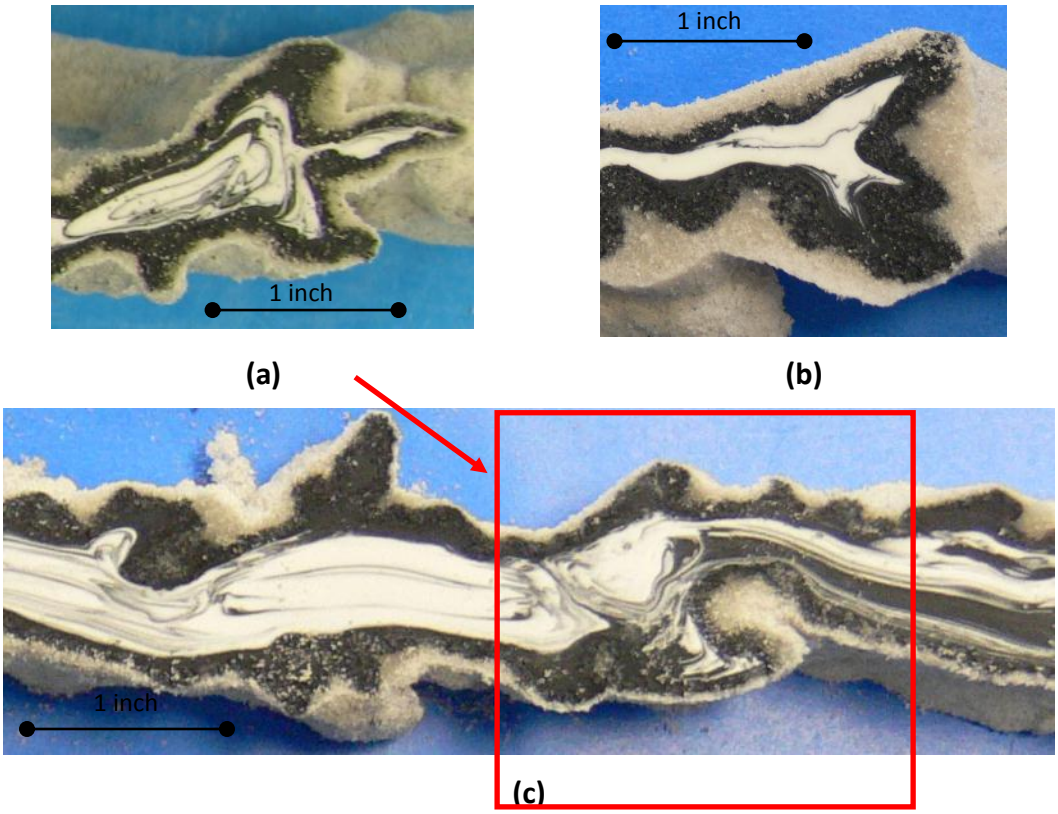

Figure 5.25. Triple splitting tips. (a) and (b) show two examples of triple splitting tips in our fractures, (c) appears to be later growth from one of these triple splitting tips.

Figure 5.26. Various forms of splitting tips along the fracture length, all at acute angles to the direction of propagation. The cross-sections are orientated such that propagation is from left to right.(a) Test 07-17-08 (b) Test 07-08-08 (c) Test 03-03-11

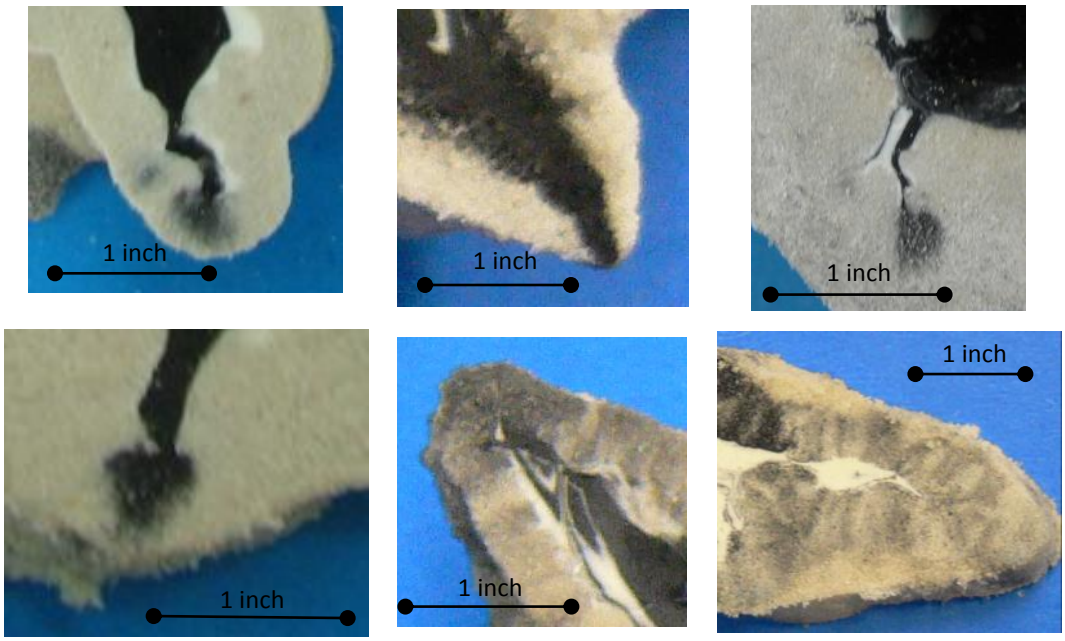

Figure 5.27. Images of various tips showing the fluid invasion ahead of the fracture tip, suggesting more of a fluidization event.

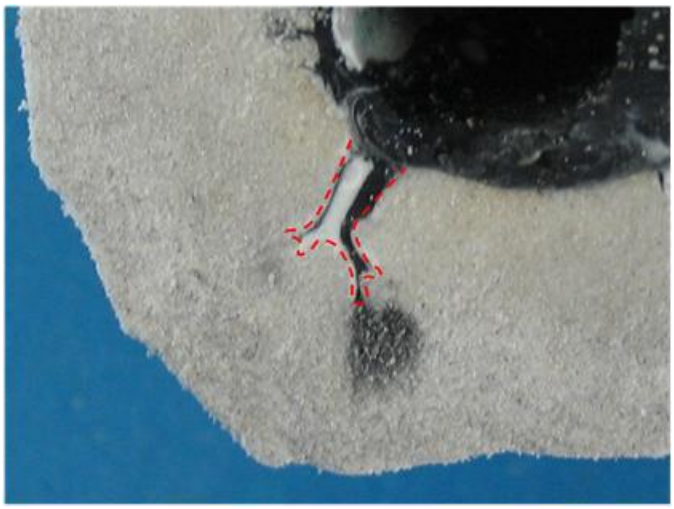

Figure 5.28. Close up view of initiation from borehole for Test 09-11-09. The red line indicates the region of pure injection fluid with multiple splitting tips. Similar to fractures shown by *Huang et al.* [2011] in the "infiltration- (or leakoff-) dominated regime."

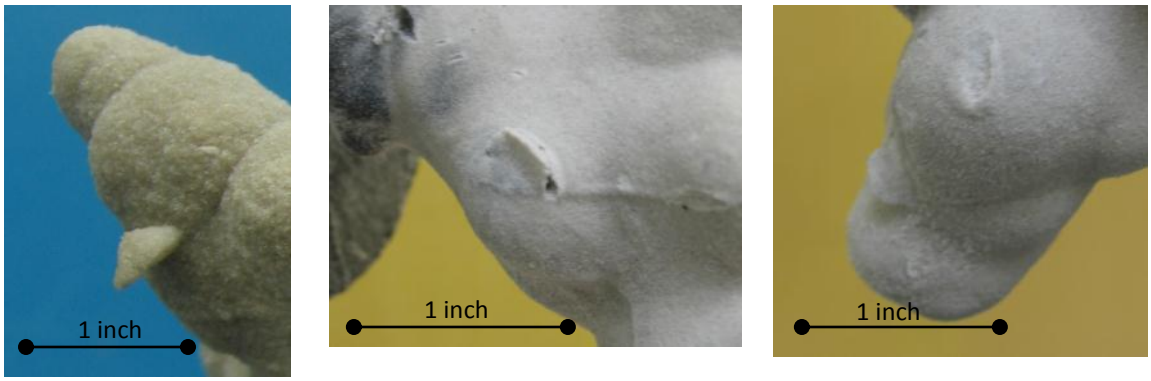

Figure 5.29. Protrusions of nearly pure silicone on the leakoff surface. The phenomenon indicates localized failure of the leakoff zone and fracturing fluid flow to the surface.

5.4.4. Observations of fluidization

Utilizing the HPTC and a manual hand pump several attempts were made to generate fractures at high confinements (2000 psi). These tests were prepared in a similar fashion as the other work presented; only a manual single piston pump was used for the injection device. Further, a special low volume high-pressure displacement chamber was also fabricated. The results were not considered particularly useful in the context of the majority of the work here (i.e., peak pressures versus confinements). However, cross-sections of the solidified forms show evidence of fluidization.

This is visible through the dense outer layer in the cross-sections. Quantitative imaging analysis was not possible due to the unique nature of the sample. However, a close inspection allows for a qualitative description of the densities of the various layers (**Figure 5.30** and **Figure 5.31**). The high-density layer appears as the white region surrounding the solidified form. The low-density region is the darker region in the

images of cross-sections. Finally, there are small regions of pure silicone within the cross-sections of the solidified form. This is peculiar due to the highly loaded state of the sample after shut-in and solidification.

The main conclusion of this experimental series is that distinct regions are developed due to the injection of a pressurized fluid. Further, the size of the fluidized region can be quite large. We obtained little direct evidence of density contrasts within the leakoff zone in our other experiments. However, these particular experiments show that these regions can and do develop under the right conditions.

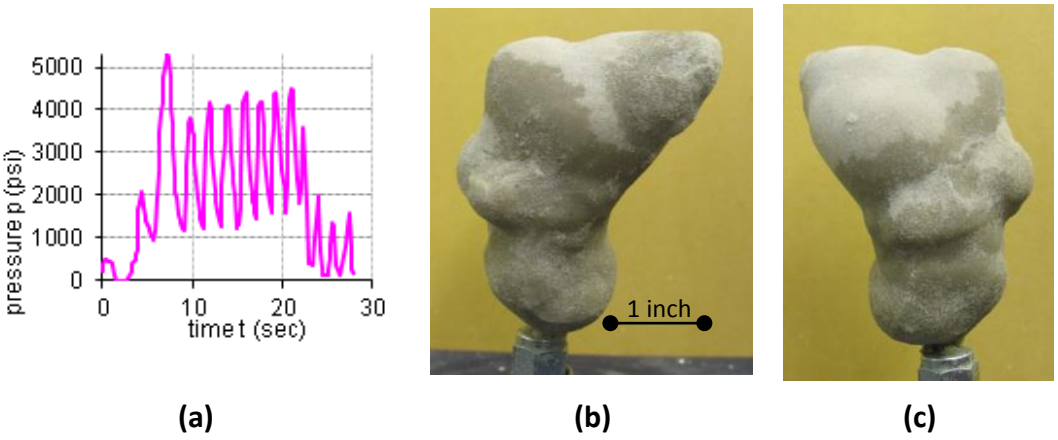

Figure 5.30. Fracture shape from high-pressure test, cross-section are in below in **Figure 5-31.** Sample was fine sand at a confinement of 1000 psi injected with medium viscosity silicone average injection rate was 1.5 ml/sec (i.e., with a hand pump).

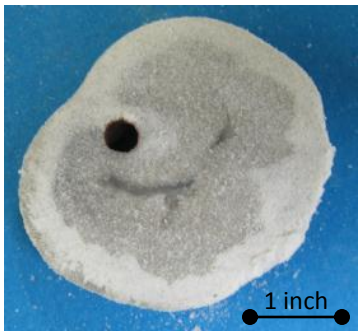

This cross-section clearly shows the dense outer leakoff zone. Inside of that is a less dense zone with small thin regions of pure silicone in the center.

This cross-section shows two distinct circular forms in the center of the solidified shape. These two circular regions are joined by a thin section of less dense material.

There is evidence of an initiation event in this cross-section. The borehole is in the center of the form and a small region of pure fluid is indicating cavity expansion with a small offshoot.

Figure 5.31. Cross-sections of a high-pressure test, pressure-time curve and complete sample form shown above in **Figure 5.30.**

5.5. Conclusions

The results of our observations of the injection tests show a complicated geometry. This geometry opens more or less perpendicular to the direction of the least principle stress. Our silicone tests focus on injection experiments when the thickness of fracture aperture is comparable to the leakoff thickness. However, a majority of the available literature on unconsolidated fractures focus on high leakoff fractures [e.g., *De Pater and Dong*, 2007; *De Pater and Dong*, 2009; *Dong and De Pater*, 2007a; 2008; *Khodaverdian and Mcelfresh*, 2000; *Khodaverdian et al.*, 2010a].

The main points of this chapter can be summarized by:

1. Stress increases will reduce fracture aperture and increase leakoff and injection pressures. In general, peak injection pressures are higher than the maximum principle stress, though fractures propagate perpendicular to minimum principle stress.
2. Increasing viscosity and reducing permeability will decrease leakoff.
3. Increase in flow rate results in decreases in leakoff in high leakoff tests. Once leakoff is reduced significantly, further changes in flow rate do not significantly alter the leakoff thickness.
4. No change in injection pressure was noticed with several orders of magnitude changes in flow rate.

5. Silica flour samples exhibit distinctly different propagation regimes. The reason could be the significant reduction in permeability or different failure characteristics compared to sand samples.
6. Changes in pore fluid do not appear to affect our experiments.
7. The dimensional analysis and experimental observations of peak pressures in our tests match very well.
8. Experimental observations indicate leakoff precedes fracture propagation perhaps during the process of tip extension.
9. The leakoff zone appears as a collection of spheroids that form the fracture walls. These spheroids are more pronounced in high permeability tests.
10. The fracture cross sections show multiple features that form acute angles to the direction of propagation. These features are more apparent in low leakoff experiments.
11. Fractures tend to propagate arbitrarily along the outer edge of the propagating fracture.
12. Our facture shapes match those in the literature that exhibit shear band development in front of the fracture tip.
13. Fluidized regions were directly observed in cross-sections of high-pressure tests.

6. TOUGHNESS-DOMINATED HYDRAULIC FRACTURE

6.1. Introduction

In this chapter, we present scaling relationships indicating that in experiments performed in the regime of limited leak-off, there is a high-pressure gradient in the leakoff zone in the direction normal to the fracture. Fluid pressure does not considerably decrease along the fracture, however, due to the relatively wide fracture aperture. This suggests that hydraulic fractures in unconsolidated materials propagate within the toughness-dominated regime. Furthermore, we show that the theoretical model of toughness-dominated hydraulic fracturing [*Detournay*, 2004] can be matched to the pressure-time dependences, observed in our experiments, with only one fitting parameter. Scale analysis shows that large apertures at the fracture tip correspond to relatively large 'effective' fracture (surface) energy, which can be orders of magnitude greater than typical for hard rocks. Finally, we utilize a similarly developed model with a representative data set obtained from a field experiment by *Murdoch and Slack* [2002].

6.2. Scaling Relationships

As a first step, we are concerned with determining the magnitude of the viscous losses within the fracture. To this end, we attempt to determine the magnitude of pressure losses by scaling analysis based on the geometry observed in the cross-sections of our created fractures.

6.2.1. Pressure gradient within fracture

Our experimental observations suggest the fracture aperture (width) is comparable to the leakoff thickness and much larger than the grain scale. In this sense, the fracture can be considered thick. This observation ignores any consideration of post shut-in fracture closing or continued leakoff, but gives a lower estimate of the fracture aperture during the final stages of fracture extension. Based on this the pressure loss due to the fluid flow along the fracture may be negligible for fractures in unconsolidated materials. Therefore, in an attempt to determine the viscous losses due to fluid flow within the fracture we present a scaling analysis. To determine the viscous losses due to fluid flow within the fracture we consider an idealized geometry shown in **Figure 6.1**. Steady laminar flow between fixed parallel plates can be described by the relationship [e.g., *Munson et al.*, 2002]

$$q = -\frac{h^3}{12\mu}\left(\frac{\partial p}{\partial x}\right) \tag{6.1}$$

between the volumetric flow rate q (per unit length), the pressure gradient $\partial \mathrm{p} / \partial \mathrm{x}$ the distance between two parallel plates h and the fluid viscosity μ. The pressure gradient scales as

$$\frac{\partial p}{\partial x} \sim -\frac{\Delta p}{l} \tag{6.2}$$

where Δp is the pressure drop between the fracture tip and borehole. Solving (6.1), (6.2) for Δp, we obtain

$$\Delta p \sim -\frac{12\mu l}{h^3} q \tag{6.3}$$

We then estimate a 2D flow rate parameter

$$q = \frac{Q}{H} \tag{6.4}$$

where H is the length of the injection source and Q is the volumetric flow rate in our experiments. Therefore, the pressure drop driving the flow within the fracture with a Newtonian fluid, scales as

$$\Delta p \sim \frac{12\mu l}{h^3} \frac{Q}{H} \tag{6.5}$$

Which is a well-known expression [e.g., *Munson et al.,* 2002]

However, this analysis assumes a Newtonian fluid. In contrast, the fracturing fluids exhibit shear-thinning behavior, and a yield stress with silicone adhesive. For this scaling, we ignore the presence of the yield stress for simplicity. It can be shown, however, that the results below still hold. For the viscous, steady-state, power law fluid flow between two parallel plates, Δp scales as [e.g., *Wilkeinson,* 1960],

$$\Delta p \sim \left(\frac{4n+2}{n} \right)^n \frac{2Kl}{h^{2n+1}} \frac{Q^n}{H^n} \tag{6.6}$$

In our experiments, $K < 10^3$ Pa·sec^n, $l < 10$ cm, $h \sim 0.3$ cm, $Q/H < 2.0$ cm^2/sec, and $n \approx 0.75$. Therefore, we obtain from (6.6) that,

$$\Delta p \leq 0.8 \text{MPa} \tag{6.7}$$

This indicates that the pressure drop due to the fluid moving within the fracture is at least an order of magnitude less than the peak pressure (~ 5 MPa for these parameters)

or even minimum injection fluid pressures as described in Chapter 4. Under low stress conditions, our peak pressures can be much lower than what is reported above (~ 0.7 MPa). The resulting fracture aperture, however, is much larger. Consequently, the scaling still results in an order of magnitude less viscous losses for the entire range of experimental parameters used in our experiments. This scaling shows that the pressure in the fracture is almost constant and is almost entirely transmitted by the fluid from the source to the fracture tip region. Therefore, to the first order, the pressure distribution can be considered uniform within the fracture. In other words, these fractures are within the toughness-dominated regime of hydraulic fracturing.

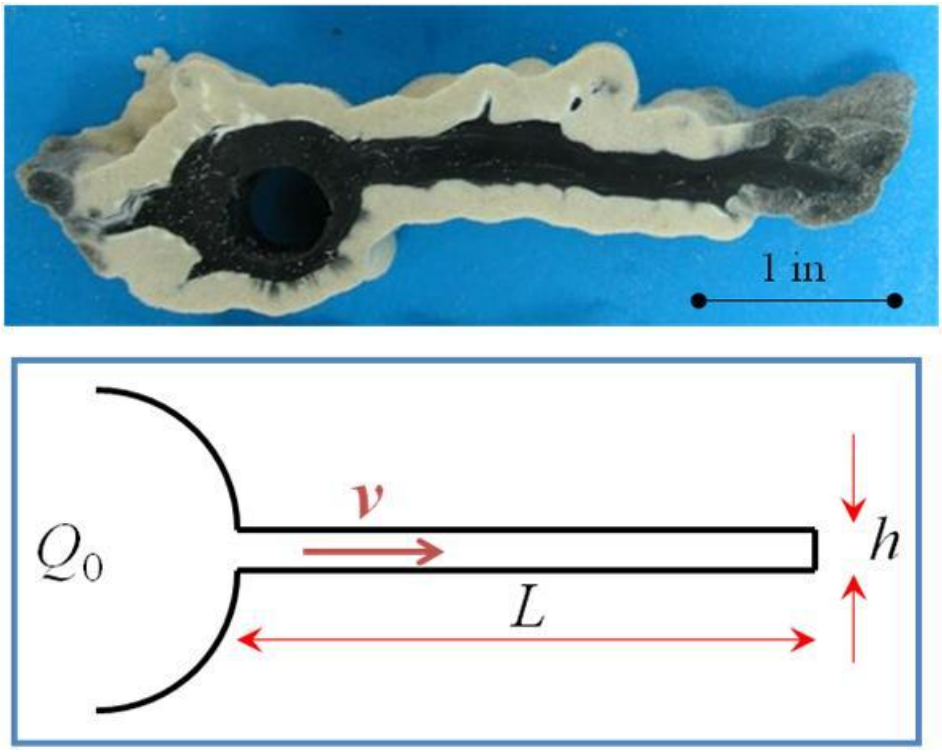

Figure 6.1. (a) cross-section from Test 09-27-07 and (b) represents the idealized fracture by parallel plates. In the fracture cross section (a), the white fluid is injected first and the black fluid follows. This illustrates that the fracturing fluid does primarily flow along the length of the fracture to the tip, confined by the existing leakoff deposited as the fracture progressed. Therefore, we consider the fluid flow to be represented as viscous flow between two parallel plates.

6.3. Mathematical Model

Hydraulic fracturing in competent rock is a complex process involving coupling of elastic deformation of the rock, processes of fracture extension, fluid flow within the fracture and fluid flow within the rock (leakoff). Recently significant advances were made in modeling hydraulic fractures in brittle materials, coupling complex fluid interactions (e.g., leakoff, lag) with elastic deformation and fracture [*Adachi and Detournay*, 2002; *Bunger et al.*, 2005a; *Desroches et al.*, 1994; *Detournay*, 2004; *Detournay and Garagash*, 2003; *Detournay et al.*, 2007; *Garagash and Detournay*, 2005; *Garagash et al.*, 2011].

In special cases these processes were adequately modeled by focusing on the primary energy dissipation mechanisms [*Adachi and Detournay*, 2002; *Bunger et al.*, 2005b; *Garagash and Detournay*, 2000; *Savitski and Detournay*, 2002]. It is possible to utilize a ratio of energy required to extend the fracture to the energy dissipated through viscous fluid flow within the fracture. If this ratio is small then the fracture is within the viscosity-dominated regime. If this ratio is large then it is considered toughness-dominated [*Savitski and Detournay*, 2002].

These more complex models have yet to be given full consideration to hydraulic fracturing in cohesionless materials. Scaling of our experimental results shows that our fractures can be considered within the toughness-dominated regime of hydraulic fracturing. That is, the pressure of the fluid within the fracture can be considered constant. Quasi-constant pressure is a product of the high fracture energy in a relatively

soft material, which is similar to the case presented by *Germanovich and Murdoch* [2010].

Here we utilize these models for hydraulic fracturing in unconsolidated formations. Closed form solutions are available for toughness-dominated hydraulic fractures with simple geometries that incorporate fracturing fluid leakoff. These geometries include radial, KGD, and PKN [e.g. *Economides and Nolte*, 2000]. The results presented here suggest that the geometry may be characterized by radial or KGD models. PKN is not considered due to the typical injection time history recorded during the tests. For PKN geometry we would expect an increasing or constant injection pressure [e.g. *Economides and Nolte*, 2000]. The pressure time histories reported here, however, show a decreasing pressure time history after the peak injection pressure. Further PKN fracture geometry is considered those with the fracture length much greater than the fracture height. Given the results of our experiments the PKN fracture geometry is the least applicable.

A schematic of the idealized fracture is shown in **Figure 6.2**. In the next section we show the modified model for toughness-dominated fractures. The derived model is then utilized to match the pressure time histories of the experiments completed in our lab. In Section 6.5, a similar model (it incorporates near surface boundary condition) is matched to data from a large scale shallow filed test reported in *Murdoch and Slack* [2002]**.** Finally, in Chapter 7, the model is instrumental in designing a large-scale high-stress test conducted independently from the bulk of the work presented here.

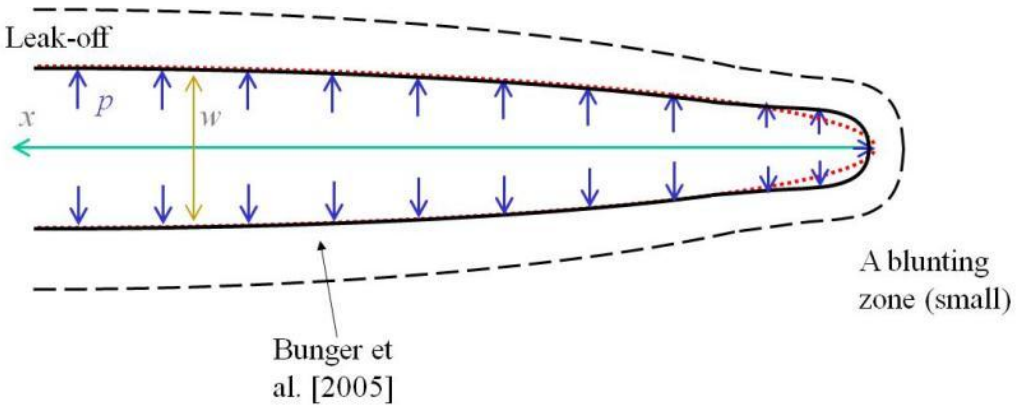

Figure 6.2. Schematic of the toughness-dominated fracturing model. The processes at the tip are considered confined to a small region and do not affect the solution (except near the fracture tip). A short distance away from the tip, the toughness-dominated hydraulic fracturing model can be applied.

6.3.1. Toughness-dominated fractures with leakoff

In general, the geometry of the fracture is an important consideration in determining the energy due to viscous dissipation. In radial fractures, under a consistent fluid injection rate, a small initial aperture coupled with high initial fluid velocity can create high viscous forces. However, the extension of the fracture over time creates a decrease in the viscous forces due to two processes. First, the increase of fracture aperture and second the decrease in fluid velocity at the crack tip. Conversely, the fracture extension energy increases with fracture size. Therefore, the fracture is said to transition from a viscosity-dominated regime to toughness-dominated regime. The transition can be characterized through a characteristic time scale [*Bunger et al.*, 2007],

$$t_m = \left(\frac{\mu'^5 Q^3 E'^{13}}{K'^{18}}\right)^{1/2} \tag{6.8}$$

with $\mu' = 12\mu$, $E' = E/(1-\nu^2)$, $K' = 4(2/(\pi)^{1/2}K_{Ic}$,) μ is the fluid viscosity, E is the elastic modulus of the host material, Q is the flow rate and K_{Ic} is the fracture toughness. If the injection time $t \ll t_m$, then the fracture is considered to be within the viscosity dominated regime. If $t \gg t_m$, then the regime is considered toughness-dominated.

Typically in rock-like materials (with limited leakoff), fracturing fluid lags behind the crack tip [*Economides and Nolte*, 2000]. This fluid lag can affect the propagation of hydraulic fractures unless the length of the lag zone is small in comparison to the fracture scale [*Desroches et al.*, 1994]. If leakoff is not considered, the viscosity-dominated regime develops the largest lag zone. In contrast, in the toughness dominated regime the lag zone is negligible [*Garagash and Detournay*, 2000]. The parameter L_μ represents the distance from the crack tip in which the effect of fluid lag vanishes,

$$L_\mu = \frac{\mu' E'^2 V}{\left(\sigma_o - p_1\right)^3} \tag{6.9}$$

with V as the crack tip velocity, so as the confining stress and p_1 as the lag pressure. The fluid lag can be ignored if $L_\mu << l$ where l is the length of the fracture. Because $l \sim Vt$ an additional characteristic time scale can be defined as:

$$t_o = \frac{\mu' E'^2}{\left(\sigma_o - p_1\right)^3} \tag{6.10}$$

We now have two characteristic time scales, t_m and t_o, in which to determine the primary regime our fractures reside in (toughness or viscosity) and whether fluid lag at the crack tip can be ignored.

For our fractures, experimental observations indicate that fluid lag is not present. In fact, injected fluid precedes the fracture tip as others have found [*De Pater and Dong*, 2007; *Dong*, 2010; *Hurt et al.*, 2005; *Khodaverdian and Mcelfresh*, 2000]. Further, our scaling indicates that our fractures can be considered thick (constant pressure) in all of our experimental conditions. *Murdoch* [1993a] also found that for cohesive soils the fractures can be considered thick. That is, the viscous losses due to fluid flow are negligible, indicating a toughness dominated regime. Therefore, if our experimental time is much greater than both characteristic times ($t >> t_o, t_m$) then our fractures can be considered zero-lag toughness dominated fractures.

If we consider that our fractures have zero lag and are toughness-dominated then there are closed form solutions available. These solutions are derived for hydraulic fractures driven by an incompressible Newtonian fluid that is injected into a permeable infinite elastic solid. Both radial and plane strain (KGD) geometries for this problem were derived by *Bunger et al.* [2005]. Use of this particular model for hydraulic fractures in unconsolidated models was first hypothesized by [*Germanovich and Murdoch*, 2010]. They did not have available experiments, however, and could not verify their hypothesis. In a toughness-dominated regime the material parameters are given by;

$$E' = \frac{E}{1-\nu^2},\ \mu' = 12\mu, K' = 4\left(\frac{2}{\pi}\right)^{1/2} K_{Ic}, C' = 2C_l \tag{6.11}$$

This solution provides the net fluid pressure *p(x,t)*, fracture aperture *w(x,t)* and fracture length *l(t)* for radial and KGD geometries when leakoff is modeled as a one dimensional diffusion process. The general scaling given in *Bunger et al*. [2005b]

$$w = \varepsilon L \Omega(\xi, \tau),\ p = \varepsilon E' \Pi(\xi, \tau),\ l = \gamma(\tau) L \tag{6.12}$$

where $\tau = t/t_L$ and $\xi = x/l(t)$ are dimensionless time and coordinate set respectively. The appropriate scaling parameters for radial and KGD toughness dominated fractures are shown in **Table 6.1**. The dimensionless fracture size is given by

$$\gamma = \left(\frac{t}{t_L}\right)^{\delta} \sum_{n=0}^{4} C_n \left(\frac{t}{t_L}\right)^{n\beta} \tag{6.13}$$

leakoff is insignificant when $t << t_L$, and leakoff is important when $t >> t_L$. The solutions presented here are valid for both geometries when $t_m << t_L$. The dimensionless fracture size γ can be determined by matching the asymptotes of large and small times as outlined in *Bunger et al*. [2005]. The coefficients in (6.13) for the dimensionless fracture size for small and large times are shown in **Table 6.2**.

Table 6.1. Scaling parameters for toughness dominated KGD and radial fractures [*Bunger et al.*, 2005].

Geometry	ε	L	t_L
KGD	$\dfrac{C'^2}{Q_o}$	$\left(\dfrac{K'Q_o}{E'C'^2}\right)^2$	$\dfrac{K'^4Q_o^2}{E'^4C'^6}$
Radial	$\left(\dfrac{C'^2K'}{Q_oE'^2}\right)^{1/3}$	$\left(\dfrac{K'Q_o}{E'C'^2}\right)^{2/3}$	$\left(\dfrac{K'^4Q_o^2}{E'^4C'^6}\right)^{2/3}$
$\Omega(\xi,t)=2^{-1/2}\gamma^{1/2}\left(1-\xi^2\right)^{1/2}$		$\Pi(\xi,t)=\dfrac{\pi}{2}2^{-5/2}\gamma^{-1/2}$	

Table 6.2. Coefficients for the dimensionless fracture size [*Bunger et al.*, 2005].

	$t/t_L \le \tau$	$t/t_L \ge \tau$
$\mathbf{C_0}$	0.8546	0.4502
$\mathbf{C_1}$	-1.110	-3.824×10^{-2}
$\mathbf{C_2}$	1.562	4.685×10^{-3}
$\mathbf{C_3}$	-1.772	-3.322×10^{-4}
$\mathbf{C_4}$	1.337	0
δ	2/5	1/4
β	3/10	-3/8

To estimate the characteristic time scale t_m for laboratory tests in brittle materials we use typical values for material parameters with the effective viscosity of our fluid (at the shear rate of 1 sec^{-1}) and our flow rate values;

$$K_{Ic} = 1\text{MPa}\sqrt{\text{m}},\ E = 3\text{GPa},$$
$$\mu = 10^5\,\text{cP},\ Q = 500\,\text{ml/min} \tag{6.14}$$

Using (6.8), we obtain $t_m \sim 3200$ s. The expected experimental time with a zero leakoff condition, with a sample size of 12 in, creating a plane strain KGD fracture, would be ~ 1.0 s. This would indicate a viscosity-dominated regime. Even with reducing the flow rate down to the lowest flow rate utilized in our tests (50 ml/min), this scaling would still indicate a viscosity dominated regime. Conversely, scaling of our experimental observations in cohesionless materials indicates a thick fracture, with zero lag. Thus, at our experimental scales we expect that the toughness-dominated model is applicable for cohesionless particulate materials. In fact, in all of our modeling $t >> t_m$ indicating that fractures in cohesionless materials exhibit different propagation regimes when compared to brittle materials under similar injection conditions.

6.3.2. Leakoff coefficient

To estimate the leakoff coefficient, we utilize direct measurement of leakoff thickness in our experiments. The silicone fracturing fluid does not exhibit significant volumes of leakoff, post shut-in. This is evidenced by the multi colored fluid injection experiments. In two stage colored fluid injection experiments there is little evidence that leakoff continues to occur after shut-in. for example, **Figure 6.3** shows two different

cross-sections of separate experiments. The majority of fluid flow is moving to the crack tip and after the first stage (color) of injection establishes the leakoff zone, the second stage does not appear to contribute significantly to leakoff. In addition, the change in leakoff color occurs rather dramatically along the length of the fracture. The demarcation of the two colors typically occurs at some location perpendicular to the propagation direction. This indicates that there may be two leakoff processes, one occurs primarily in the region of the fracture tip; the other primarily acts on the fracture face.

The leakoff that occurs at the crack tip is not considered in this model. If we consider that this leakoff is primarily due to tip extension processes, than the amount of leakoff due to the 1D diffusional process would be negligible. We are primarily concerned with the leakoff that occurs through the fracture face, when calculating a leakoff coefficient. We have two limiting cases. One there is no leakoff away from the fracture tip. Second, all the leakoff occurs through the fracture face. The case of no leakoff corresponds to a leakoff coefficient of zero (no leakoff other than that due to tip processes). As an initial estimate, we include the leakoff coefficient, and consider that the leakoff measured in our fracture cross-sections occurred through the fracture face.

For the silicone injection test the leakoff thickness is measured directly. Experiments utilizing guar fracturing fluid do not preserve the fracture aperture and colored phases are not practical, so we extend our observation in silicone test to the guar tests and assume no significant post shut-in leakoff. This is also verified by the pore

fluid volume response of the sample both during and after the injection event. The guar tests are measured for total thickness, and this is considered twice the leakoff thickness (fracture aperture is not preserved).

The evidence of a complex fluid flow regime in the process of leakoff, limits the applicability of a 1D diffusion formulation. Therefore, we estimate an "effective" leakoff coefficient through direct measurement of the leakoff layer thickness. The equation is

$$b = 2C_L\sqrt{t} \tag{6.15}$$

where b is the leakoff thickness, t is the experimental time, and C_L is the effective leakoff coefficient. In this chapter we present the pressure time histories from the results generated in our lab. The results presented in this chapter are not sensitive to the leakoff coefficient. The model does calculate the width of the fracture and leakoff zone. However, because we utilize the thickness of the leakoff zone to calculate the leakoff coefficient, the results are not particularly surprising.

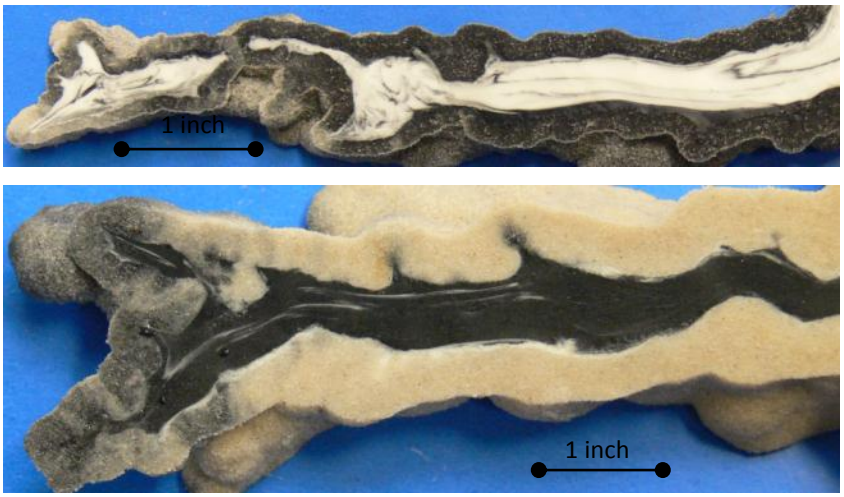

Figure 6.3. The leakoff thickness of fractures. (a) black colored fluid injected first fracture Test 07-02-08, and (b) white fluid injected first fracture Test 09-27-07. The majority of the new fluid injected is transported to the tip (or other small regions with localized deformation.)

6.3.3. Fracture toughness

Estimations of effective fracture toughness for laboratory experiments of hydraulic fracturing in soils have varied significantly $0.01\ \text{MPa x m}^{1/2}$ to $1.0\ \text{MPa x m}^{1/2}$ [*Chang*, 2004; *Harison et al.*, 1994; *Murdoch*, 1993c; *Wang et al.*, 2007]. In soils, the fracture toughness is not a material parameter, but is utilized as an effective parameter. Effective fracture toughness in soils is a particular way to quantify the energy required to extend the fracture, without considering the mechanisms of the fracture extension.

For this model, we calculate the effective fracture toughness utilizing the relationships from above coupled with the known fracture radius and the minimum injection pressure. We can now use the dimensionless fracture length to calculate fracture toughness. Because

$$\gamma(t) = \frac{R(t)}{L} \tag{6.16}$$

we can combine (6.16) with equation (6.12) for pressure, we have (for KGD geometry)

$$p(t) = \frac{\varepsilon E}{2\sqrt{2\gamma(t)}} \tag{6.17}$$

Using the scaling parameters ε and L from **Table 6.1,**

$$p(t) = \frac{\varepsilon E}{2\sqrt{2R(t)\frac{(\varepsilon E)^2}{K_I^2}}} \tag{6.18}$$

and

$$p(t) = \frac{K_I}{2\sqrt{2R(t)}} \tag{6.19}$$

finally

$$K_I = 2p(t)\sqrt{2R(t)} \tag{6.20}$$

Utilizing the minimum pressure at the conclusion of the tests $p(t_{max})$ at a known radius

$$K_I = 2p_{\min}\sqrt{2R_{\max}} \tag{6.21}$$

To calculate for the "effective" fracture toughness K_{Ic} we used

$$K_{Ic} = \frac{1}{4}\sqrt{\frac{\pi}{2}}K_I \tag{6.22}$$

Similar expressions for radial geometry are derived in the same fashion.

6.3.4. Other model parameters and curve fitting technique

In this section, we describe the remaining model parameters and the process of curve fitting. The stiffness (E) is taken as the value reported from the triaxial data listed in Chapter 3. The solution for the pressure-time history is not sensitive to the material stiffness, so in general we use a stiffness value of ~ 90 MPa. Sensitivity of the model to the stiffness comes from the calculation of fracture aperture.

The viscosity parameter (μ) we utilize here is the consistency index of the injected fluid; we use the effective viscosity at 1 sec^{-1}. This model is derived for a Newtonian fluid, yet the fluids used in our tests are of a power law or Herschel-Bulkley rheology. This complicates the fluid flow modeling component. We consider our fractures to be toughness-dominated; as a result the only significant inaccuracies should be from the quantification of the leakoff process. To characterize the leakoff process, we are utilizing an *ad hoc* effective leakoff coefficient and representing a complex leakoff regime with a one dimensional diffusion process. Finally, the viscosity only enters the model solution through the characteristic time scales t_o and t_m therefore the modeling of pressure-time history is unaffected by inaccurate viscosity estimations.

For our modeling, the pressure-time history is typically normalized by the minimum pressure. This is not a necessity, however, and computed dimensional pressures can be utilized as well (as in the field scale modeling in section 6.5). To illustrate the pressure-time curve fitting we show the normalized pressure formulation.

The normalized pressure can be calculated as follows. Starting with equation (6.12) for pressure $p = \varepsilon E' \Pi(\xi, \tau)$ and recognizing that $\Pi(\tau)$ is proportional to $\gamma(\tau)^{-1/2}$ results in

$$p(\tau) = \varepsilon E' \frac{1}{2\sqrt{2\gamma(\tau)}} \tag{6.23}$$

(the $1/2\sqrt{2}$ term is from the KGD geometry) recall that

$$\tau = \frac{t}{t_L} \tag{6.24}$$

we know the pressure $p(t_{\max})$ and time at the end of the experiment

$$\frac{p(\tau)}{p(\tau_{\max})} = \sqrt{\frac{\gamma(\tau_{\max})}{\gamma(\tau)}} \tag{6.25}$$

finally,

$$\frac{p(\tau)}{p(\tau_{\max})} = \sqrt{\frac{\gamma\left(\frac{t_{\max}}{t_L}\right)}{\gamma\left(\frac{t}{t_L}\right)}} \tag{6.26}$$

where the dimensionless fracture size function $\gamma(\tau)$ is given above in equation (6.13) and t_L is computed by

$$t_L = \frac{K'^4 Q_o^2}{E'^4 C'^6} \tag{6.27}$$

The model is fitted to the experimental data by introducing a time shift parameter t_{shift}.

$$P(t,t_L,t_{\max},t_{shift}) = \sqrt{\frac{\gamma\left(\frac{t_{\max}-t_{shift}}{t_L}\right)}{\gamma\left(\frac{t-t_{shift}}{t_L}\right)}} \tag{6.28}$$

where P is the dimensionless pressure. The fitting was accomplished by adjusting t_{shift} until the peak pressures of the model and experiment appeared to match at t_{peak}. Obviously, this model does not model pre peak injection pressure behavior.

Solutions for the fracture aperture and leakoff thickness are computed in a similar manner. We present the pressure-time histories as the aperture and leakoff time histories are somewhat obscured by the complications in estimating the leakoff coefficient and the assumption of contributions from competing leakoff processes (tip or fracture face processes). The final values of fracture aperture and leakoff thickness match the experimental data well, but it is trivial as we are using the final leakoff thickness in the calculation of the leakoff coefficient.

6.4. Comparison to Experimental Results

To ease in plotting the model and experimental data, we normalize the injection pressure by dividing the injection pressure by the minimum injection pressure. Due to this normalization the model is matched to the minimum pressure at the maximum time (the time where the fracture reached the boundary or radius of ~ 6 in). A fitting parameter is then utilized to match the peak pressure of the experimental data.

The tests shown in **Figure 6.4** thru **Figure 6.16** show the modeling results along with images of the resulting fractures. **Table 6.3** contains the test parameters and

results including the calculation of fracture toughness. **Figure 6.17** is a plot showing an increase in effective fracture toughness with increasing confinement. The estimated effective fracture toughness follows similar trends to our scaling. That is, fracture toughness increases by primarily the confining stresses; other experimental parameters provide second order effects.

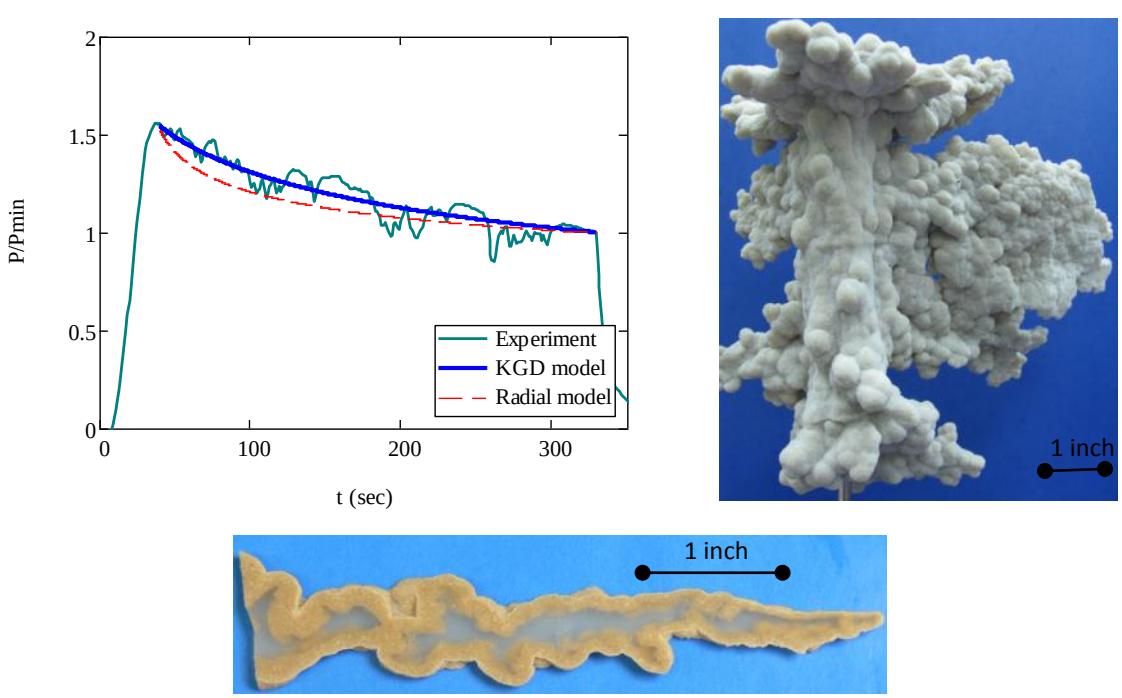

Figure 6.4. Experimental curve fitting, image and cross-section for Test 05-17-06.

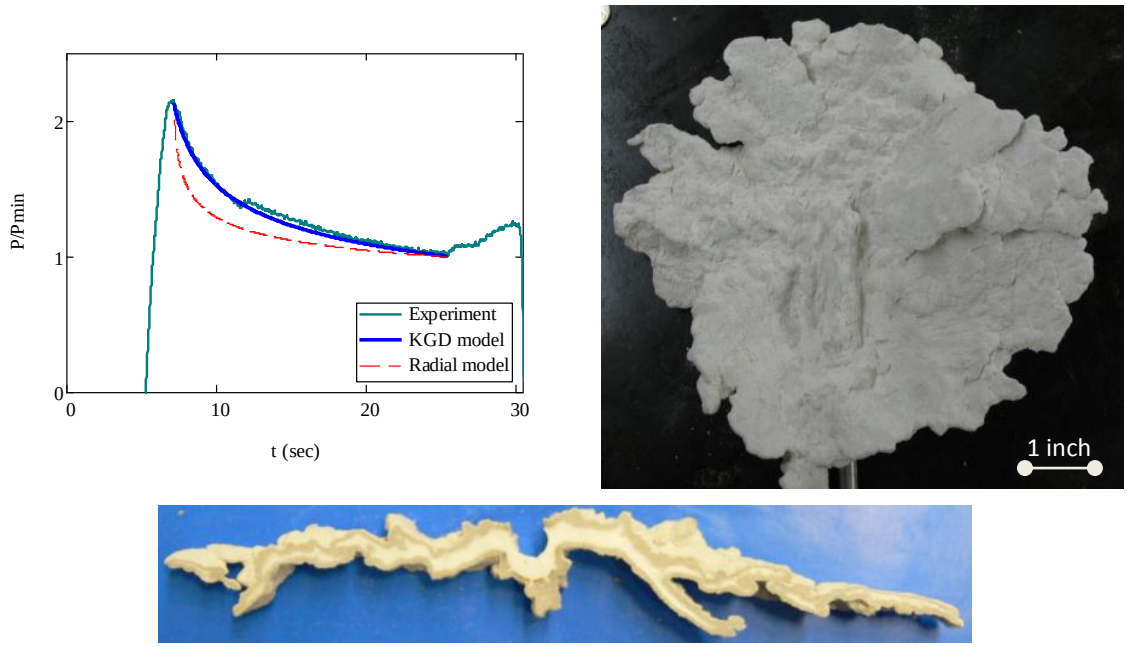

Figure 6.5. Experimental curve fitting, image, and cross-section for Test 11-05-10.

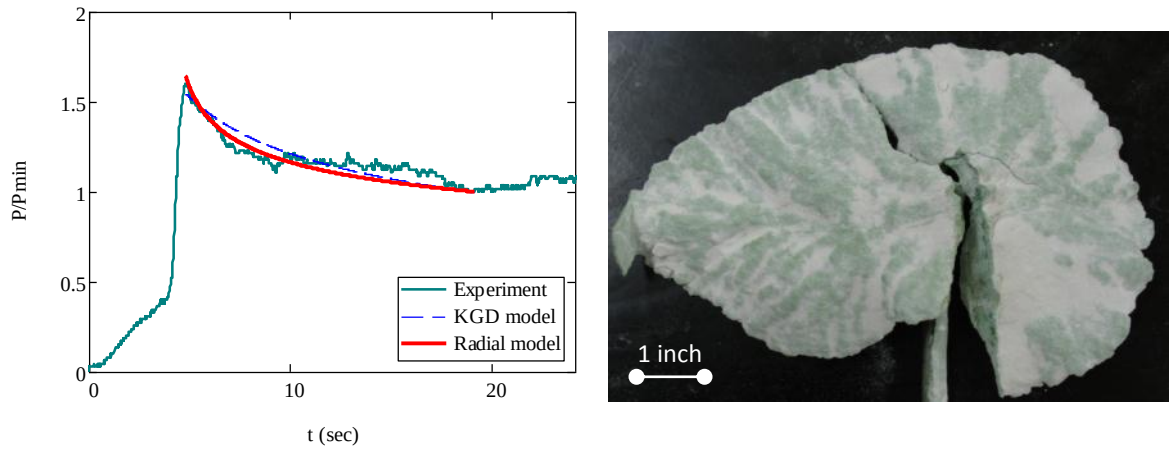

Figure 6.6. Experimental curve fitting and image for Test 10-14-10.

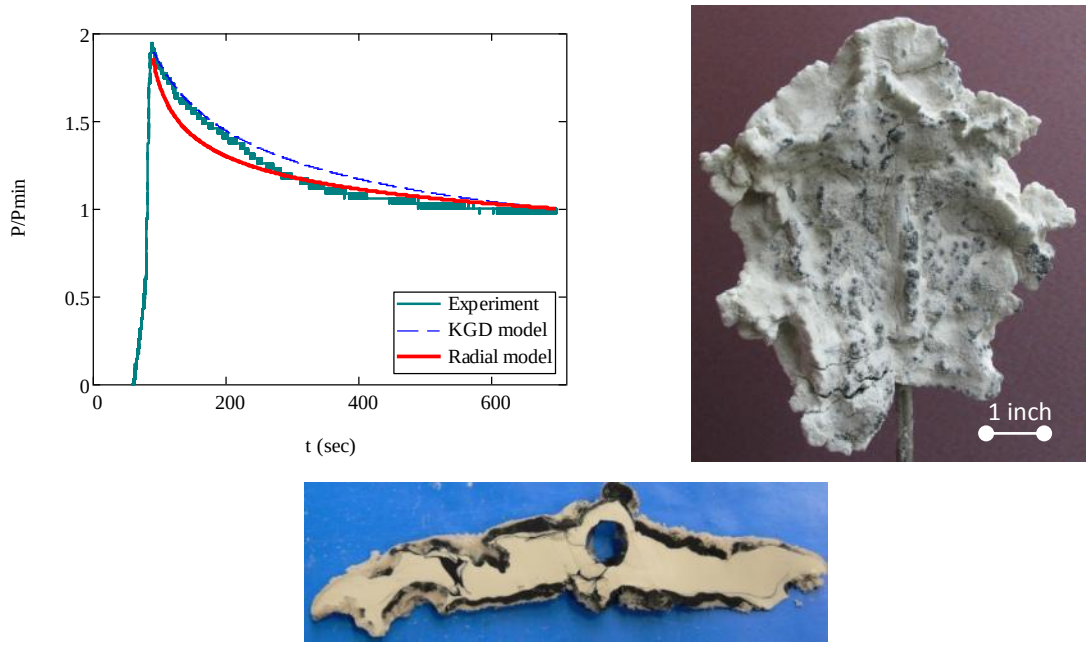

Figure 6.7. Experimental curve fitting, image, and cross-section for Test 03-10-11.

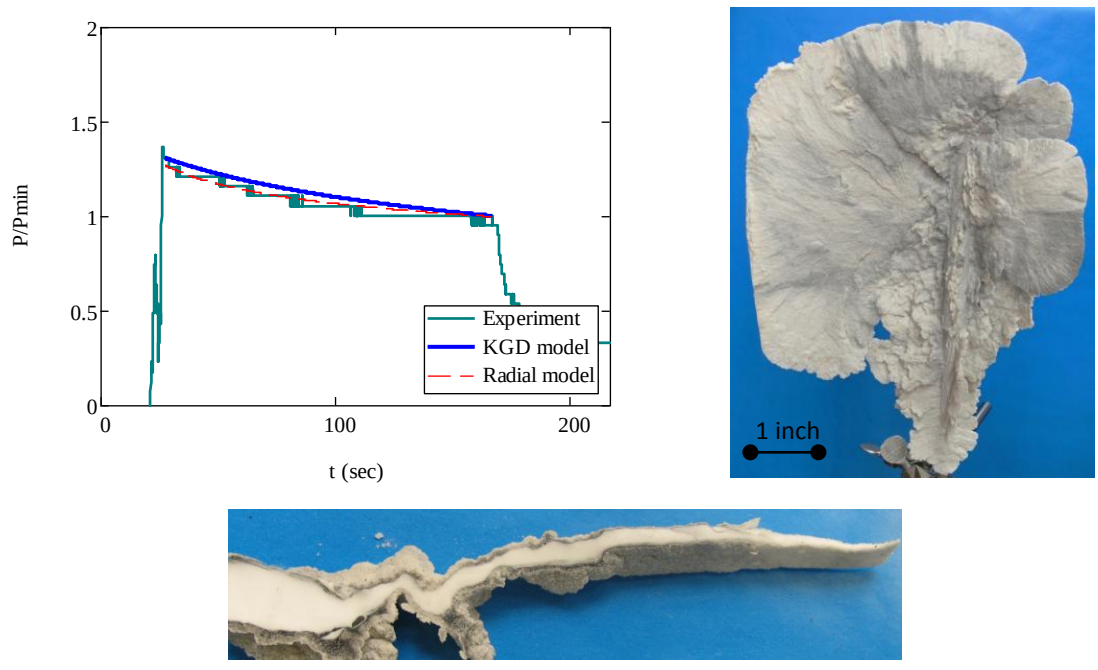

Figure 6.8. Experimental curve fitting, image, and cross-section for Test 05-12-11.

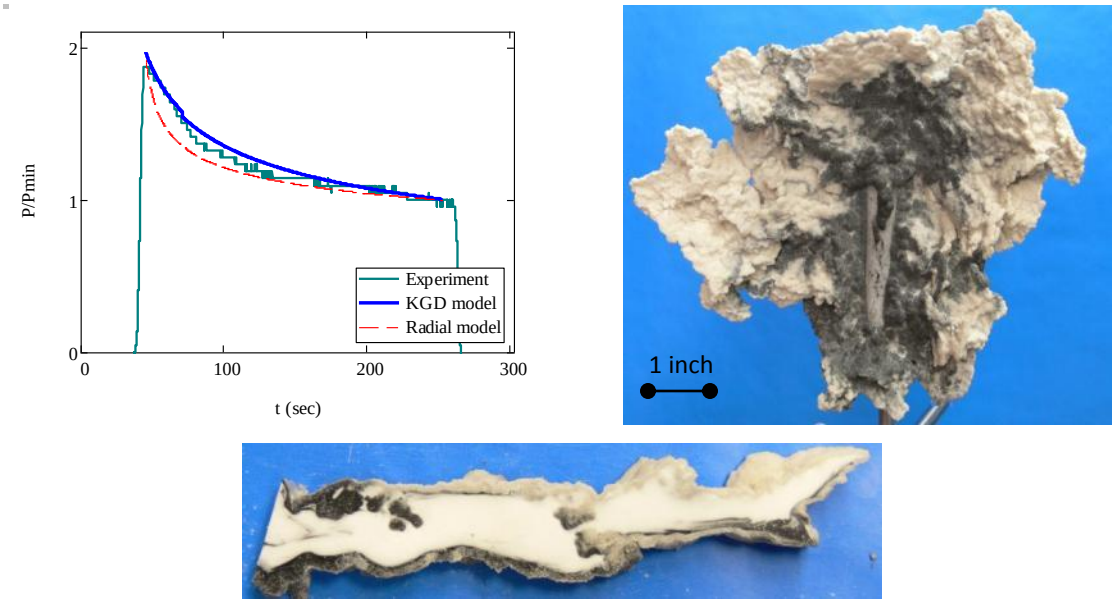

Figure 6.9. Experimental curve fitting, image, and cross-section for Test 03-30-11.

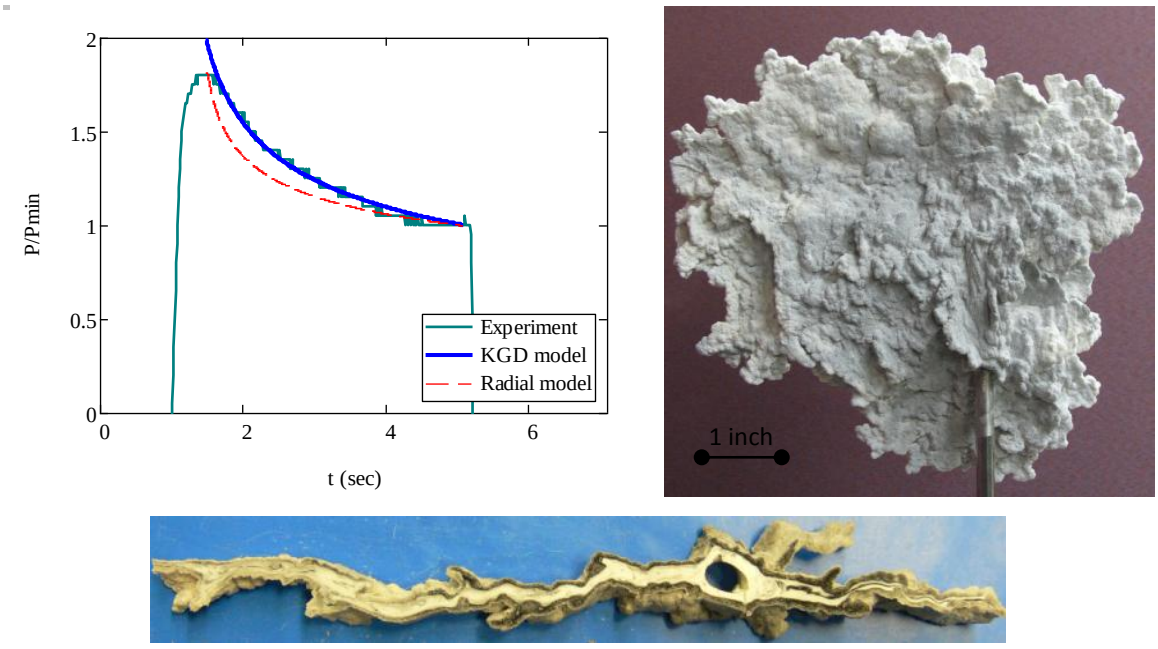

Figure 6.10. Experimental curve fitting, image, and cross-section for Test 01-31-11.

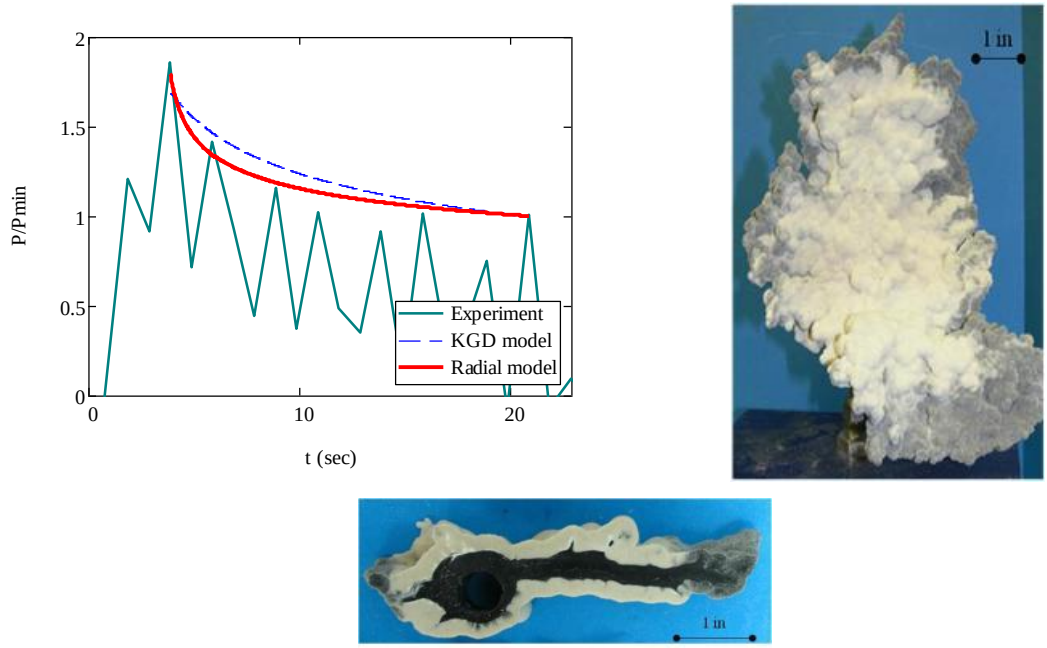

Figure 6.11. Experimental curve fitting, image, and cross-section for Test 09-27-07.

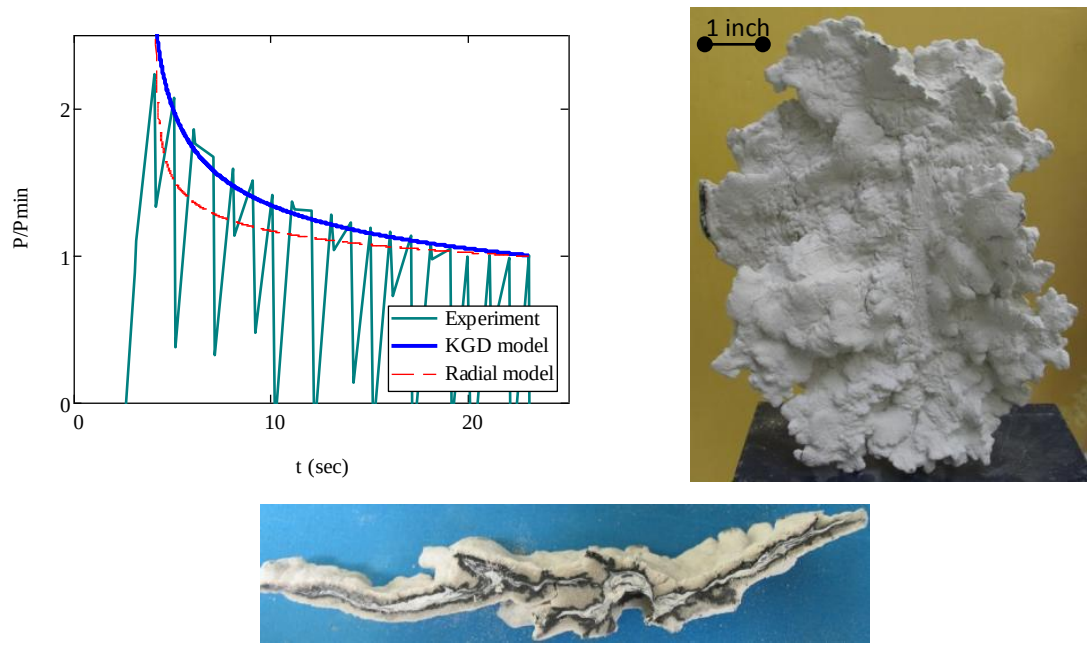

Figure 6.12. Experimental curve fitting, image, and cross-section for Test 11-17-08.

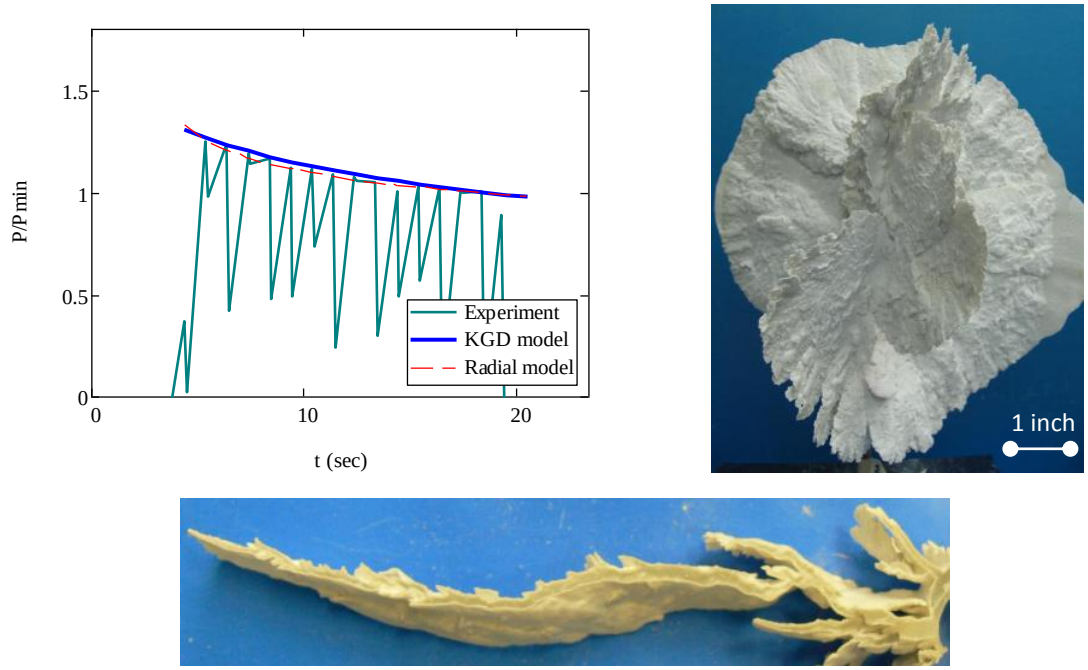

Figure 6.13. Experimental curve fitting, image and cross-section for Test 08-14-08.

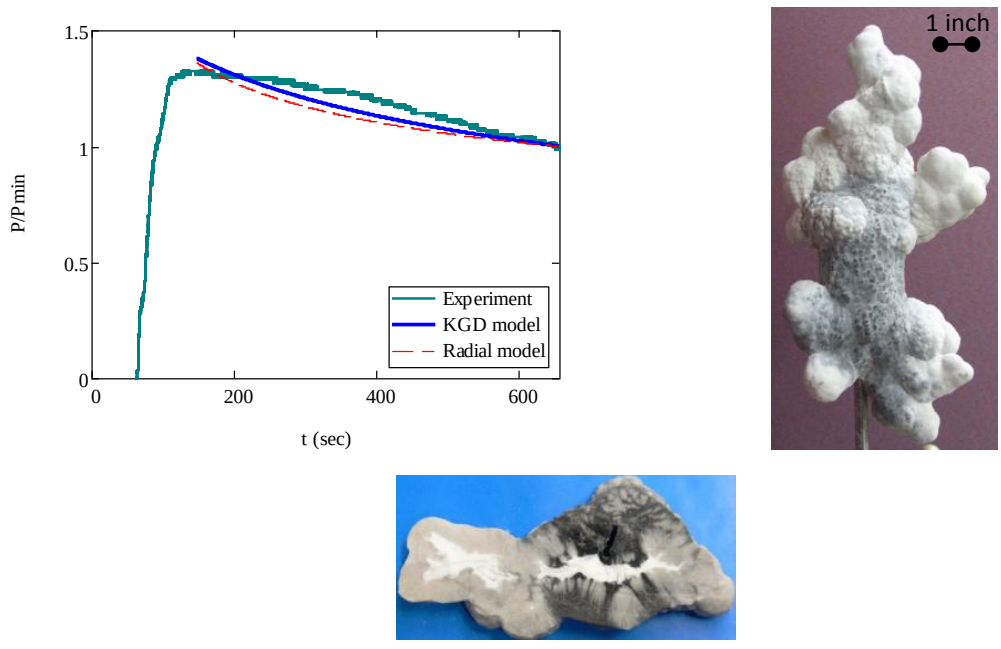

Figure 6.14. Experimental curve fitting, image, and cross-section for Test 02-10-11.

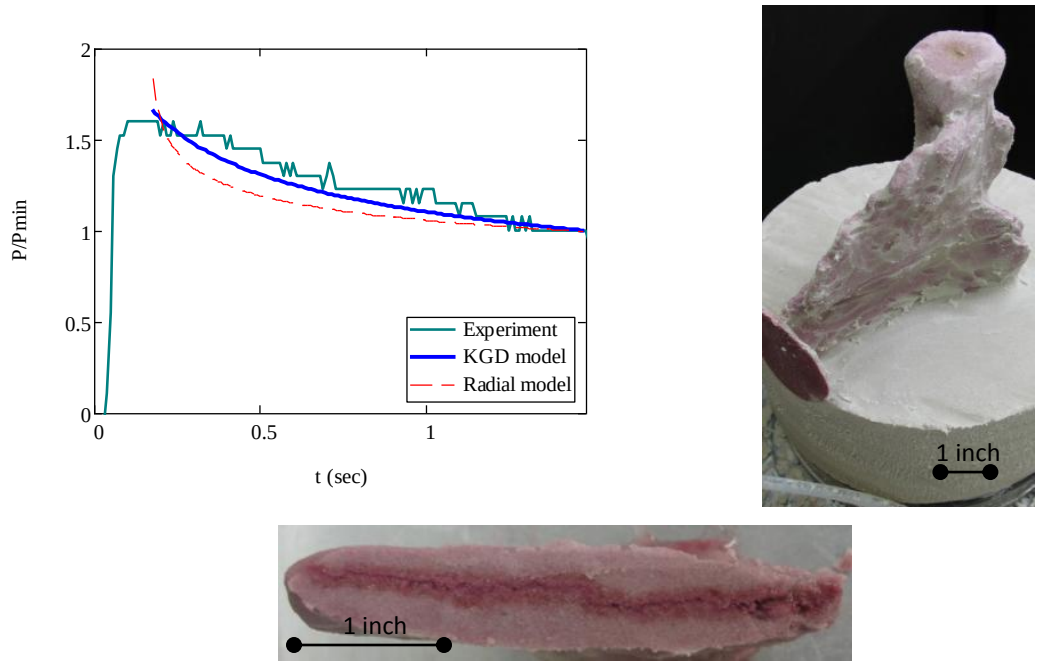

Figure 6.15. Experimental curve fitting, image, and cross-section for Test 08-03-10.

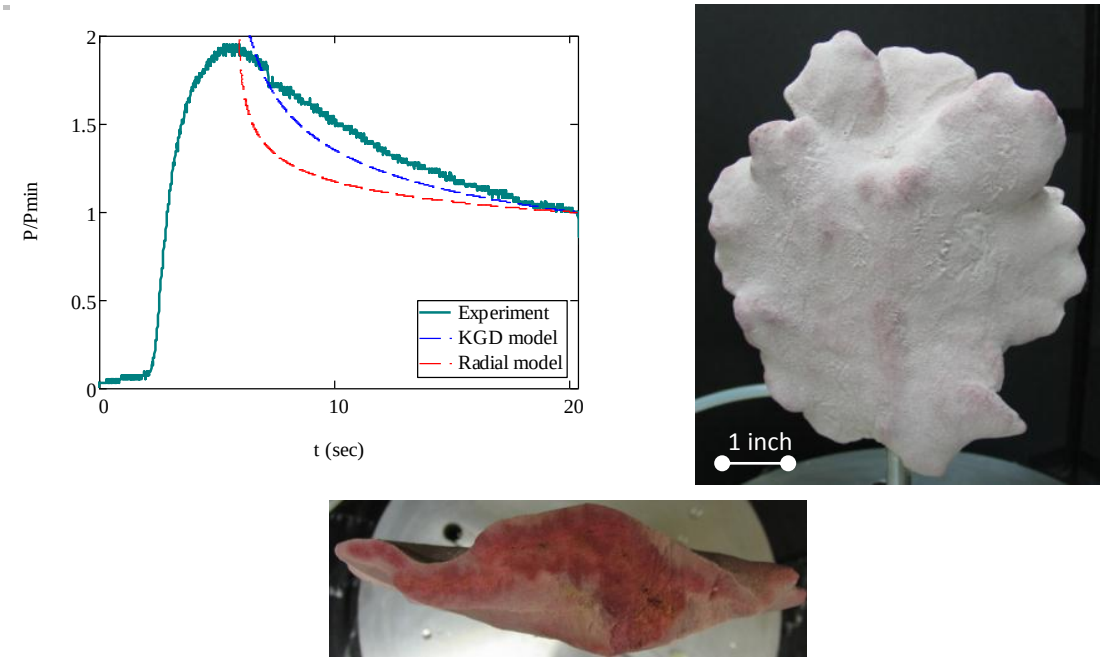

Figure 6.16. Experimental curve fitting, image, and cross-section for Test 08-10-10.

Table 6.3. Data from tests shown above including calculated effective fracture toughness.

TEST	KGD Fracture		Stress	Viscosity	Perm	Flow-rate	Injection Pressure		t_{max}
	Toughness	Energy	σ_3	K	k	Q	$Peak$	Min	
	MPa $m^{1/2}$	kJ/m^2	MPa	cP secn	mD	ml/min	MPa	MPa	s
05-12-11	0.22	0.24	0.06	7.E+05	350	50	0.869	0.6	154
03-30-11	0.24	0.30	0.06	7.E+05	1000	50	1.331	0.69	253
03-10-11	0.41	0.84	0.06	1.E+06	1000	50	1.514	0.44	698
06-17-05	1.15	6.73	0.14	7.E+05	1000	50	5.199	3.15	330
02-10-11	0.90	4.10	0.55	7.E+05	1000	50	4.05	2.89	767
01-31-11	1.12	6.34	0.55	7.E+05	350	5000	5.677	3.13	5
05-10-11	1.00	5.06	0.55	7.E+05	350	500	6.086	3	25
10-14-10	0.63	2.01	0.55	7.E+04	350	500	2.827	1.68	20
08-10-10	0.50	1.26	0.55	7.E+04	1000	1500	2.852	1.27	20
08-03-10	0.69	2.42	0.55	7.E+04	1000	15000	3.007	1.66	2
11-17-08	1.17	6.89	0.55	7.E+05	350	1700	8.167	3.61	24
08-14-08	1.28	8.32	0.55	7.E+05	25	1700	5.612	3.97	22
05-04-11	2.40	29.12	5.52	7.E+04	350	500	20.9	6.55	289

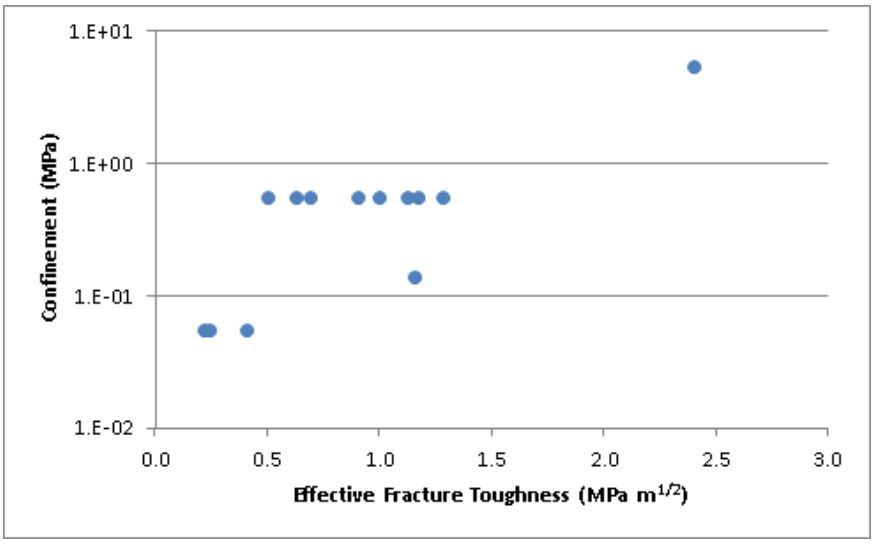

Figure 6.17. Confinement versus effective fracture toughness (KGD).

6.5. Comparison to a Field Experiment

Our laboratory experiments are constrained to a relatively small sample size. In the laboratory, we can achieve a fairly broad range of boundary conditions. Laboratory experiments, however, are constrained by sample size. Alternatively, shallow field scale experiments are useful in producing a relatively large-scale fracture, yet still allowing for direct observation of the produced fracture, albeit at low stresses. Hydraulic fractures created at shallow depths have useful environmental applications and for this reason their form has been investigated in some detail [*Murdoch*, 1995a; *Murdoch*, 2002; *Murdoch et al.*, 2006a; *Wong and Alfaro*, 2001].

Here we utilize a slightly modified form of the model developed above, taking into account the free surface. The model is able to match the observed pressure-time dependence and measured uplift-time response during the fracturing event of a shallow

hydraulic fracture. The fracture shown below in **Figure 6.18** (c) is one such fracture published by *Murdoch and Slack* [2002]. This particular fracture was created in a fine-grained formation at a depth of $1.5\ \mathrm{m}$. The fracture was initiated by injecting water at a rate of 20 to $40\ \mathrm{L/min}$. Subsequently, a slurry of cross-linked guar gel and sand was injected as the fracture propagated away from the borehole. After the fracture event the guar carrying fluid was formulated to leakoff into the soil mass completely leaving the sand in place to prop open the fracture. The maximum lateral extent of the fracture was of the order of 5 to $8\ \mathrm{m}$. The vertical displacements in the proximity of the borehole and injection pressures were monitored during the injection event **Figure 6.18** (c) and (d). The soil mass was then mined back and the fracture was mapped.

The model was matched to the pressure-time history in a similar fashion to our experiments above, with a single fitting parameter. In addition, we also matched the uplift displacement history by utilizing an additional parameter, the soil mass stiffness (E). The data is plotted in **Figure 6.18** (c) and (d). The model is theoretically identical to the uplift-time and the pressure-time histories. The resulting effective toughness is 0.11 $\mathrm{MPa\ m^{1/2}}$ while the soil stiffness used for the displacement data fitting was $65.4\ \mathrm{kJ/m^2}$.

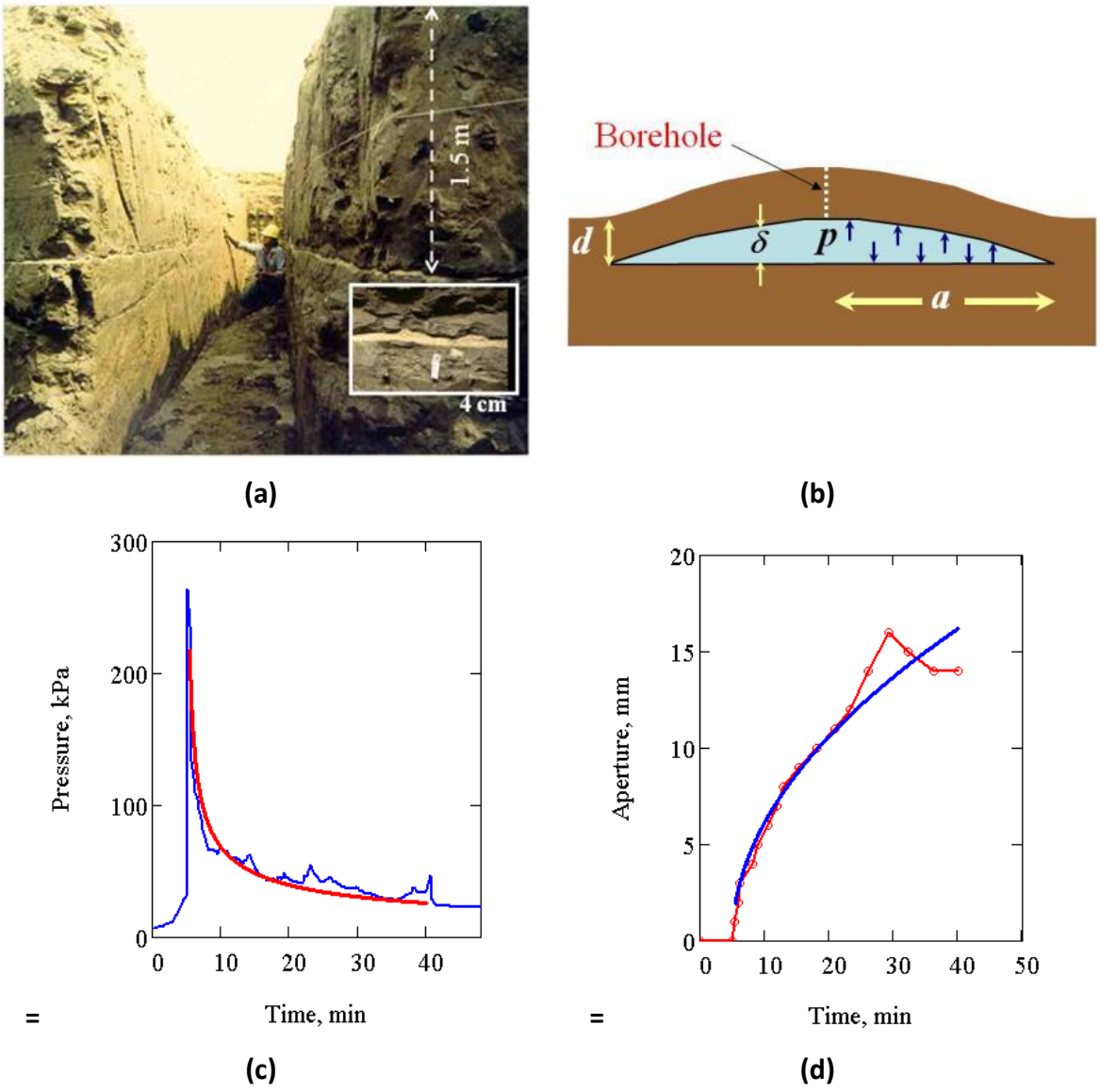

Figure 6.18. Experimental Data from a Field Test Presented by Murdoch and Slack [2002] (a) the mined backed fracture showing the sand proppant (b) schematic of the experimental results (c) the pressure time record (blue) and model (red) (d) displacement-time record (red) and model fitting (blue).

6.6. Conclusions

The model of the experimental data presented above highlight the general trends of the generated results. In general most of the experiments are best modeled through the KGD fracture geometry. The reason could be that the plane strain model better represents the stepwise growth of the fracture. In general, we do not expect a uniform progression of a radial boundary. Our fractures tend to grow in stages or steps.

The model reinforces the dimensional analysis that we developed in Chapter 4. The effective fracture toughness increases with increasing confinement. This is a direct result of the estimation of fracture toughness by equation (6.22). We utilize the minimum pressure and fracture length to calculate the effective fracture toughness. The values of effective fracture toughness we calculated from the modeling of our experimental results (0.02 MPa $\mathrm{m}^{1/2}$ to 2.0 MPa $\mathrm{m}^{1/2}$) are the same order of magnitude as those in the literature for hydraulic fracturing of soils (0.01 MPa $\mathrm{m}^{1/2}$ to 1.0 MPa $\mathrm{m}^{1/2}$) [*Chang*, 2004; *Harison et al.*, 1994; *Murdoch*, 1993c; *Wang et al.*, 2007].

A notable trend from the fitting is the decrease in fitting quality with increasing permeability. We contend that the modeling of the leakoff process through a 1D diffusion process does not capture the complexities of the process. In fact, our experimental observations suggest that the leakoff primarily occurs at the tip of the fracture in a stepwise, point source, 3D process. This trend may be expected if the experimental observations correctly characterize the dominance of the fracture tip in the leakoff process. To mitigate issues with the classical one dimensional Carter's leakoff

formulation, we calculate the leakoff coefficient directly from observations of the leakoff thickness. We would expect that this ad hoc estimation of the leakoff coefficient would lead to increasingly greater inaccuracies with larger volumes of leakoff.

This model was utilized successfully in predicting the pressure-time dependence for our extensive laboratory data set. It also accurately predicted the experimental results of a high-stress true triaxial test conducted at a separate facility (Chapter 7). Further, it accurately matched pressure-time and displacement time histories available from shallow field scale tests described in the literature with only two fitting parameters. These results indicate that the fractures we modeled in unconsolidated particulate materials are indeed toughness-dominated fractures.

We contend that there exists many assumptions and other factors are not included here. However, the main result of this modeling is that our fluid-driven fractures can be considered thick. This is important, in that a majority of the energy dissipation mechanisms are confined to the tip region and, by extension, to the processes of crack tip growth. In addition, if the toughness-dominated regime is applicable to unconsolidated materials at field scales it would be in stark contrast to models typically used in the oil and gas industry. The models used for characterizing stimulation of petroleum reservoirs primarily viscosity dominated.

7. FLUID-DRIVEN FRACTURES WITH INDUSTRIAL FLUIDS

7.1. Introduction

The work detailed in this chapter focuses on the use of an industrial fluid to induce hydraulic fractures in unconsolidated materials. The silicone injected experiments presented in Chapters 6 and 7 are instrumental to this work, due to the ability to characterize the fracture aperture. It may be, however, that its particular rheological characteristic is significantly different than industrial fluids typically utilized to hydraulic fracture unconsolidated formations. Therefore, we present an independent series of experiments that utilize a fluid similar to those in industrial applications. It will be shown that the results presented in this chapter are consistent to those in Chapters 4 and 5. This suggests that even though we do not have the capability to measure fracture aperture directly, the generated fractures presented here are also within the toughness-dominated regime.

In essence, the results of our experimental work with silicone fracturing fluids are reinforced and enhanced. Further, this series culminated in a large-scale test being conducted at TerraTek, (a Schlumberger Company) a testing company specializing in large-scale geomechanics tests (especially hydraulic fracturing). The primary driver for this work was to develop the prediction of an unconsolidated fracture test conducted in a true triaxial cell at high stresses. The fluid selected is a cross-linked guar polymer with a proprietary resin system that allows for consolidation, or solidification, of the leakoff zone. The resin system acts to bond the particulate material and it will not solidify

independent as it only dehydrates. Therefore, the fracture aperture is not preserved; though there is evidence of fracture traces in the cross-section (**Figure 7.4**).

The equipment utilized, sample materials and procedures for the experiments are described in detail in Chapter 3. The large-scale high-stress test is described in detail in this chapter. The outline of this chapter is as follows.

- The experimental results from the tests completed in our large triaxial cell (LTC) and high-pressure triaxial cell (HPTC) are presented.
- The prediction and the model from Chapter 6 are explained.
- The test procedures and equipment utilized in the TerraTek (a Schlumberger Company) large-scale true triaxial cell (TTC) test are described.
- The results of the (TTC) tests are illustrated.
- Conclusions

7.2. Preliminary Results

The results of several tests are presented in this section. The description of the equipment, materials and procedures are available in Chapter 3. Fractures generated by guar fluids, in similar experimental conditions to the silicone tests, exhibited different fracture morphologies. However, the parameter effects remain theoretically identical. This section is focused on the work completed in the LTC and HPTC. The LTC results are presented first, followed by the HPTC.

7.2.1. Dimensional analysis and pressure-time curve characteristic.

The results of the dimensional analysis presented in Chapter 4 remains valid for the guar fluid tests. The data used to generate **Figure 4.4** contains peak pressure data from tests injected with guar. For completeness, we present the guar data independently in **Figure 7.1**. The data follows the same trend as the silicone tests. This reinforces the conclusions from Chapters 4 and 5; confining stresses play an important role in contributing to the magnitude of the peak pressures. The complete data set including guar and silicone injected tests is presented in Figure 7.2. The power law fitting is consistent with that presented for the silicone tests in Chapter 4.

The characteristic pressure curve for guar injected tests remained similar to that of the silicone tests. **Figure 7.3** illustrates that a pressure curve can be matched between samples fractured by silicone and guar, when normalized. Due to the significant differences in rheology, the peak pressures are significantly different, however. Three different pumps at different flow rates were utilized. Two of the samples were F110 and one was the silica flour mixture. Further, three different fluids were injected. Yet the normalized pressure curves are effectively the same.

7.2.2. Fracture morphologies

The fracture morphologies were significantly different between the silicone and guar gel tests, when experiments were conducted under similar conditions. The guar tests focused on the low permeability fine sand and silica flour mixture. This was chosen due to the limited leakoff at high confinements. Pure F110 samples did not produce

much evidence of fracture propagation at high confinements (> 80 psi), unless injection rates were higher than 5000 ml/min. Therefore, we only used F110 in the LTC to compare differences in permeability. There was a significant difference in the fine sand samples, and fine sand and silica flour mixtures. The results from the fine sand experiments are presented first followed by the samples of the mixture.

Only low injection rates at high confinements of 800 psi produced the characteristic bubbly surfaces similar to that of the silicone injection tests (**Figure 7.8** (b) and (c). The fine sand experiment shown in **Figure 7.5** illustrates the typical morphology of fractures in fine sand. There is clear evidence of a separation of the fracturing fluid. This appears to be a consequence of the development of an internal and external filter cake. That is, the polymer chains of the guar fluid are separated from the solvent. Within the leakoff zone, there are two distinct zones. Technically, in rock materials the external filter cake is considered outside the host material and inside the fracture. In this example, both layers are within the sample material. However, due to the closure of the fracture after the injection event it is possible that any external filter cake leaked off into the formation. The pressure curves for two separate experiments are shown in **Figure 7.4**. The curve shows similar characteristics of the curves from experiments injecting with silicone. By increasing the injection rate, we can greatly reduce the leakoff, yet the (adjusted) peak pressures remain essentially the same. The guar driven fractures generated in fine sand required high injection rates to control leakoff (+1500

$\mathrm{ml/min}$). These injection rates could not be utilized in our HPTC, due to the limited sample size.

The injection tests conducted in the fine sand/ silica flour samples exhibited a significant decrease in leakoff. The two-phase leakoff zone, mentioned above, is not apparent. Further, the injection rate could be much lower ($50\ \mathrm{ml/min}$) and still create low levels of leakoff. The consolidated leakoff zone was quite strong and brittle compared to the fine sand tests. Such a dramatic shift in the leakoff zone characteristics was not observed in our silicone injection tests.

The peak pressures are similar for all the tests conducted at $80\ \mathrm{psi}$ confinement. The average peak pressure for samples of fine sand was $\sim 450\ \mathrm{psi}$. For samples in fine sand silica flour mixtures the average was 420 psi. That is less than 10% decrease in peak pressure with an order of magnitude decrease in flow rate and permeability.

The post peak response of the pressure curve does show a somewhat different response; it is not as smooth. A number of other tests were completed at various rates and stress conditions. The trends of fracture evolution with the chosen parameters remain the same as those presented in Chapter 4. Experiments with low confinements showed very thin fractures, which were not stable during excavation. For example, the injected volume prior to reaching the boundary in the fractures featured in **Figure 7.6** was ~175 ml. In low stress experiments, the injection volume was ~80 ml. The reduction in the thickness of the leakoff zone created fractures that were not competent enough for excavation.

We assume that fracture aperture also remains correlated with confining stresses. However, we cannot verify this assumption by direct experimental observations. In the next section, we describe the HPTC experiments and the correlation of the results to the LTC results presented here.

7.2.3. HPTC results

The HPTC was used to increase the magnitude of confinements in our injection tests (Chapter 3). Confinements of up to 5000 psi were tested in the HPTC though injection tests were limited to confinements of 800 psi due to the limited sample size and the necessity to control leakoff. The leakoff must be limited and the primary ways of affecting leakoff in our tests are flow rate and permeability (fluid rheology and stresses are fixed). Flow rates of 500 ml/min were considered the highest possible rates, given the small size of the HPTC, our experimental time were typically 6 s before the injection fluid reached the sample boundaries. We could not easily decrease permeability of the sample any further without possibly significantly changing the deformation characteristics of the sample and complicating the saturation capabilities. Finally, we only needed to increase stresses in the HPTC an order of magnitude greater than the LTC for the scaling analysis.

The initial tests of the HPTC were to determine the scale effect on peak pressures and fracture morphologies. Our experience with the STC and silicone tests suggests that the limited geometry of the sample would decrease the peak pressures by $\sim 20\%$. The results of a scale test, compared to a LTC result, are presented in **Figure 7.7**

below. The peak pressure is 350 psi while the large scale tests average ~ 410 psi, a relative change of 84%. One important aspect of the scale tests is that the injection system is entirely the same configuration for both cells. The injection source is the same configuration as that utilized in the LTC and described in detail in Chapter 3.

The stresses were increased and multiple samples were injected to determine peak pressures (**Figure 7.8**). Only the peak pressures are considered in these tests. We determined that sample size effect the results in injection pressures in our HPTC; therefore the characteristic of the post peak response in the pressure time histories is not analyzed.

In **Figure 7.8** the experiments were completed at injection rates of 500 ml/min (a) and 50 ml/min (b) and (c). The peak pressures the experiments pictured in **Figure 7.8** were (a) 2650 psi (b) 2527 psi and (c) 2489 psi. The experiments show the same trend as those presented in Chapter 4 and Chapter 5 and the section above. The leakoff is increased when the injection rate is decreased yet peak pressures remain effectively the same.

7.2.4. Summary of the guar gel tests

In summary, the guar tests followed the same trends, with parameter manipulation, as the silicone tests presented in Chapters 4 and 5. The general trends are shown graphically in **Figure 7.9**. When compared to the silicone injection tests, there were not as many tests, and there was significantly less leeway in the parameter selection in the guar injected tests. Nevertheless, the dimensional analysis remains

valid, and the experimental observations on parameter affects are similar. There was a dramatic shift in the leakoff characteristic when permeability was reduced from 1000 mD to 350 mD For the high permeability samples we observed two distinct layers in the leakoff. The low permeability sample exhibited a uniform leakoff layer that was consistent, for the scale of our observations. With STC tests we consistently observed initiation pressures that were $\sim 20\%$ less than experiments under the same conditions in the LTC. In the next section we utilize the results generated in the experimental series presented here to design a large-scale high-pressure injection test.

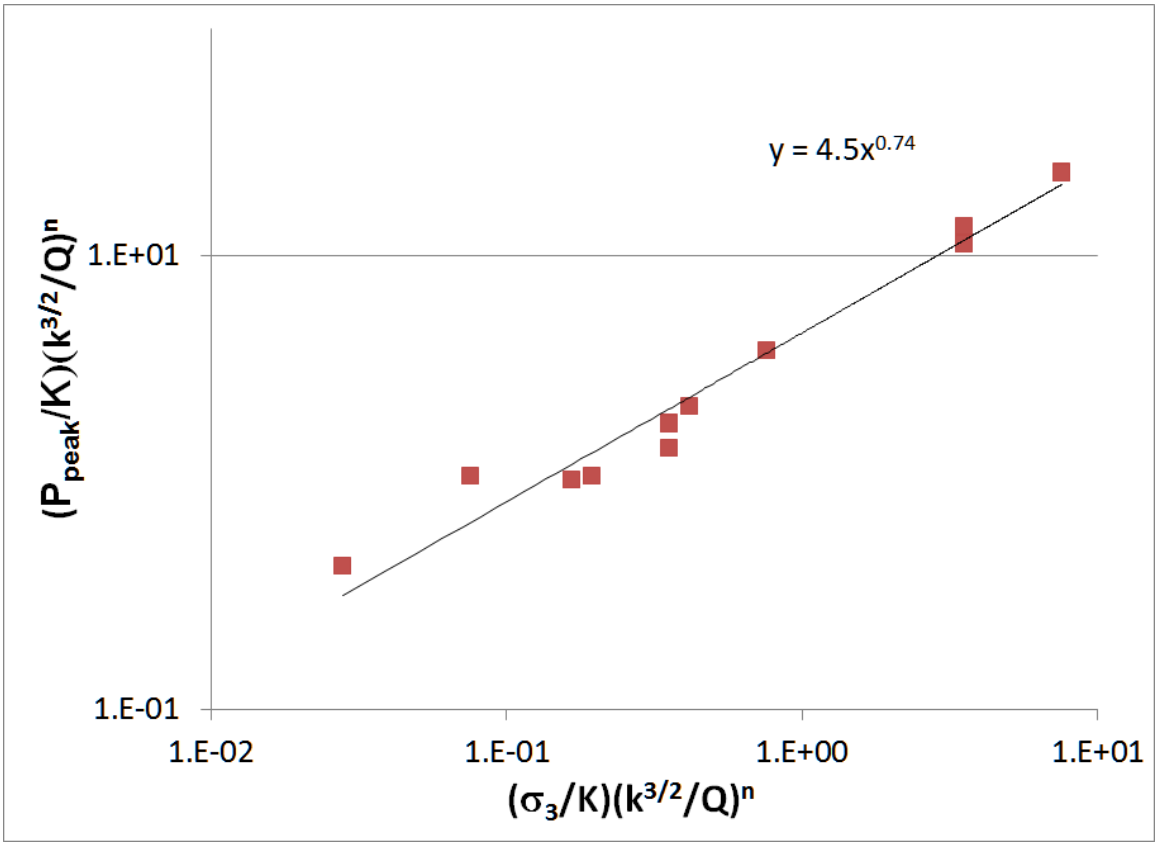

Figure 7.1. Dimensionless peak injection pressure versus dimensionless stress (guar injected tests only).

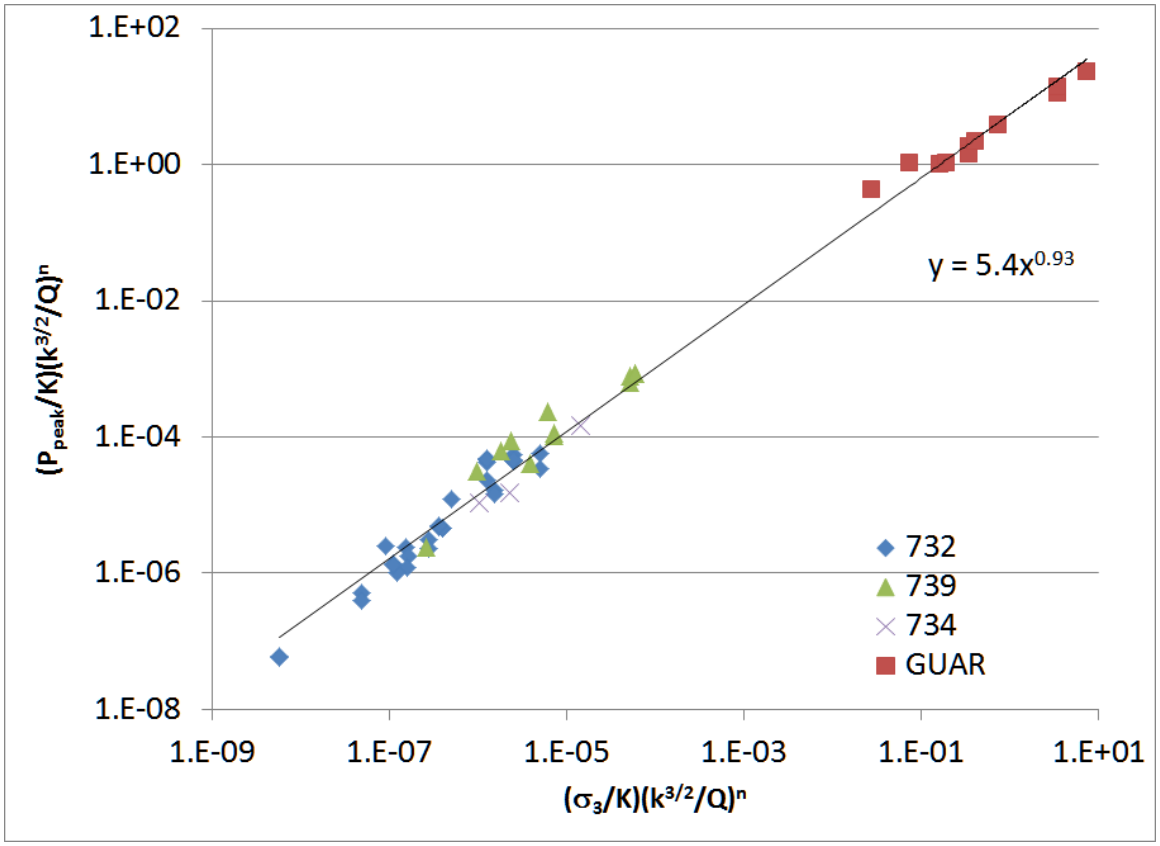

Figure 7.2. Dimensionless peak injection pressure versus dimensionless stress with Guar fluid tests and silicone adhesives.

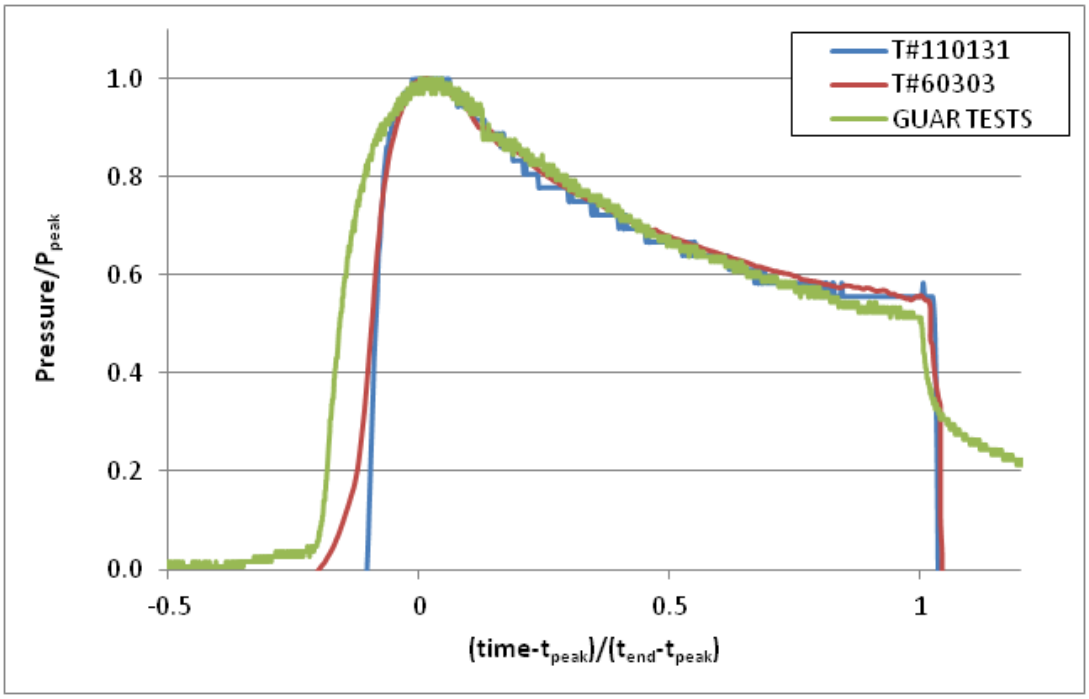

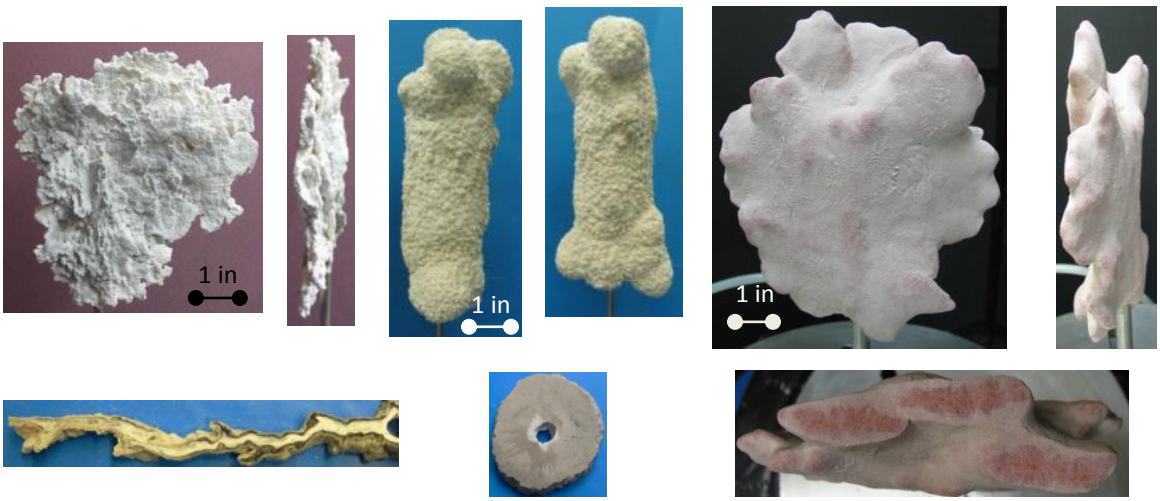

Test	01-31-2011	03-03-2006	08-10-2010
Sample	F110 mixture	F110	F110
Fluid	Med Visco. Silicone	Low Visco. Silicone	Guar Gel
Flow-rate	500 ml/min	50 ml/min	1500 ml/min
Conf.	80 psi	80psi	80 psi

Figure 7.3 Normalized pressure curves identical for different morphologies. Tests data are listed. Notice signifcantly different parameters with similar normalized pressure curves.

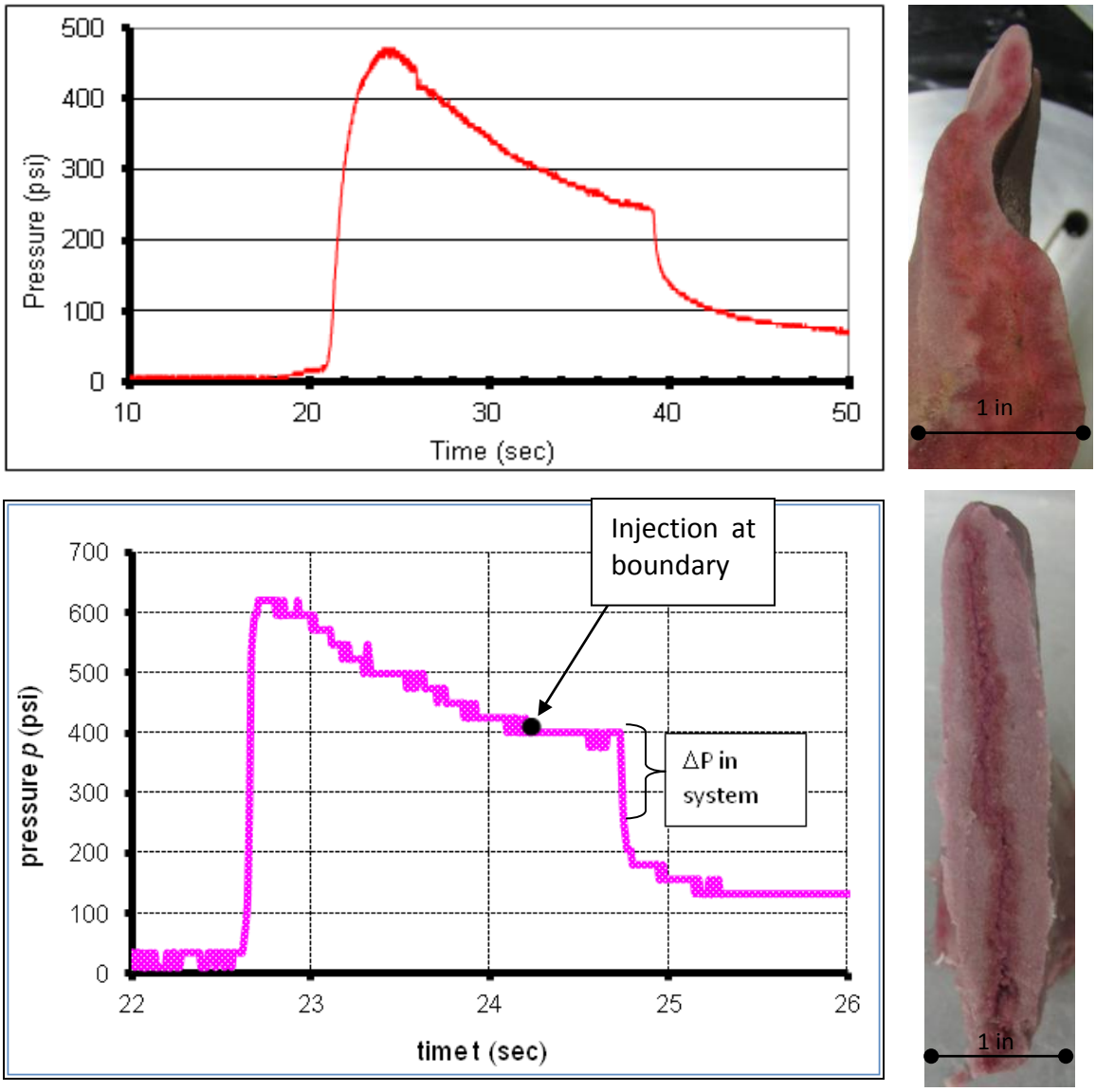

Figure 7.4. Unadjusted pressure cures and cross sections for experiments shown below in **Figure 7.5**. Injection tests in fine sand sample at 80 psi confinement injected with guar fluid at 1500 ml/min and 15000 ml/min. Steps in pressure curve are due to precision of pressure gauge, we consider these two curves to have the same characteristic shape. Adjusted peak pressures are ~450 psi for both experiments.

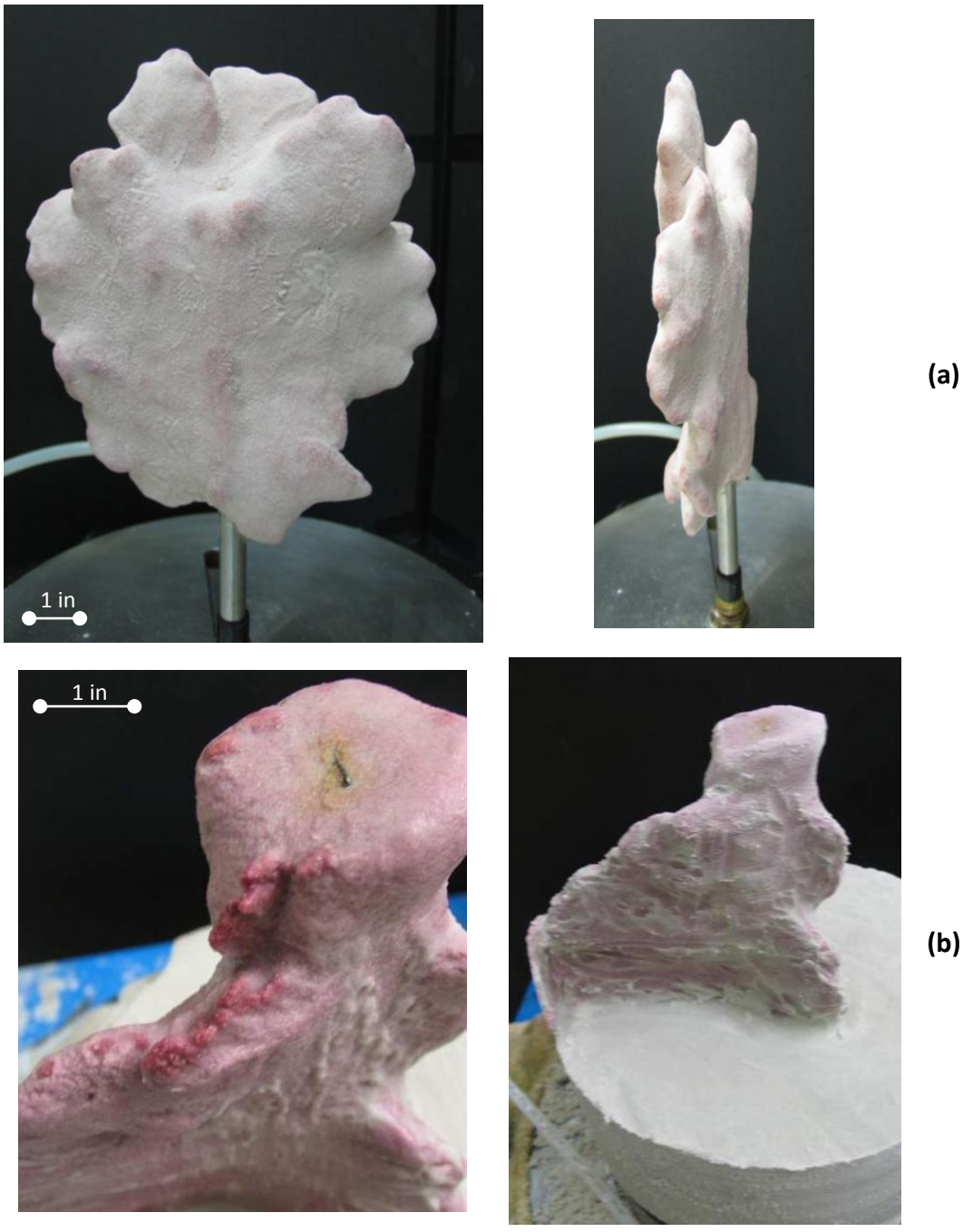

Figure 7.5. Injection test in a fine sand sample injected with guar fluid at 1500 ml/min (a) and 15000 ml/min (b). Notice that leakoff is mitigated by greater injection rates.

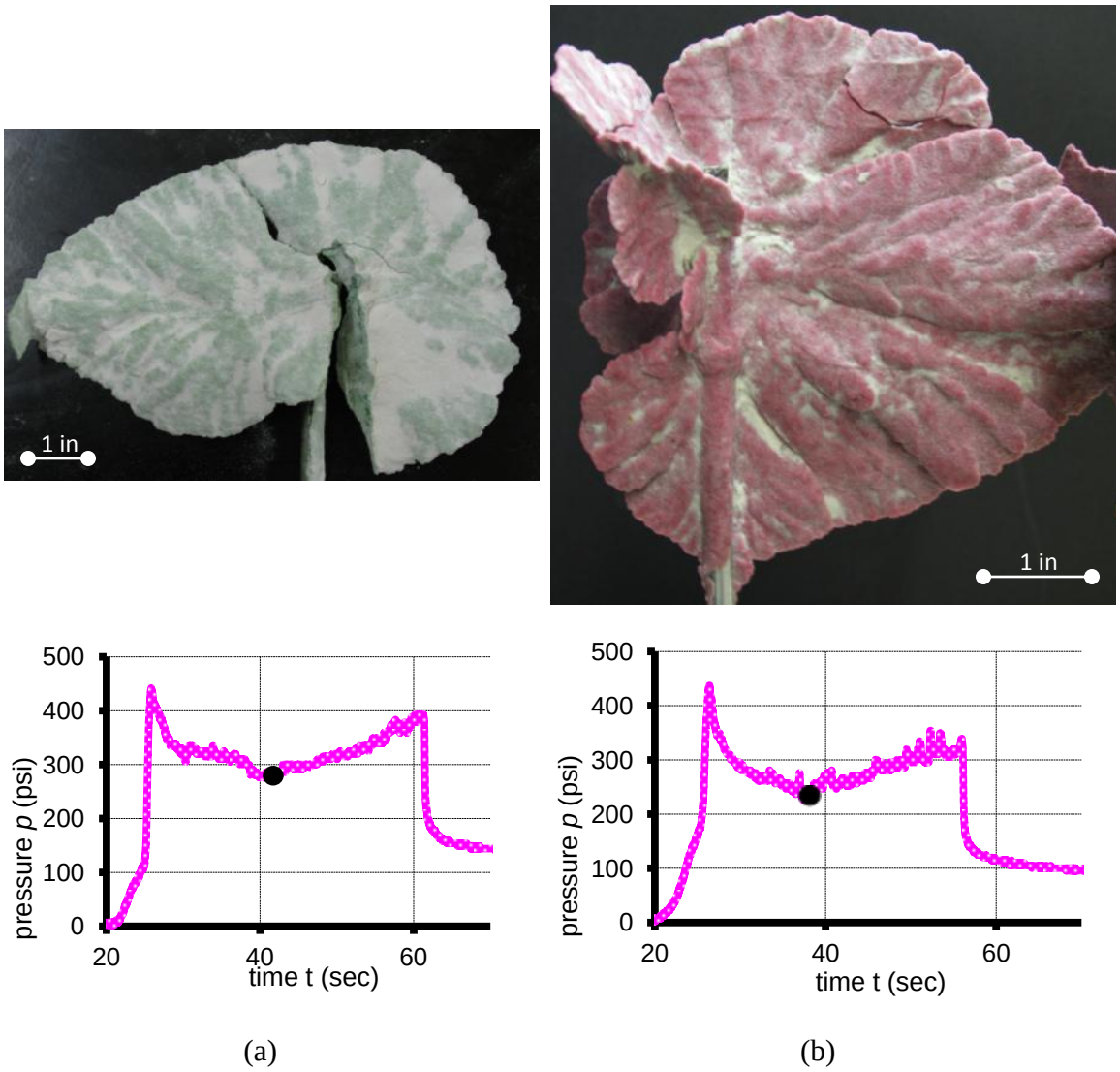

Figure 7.6. Fractures generated in samples of fine sand/silica flour at 80 psi confinement injected at a rate of 500 ml/min. Fractures are planar and quite thin. Both fractures reached the boundary at the low point in the center of the pressure versus time plot (dots on pressure curves represent when). Adjusted peak pressures are approximately 410 psi for both experiments.

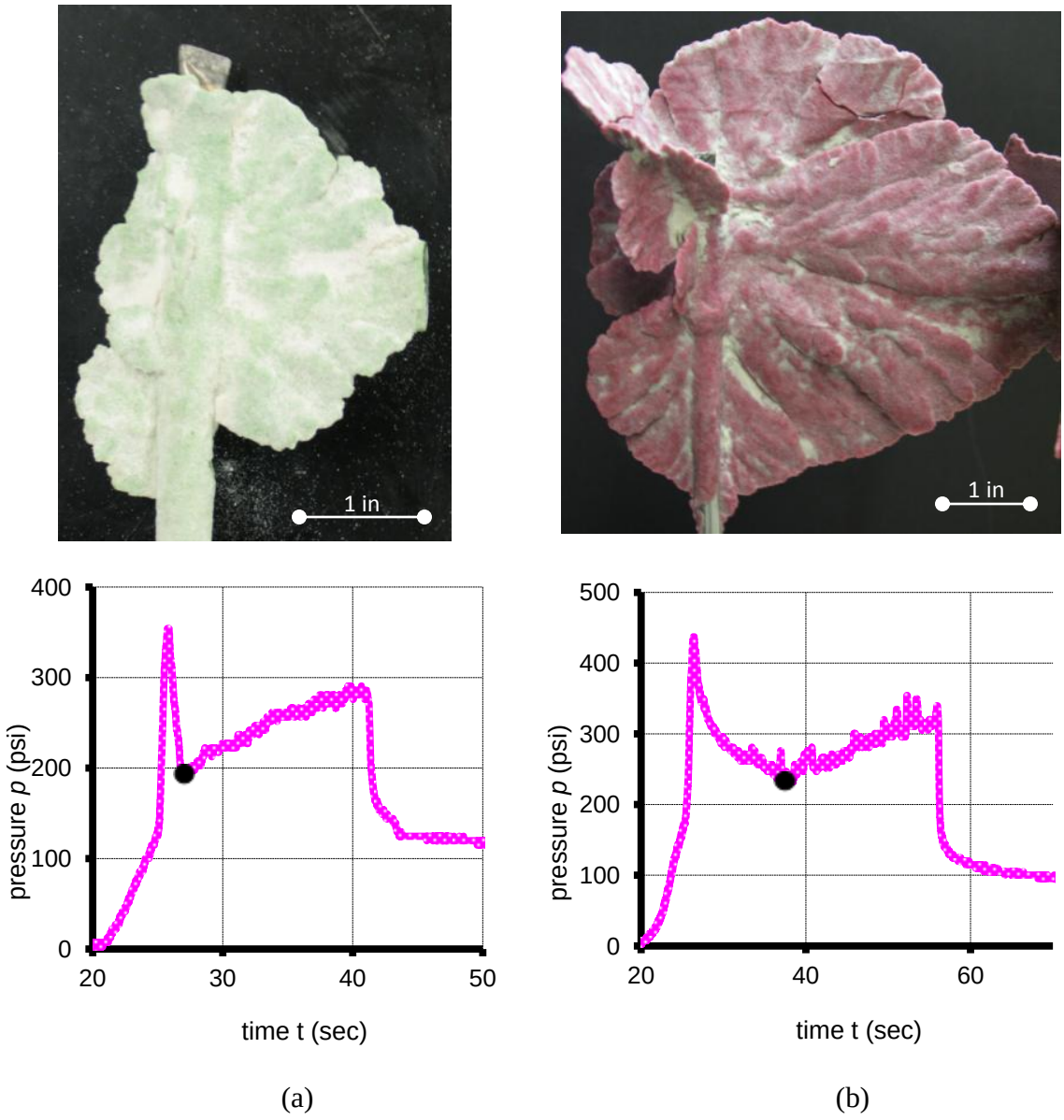

Figure 7.7. The comparison of fracture tests completed in the HPTC and LTC. Samples were fine sand silica flour mixture at 80 psi confinement injected at 500 ml/min. The HPTC peak pressure is approximately 80% lower.

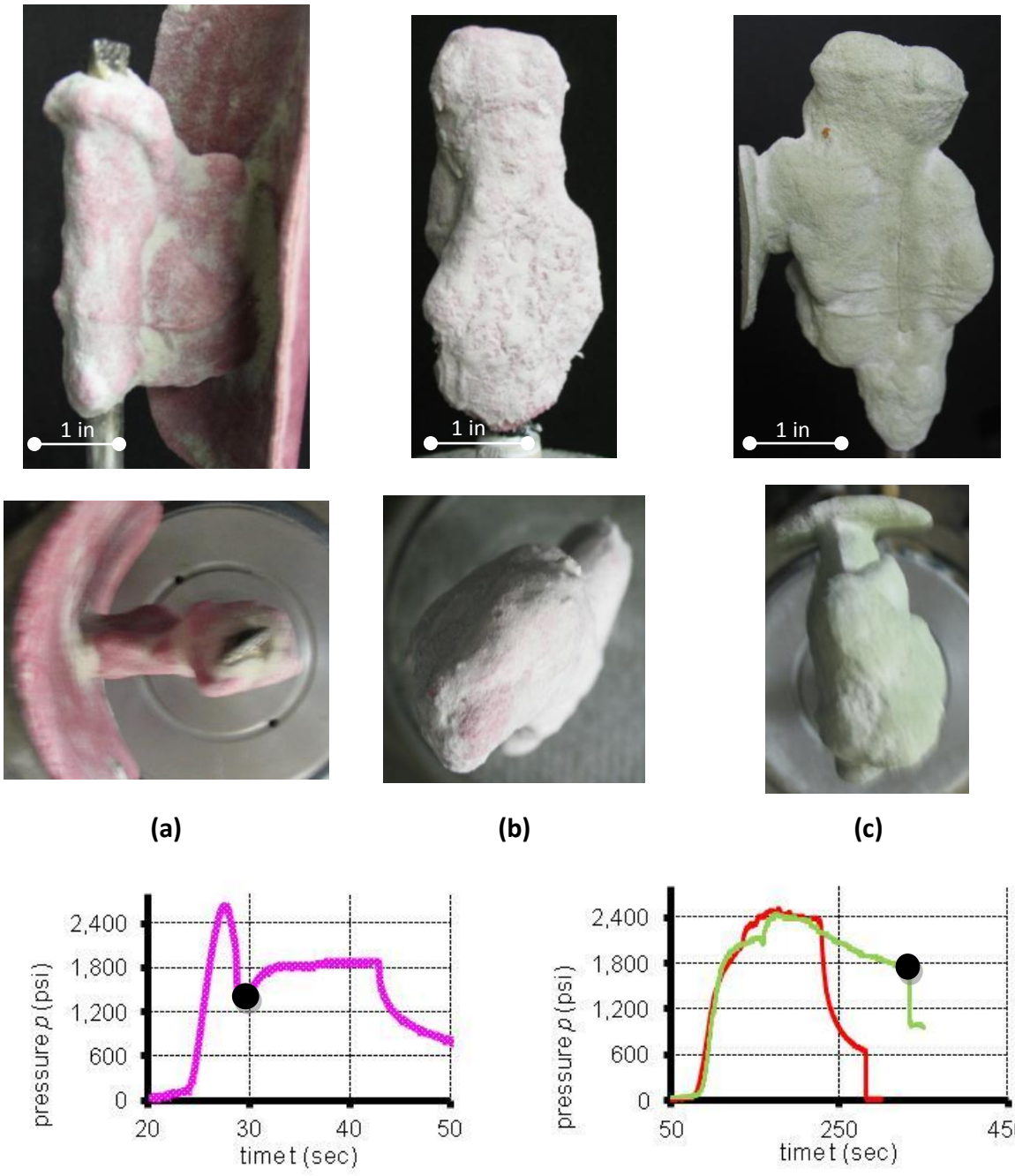

Figure 7.8. Three examples of the HPTC experiments. Samples were fine sand with silica flour at 800 psi confinement, injected at rates of 500 ml/min (a) and 50 ml/min (b) and (c). (a) and (c) contacted the boundary (dots on pressure curves represent when).

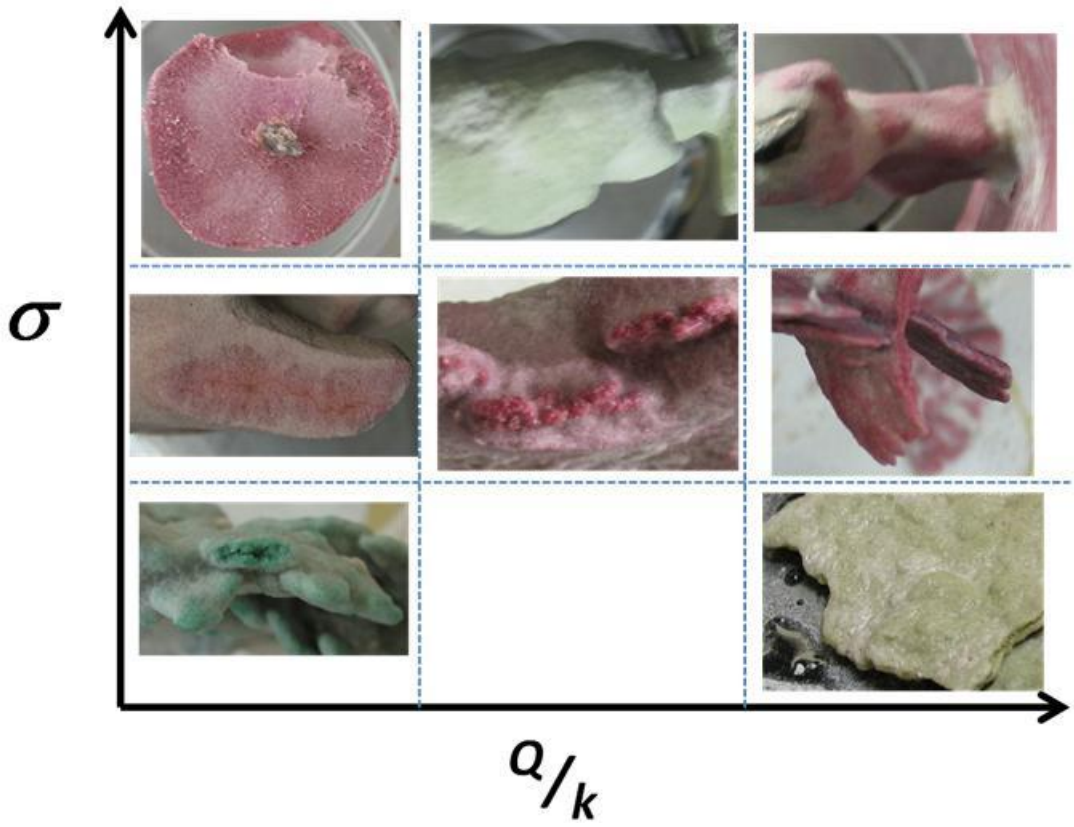

Figure 7.9. The Experimental Observations of the Guar Tests, similar to **Figure 5.17.** Leakoff increases as the stress increases. Leakoff decreases as flow rate increases or permeability decreases.

7.3. Development of High-Stress Injection Test

The average peak pressure for our high-pressure tests, regardless of injection rate was ~ 2600 psi. This coupled with the expected increase in pressure with a larger sample gave an expected peak pressure for the TerraTek test of ~ 3000 psi if the same experimental parameters are utilized.

The toughness-dominated model of hydraulic fracturing, presented in Chapter 6, provides an expected pressure time response after the initiation pressure. Typically, we use the minimum injection pressure as the model input parameter. In this instance, we only estimated the expected initiation pressure. All other model parameters are those developed in Chapter 6. **Figure 7.10** is the expected pressure-time history for the TTC test.

We estimated the experimental time assuming radial and KGD geometry. Together with the expected leakoff thickness generated in the HPTC test, we calculated an experiment time of ~ 60 s at an injection rate of 500 ml/min. We considered a model of cavity expansion in a Mohr-Coulomb to calculate the peak time [*Yu*, 2000]. The peak time was estimated at ~ 0.5 s. This assumes the fracture initiates at peak time, with an injection pressure of 3000 psi. The model indicates an injection pressure of 1300 psi at the end of the test.

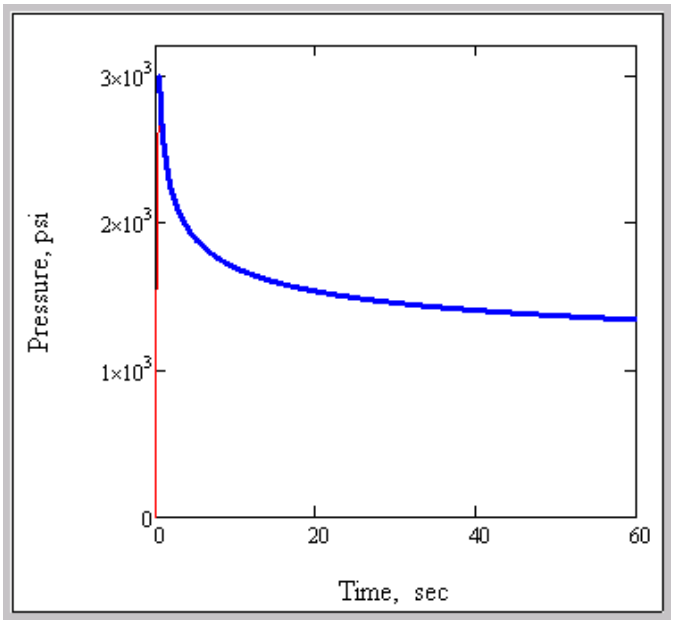

Figure 7.10. Pressure-time history from the toughness-dominated model. This is the estimated pressure-time history for the large scale high pressure test.

7.4. Experimental Results

This represents an attempt to conduct a hydraulic fracturing experiment in unconsolidated materials, at these scales. The parameters were chosen for the large-scale test utilizing the results presented here and in Chapter 4, coupled with the toughness-dominated unconsolidated fracture model presented above. The selected test conditions were as follows.

- The sample dimensions were 11.5 in by 11.5 in by 24.5 in
- Sample would consist of fine sand and silica flour mixture with a permeability of 350 mD
- The stress conditions σ_1=1600 psi, σ_2=1200 psi, σ_3=800 psi
- The fluid would be the guar based resin system
- The flow rate would be 500 ml/min

The test conditions were implemented to mimic the conditions of our tests conducted in the LTC and HPTC. However, any minor differences were a consequence of the different cell designs. The ability to provide true tri-axial conditions is an important aspect of this cell design. Our results indicate that unconsolidated fractures tend to propagate perpendicular to the least principle stresses. The effect of the intermediate stress on fracture growth and development, however, is still not fully addressed [*Golovin et al.*, 2010; *Jasarevic et al.*, 2010]. In this section, we describe the preparation of the sample, the test operation, and the results.

7.4.1. Sample preparation and injection test

The sample is prepared in a rigid container that is constructed 18 gauge steel box. The top and bottom of the sample are sealed by two 1 in urethane sheets. A series of acoustic sensors were placed on the walls of the container to record both active and passive acoustic emissions (**Figure 7.11** (a) and (b)). The bore hole was in a similar configuration as the boreholes utilized in our tests. It was made longer to accommodate the larger sample. The borehole was placed in the center of the sample with temporary bracing to locate the borehole in the center of the sample. The bottom of the injection source was not affixed to the bottom urethane sheet; it remained in the center due to friction (**Figure 7.11** (b)).

The sand and silica flour material was oven dried and compacted in layers, similar to the procedure outlined in Chapter 3. Each layer was compacted with a solid rod with a diameter of 1 in. Nineteen layers were compacted; each layer weighed ~ 6 lbs. The measured sample density was 1.88 g/cm^3, the same maximum density achieved in preparation of our samples. Once the sample was complete a urethane sheet was placed on top of the sample and sealed in place with liquid urethane (**Figure 7.12** (a)). The urethane was allowed to set overnight, then the top platen was affixed and a temporary frame was installed to load the completed sample into the loading frame (**Figure 7.12**(b)).

The lateral sample boundaries are loaded by “flat jacks”. These are simply two pieces of stainless steel welded together (**Figure 7.12** (c)). The load is applied by

applying hydraulic pressure to the flat jack. The two horizontal axes are controlled independently; the two flat jacks on the same axis are controlled in parallel to ensure equal pressure on both sides of the sample. The top and bottom loads are applied by hydraulic rams directly to the end platens of the sample (this test only utilized the top ram). The top of the sample includes a spacer to provide access to the bore hole. The completed loading frame is shown in **Figure 7.12** (d).

Next, the sample was saturated. The saturation procedure was accomplished by pulling a vacuum on the sample for several hours. Then pore fluid (tap water) was flushed into the sample. The flow of the pore fluid was set at a low rate. The configuration of the cell does not allow for pore fluid flow from top to bottom of the sample. There is one inlet tube in the bottom of the sample (shown in the lower right-hand corner of **Figure 7.11** (a)). The borehole is used as the outlet.

The sample was loaded isotropically 100 psi. Then the boundary conditions were applied to maintain the load proportions up to the desired loading conditions (800 psi, 1200 psi, 1600 psi). The test was conducted under drained pore pressure conditions with no back pressure. The testing apparatus allows for complete control and monitoring of the load applied along with the volume of the flat jacks. There is precise control and monitoring of the fracture fluid injection system as well.

The injection event was initiated by a small initial flow rate until the bore hole was purged of pore fluid. Once prefill was complete the sample was fractured. Following the peak, the test was halted when there was evidence of fracture boundary

interaction. This manifested itself as a constant propagation pressure, similar to our tests in the LTC and HPTC. Once the injection event was completed, the sample remained under stress overnight while the fracture was allowed to consolidate. The excavation process is presented in **Figure 7.15**.

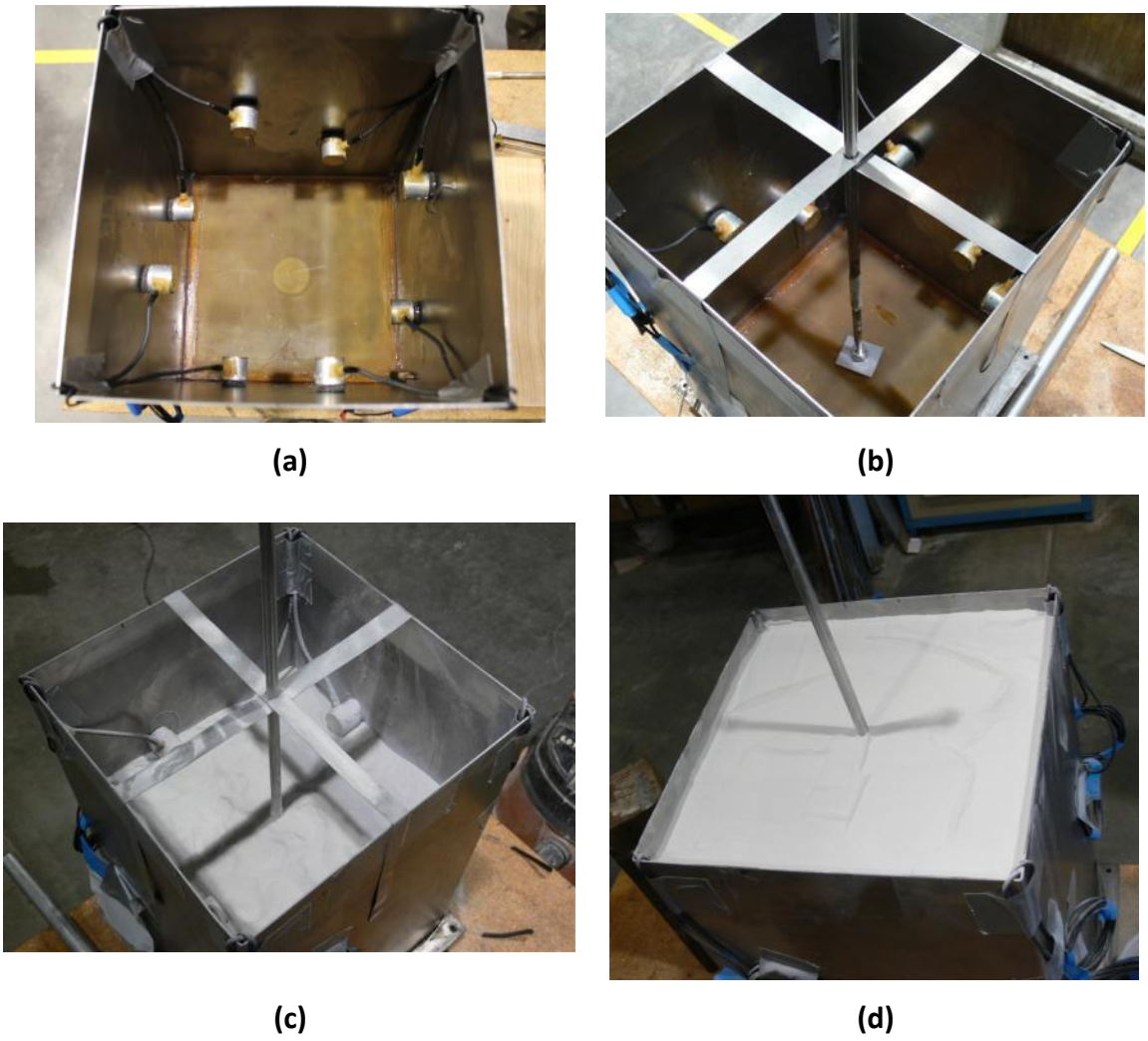

(a) **(b)**

(c) **(d)**

Figure 7.11. (a) Sample container with seismic sensors installed, (b) Sample container with borehole casing and temporary support (c) During sample compaction (d) After sample completion.

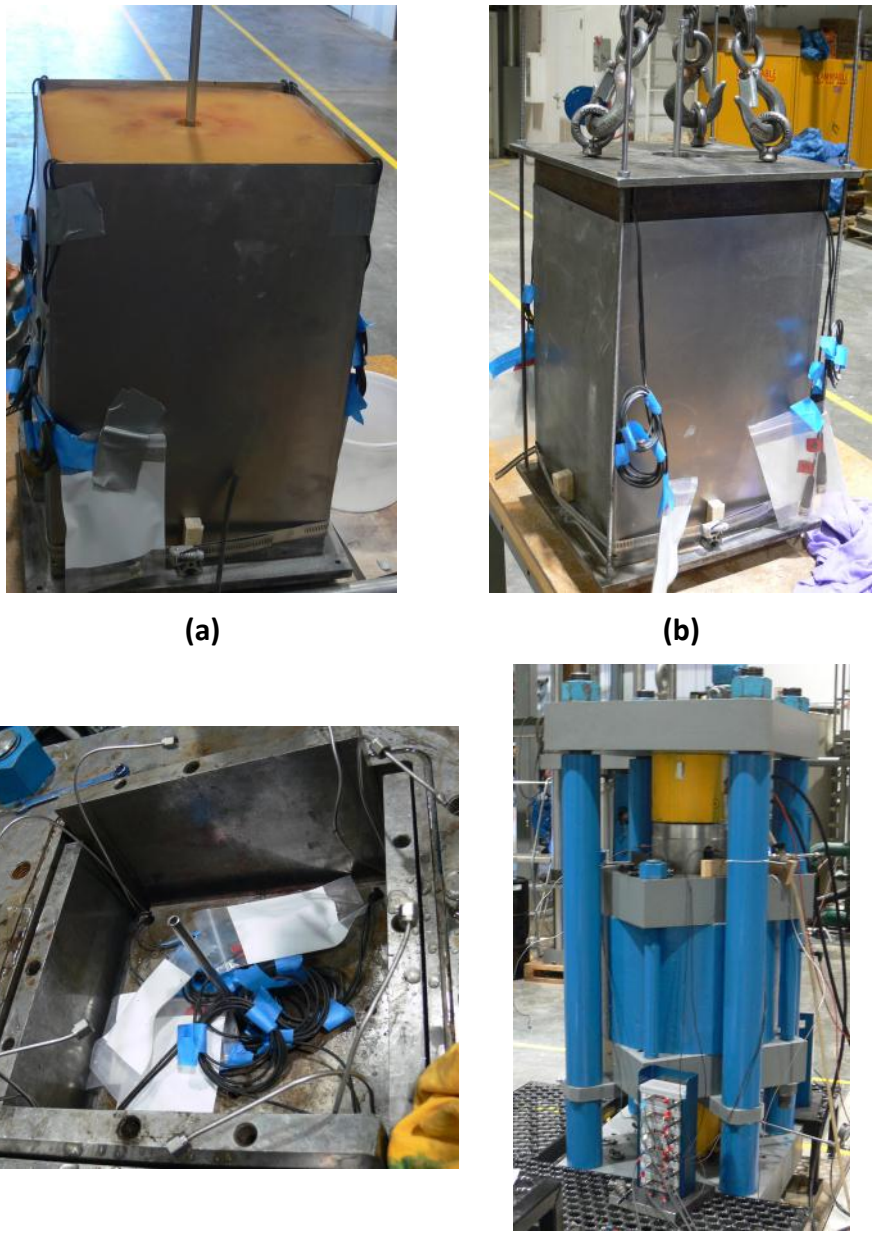

Figure 7.12. (a) Sample after urethane plate installed, (b) Completely assembled sample, ready for loading frame (c) Sample loaded in frame, flatjacks installed (looking down from top of frame, borehole in center, the $1/8in$ stainless tubing is the feed for the flat jacks)(d) Assembled loading frame with, multi channel acoustic reciever in forground.

7.4.2. TTC test results

The results of the data collection during the test are presented in **Figure 7.13** and **Figure 7.14**. The peak injection pressure was $3022\ \mathrm{psi}$. There was a significant drop in fluid pressure after the peak, indicating a fracturing event. The flat jack in the minimum principle stress direction shows some displacement prior to the peak pressure, qualitatively this indicates that there was a non-spherical form propagating prior to the peak pressure. This flat jack response is. In contrast, there was no measured volume displacement in the intermediate or maximum principle stress directions prior to the peak. Post peak flat jack response indicates a fracture perpendicular to the minimum principle stress. There is measurable expansion in the flat jack applying the intermediate stress. After shut-in there is a reaction of the flat jack in the minimum principle stress direction signifying fracture closure. These flat jack responses provide only a qualitative representation of global sample response.

The sample was excavated after $20\ \mathrm{hrs}$, then the sample was photographed and X-ray Computed Tomography (CT) scanned. A 3D scan of the resulting fracture shape is shown in **Figure 7.16**. The main features that can be observed are shown in **Figure 7.17**. For the sake of discussion, these features are classified as; (1) thick bubbly feature (2) radial fracture (3) multi-segmented fracture. These features are discussed more in detail separately below.

7.4.2.1. Thick Bubbly Fracture

The thick bubbly portion of the created fracture is most like the fractures generated in the HPTC under high confinements (**Figure 7.19**). This appears to be analogous to the spheroidal features that are present in the silicone injection tests presented in Chapter 4. This feature is also the most connected to the injection source. We assume that this feature was created first.

There has been evidence of fracture development prior to the peak injection pressures in many of our tests conducted in the LTC with both silicone and guar injections. To look at the possibility of the bubbly initial feature as being formed prior to the peak pressure we compare the volume injected prior to the peak with that of a volume estimate of the feature. The injected volume prior to the peak pressure is ~ 200 ml (**Figure 7.13**). If we approximate the initial bubbly feature by an ellipsoidal shape, then its volume is estimated by

$$V = \frac{4}{3}\pi abc$$

a and b are the equatorial radii and c is the polar radius. Taking into account the initial porosity, the volume of fluid occupying the pore space of this feature is

$$V_{fracture\ fluid} = \frac{4}{3}\pi abc\phi$$

We estimate the values a, b, and c of the feature (**Figure 7.13**) as $a \sim 12$ cm, $b \sim 6$cm, $c \sim 2$cm. The original sample porosity from the measured density, ϕ=29^{o}. The estimate of the fracture fluid volume of the bubbly feature is $V_{fracture\ fluid} \sim 174$ ml.

This estimation reasonably matches the injected volume prior to peak pressures. Further, the porosity is likely to be greater due to sample disturbance during the initial cavity expansion process. Additionally, the sample volume response measured by the flat jack does indicate volume expansion in the minimum principle stress direction prior to peak (**Figure 7.14**) (actual volume of sample expansion is not known, this is a qualitative measure).

7.4.2.2. Radial Feature

The radial feature is detailed in **Figure 7.20**. The feature appears to be a single continuous fracture and the front appears to be radial. The fracture approached the sample boundary, yet arrested prior to reaching it. This can likely be attributed to the boundary conditions of the sample. The leakoff surface is significantly reduced when compared to the initial bubbly feature. The thickness of the feature is $\sim 25\%$ of the initial feature.

This transition of features may be similar to the transition observed in the silicone adhesive tests shown in Chapter 4. In both examples, there is a dramatic shift in fracture morphology at a particular instance in the injection sequence. We observe no indication of any transition of fracture morphologies in the recorded injection pressure

in the silicone injection tests. In this test, the results indicate a significant drop in injection pressure signifies the transition in morphologies.

The rate of change in the E.W. flat jack volume providing the least principle stresses is an additional observation (**Figure 7.14**). At the same time, as the break down in the pressure curve is recorded, there is a high rate of change in the E.W. flat jack. The rate of change during the rest of the propagation regime is more or less constant at a lower rate. This may indicate the largest fracture feature is responsible for the recorded flat jack response. The radial feature does appear to be the largest singular feature. Thus, it likely formed immediately after the peak pressure.

7.4.2.3. Multi-segmented Feature

The multi-segmented feature (**Figure 7.21**) is the most complicated form to determine the evolution of geometry during the injection event. No portion of the segmented feature touched the lateral boundary. In fact, the lateral extent of each of the segments forms a nearly parallel line with the boundary. This feature also suggests a complicated stress regime due to boundary conditions. Similar to the radial feature the fracture arrest indicates the boundary conditions contribute to impeding fracture growth.

The sample contacted the lower boundary along the entire width of the sample (**Figure 7.21** (b)). In our previous tests, once the fracture contacted the boundary, the fracture did not grow within the sample significantly, just on the boundary. This

suggests that the fracture grew as a more or less stable linear front (similar to KGD) until it reached the lower boundary.

7.4.2.4. CT Scans of the Solidified Fracture

The CT scans of the fracture are shown in **Figure 7.24**, **Figure 7.25**, and **Figure 7.26**. The scans indicate zones of highest density as white. The CT scans show the dense leakoff zone; internal to this zone are thin dark lines that represent the remnants of the fracture. The scans with section of high leakoff (7), (8) and (9) in **Figure 7.26** resemble high leakoff fractures in the literature on unconsolidated materials [*Dong*, 2010; *Dong and De Pater*, 2007a].

The low leakoff fracture features represent a transition in the fracture morphologies. This is also is apparent in the CT images. There is no reference in the literature to this transition of fracture morphology/phenomenon. However, *Bohloli and Depater* [2006] showed an experiment with two different morphologies in which they call the thin zero leakoff fractures "secondary" (shown in **Figure 7.27**). These secondary fractures (**Figure 7.27**) may be a manifestation of a similar phenomenon. In both tests the initial fractures exhibit greater volumes of leakoff compared to the features that followed. Additionally the initial features in *Bohloli and Depater* [2006] appear to be the same order of leakoff thickness and fracture aperture as our thick features. However, the authors did not describe the features or experiment with enough detail to directly compare.

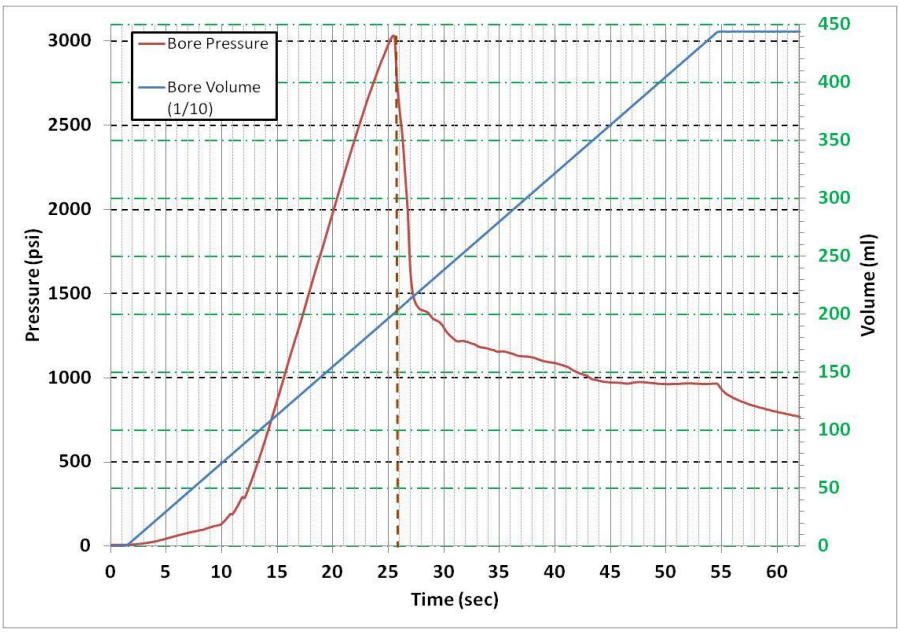

Figure 7.13. Pressure and borehole volume record from the TTC test 200 ml of fluid was injected prior to the peak of injection pressure.

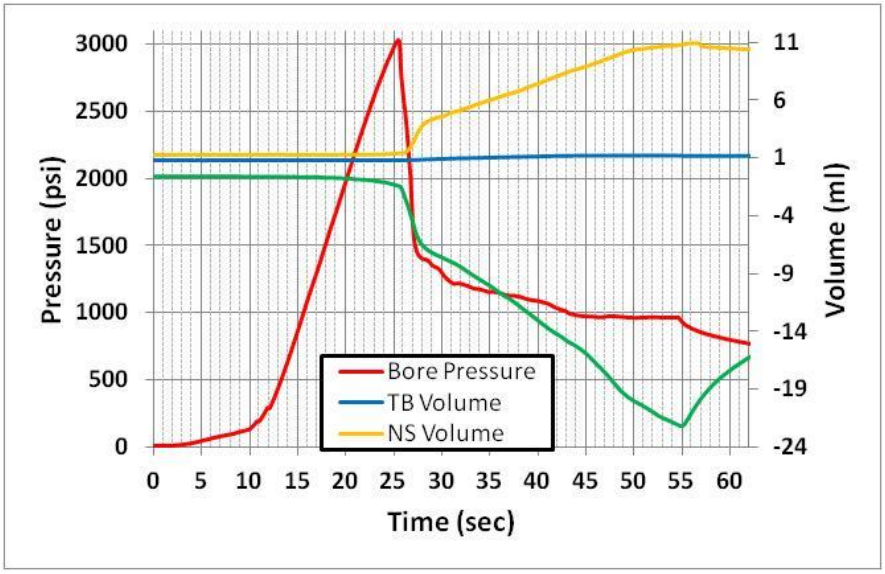

Figure 7.14. Pressure response along with the change in flat jack volume. E.W. is the flat jack applying the minimum principle stress. There is measurable flat jack response in the E.W. flat jack prior to peak pressure.

(a)

(b)

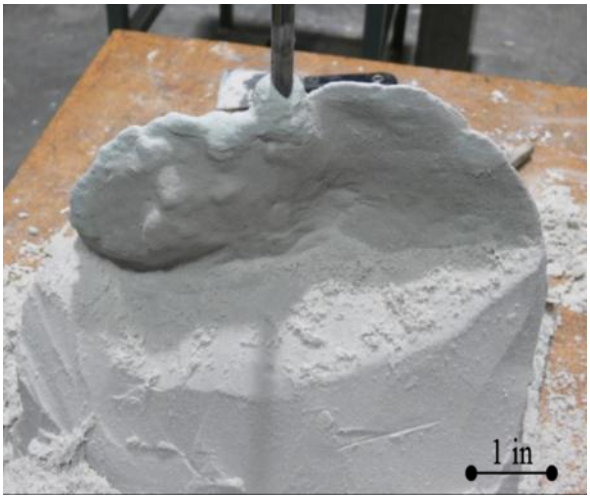

(c)

(d)

Figure 7.15. The excavation process of the sample. The sample was excavated to expose the top of the fracture (b). Then the outer steel can was cut away and excavation continued (c). Final excavated fracture is shown in (d).

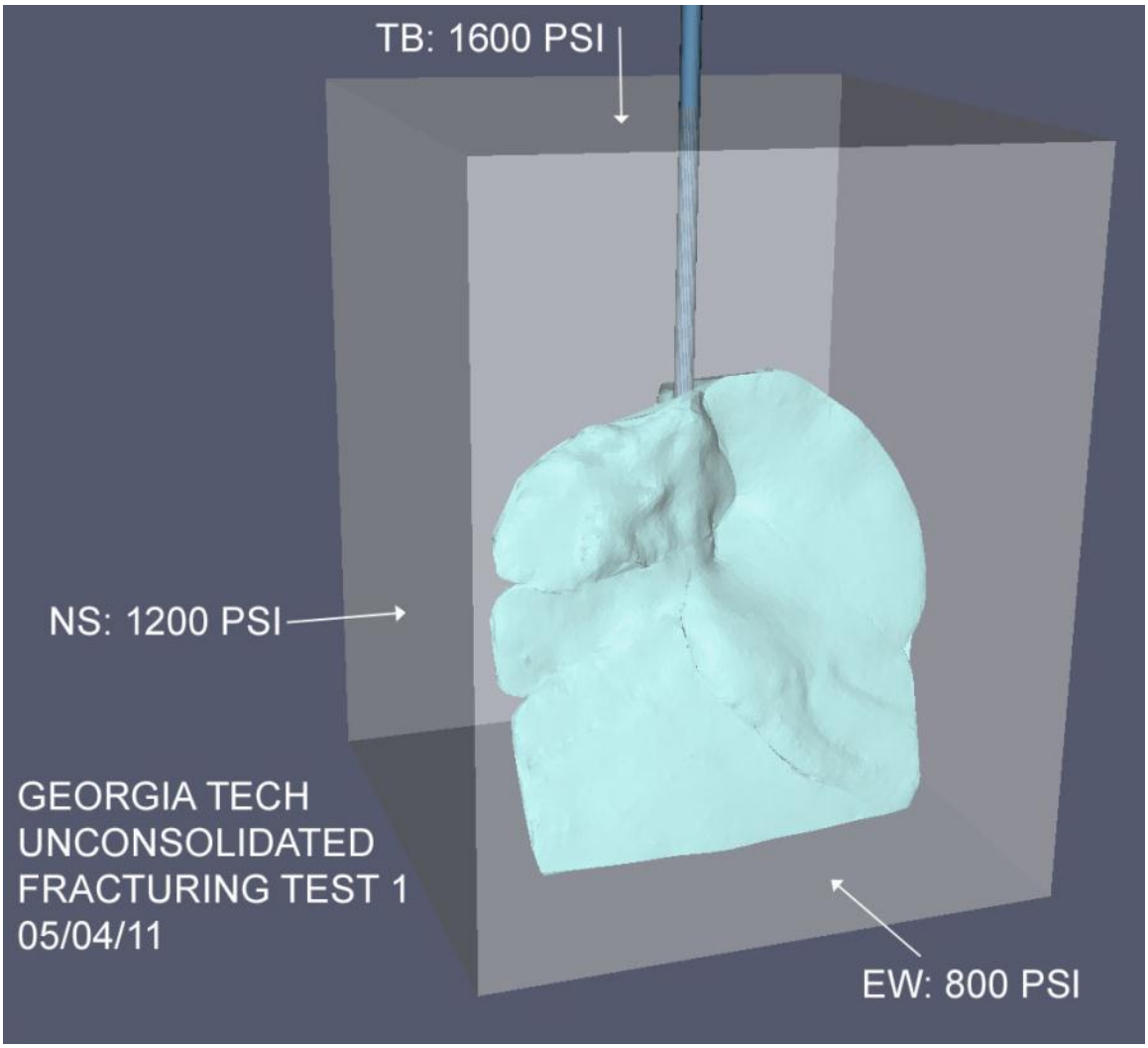

Figure 7.16. Three dimensional scan of the solidified fracture showing the boundary conditions (provided by TerraTek).

(a) **(b)**

Figure 7.17. Image of solidified fracture, there are three distinct regions visible in this image; (1) the thick bubbly region in the vicinity of the injection source, (2) the radial fracture left of the injection source and (3) the splitting pedal-like feature on the right. The fracture propagated down ward, a feature not observed in our tests.

Figure 7.18. Top view of the TTC fracture. “Bubbly” feature is center, around bore-axis.

Figure 7.19. The thick bubbly initial feature. The thin fracture features appear to emanate from the thick feature.

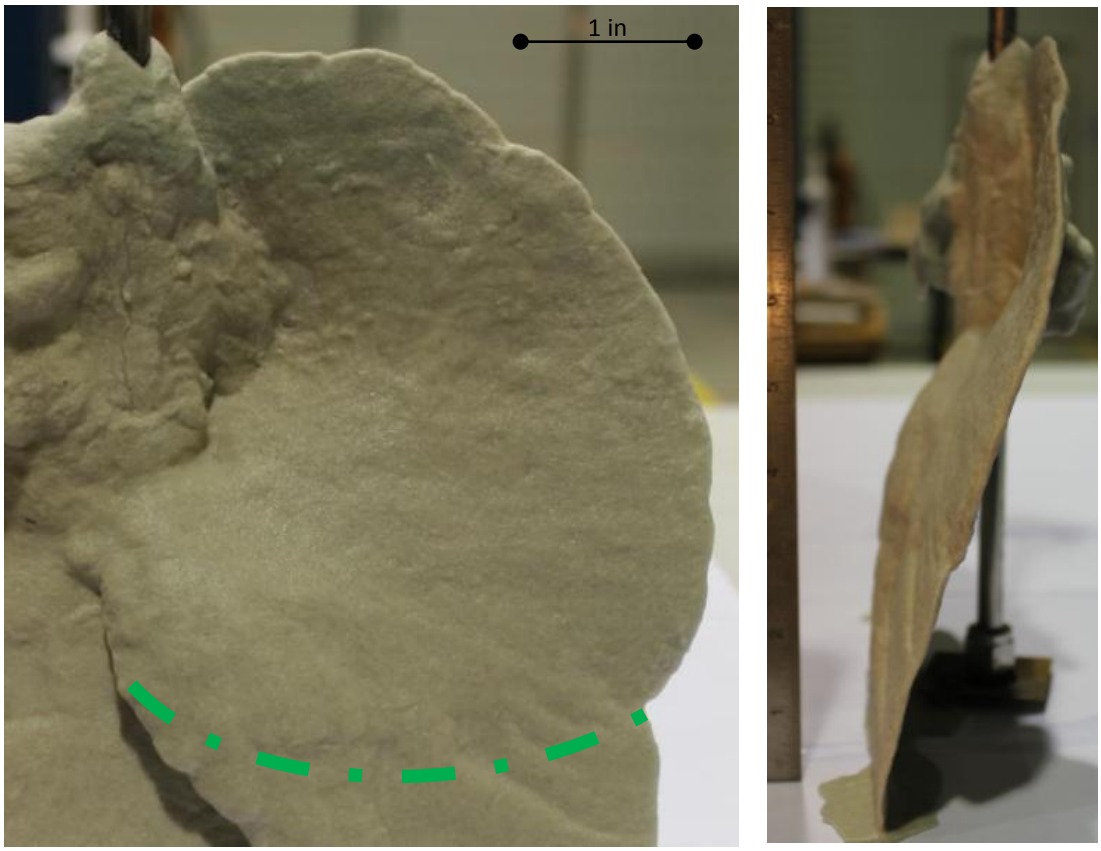

(a) (b)

Figure 7.20. Radial feature the dashed line in (a) represents the front of the feature. The sharp front of the feature is shown in (b).

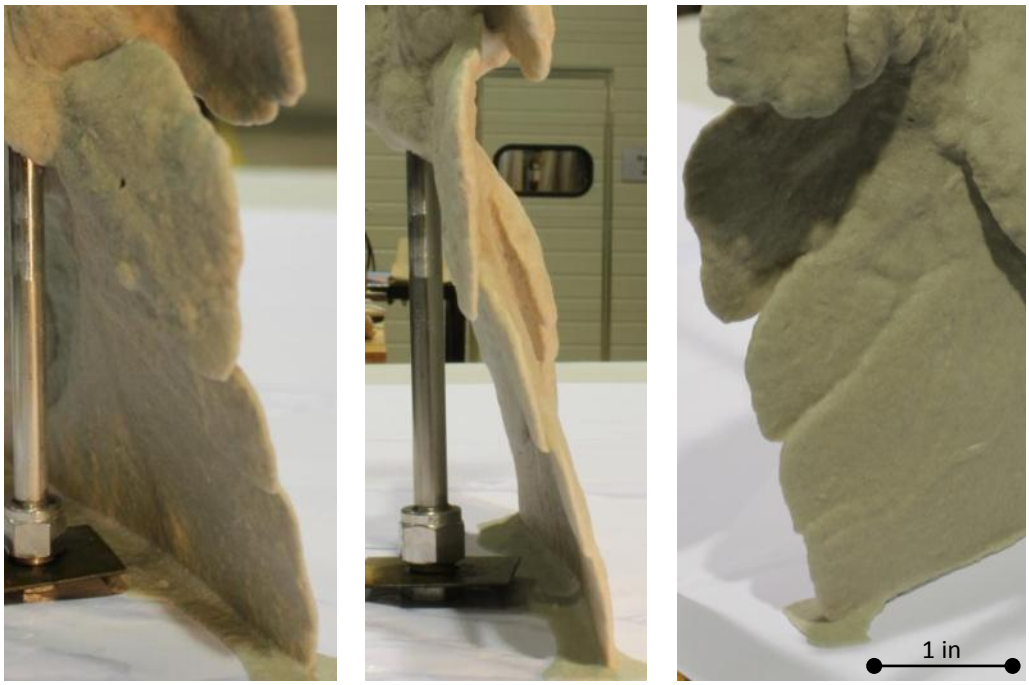

Figure 7.21. Multisegmented feature. The fracture contacts the lower boundary the entire length of the boundary (a) and (b). The segments allign parallel to the boundary bout do not touch it (c).

Figure 7.22. Cross-section of the TTC test. This clearly shows a transition from thick tortuous fracture (above) to thin continuous feature (below). Both regions appear to have a dense outer zone within the leakoff layer.

Figure 7.23. Cross-sections of the TTC test. (a) Near the bore hole thick tortuous fracture, appears to be a dense outer layer in the leakoff zone. (b) Thin brittle-like fracture still contains a dense outer layer just significantly reduced in thickness. Notice the brittle-like fracture interaction ("lower" fracture turning into "upper") in cross-section (b).

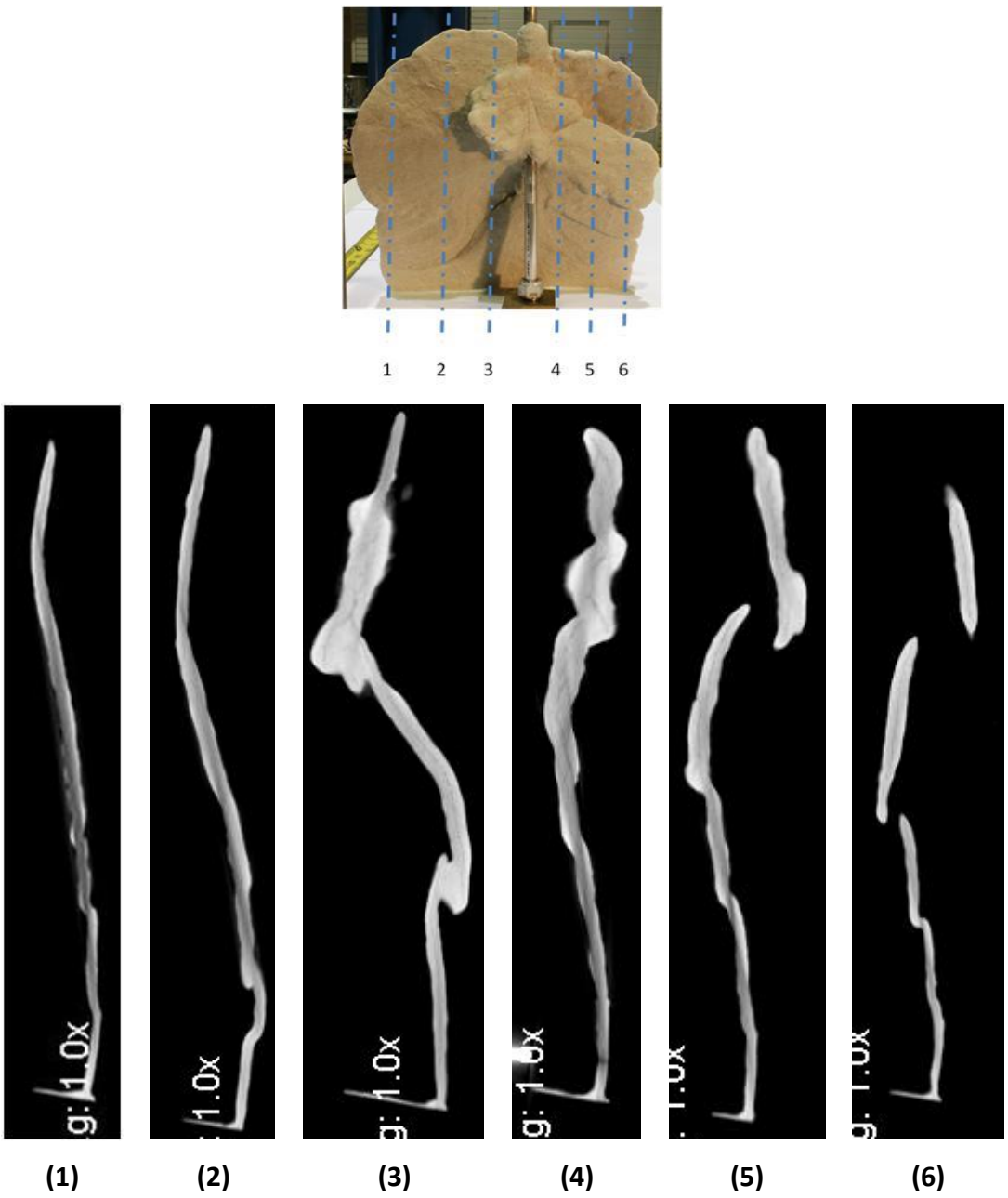

Figure 7.24. CT scans of the fracture slices are parallel to the bore axis. Slices (3) and (4) contains high leakoff features along with the brittle-like features. The high leakoff features show significantly greater amounts of fracture tortuosity compared to the thin features.

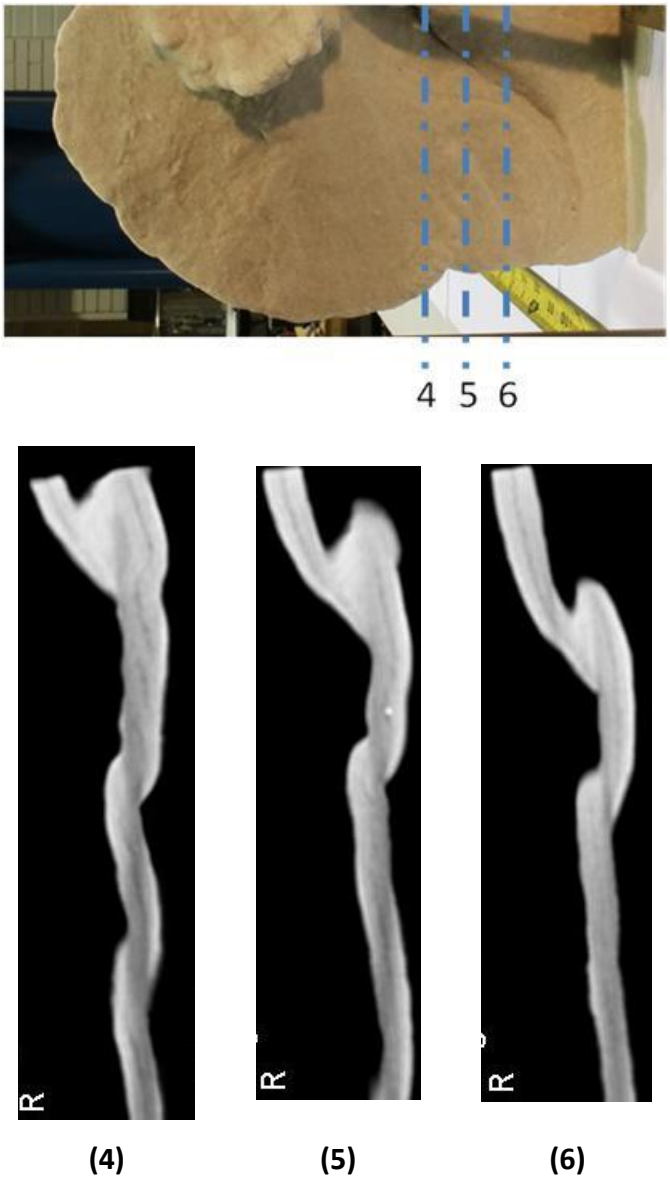

Figure 7.25. CT scans of fracture slices are perpendicular to the bore axis. The leakoff zone apears as the dense outer region. Fracture is present in all cross-sections as dark line in the center. Section (a) shows a distinct multi-segmented fracture.

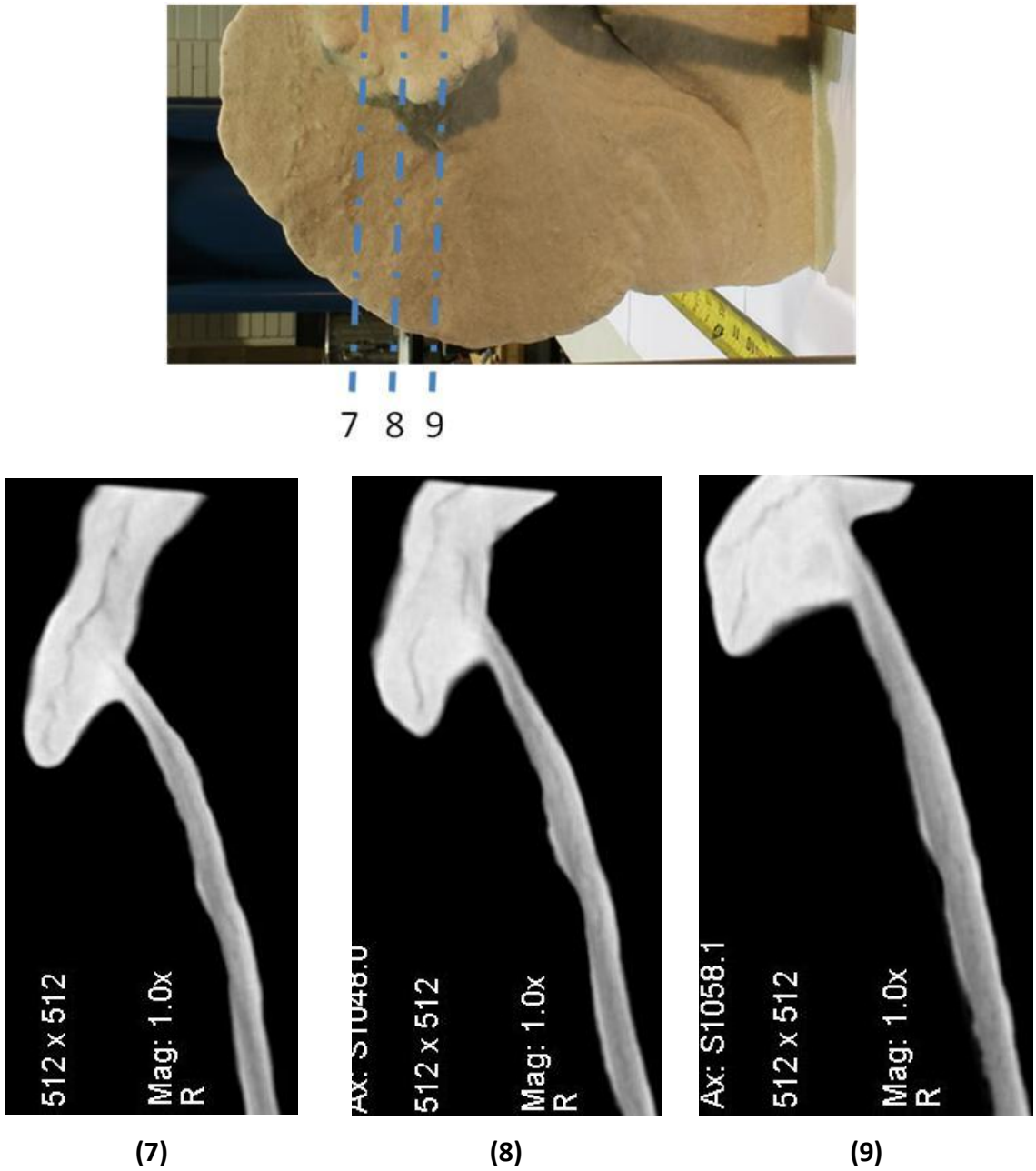

Figure 7.26. CT scans of the fracture slices are perpendicular to the bore axis. These slices show the high leakoff intial feature in contrast with the radial brittle-like feature. The remaining dark line in the center of the white zone is the remanants of the fracture. The thinner feature has a less distinctive fracture signiture.

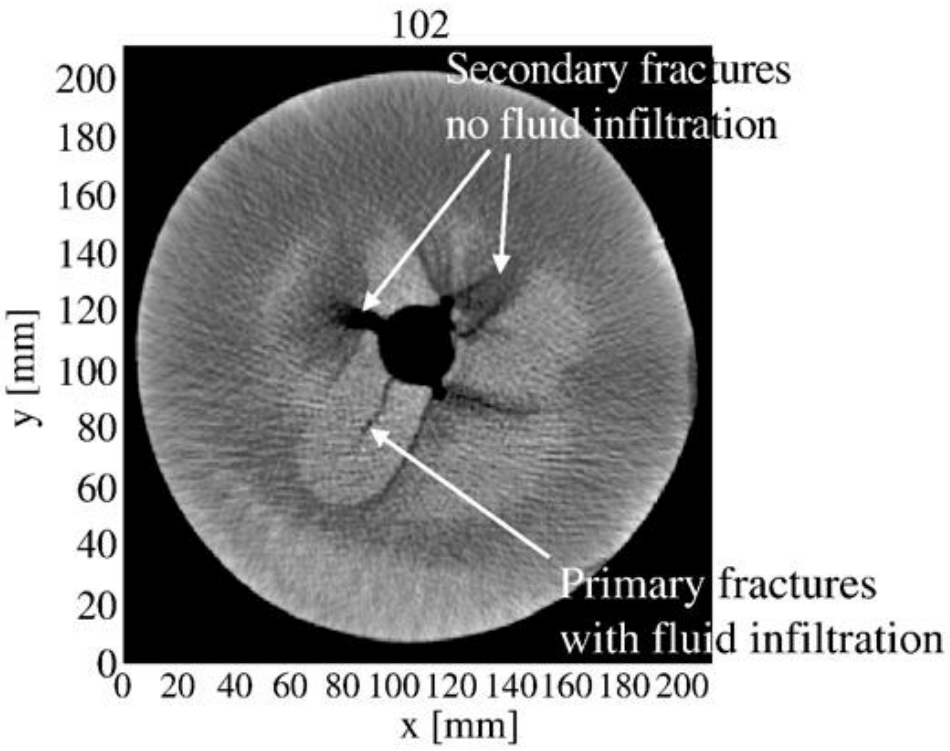

Figure 7.27. From [*Bohloli and Depater*, 2006] CT scan of an injection test in fine sand, showing two different propagation regims. Similar to our transition test results (Figure 4-17, Figure 4-18 and this chapter), the initial fracture feature contains high leakoff (fluid infiltration). In contrast, secondary fractures there is little or negligible leakoff.

7.4.3. Comparison of results to model

The initial estimation matched the peak pressure accurately. Our prediction for the peak pressure was 3000 psi, while the actual was 3022 psi. The propagation time was expected to take 60 s and the final injection pressure to be 1300 psi. The total injection time for the experiment was 42 s. The final injection pressure prior to reaching the boundary was 1055 psi. There are several factors that may have contributed to the minor discrepancy in the final values of the model. For example, the fracture shape is

not ideally radial or plane-strain KGD. Further, the leakoff thickness changed significantly during the fracture event.

The cavity expansion model is inadequate for characterizing the initial injection pressures response prior to peak pressure. This is likely due to propagation of the initial "high-leakoff" fracture, prior to the peak injection pressure as outlined above. The high leakoff feature was possibly in place prior to the peak so the process of cavity expansion was perhaps short lived, or at least mitigated by the initial high leakoff fracture. Almost half of the injected fluid was injected into the sample prior to the breakdown pressure.

The leakoff was generally overestimated in the initial prediction. We assumed that the level of leakoff of the initial feature would be present throughout the experiment. However, it appears that it was only present during the initial stages of fracture development. As a consequence, this would significantly reduce the experiment time as the volume of fluid in the leakoff zone is decreased. For a comparison, the results are fitted with the toughness-dominated model in the same fashion as those in Chapter 7. This is presented in **Figure 7.28**.

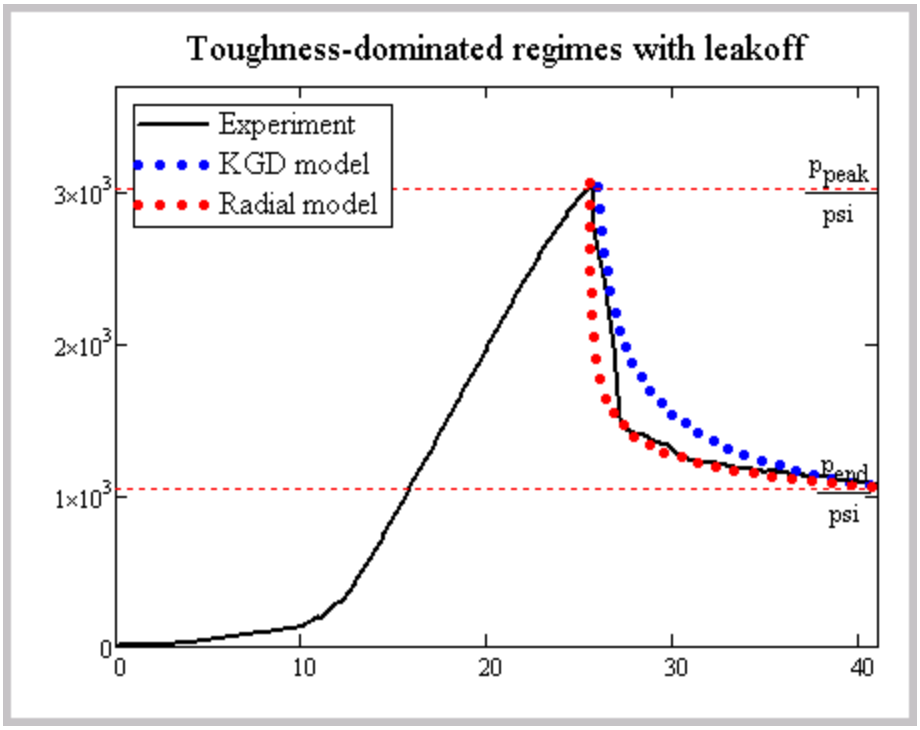

Figure 7.28. Model with the resulting pressure-time history from the TTC. The radial model provides the best fit.

7.5. Conclusions

The results of this section parallel the results at the conclusion of Chapters 4 and 5. In this chapter, we presented a series of experiments conducted with a fluid employed in typical industrial applications. Utilizing the experience from tests conducted with silicone and guar injection fluids coupled with a toughness-dominated hydraulic fracturing model, we were able to predict, with surprising accuracy, the expected initiation pressure of a hydraulic fracturing experiment at scales not yet attempted.

The results from the TerraTek Cell (TTC) are instrumental in connecting the results of our silicone tests and guar based tests. The leakoff features of the different fluids were significantly different. However, with each fluid we utilized in our fracture tests we were able to generate fractures that exhibited a transition in morphologies. This transition may indicate a significant change in fracture propagation mechanism. The main conclusions from this chapter can be summarized as follows:

1. In these tests, permeability did not have a significant impact on peak pressure, but it was important to control leakoff.
2. Guar based fluid exhibits complex leakoff patterns that are dependent on permeability.
3. The dimensional analysis developed in Chapter 4, is valid for the guar fluid injection tests presented here.

4. Small samples (with a diameter of 4 in) show a constant 20% reduction in peak pressures when compared to samples in larger cells (with a diameter of 12 in).
5. Peak injection pressures may not be a sufficient indicator of initiation of fractures.
6. Injection pressures during propagation are not an effective way to predict the propagation regime (as of yet).
7. Fractures may transition from a high leakoff feature to a low leakoff feature that can significantly alter the fracture morphology, and perhaps the mechanisms of propagation.

8. DISCUSSION AND FUTURE WORK

In this work we present a comprehensive experimental program that focuses on the process of hydraulic fracturing in cohesionless materials. Much of this work would not have been possible without the ability to generate large amounts of experimental results. Important new insights are presented and verified through scaling and modeling. The physical experimental development focused on four main parameters: (1) confining stresses, (2) fluid rheology, (3) injection rate and (4) permeability. We developed a dimensional analysis that describes the effects of parameter on peak pressures during fluid injection. We used scaling of the observed fracture geometry to determine that our fractures can be considered thick during propagation. We modeled propagation with a toughness-dominated model of hydraulic fracturing. Finally, we observed characteristic features in our fractures that suggest that fluidization and shear deformation are processes of fracture propagation. Here we review each of these details.

8.1. Dimensional Analysis

The dimensional analysis is an important result of this work. The ability to predict initiation pressures across multiple scales has profound implications across many disciplines. To evaluate the performance of our dimensional analysis we collected data of initiation pressures from the literature. The Delft Group provides all the pertinent data to accomplish this. **Figure 8.1** shows the compilation of our data together with that

of the Delft Group. This additional data provides confidence that the dimensional analysis correctly characterizes initiation pressures for fluid-driven fractures in cohesionless materials. The data from the Delft group utilized a power law fluid (with viscosity parameters of $K = 900$ cP $\sec^n$, $n=0.6$) and a Newtonian fluid (with a viscosity of 50000 cP). It is shown that the dimensional analysis is not particularly sensitive to the value of n.

Significant amounts of field data have been published on unconsolidated fracturing in petroleum reservoirs of the Gulf of Mexico. Unfortunately, most of the available literature does not report all the necessary parameters to complete the dimensional analysis, as derived in Chapter 4. The closest data set we could find to verify this works on the field scale was presented by *Barree et al.* [1996].

Barree et al. [1996] published the results of a series of 17 fracturing stimulations in the Gulf. Only 8 of the completions recorded significant decreases in the injection pressures during the event. The data from these 8 treatments are what we utilize here. There are a number of assumptions and estimations that must be utilized; however, the reported data is complete enough for the dimensional analysis.

The viscosity is estimated by a power law fluid (K=2.0 Pa $\sec^n$, n=0.477). Three effective viscosities at different shear rates, for the injected fluid, were reported in *Barree et al.* [1996]. We fit these three data points with a power-law model and calculated the necessary rheological parameters. The calculated values agree with typical fracturing fluids utilized in industrial processes.

The stress used here is also interpreted as an effective maximum stress. The in-situ stresses are not directly measured and only the total vertical depth (TVD) and bottom hole pore pressure (BHP) are reported. The overburden pressure gradient is estimated as 1.0 psi/ft [*Barree et al.* 1996]. Therefore, the vertical effective stress is calculated from TVD x 1.0 psi/ft - BHP. Further, we do not estimate the horizontal minimum effective stress. The results of the dimensional analysis will remain as all of these fracture jobs occurred within the same reservoir.

The plots of the peak injection pressures and vertical stress are **Figure 8.2** and **Figure 8.3**. **Figure 8.2** plots the peak injection pressure versus the vertical stress. There is an increase of peak injection pressures with vertical stress. A power-law fitting of the data produces a coefficient of determination (r^2) value of 0.77. In a similar fashion to the results presented in Chapter 4, **Figure 8.3** plots the normalized peak injection pressure versus confinement. A power-law fitting of the data produces an r^2 value of 0.29. **Figure 8.4** is a plot of the dimensionless stress versus dimensionless peak injection pressure, the r^2 value is 0.99. This data shows promise in extending the dimensional analysis to the field scale. The range of parameters is limited however.

Figure 8.5 pots the dimensional parameters for the results presented in Chapter 7 (guar injection fluid) along with the power-law fluid injection test data from the Delft group and the field data from *Barree et al.* [1996]. Finally in Figure 8.6 all the data generated from the results presented in this work, along with other experimental work

in the literature and real published field data show that the dimensional analysis developed here is valid for multiple scales. Therefore, this may provide a viable way to characterize breakdown pressures estimated at the laboratory scale to field scale. To our knowledge, this has yet to be accomplished in a systematic way.

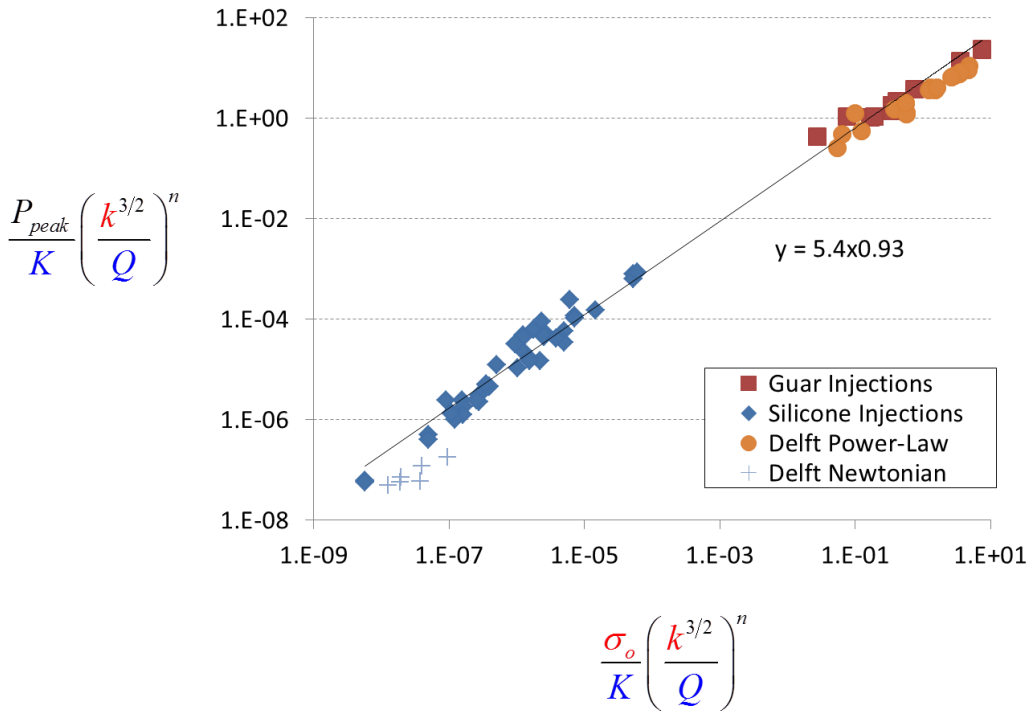

Figure 8.1. Dimensional groups with data added from the Delft group.

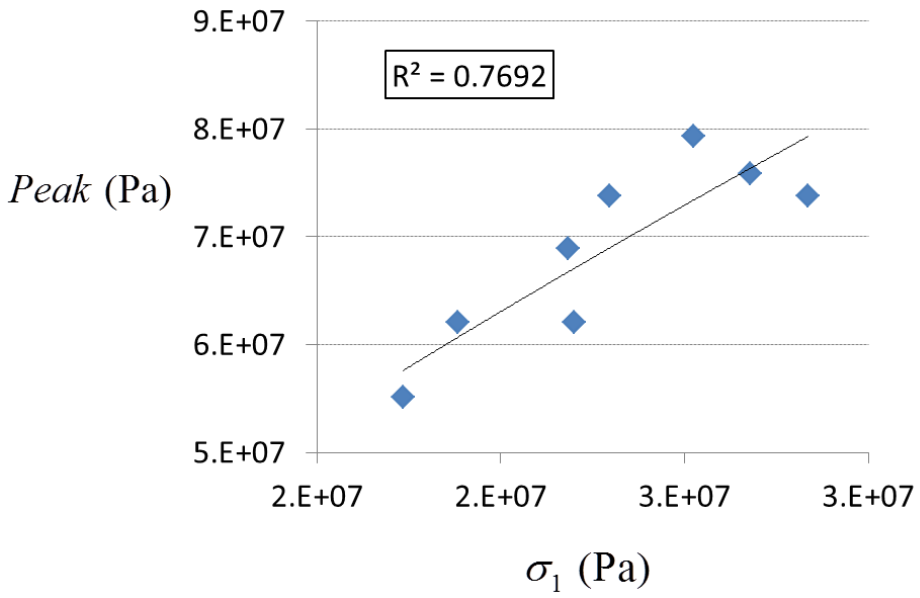

Figure 8.2 Raw field data peak injection pressure versus maximum vertical effective stress taken from *Barree et al.* [1996].

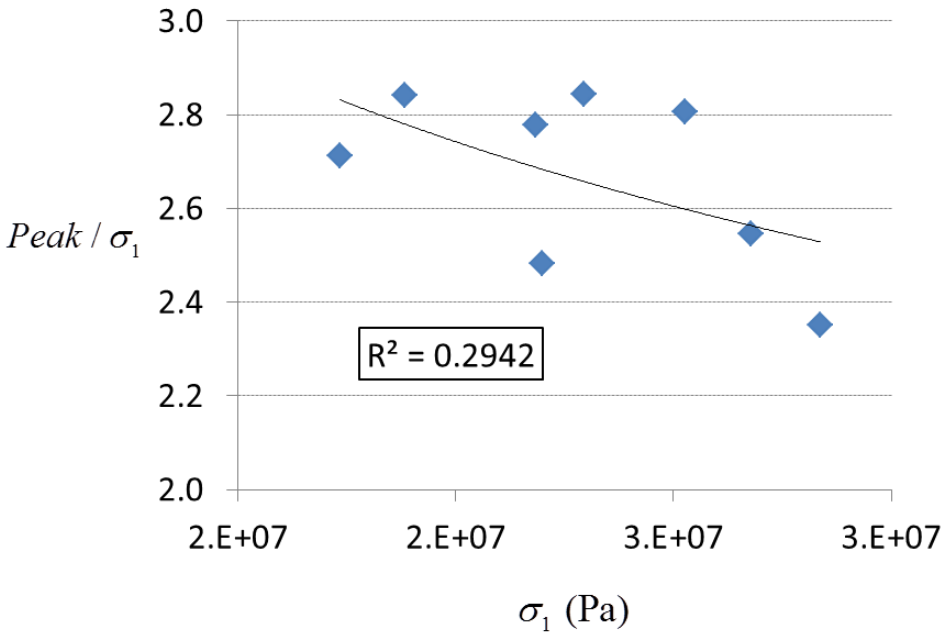

Figure 8.3 Raw field data normalized peak injection pressure versus maximum vertical effective stress taken from *Barree et al.* [1996].

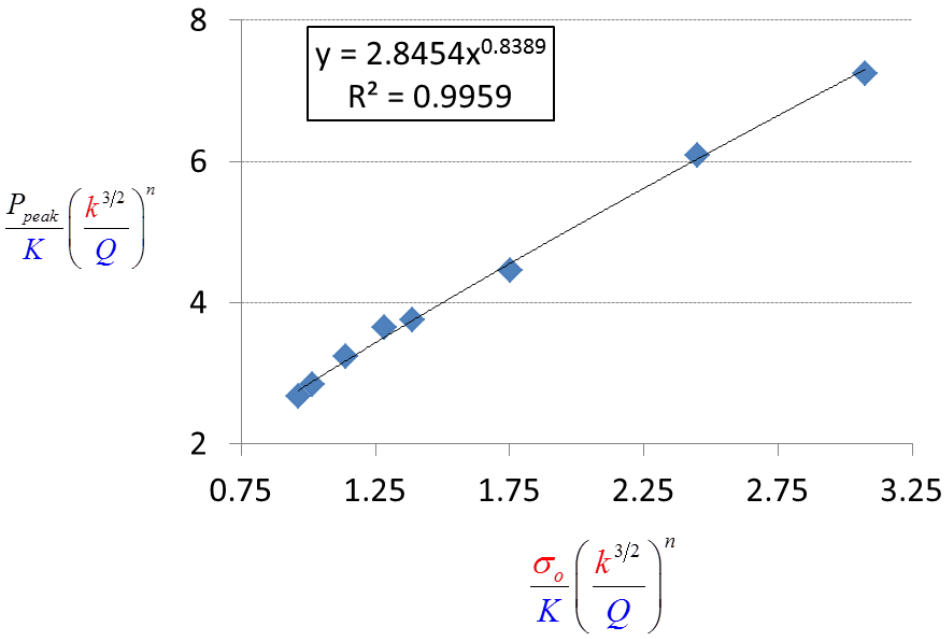

Figure 8.4 Our developed dimensional analysis applied to field data taken from *Barree et al.* [1996].

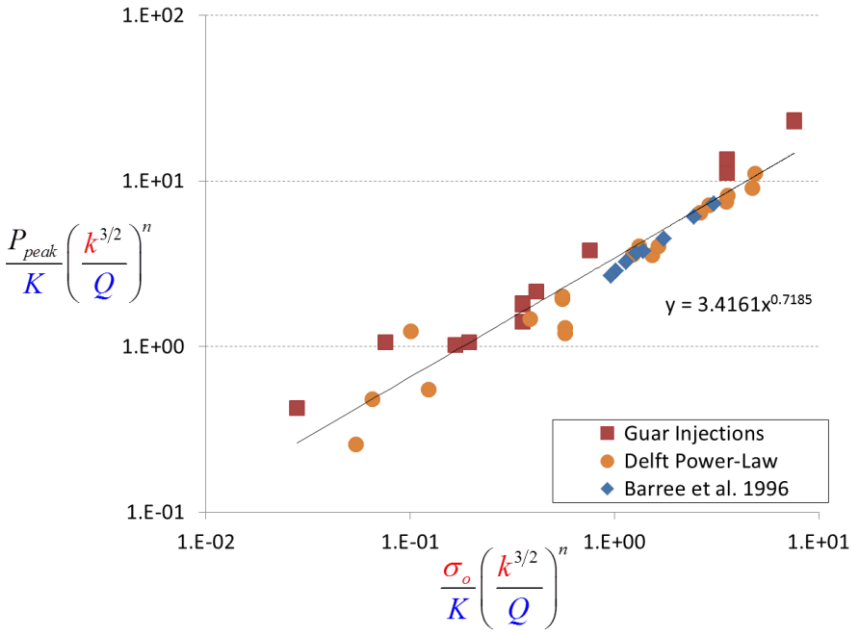

Figure 8.5. The data reported in Chapter 7 (Guar injected tests) along with similar fluids (Power-Law $K \sim 1000$ cP sec^n, $n \sim 0.6$) in other experimental work (Delft Group) and field data *Barree et al.* [1996]

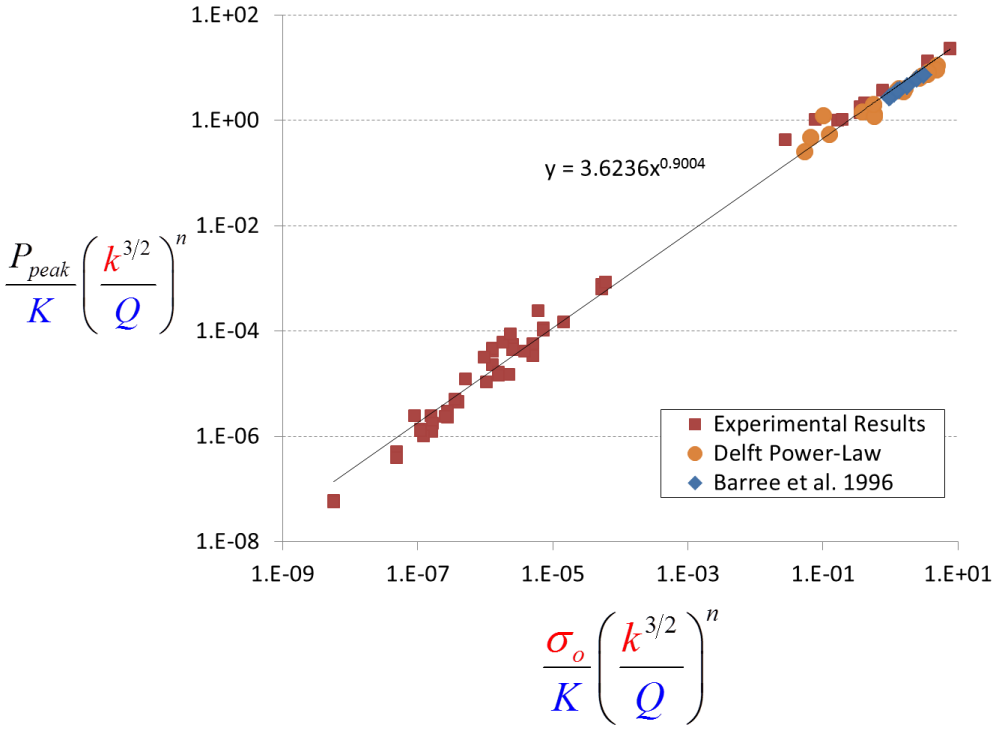

Figure 8.6. The data reported in Chapters 4 and 5 (Silicone injected tests), Chapter 7 (Guar injected tests) along with similar fluids (Power-Law $K \sim 1000$ cP sec^n, $n \sim 0.6$) in other experimental work (Delft Group) and field data *Barree et al.* [1996].

8.2. Toughness-Dominated Fractures

Our scaling suggests that our fractures can be considered thick, within the range of parameters we utilized. We employed a model of toughness-dominated hydraulic fracturing (Chapter 6). This model was utilized successfully in predicting the pressure-time dependence for most of our laboratory data set. It also accurately modeled the experimental results of a high-stress, true triaxial fracture test of saturated unconsolidated materials conducted at a separate facility (Chapter 7). Further, it accurately matched pressure-time and displacement-time histories available from a shallow field scale tests described in the literature with only two fitting parameters. These results indicate that the fractures we have modeled in unconsolidated particulate materials are indeed toughness-dominated fractures.

8.3. Analysis of fracturing fluid leakoff

The observation of leakoff primarily confined to the fracture tip is prevalent in many of our experiments. Here we define two leakoff processes. One is due to fracture extension and is the initial fluid that invades the formation ahead of the fracture. Second, is the steady flow of fracturing fluid into the formation, due to the pressurized fracture, primarily perpendicular to fracture direction. The time scales of our experiments are relatively short (5 sec to 10 min). Therefore, we present a simple model to determine the dominate leakoff process. We consider that this leakoff initiates after the fracture is emplaced, and the initial leakoff due to tip extension processes is established.

Starting from Darcy's law we have,

$$\phi \dot{b} = \frac{k}{\mu}\frac{\partial p}{\partial x} \tag{8.1}$$

where, ϕ is the porosity, b is the thickness of the leakoff zone, k is the permeability, μ is the fluid viscosity, and $\partial p / \partial x$ is the pressure gradient. Here $\dot{b} = db / dt$, therefore

$$\phi \frac{db}{dt} = \frac{k}{\mu}\frac{\Delta p}{b} \tag{8.2}$$

rearranging,

$$\phi b db = \frac{k}{\mu}\Delta P dt \tag{8.3}$$

integrating,

$$\phi \int_{b_o}^{b} b db = \frac{k}{\mu}\Delta P \int_{0}^{t} dt \tag{8.4}$$

finally,

$$\phi \frac{b^2 - b_o^{\,2}}{2} = \frac{k}{\mu}\Delta P t \tag{8.5}$$

From Equation 8.5 we solve for the total leakoff thickness, b,

$$b = b_o \sqrt{1 + \frac{2k}{\phi\mu}\frac{\Delta P}{b_o^{\,2}} t} \tag{8.6}$$

therefore

$$b \cong b_o \ \ if \ \ \frac{2k}{\phi\mu}\frac{\Delta P}{b_o^{\,2}}t \ll 1 \tag{8.7}$$

The viscosity term in Equation 8.7 is an effective viscosity, and not known directly. If we consider a collection of tubulars to represent the porous matrix, we can utilize one tubular to estimate the effective viscosity. We use the Hagen-Poiseuille equation, along with the solution for a power law fluid flowing through a pipe. For simplicity, we ignore the yield stress of the silicone adhesive injection fluid and only consider the power law nature of the fluid. The consequence of this assumption in this analysis is to overestimate the leakoff thickness.

For a Newtonian fluid flowing in a tube, the Hagen-Poiseuille equation is,

$$\Delta P = \frac{8\mu L Q_1}{\pi a^4} \tag{8.8}$$

where, L is the length of the tube, a is the radius, ΔP is the pressure drop across the leakoff layer, and Q_1 is the flow rate, through one tubular. We define the length of the tubular to be the initial, or primary, leakoff thickness, b_o. Therefore,

$$Q_1 = \frac{\pi a^4}{8\mu}\frac{\Delta P}{b_o} \tag{8.9}$$

The flow rate for a power law fluid in a tube is,

$$Q_1 = \frac{\pi a^3}{3+1/n}\left[\frac{\Delta P}{b_o}\frac{a}{2K}\right]^{1/n} \tag{8.10}$$

setting Equation 8.10 equal to Equation 8.9, and solving for $1/\mu$,

$$\frac{1}{\mu} = \frac{2^{4-2/n}}{3+1/n}\left[2a\frac{\Delta P}{b_o}\right]^{1/n-1} K^{-1/n} \tag{8.11}$$

combining Equation 8.11 with 8.7

$$b \cong b_o \quad if, \ \frac{2k}{\phi b_o 2a}\frac{2^{4-2/n}}{3+1/n}\left[\frac{2a}{K}\frac{\Delta P}{b_o}\right]^{1/n} t \ll 1 \tag{8.12}$$

For silicone injected tests the parameters scale as,

$$\begin{aligned} &\Delta P \sim 10^6\, Pa, \ \ t \sim 100\, sec, \ \ n = 0.75, \ \ K \sim 10^2\, Pa\, sec^n, \\ &b_o \sim 1 cm, \ \ a \sim 10^{-5}\, m, \ \ k \sim 10^{-13}\, m^2, \ \ \phi \cong 0.3 \end{aligned} \tag{8.13}$$

resulting in,

$$\frac{2k}{\phi b_o 2a}\frac{2^{4-2/n}}{3+1/n}\left[\frac{2a}{K}\frac{\Delta P}{b_o}\right]^{1/n} t \sim 10^{-3} \tag{8.14}$$

The results of this exercise indicate that the secondary leakoff process (Carter's Leakoff model) does not contribute significantly to the leakoff thickness of the tests at time scales of the experiments. This result is only valid for the silicone adhesive tests. The lower viscosity and complex leakoff characteristics of the guar cross-linked gel make the extension of the above results difficult.

8.4. Propagation Mechanisms

The inspections of the cross-sections from our tests indicate that there is a blunting mechanism at the fracture tip. Further, there is a scale associated with this blunting mechanism. This scale may be associated with the energy dissipation mechanism at the fracture tip. Here we offer two kinematically admissible mechanisms for crack tip extension; (1) fluidization and (2) shear band formation (**Figure 8.7**). These two mechanisms were suggested for hydraulic fracturing in dry particulate materials by Chang [2004]. Our direct experimental observations suggest that these mechanisms may still be applicable for saturated particulate materials.

The splitting tips and multiple offshoots present in the cross-sections of our fractures suggest a localized shear displacement. There is evidence in the literature that shear failure in the leakoff zone is the primary propagation mechanism in hydraulic fracturing of cohesionless soils [*Chang*, 2004; *Dong and De Pater*, 2008; *Khodaverdian and Mcelfresh*, 2000](among others). However, questions remain concerning the validity of the shear failure as the primary mechanism in hydraulic fracturing of unconsolidated materials [*Olson et al.*, 2011; *Shin and Santamarina*, 2010]. Our experiments indicate that although leakoff typically precedes fracture propagation, low levels of leakoff likely require deformation processes outside of the leakoff zone. That is, the fluidized zone ahead of the crack tip is small relative to the fracture aperture, in tests with limited leakoff. Finally, the fracture morphology we have seen in several of our experiments is similar to that reported by *Dong* [2010], in which shear bands were observed ahead of

the crack tip by CT imaging (**Figure 5.23**). The author attributes the shear deformation ahead of the crack tip to the reduction of the effective stresses by fluid flow preceding the fracture tip. The limited leakoff in our tests suggest that shear bands ahead a propagating crack may not be confined to the fluidized region of leakoff.

High-pressure tests show significant changes in density of particle concentrations within the leakoff zone (**Figure 5.30** and **Figure 5.31**). Further, fracture cross-sections with significant leakoff suggest diffuse flow ahead of the fracture tip. This could be due to tensile strain at the crack tip, creating an increase in porosity ahead of the crack tip, as suggested by *Shin and Santamarina* [2010] among others [*Chang*, 2004; *Chang et al.*, 2003; *Germanovich and Hurt*, 2007]. The evidence for both propagation regimes may represent competing mechanisms for fracture propagation.

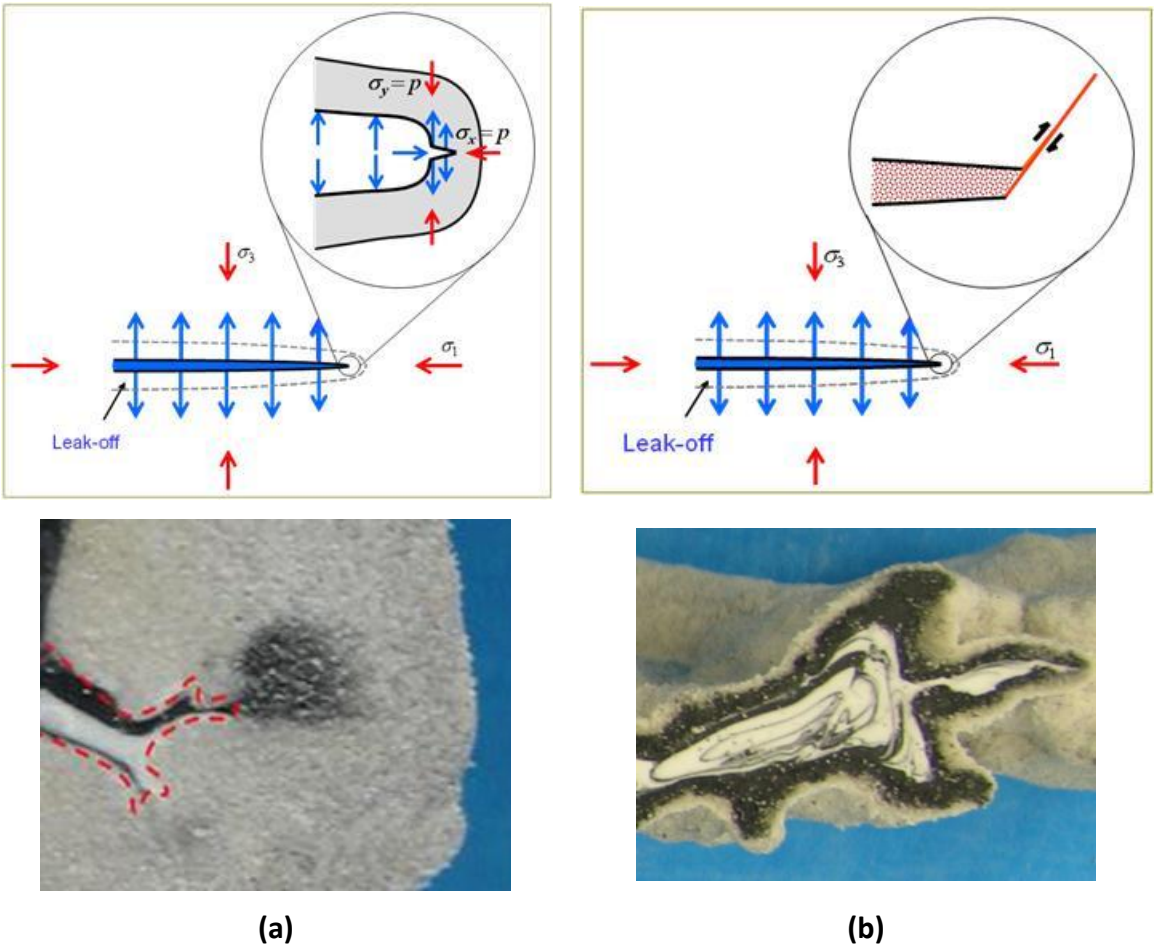

(a) **(b)**

Figure 8.7. Fracture propagation mechanisms (a) fluidization (b) shear bands.

8.5. Other Observations

Injection pressure signatures independently may not be sufficient in characterizing the fracturing process. We showed multiple instances where normalized pressure curves are identical for dramatically different fracture morphologies. Additionally, the fracture morphology may significantly change during an experiment with no indication within the pressure signature.

The most prevalent fracture morphology in our tests suggests a localized process that acts in a stepwise fashion throughout the fracture propagation. It appears that this process is dependent on the localized fluid flow ahead of the crack tip. However, several of our experiments contain evidence of a fracture morphology that is more analogous to traditional brittle failure. In this instance, there may be a transition of failure mechanisms. The magnitude of leakoff may be significant in the mechanism of the propagation regime.

The fluid flow in the formation must be adequately characterized to determine the fracture morphology. Work presented and ongoing by *Huang et al.* [2011] represent an important opportunity to resolve the relationships of the fluid flow component to the fracture morphology. Our results suggest that over simplification of the leakoff process (i.e., Carter's leakoff formulation) may lead to significant discrepancies between calculated and the actual magnitude of leakoff.

The brittle-like features displayed in the transition experiments, such as the one in **Figure 4.19**, appear similar to fractures created by the use of the industrial fluids

described in Chapter 7. The fractures in Chapter 7 also indicate a less localized leakoff phenomenon. The question remains whether the fracture extension process also transitions. The existence of these similarities suggests that the difference between the industrial fluid and silicone may simply be due to the magnitude of leakoff. The transition experiments are significant in that they may represent a regime of hydraulic fracturing in cohesionless materials that has yet to be considered or resolved.

8.6. Recommendations for Future Work

1. The first recommendation is to perform large-scale high-pressure tests. Our scale is adequate for initiation. It limits the analysis of fracture propagation, however. Extending the fracture size will also allow for greater flow rates, thus mitigating the effects of leakoff. As a first step, a large-scale test could maintain the same experimental parameters as the high-stress test presented in Chapter 7, and thus be executed just at a larger scale.
2. Similar experiments to *Huang et al.* [2011] should be designed utilizing an applied load. This would allow for propagating the fracture with a defined plane. In addition, visualizing the propagating fracture tip may allow for determining how the tip propagates in real time and if various regimes correspond to separate deformation mechanisms. Further, it would provide important insights into the leakoff process and how it evolves with propagation of the fracture.
3. The transition experiments need to be investigated. Thus far, there is not sufficient data to determine if this phenomenon is simply an experimental artifact or a separate propagation regime. Our data set provides a range of parameters that would allow focus on this particular regime.
4. Use of Newtonian fluids would ease the viscosity considerations and may simplify the analysis. We showed several regimes of propagation with two different shear-thinning fluids. The complete analysis of our work requires characterizing the shear rate within the leakoff zone and fracture. Newtonian fluid simplifies the quantification of the fluid viscosity.

5. Complete data sets (with the parameters we utilize here) are not typically available in the literature. A compilation of the available data from the literature would prove useful in refining the dimensional analysis.

APPENDICES

A. Experimental Parameters

Date	CELL	Conf.	Injection	Cons. Index (K)	Fluid index	Sample	Perm	Flow rate
		psi	fluid	cP sec^n	n		mD	ml/min
6-17-2005	LTC	20	732	716981	0.19	F110	1000	50
9-2-2005	LTC	20	732	716981	0.19	F110	1000	50
9-14-2005	LTC	40	732	716981	0.19	F110	1000	50
9-21-2005	LTC	20	732	716981	0.19	F110	1000	50
10-5-2005	LTC	40	732	716981	0.19	F110	1000	50
10-7-2005	LTC	20	732	716981	0.19	F110	1000	50
10-28-2005	LTC	40	732	716981	0.19	F110	1000	50
11-11-2005	LTC	40	732	716981	0.19	F110	1000	50
12-4-2005	LTC	80	739	1206754	0.16	F110	1000	50
12-4-2005	LTC	80	739	1206754	0.16	F110	1000	50
2-1-2006	LTC	80	739	1206754	0.16	F110	1000	50
2-14-2006	LTC	70	739	1206754	0.16	F110	1000	50
3-3-2006	LTC	80	734	100000	0.19	F110	1000	50
4-14-2006	LTC	70	739	1206754	0.16	F110	1000	50
8-11-2007	LTC	80	734	100000	0.19	F110	1000	600
9-17-2007	LTC	80	734	100000	0.19	F110	1000	1700
9-27-2007	LTC	80	732	716981	0.19	F110	1000	1700
6-18-2008	LTC	80	739	1206754	0.16	F110	1000	1700
6-25-2008	LTC	80	739	1206754	0.16	F110	1000	1700
7-2-2008	LTC	80	732	716981	0.19	F110	1000	1700
7-8-2008	LTC	80	739	1206754	0.16	10% Silica	500	1700
7-17-2008	LTC	20	739	1206754	0.16	10% Silica	500	1700
8-14-2008	LTC	80	732	716981	0.19	Silica	25	1700
8-25-2008	LTC	20	739	1206754	0.16	F110	1000	1700
8-30-2008	LTC	20	732	716981	0.19	F110	1000	1700
9-15-2008	LTC	80	732	716981	0.19	LAYER	25	1700
9-22-2008	LTC	80	739	1206754	0.16	Silica	25	1700
10-20-2008	LTC	80	732	716981	0.19	10% Silica	500	1700
11-6-2008	LTC	80	732	716981	0.19	20% Silica	350	1700
11-17-2008	LTC	80	732	716981	0.19	20% Silica	350	1700

Date	CELL	Conf. psi	Injection fluid	Cons. Index (K) cP sec^n	Fluid index n	Sample	Perm mD	Flow rate ml/min
9-11-2009	LTC	80	732	716981	0.19	F110	1000	50
9-23-2009	LTC	20	732	716981	0.19	F110	1000	50
8-3-2010	LTC	80	GUAR SL5	69606	0.19	F110	1000	15000
8-10-2010	LTC	80	GUAR SL5	69606	0.19	F110	1000	1500
9-3-2010	LTC	80	732	716981	0.19	F110	1000	1500
9-13-2010	LTC	80	732	716981	0.19	F110	1000	1500
10-13-2010	HPTC	800	GUAR SL5	69606	0.19	20% Silica	350	500
10-13-2010	HPTC	800	732	716981	0.19	20% Silica	350	500
10-14-2010	HPTC	80	GUAR SL5	69606	0.19	20% Silica	350	500
10-14-2010	HPTC	80	GUAR	69606	0.19	20% Silica	350	500
10-21-2010	HPTC	800	GUAR	69606	0.19	20% Silica	350	500
10-21-2010	HPTC	80	GUAR SL5	69606	0.19	20% Silica	350	500
11-5-2010	LTC	80	732	716981	0.19	20% Silica	350	500
11-9-2010	HPTC	800	732	716981	0.19	20% Silica	350	500
11-11-2010	LTC	80	732	716981	0.19	20% Silica	350	50
11-19-2010	LTC	80	GUAR SL5	69606	0.19	20% Silica	350	50
11-30-2010	LTC	80	GUAR SL5	69606	0.19	20% Silica	350	5000
1-31-2011	LTC	80	732	716981	0.19	20% Silica	350	5000
2-10-2011	HPTC	800	GUAR	69606	0.19	20% Silica	350	50
2-10-2011	LTC	80	732	716981	0.19	F110	1000	50
2-23-2011	LTC	80	732	716981	0.19	20% Silica	350	1500
3-3-2011	LTC	80	732	716981	0.19	20% Silica	350	5000
3-10-2011	HPTC	800	GUAR	69606	0.19	20% Silica	350	50
3-10-2011	LTC	8	739	1206754	0.16	F110	1000	50
3-17-2011	LTC	8	739	1206754	0.16	20% Silica	350	50
3-30-2011	LTC	8	732	716981	0.19	F110	1000	50
4-5-2011	LTC	80	732	716981	0.19	20% Silica	350	500
4-22-2011	LTC	80	732	716981	0.19	20% Silica	350	50
5-4-2011	TTC	800	GUAR	69606	0.19	20% Silica	350	500
5-12-2011	LTC	8	732	716981	0.19	20% Silica	350	50
5-19-2011	LTC	80	732	716981	0.19	F110	1000	5000
5-26-2011	LTC	8	GUAR SL5	69606	0.19	20% Silica	350	50
6-2-2011	LTC	8	GUAR SL5	69606	0.19	F110	1000	5000

B. Experimental Results

Date	PRESSURE			TIME			Reached	VOLUME	
	P_{peak}	P_{min}	P_{drop}	t_{start}	t_{peak}	t_{end}	boundary	@P_{peak}	TOTAL
	psi	psi	psi	s	s	s		ml	ml
6-17-2005	754	457	150	10	49	340	no	33	275
9-2-2005	716	645	120	10	47	88	no	31	65
9-14-2005	885	695	140	10	56	119	no	38	91
9-21-2005	668	551	50	10	54	177	no	37	139
10-5-2005	708	307	900	10	58	272	yes	40	218
10-7-2005	717	540	130	10	43	161	no	28	126
10-28-2005	729	497	130	10	51	165	no	34	129
11-11-2005	711	533	130	10	56	195	no	38	154
12-4-2005	1130	862	600	8	62	242	no	45	195
12-4-2005	1130	862	600	8	62	242	no	45	195
2-1-2006	1133	638	600	10	51	341	no	34	276
2-14-2006	984	612	400	10	60	343	no	42	278
3-3-2006	823	456	80	10	168	471	no	132	384
4-14-2006	838	499	300	10	126	797	no	97	656
8-11-2007	535	383	80	10	22	60	no	120	500
9-17-2007	840	137	500	10	13	28	no	85	510
9-27-2007	1079	400	600	11	15	34	yes	113	652
5-22-2008	197	140	0	31	35	41	yes	105	283
5-28-2008	222	145	0	2	5	8	yes	71	170
6-5-2008	336	245	100	10	14	31	no	108	592
6-10-2008	314	188	100	10	15	32	no	142	623
6-18-2008	1668	495	1500	10	16	30	no	167	567
6-25-2008	1365	392	1500	10	16	32	no	167	623
7-2-2008	1369	393	850	10	16	32	yes	167	623
7-8-2008	1154	400	1500	11.9	16	33	yes	113	598
7-17-2008	864	244	1500	10	17	33	yes	196	652
8-14-2008	814	576	500	10	17	32	yes	198	618
8-25-2008	694	480	1500	13	19	32	no	167	533
8-30-2008	550	379	500	12	18	34	no	167	612
9-15-2008	867	566	500	12	17	33	yes	139	589
9-22-2008	753	430	1500	10	16	29	no	167	536
10-20-2008	879	569	500	12	18	36	yes	170	680
11-6-2008	937	373	900	12	18	32	yes	167	567
11-17-2008	1185	524	1500	12	17	36	yes	139	680

	PRESSURE			TIME			Reached	VOLUME	
	P_{peak}	P_{min}	P_{drop}	t_{start}	t_{peak}	t_{end}	boundary	@P_{peak}	TOTAL
Date	psi	psi	psi	s	s	s		ml	ml
9-11-2009	916	436	25	27	89	379	yes	52	293
9-23-2009	365	228	25	50	252	484	yes	168	362
8-3-2010	436	241	150	22.25	22.7	23.88	yes	113	408
8-10-2010	414	185	50	18.746	24.1	39	no	134	506
9-3-2010	914	581	250	21.6	23	33	yes	30	280
9-13-2010	924	459	250	20.9	24	38	yes	83	423
10-13-2010	2883	770	200	22	28.9	30	yes	58	67
10-13-2010	2553	2413	450	21.3	28	30.3	yes	56	75
10-14-2010	410	244	30	20	25.8	39.9	yes	48	166
10-14-2010	317	156	30	20.7	25.8	26.9	yes	43	52
10-21-2010	2513	1218	100	20	27.4	29	yes	62	75
10-21-2010	405	205	30	19.7	26.4	37.2	yes	56	146
11-5-2010	883	436	1000	20.28	27	45	yes	58	210
11-9-2010	2558	2558	450	10	19	19.1	yes	75	76
11-11-2010	862	281	100	126	189	311	yes	53	154
11-19-2010	402	317	80	12	96	147	yes	70	113
11-30-2010	492	170	75	17	18.2	19.7	yes	100	225
1-31-2011	823	453	1500	15.36	17	20	yes	108	382
2-10-2011	2453	2093	0	12	157	320	yes	121	257
2-10-2011	587	419	100	76	197	843	no	101	639
2-23-2011	667	417	786	17.6	21	34	yes	93	418
3-3-2011	646	524	1800	14.59	16	19	yes	148	331
3-10-2011	2415	1773	0	11	165	300	yes	128	241
3-10-2011	220	64	200	22.21	109	720	no	73	581
3-17-2011	204	55	200	35	132	434	yes	81	333
3-30-2011	193	100	120	17	54	270	no	31	211
4-5-2011	661	280	400	10	18	47	yes	67	308
4-22-2011	748	246	150	15	53	179	no	32	137
5-4-2011	3032	950	0	11	165	300	yes		2408
5-12-2011	126	86	30	64	87	218	yes	19	128
5-19-2011	618	538	900	17.2	19	22	no	142	358
5-26-2011	112	39	0	23	55	84	yes	27	51
6-2-2011	122	58	15	14.4	15.5	19	no	92	383

C. Experimental Measured Leakoff and Aperture Thickness

EXP DATE	Spheroid size	Aperture in	Leakoff in	EXP DATE	Spheroid size	Aperture in	Leakoff in
6-17-2005	0.402	0.199	0.149	9-22-2008	N-A	0.141	0.072
9-14-2005	0.440	0.164	0.254	10-20-2008	N-A	0.182	0.182
9-21-2005	0.300	0.231	0.147	11-6-2008	0.262	0.173	0.117
10-5-2005	0.540	0.240	0.227	11-17-2008	N-A	0.162	0.119
10-7-2005	0.300	0.222	0.161	9-11-2009	0.850	0.172	0.464
10-28-2005	0.362	0.344	0.156	9-23-2009	0.270	0.341	0.174
11-11-2005	0.265	0.208	0.144	9-3-2010	0.262	0.165	0.126
2-1-2006	0.542	0.233	0.275	9-13-2010	0.289	0.186	0.156
2-14-2006	0.488	0.117	0.196	11-5-2010	N-A	0.152	0.086
3-3-2006	1.580	0.000	0.859	11-11-2010	N-A	0.090	0.057
4-14-2006	0.635	0.332	0.331	1-31-2011	N-A	0.186	0.064
8-11-2007	0.850	0.100	0.466	2-10-2011	0.798	0.343	0.413
9-17-2007	0.536	0.190	0.279	2-23-2011	0.260	0.203	0.162
9-27-2007	0.406	0.239	0.209	3-3-2011	N-A	0.175	0.059
6-18-2008	N-A	0.141	0.159	3-10-2011	N-A	0.411	0.101
6-25-2008	0.522	0.279	0.176	3-17-2011	N-A	0.450	0.068
7-2-2008	0.260	0.363	0.126	3-30-2011	N-A	0.409	0.093
7-8-2008	0.250	0.216	0.120	4-5-2011	N-A	0.148	0.073
7-17-2008	N-A	0.277	0.105	4-22-2011	N-A	0.125	0.073
8-14-2008	N-A	0.097	0.021	5-12-2011	N-A	0.240	0.027
8-25-2008	0.230	0.319	0.141	5-19-2011	N-A	0.154	0.144
8-30-2008	0.223	0.366	0.100	4-27-2011	N-A	0.387	0.080
9-15-2008	N-A	0.113	0.033	4-19-2011	N-A	0.545	0.077

D. Experimental pictures and plots

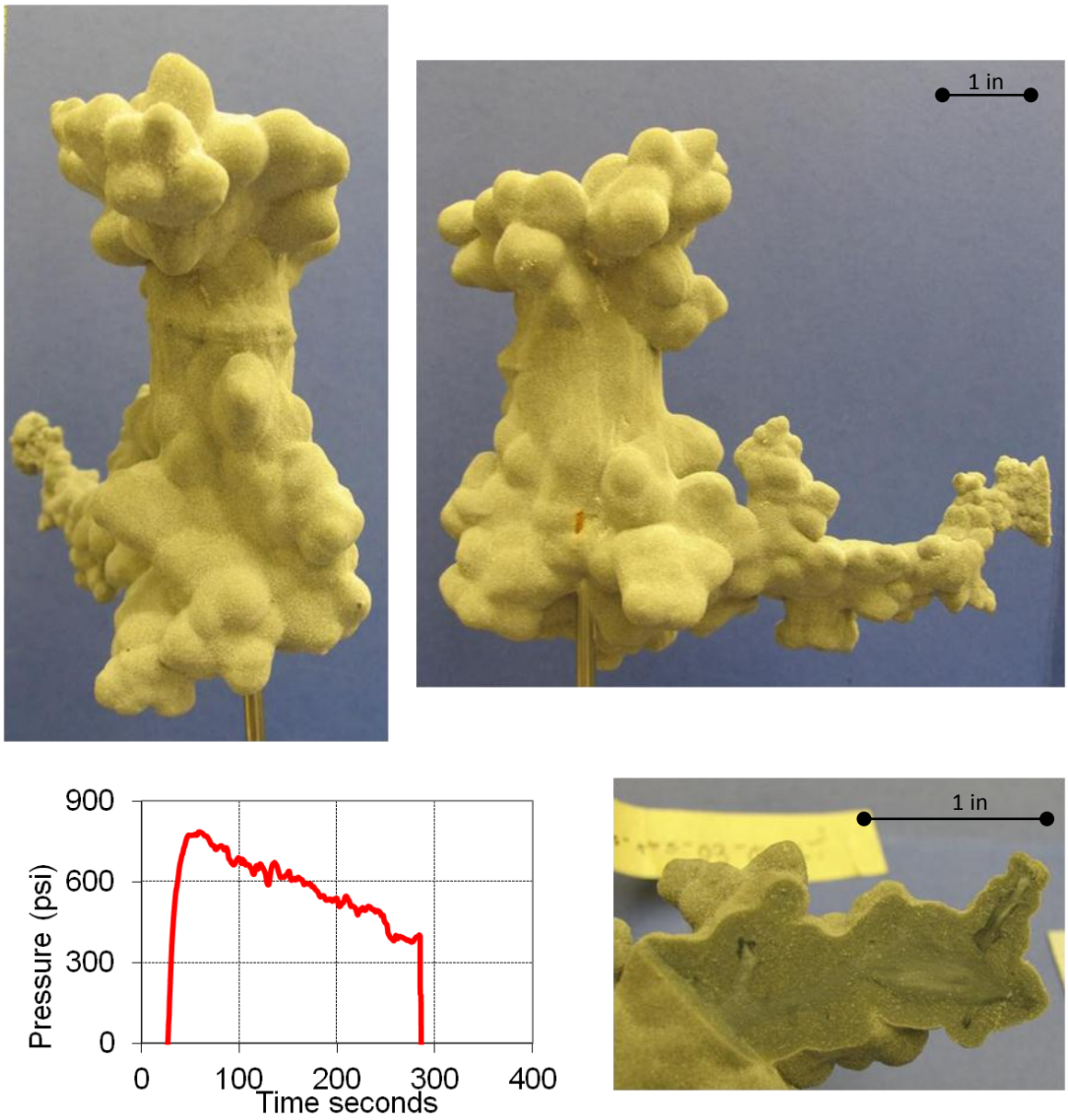

Figure A.1. Test 5-10-2005.

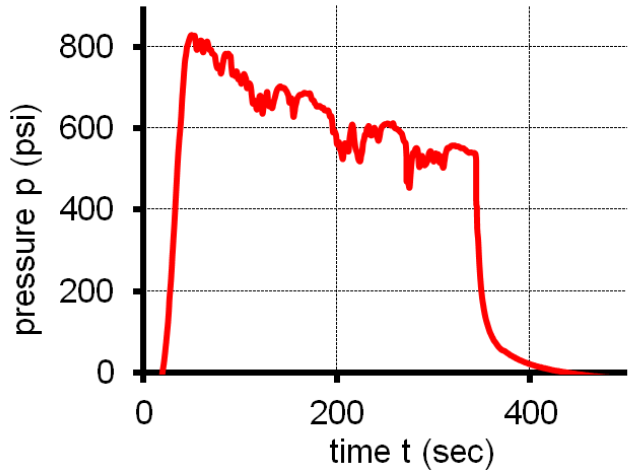

Figure A.2. Test 6-17-2005.

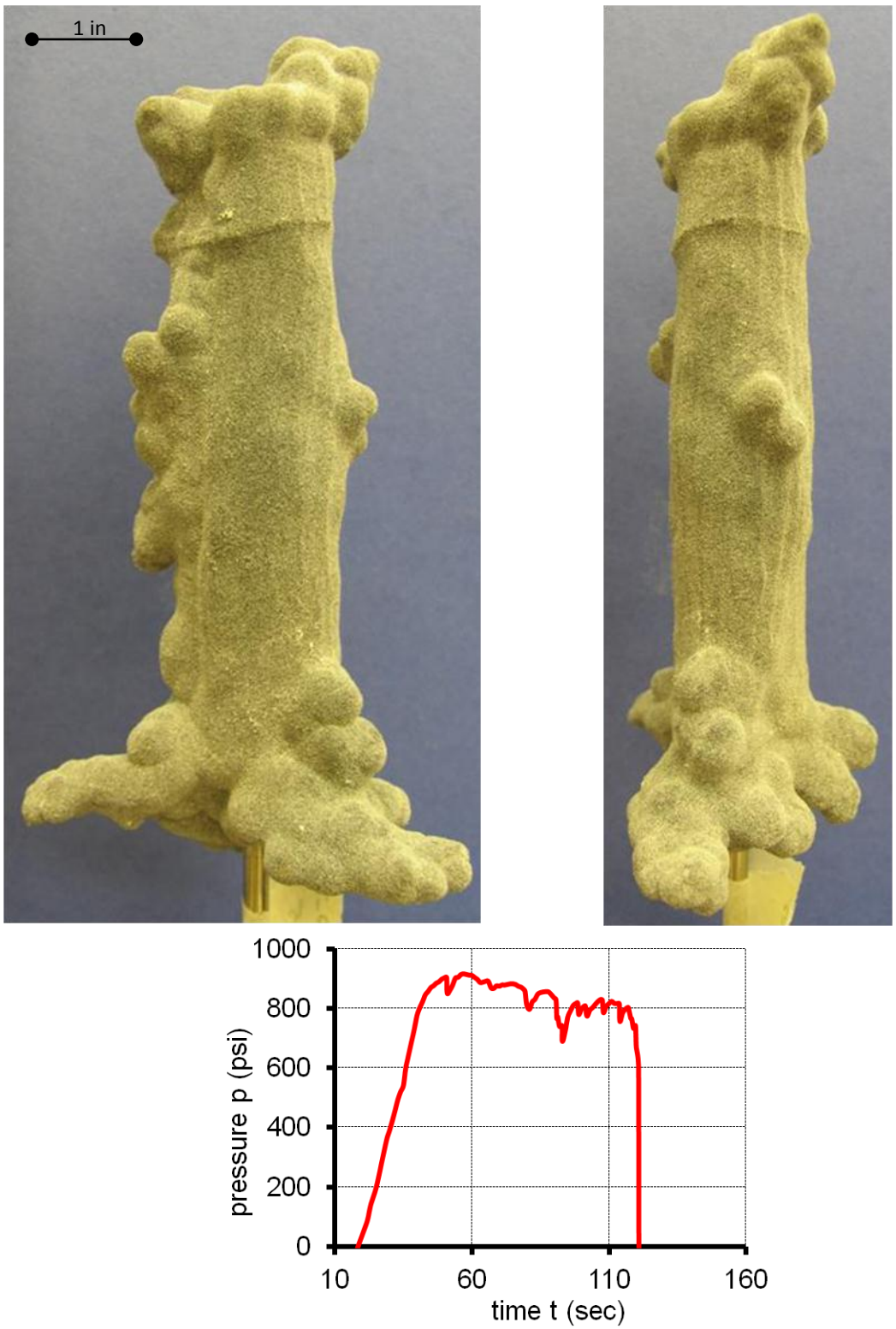

Figure A.3. Test 9-14-2005.

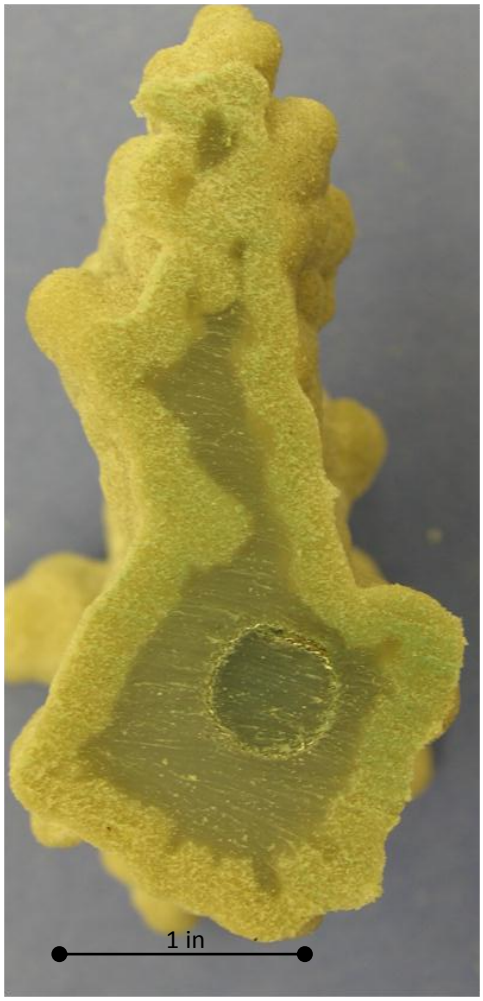

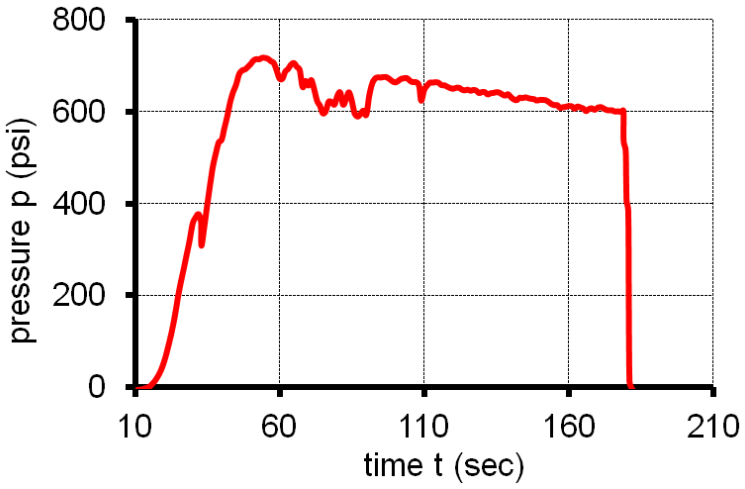

Figure A.4. Test 9-21-2005.

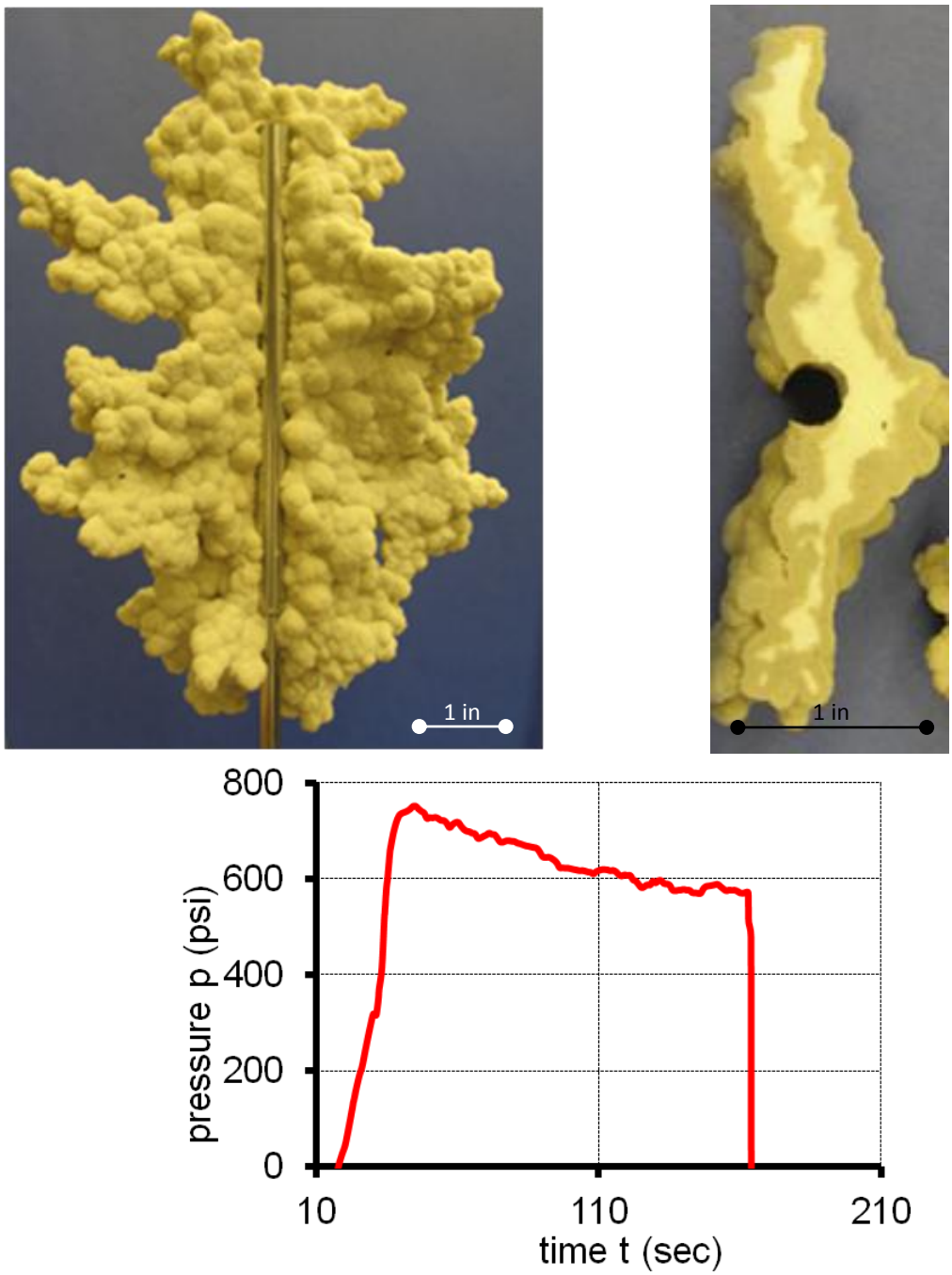

Figure A.5. Test 10-07-2005.

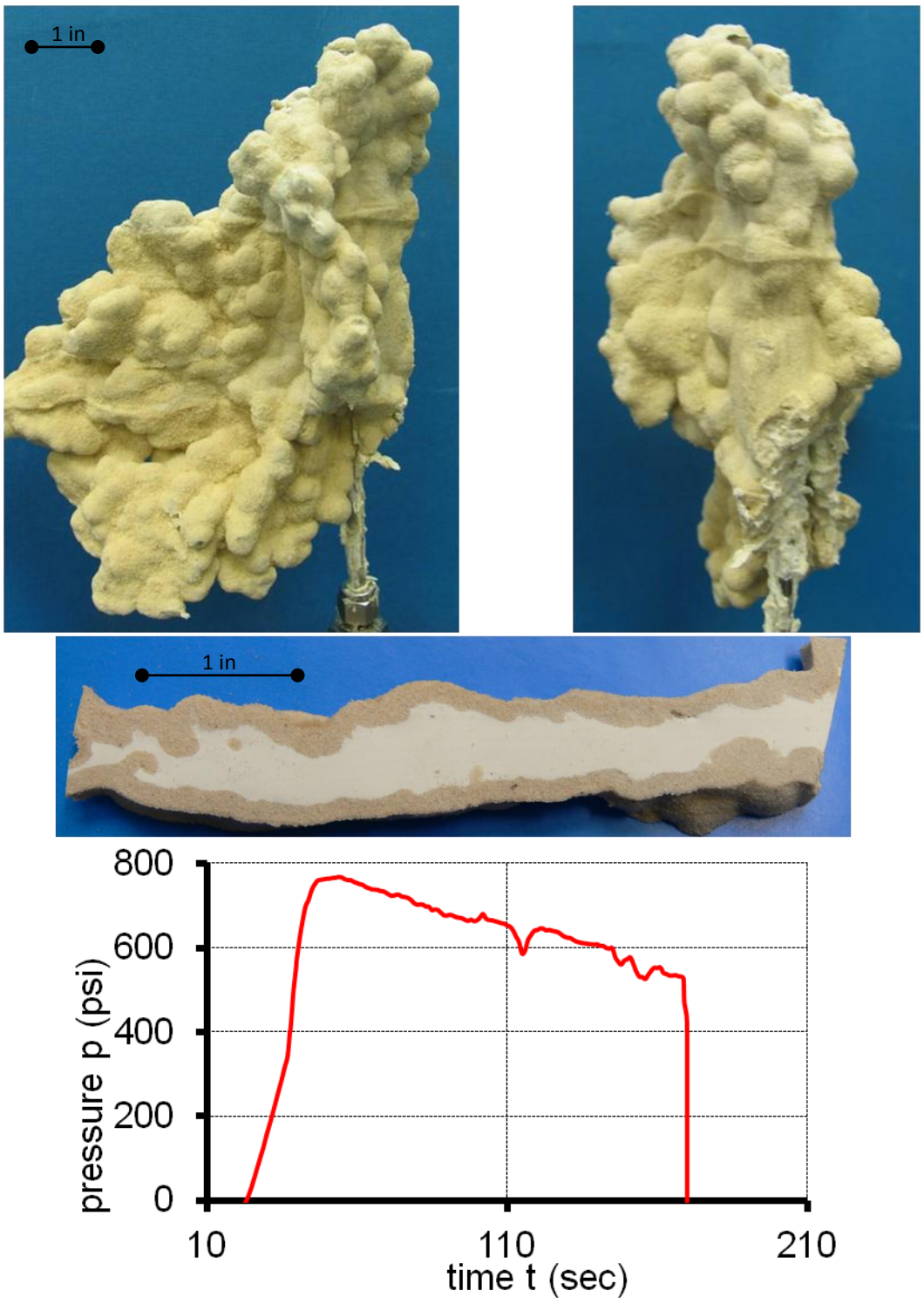

Figure A.6. Test 10-28-2005.

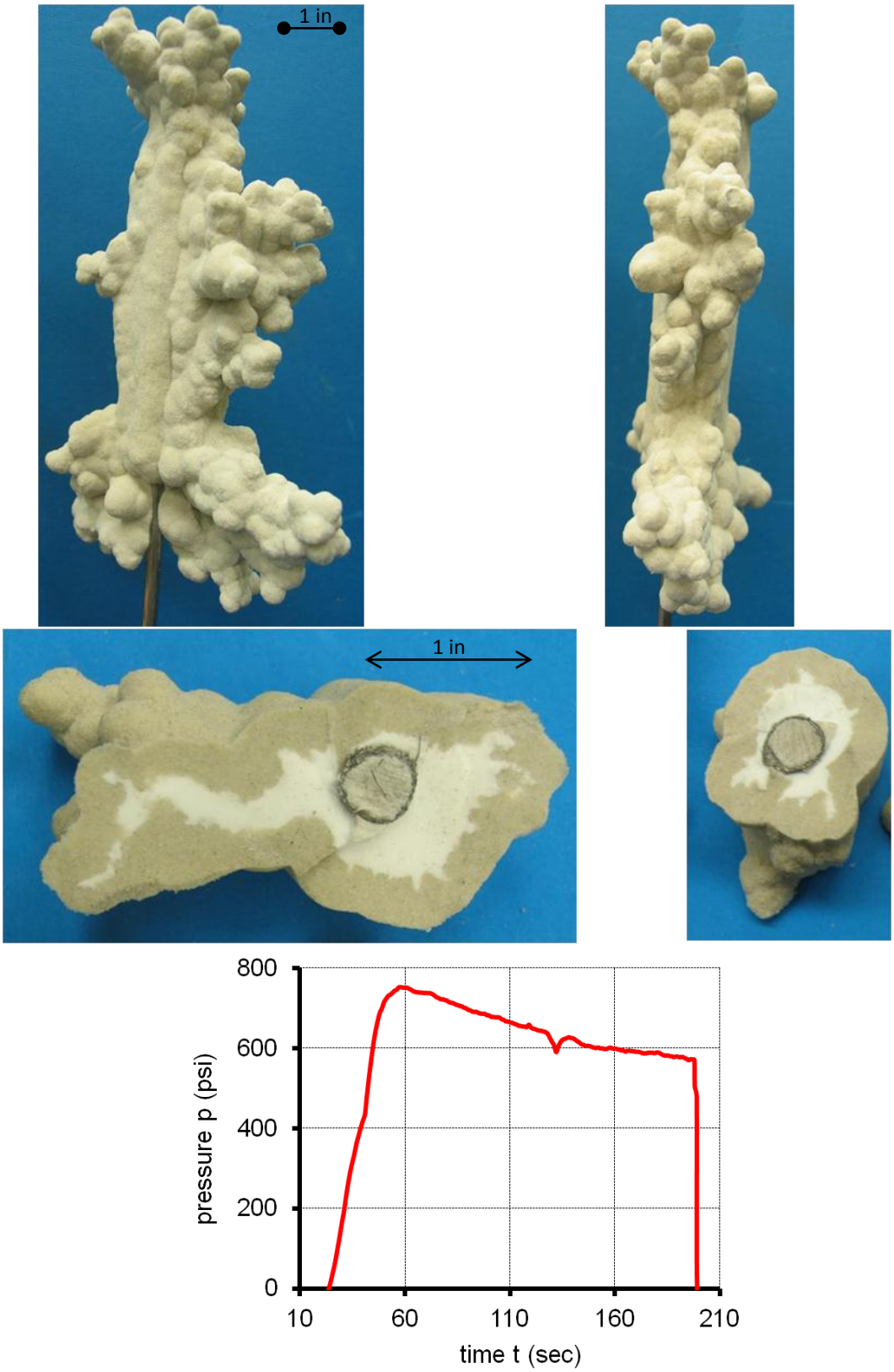

Figure A.7. Test 5-10-2005.

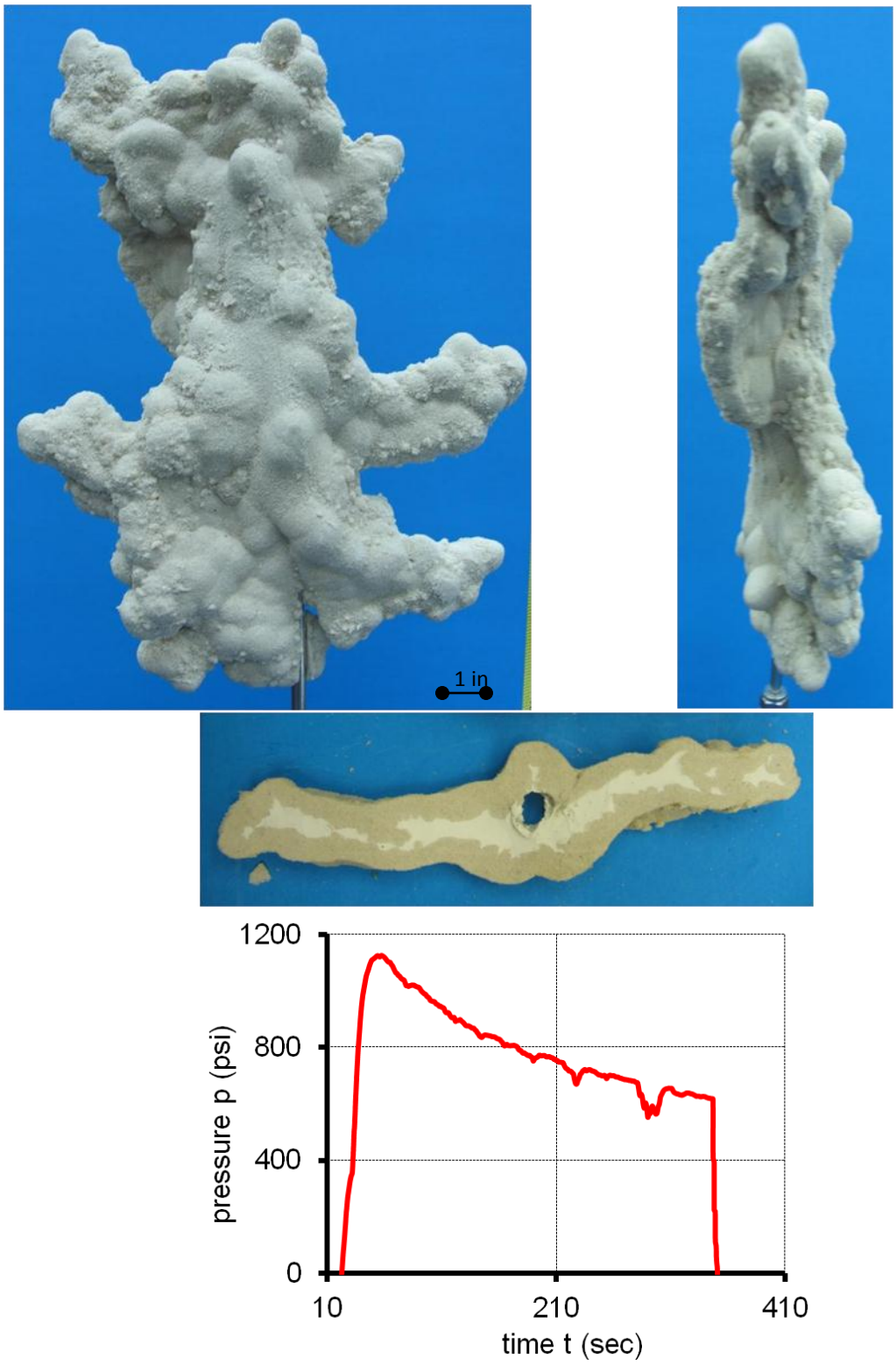

Figure A.8. Test 2-01-2006.

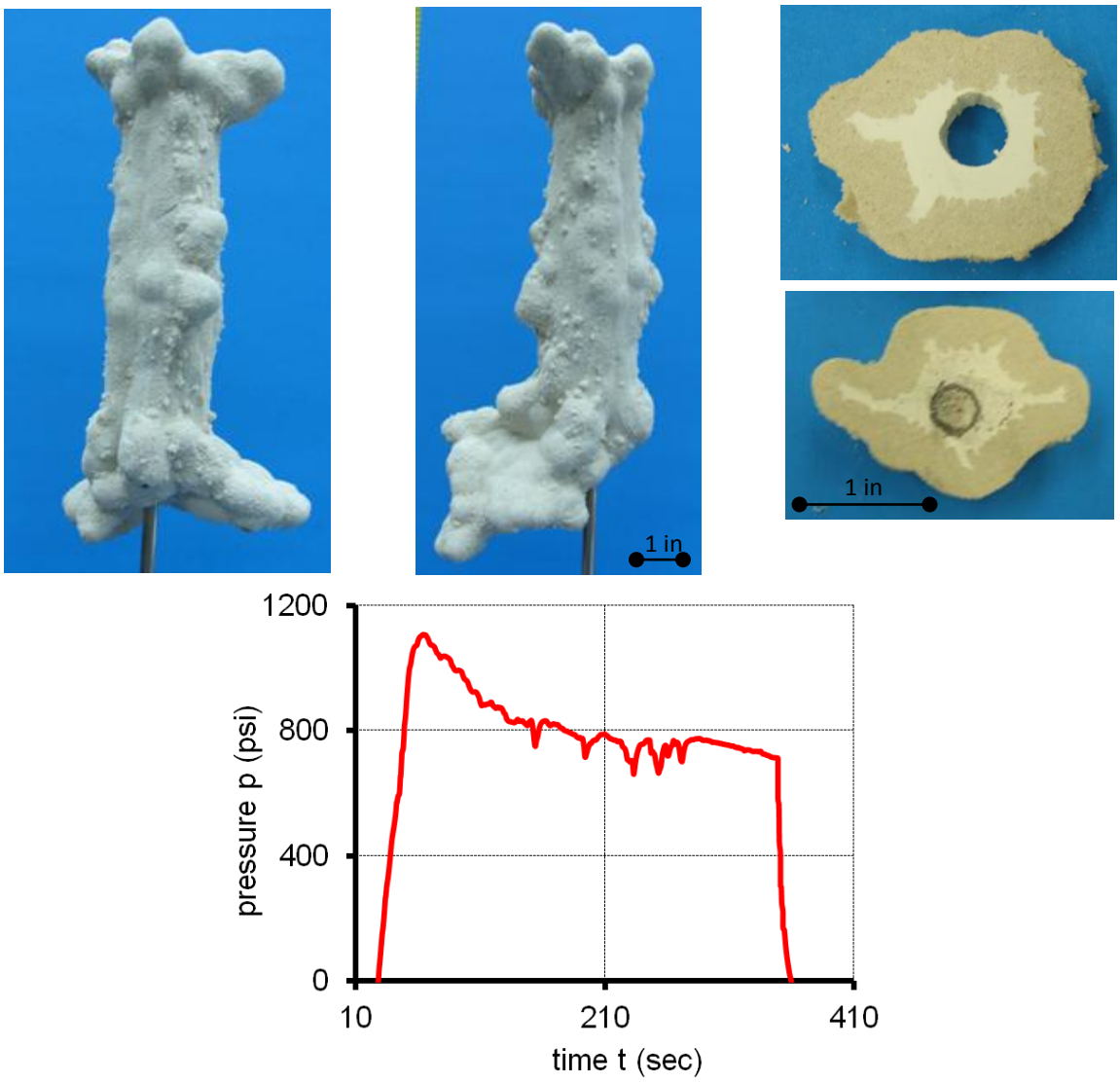

Figure A.9. Test 2-14-2006.

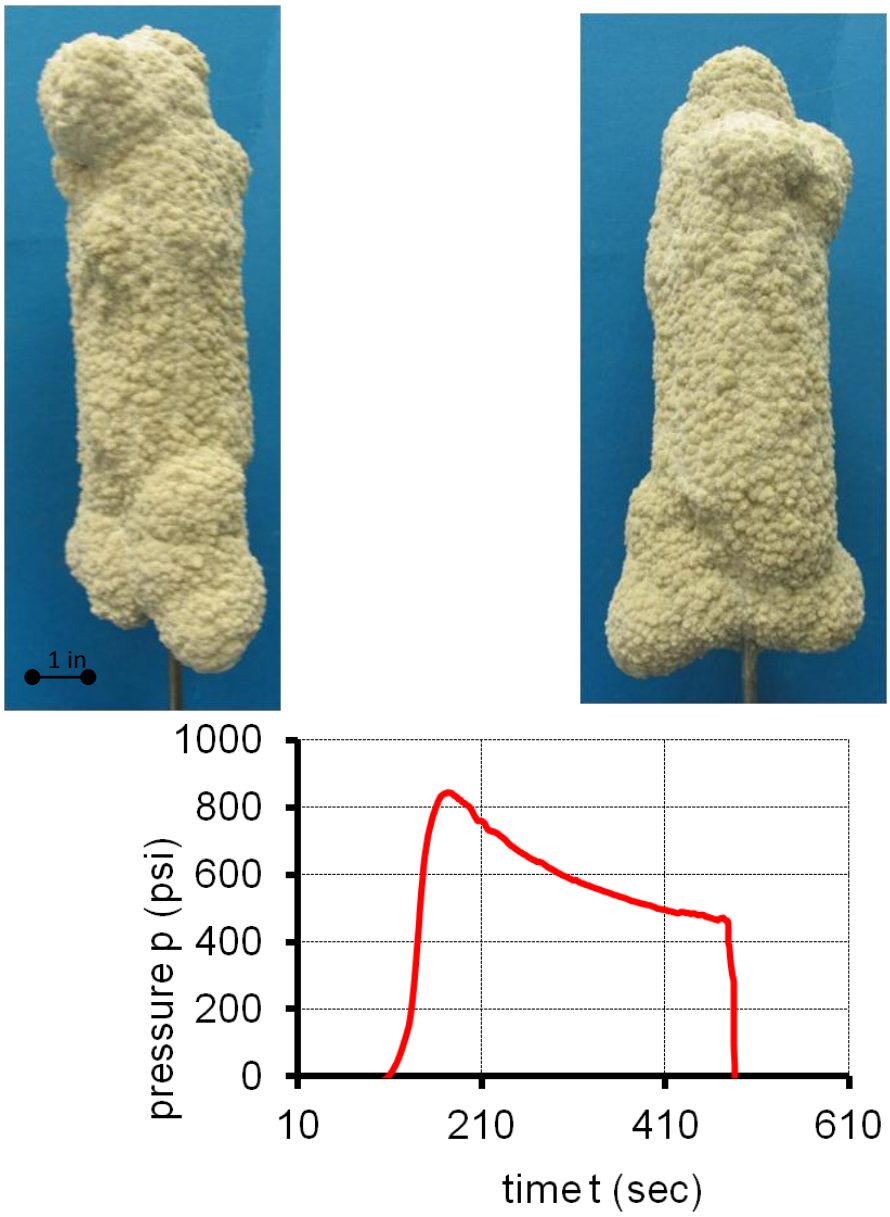

Figure A.10. Test 3-03-2006.

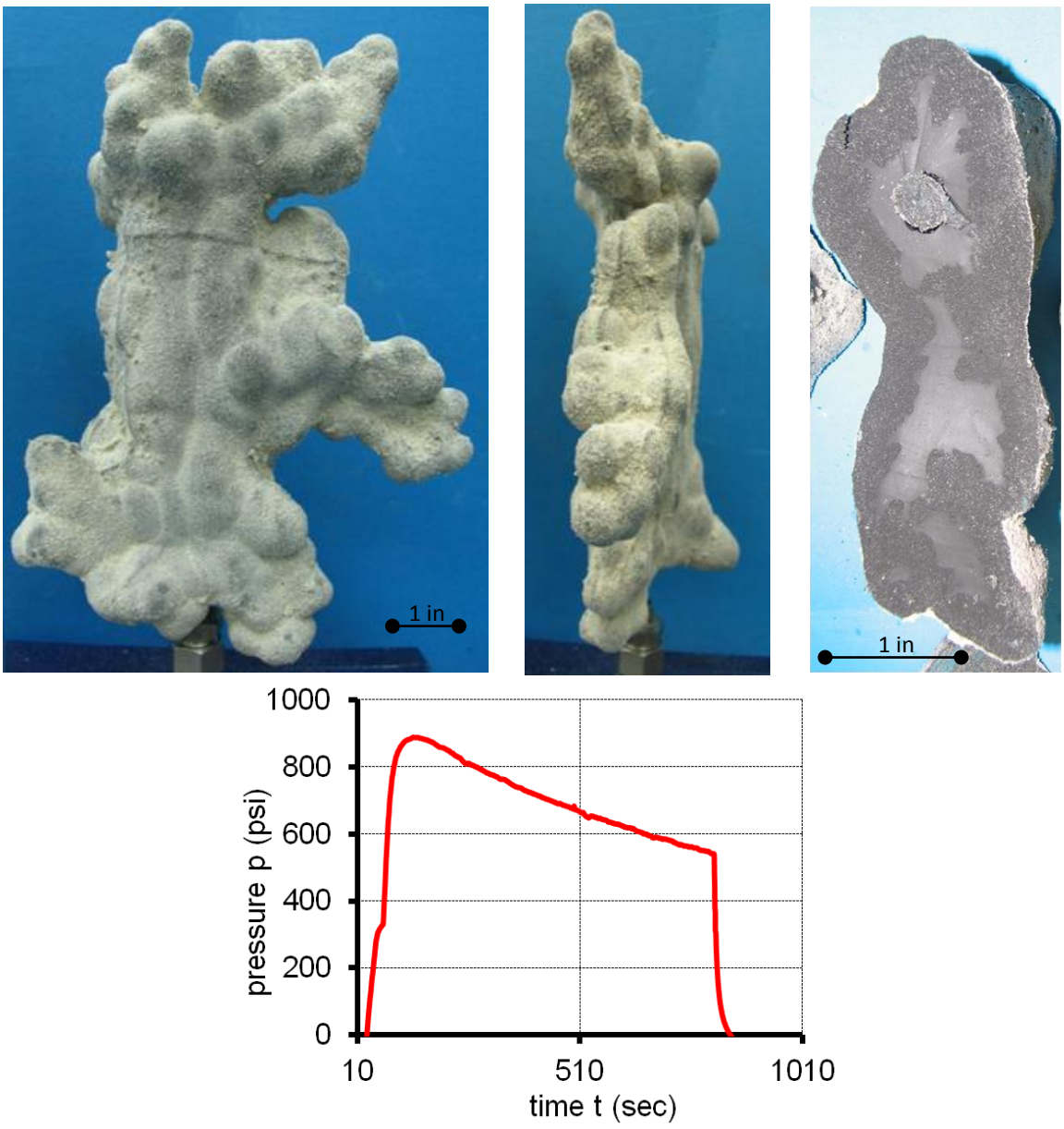

Figure A.11. Test 2-14-2006.

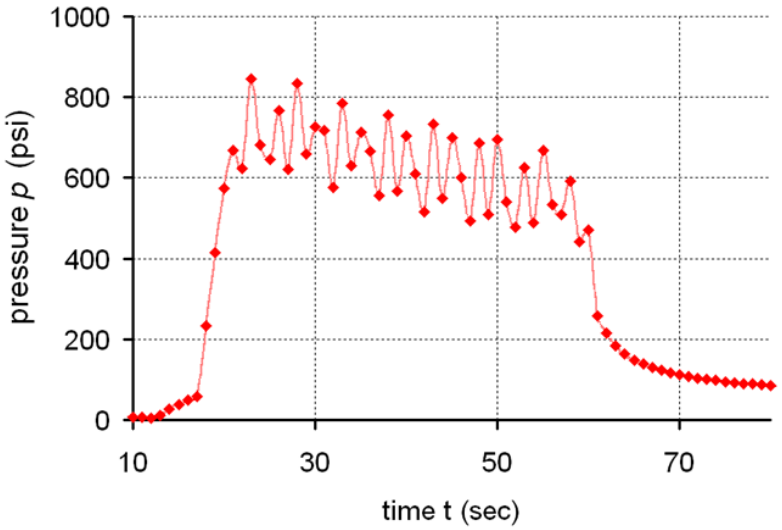

Figure A.12. Test 8-11-2007.

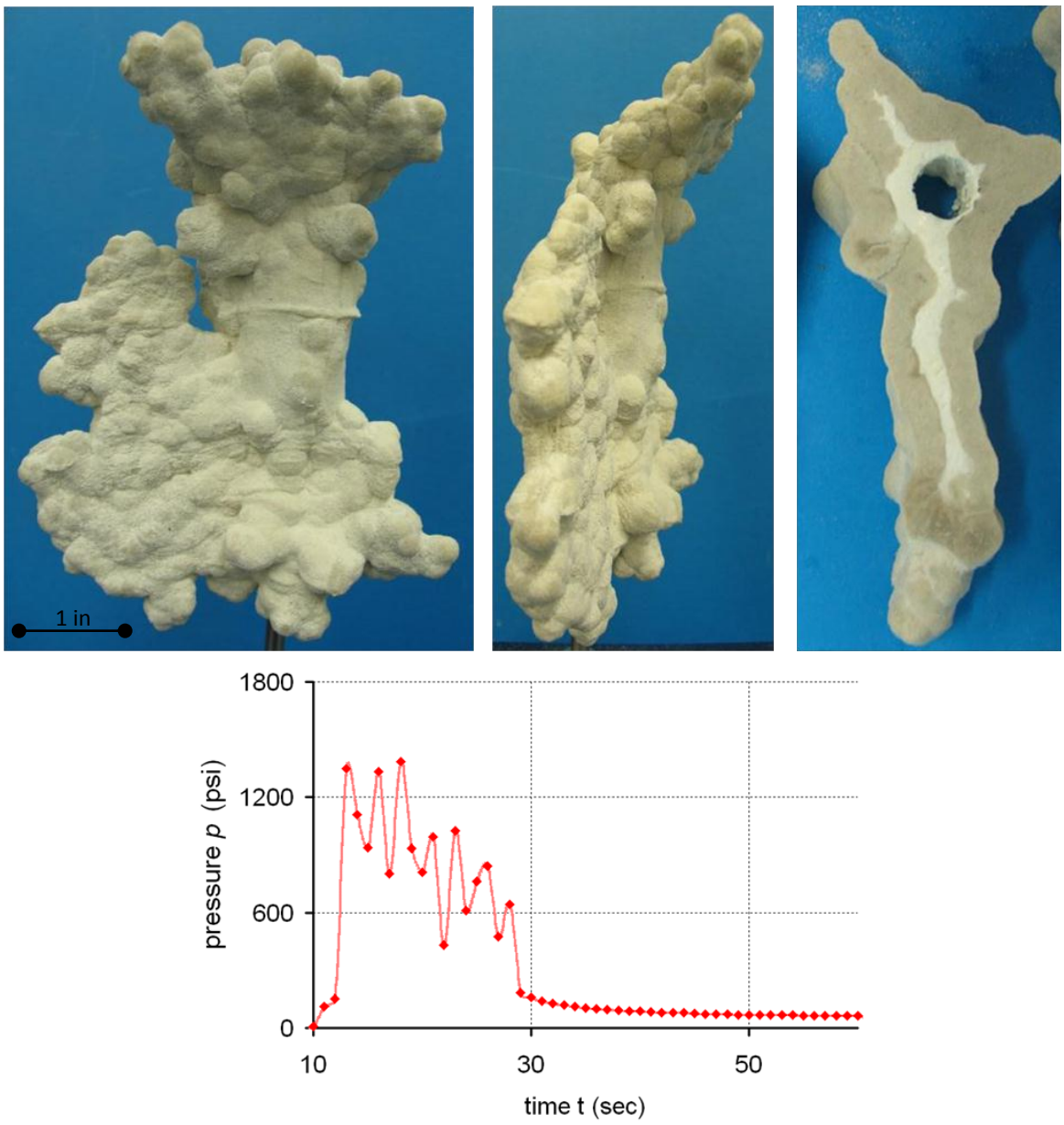

Figure A.13. Test 9-17-2007.

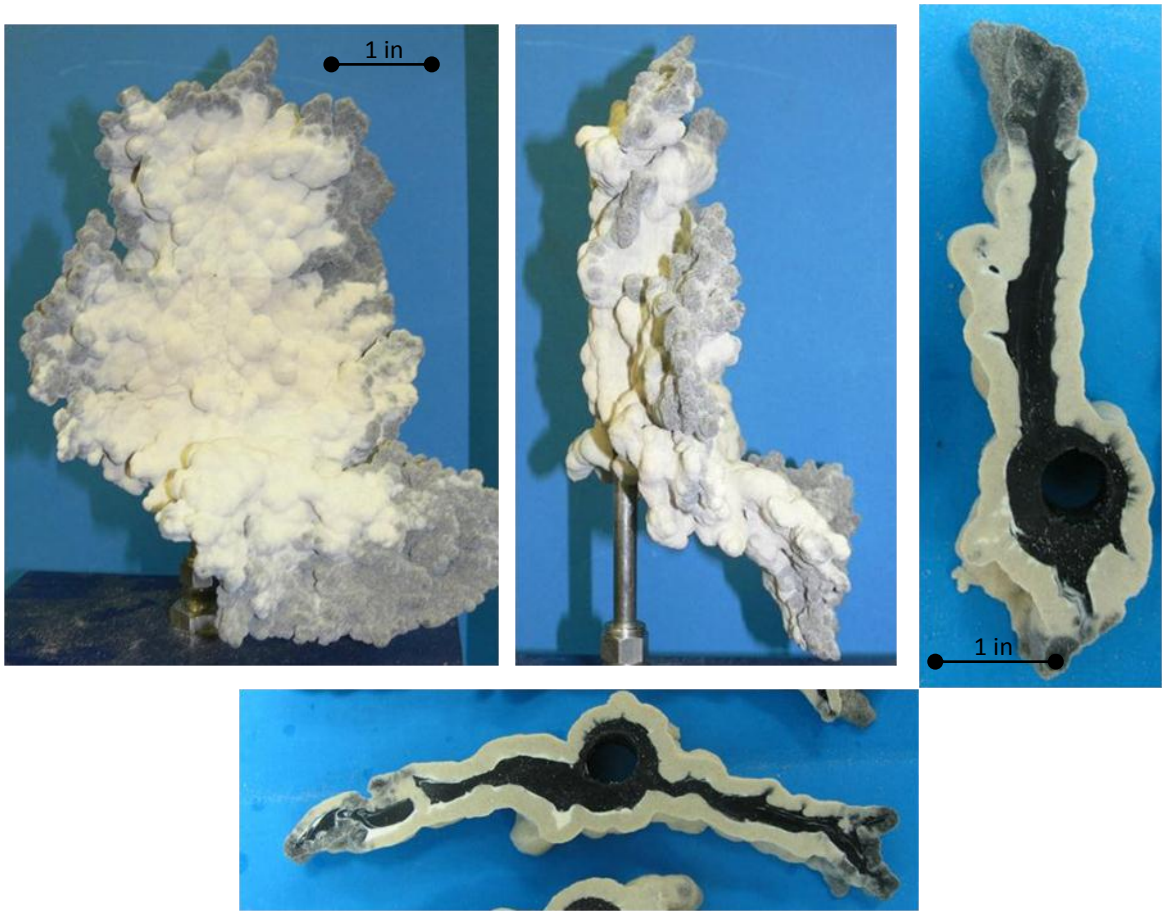

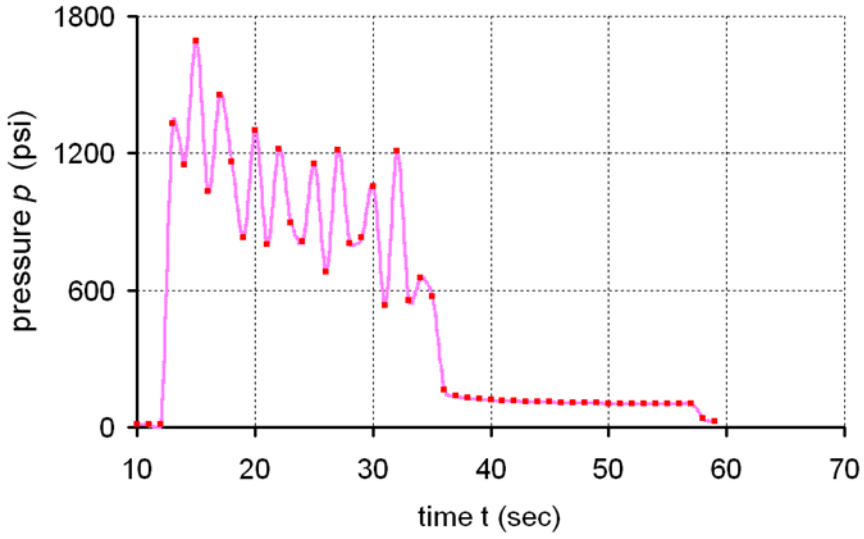

Figure A.14. Test 9-27-2007.

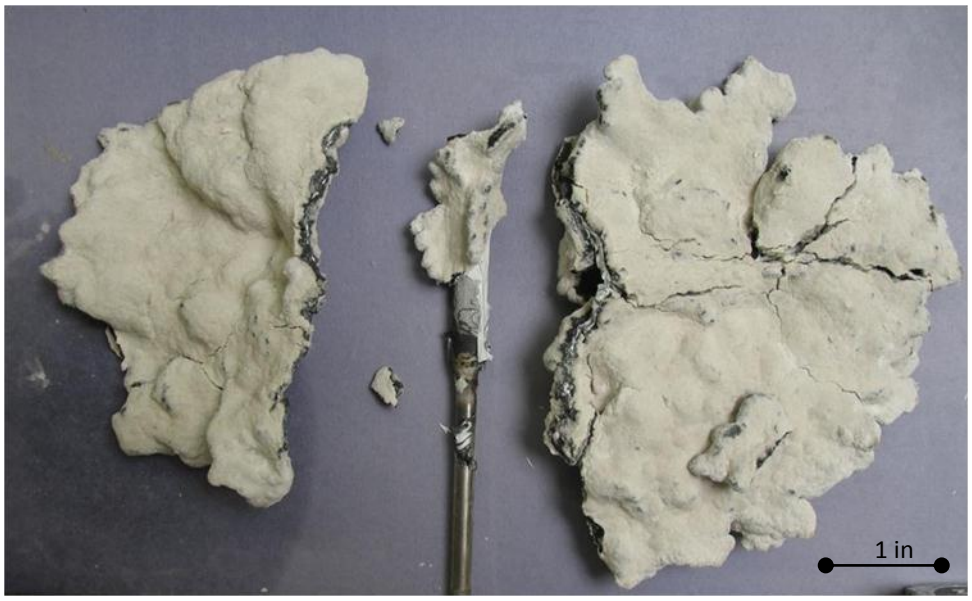

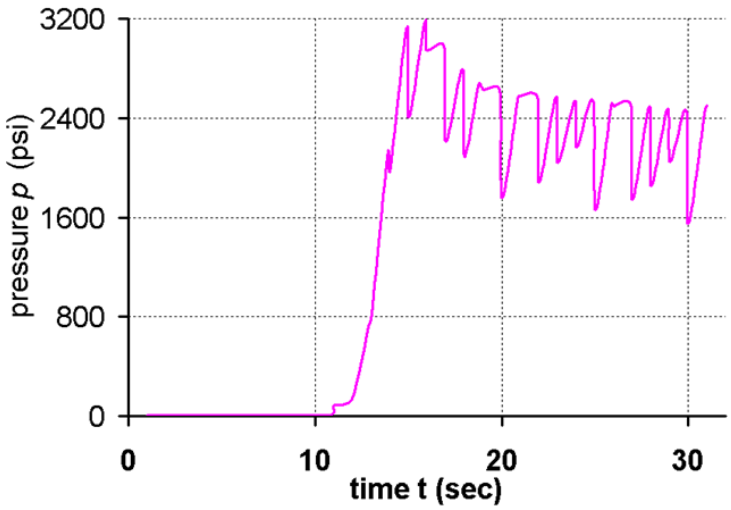

Figure A.15. Test 6-18-2008.

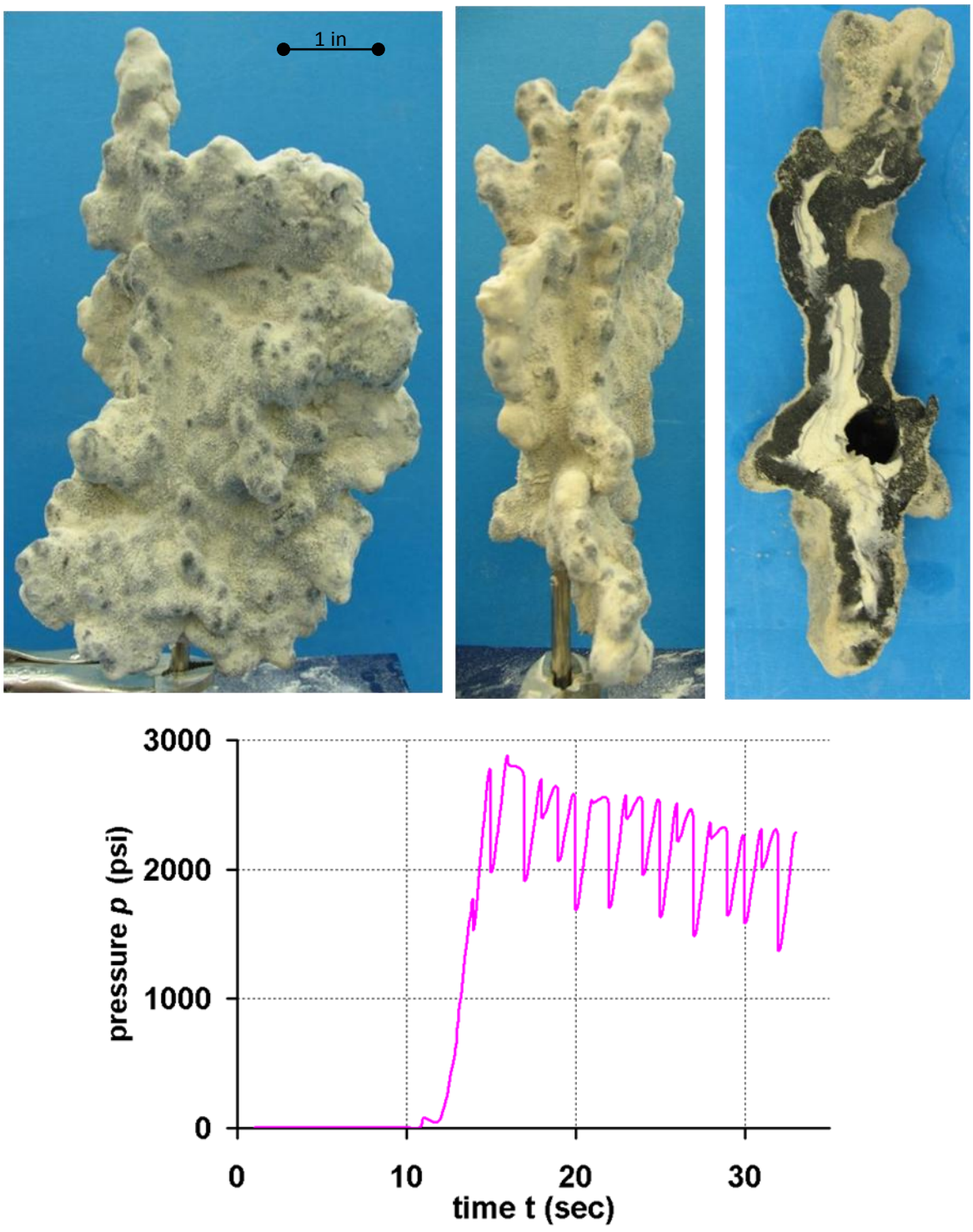

Figure A.16. Test 6-25-2008.

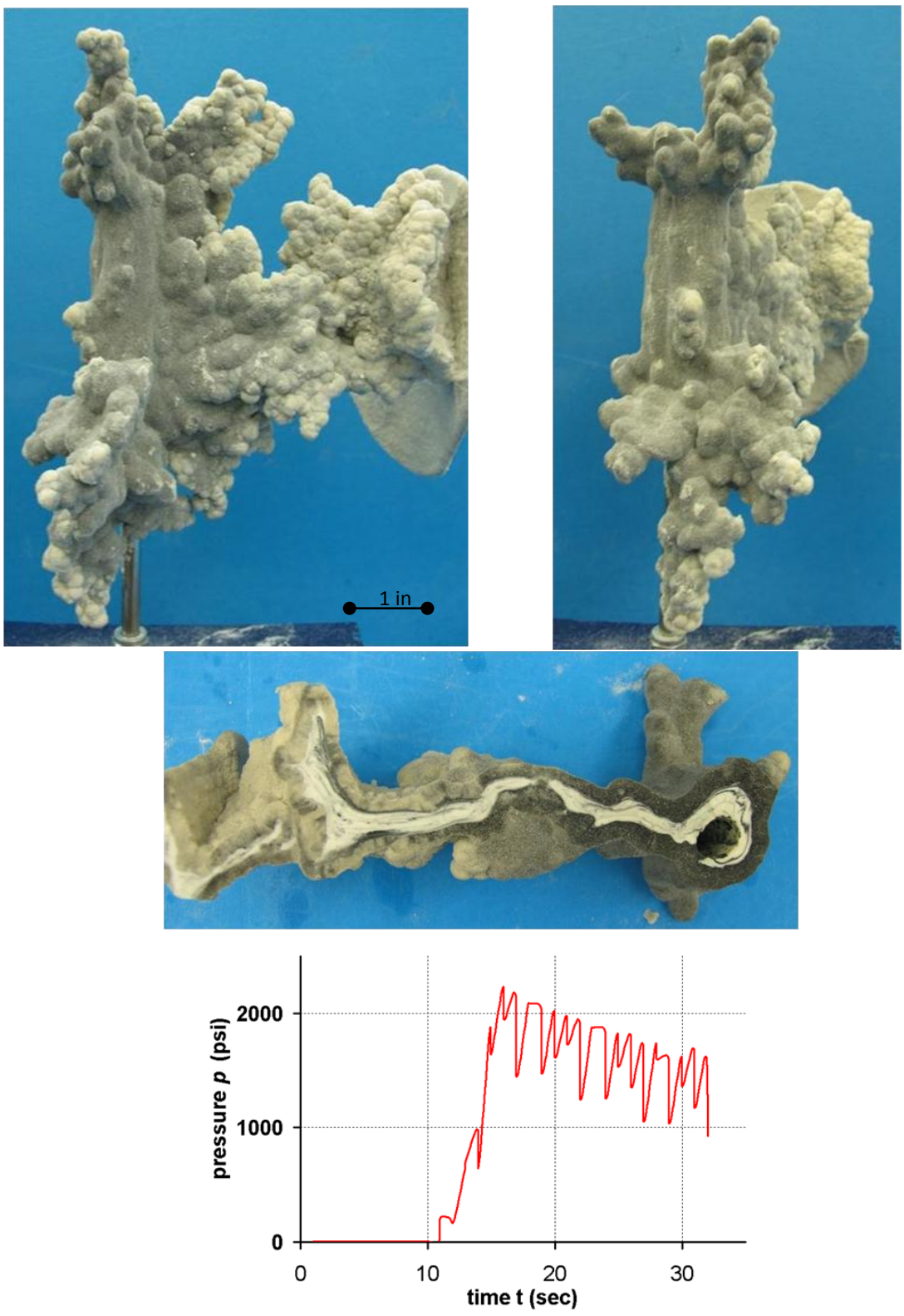

Figure A.17. Test 7-02-2008.

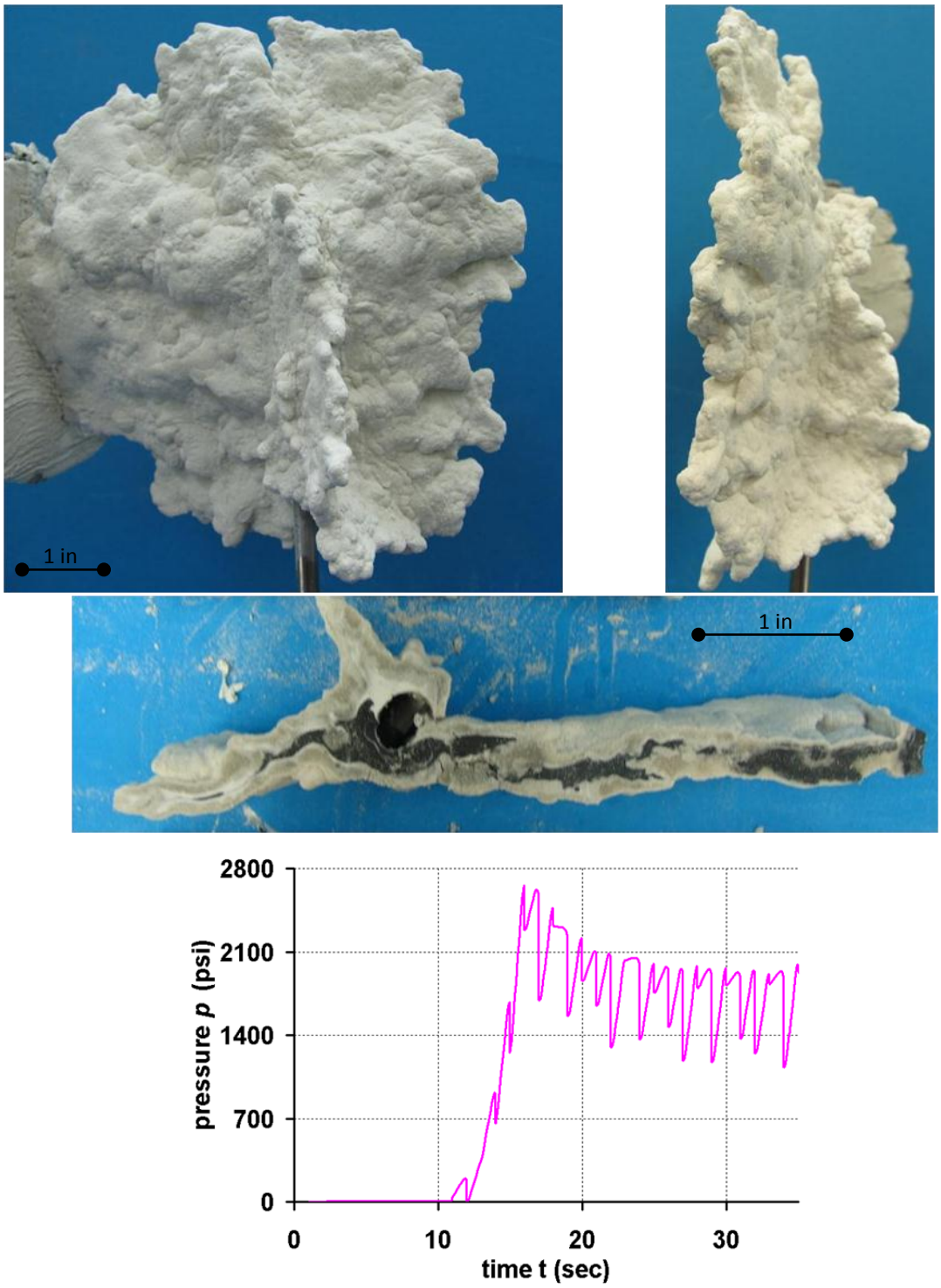

Figure A.18. Test 7-08-2008.

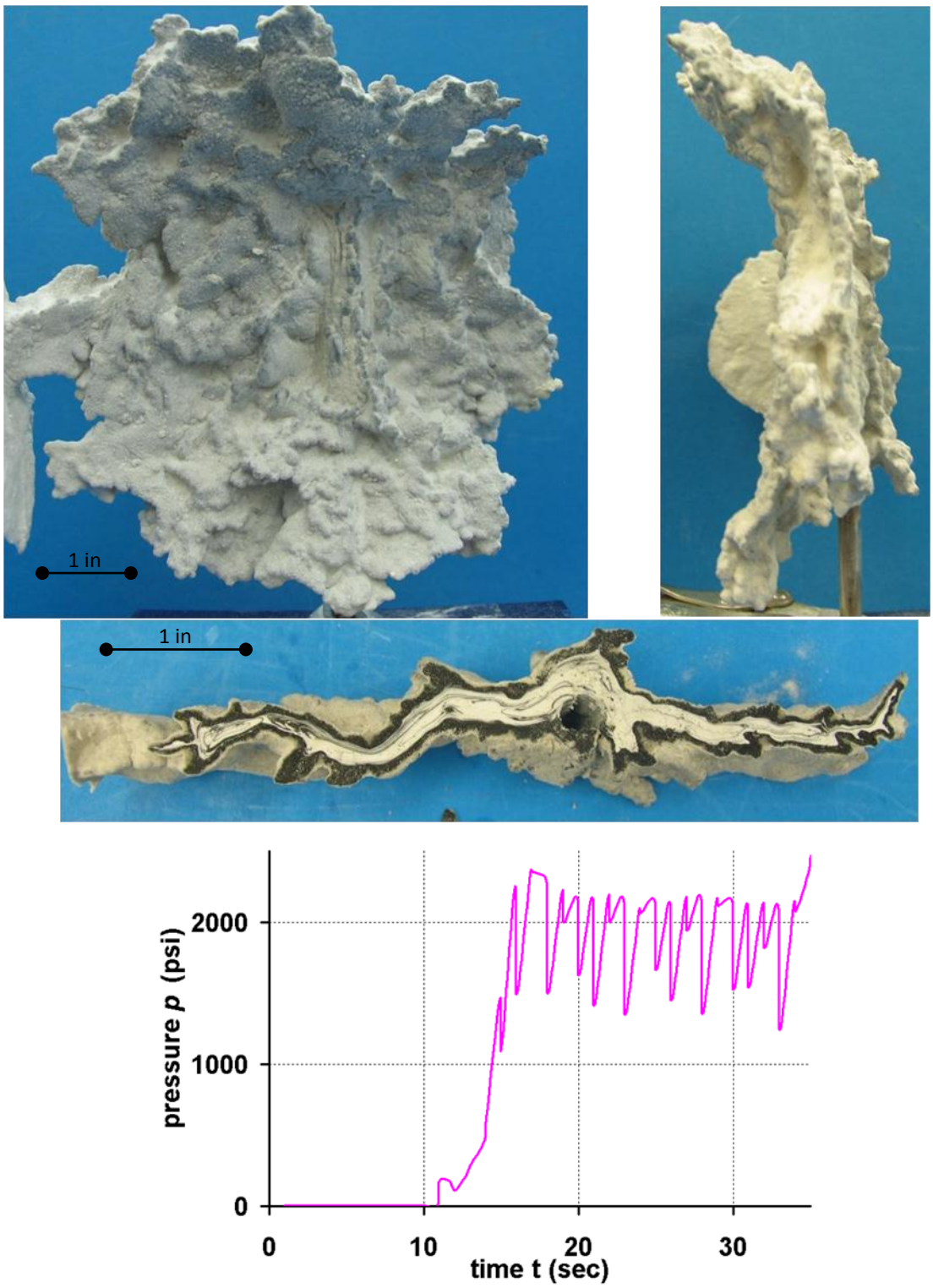

Figure A.19. Test 7-17-2008.

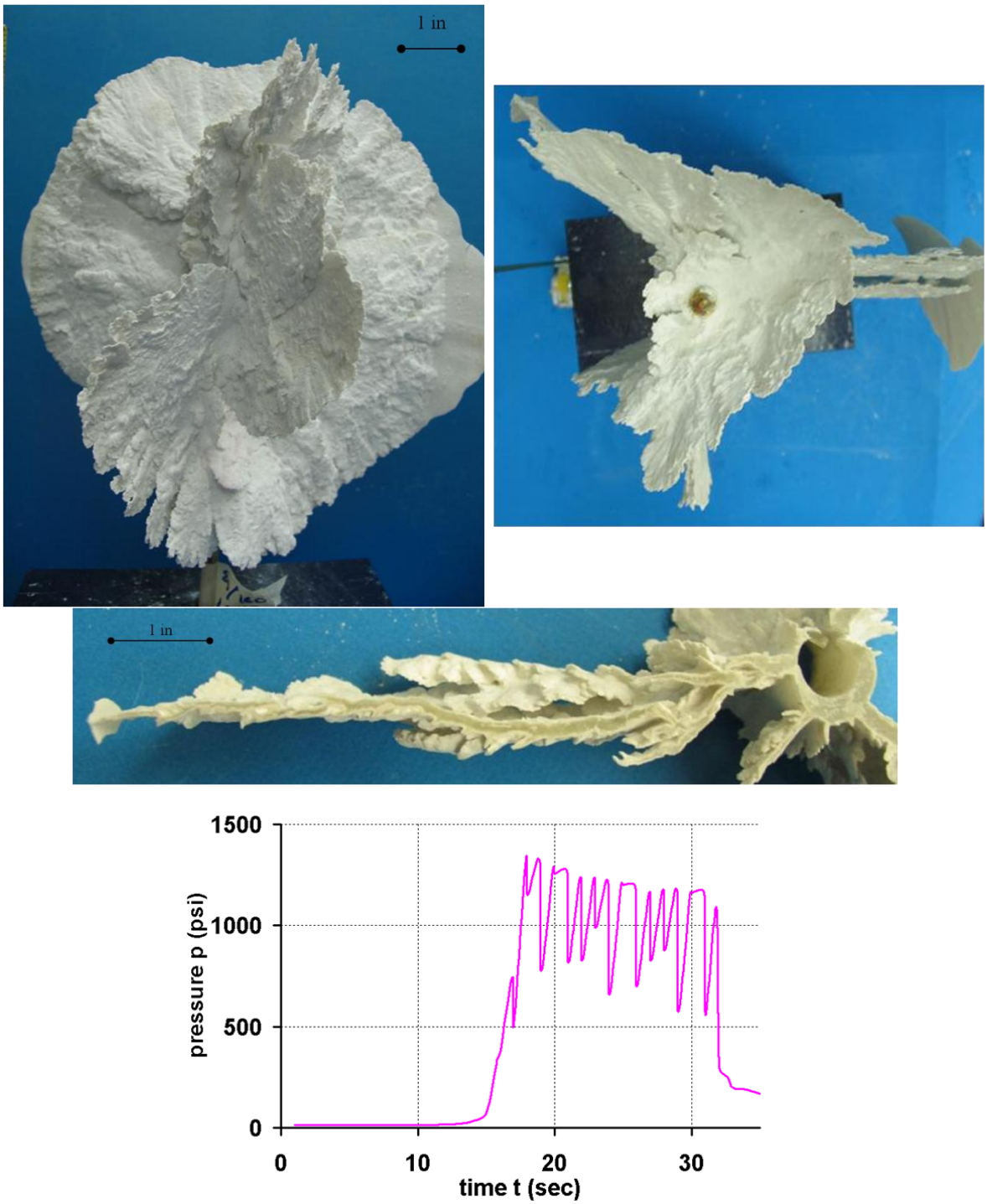

Figure A.20. Test 8-14-2008.

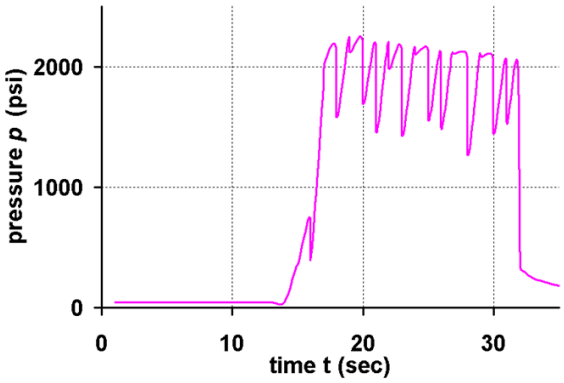

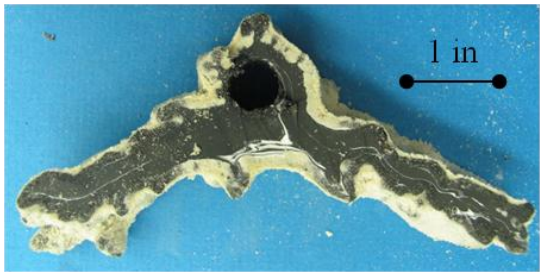

Figure A.21. Test 8-25-2008.

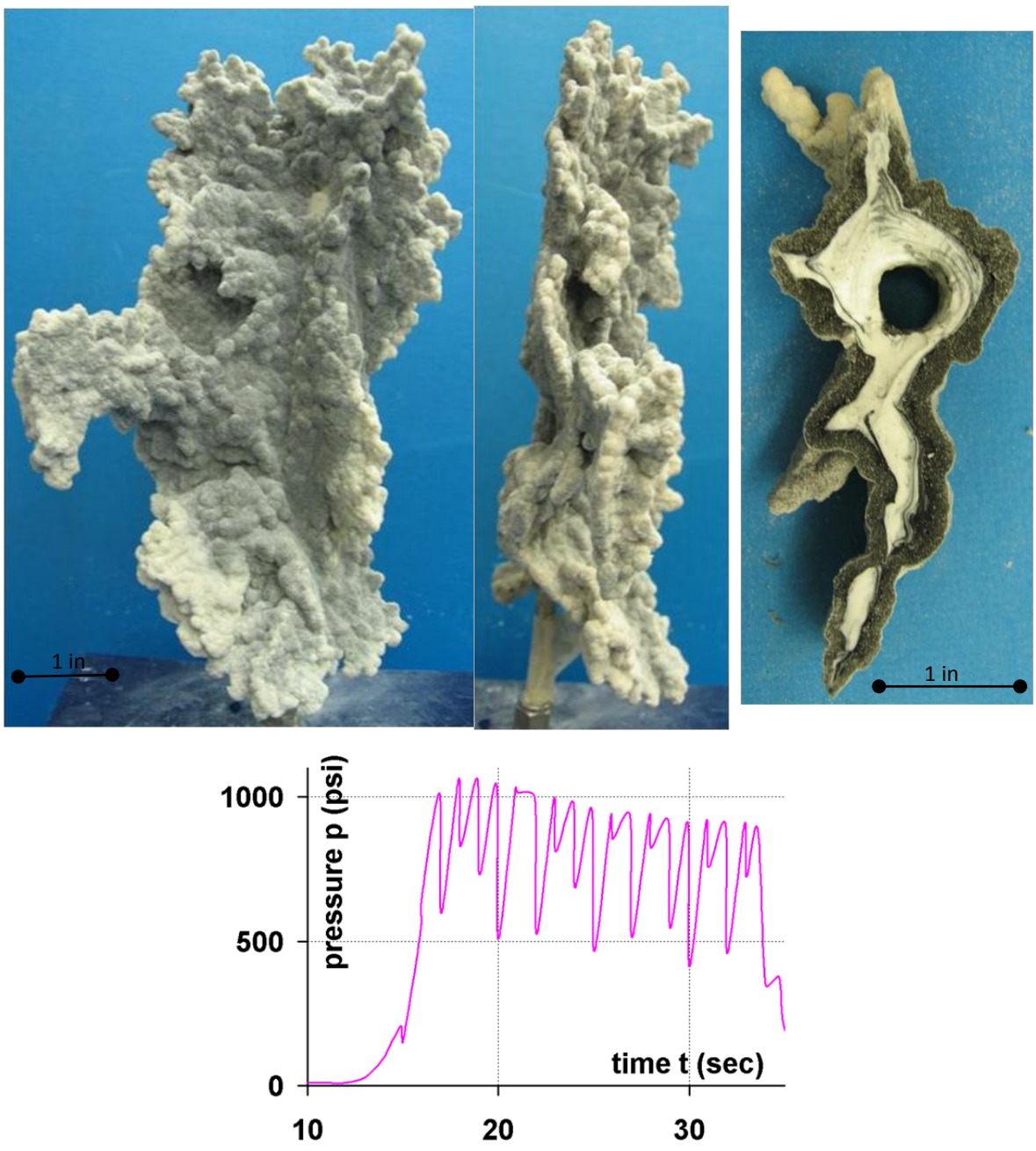

Figure A.22. Test 8-30-2008.

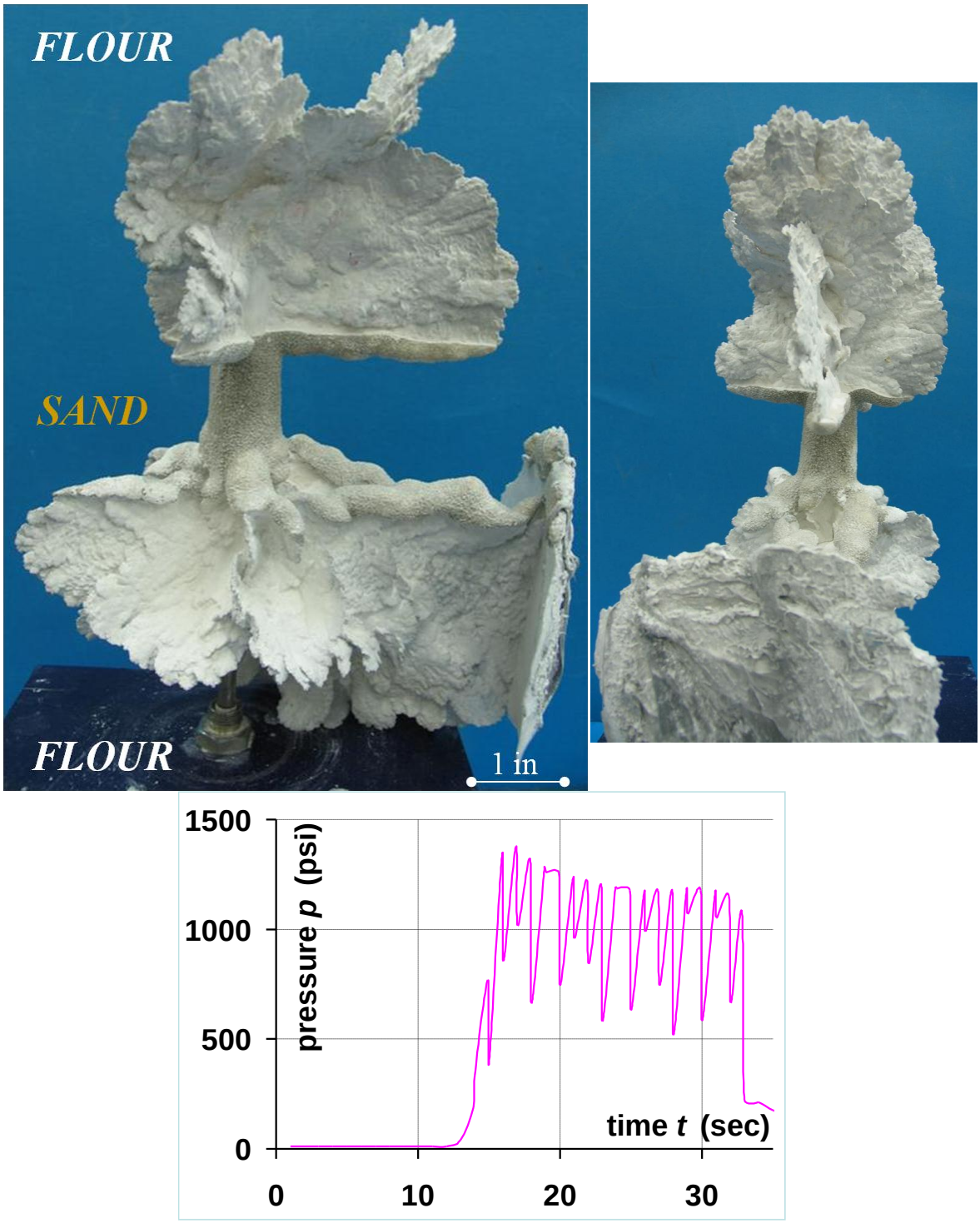

Figure A.23. Test 9-15-2008.

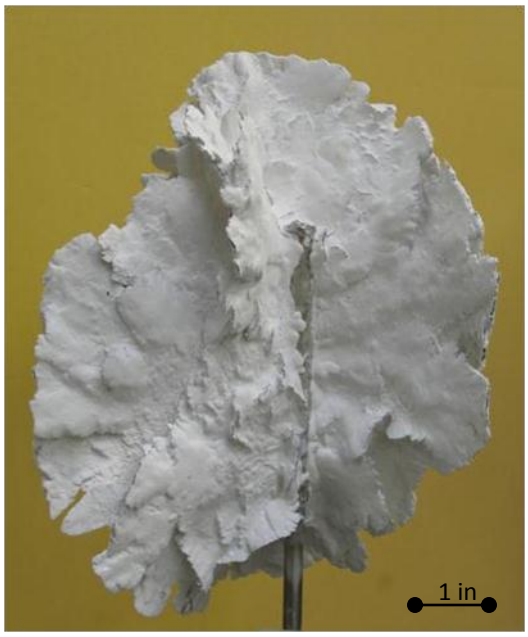

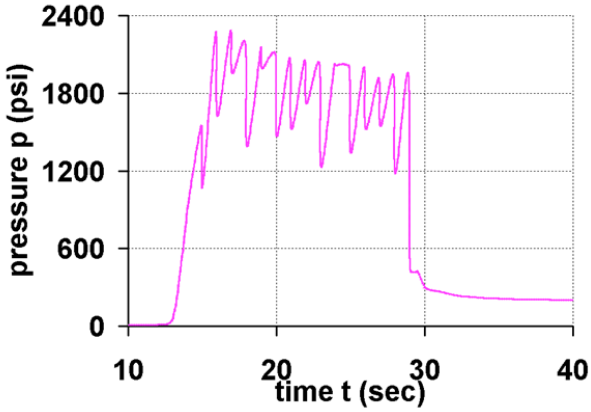

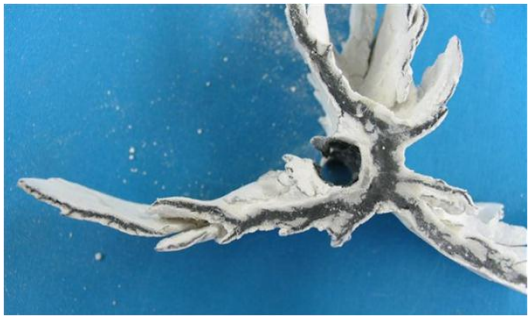

Figure A.24. Test 9-22-2008.

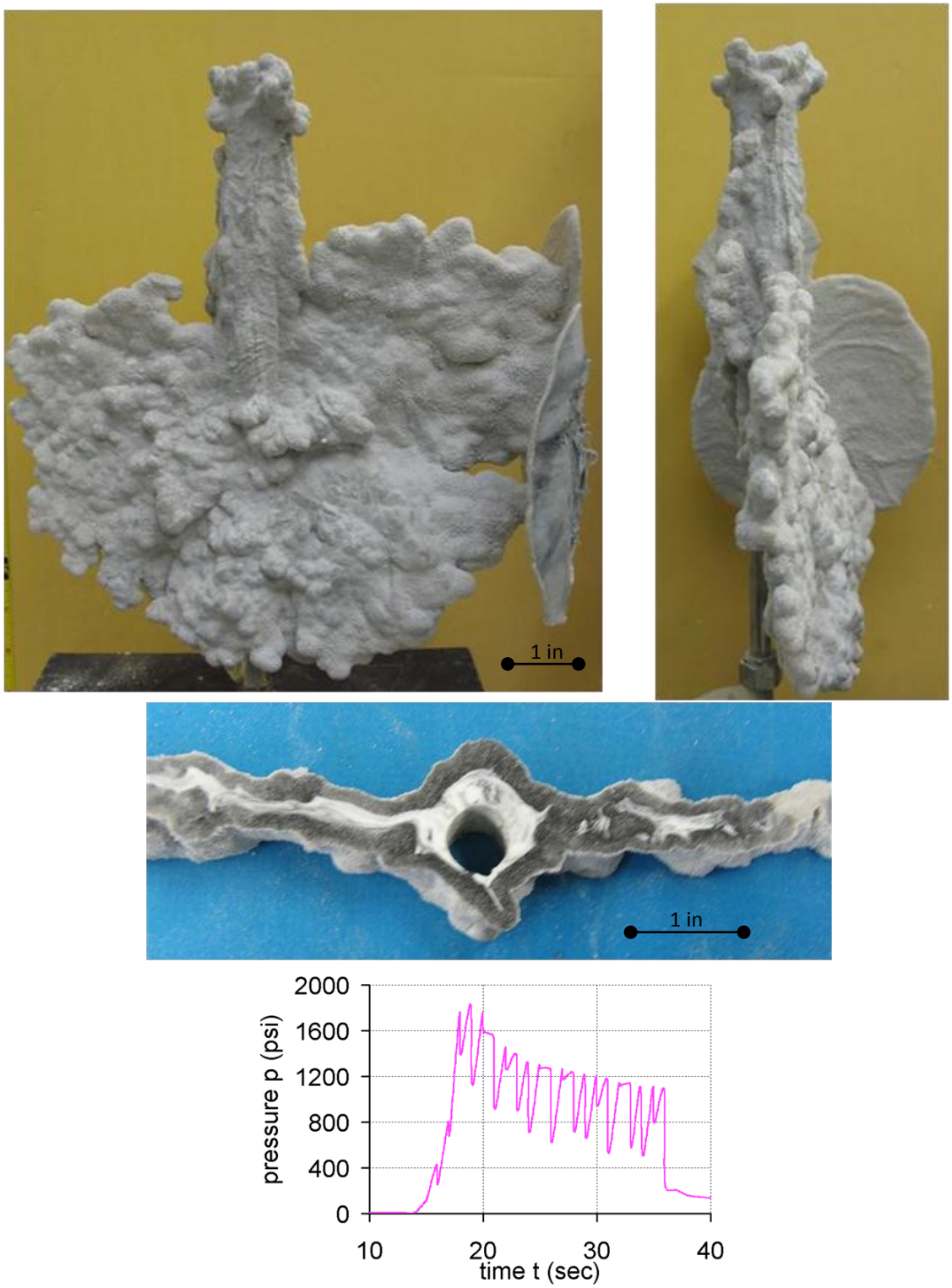

Figure A.25. Test 10-20-2008.

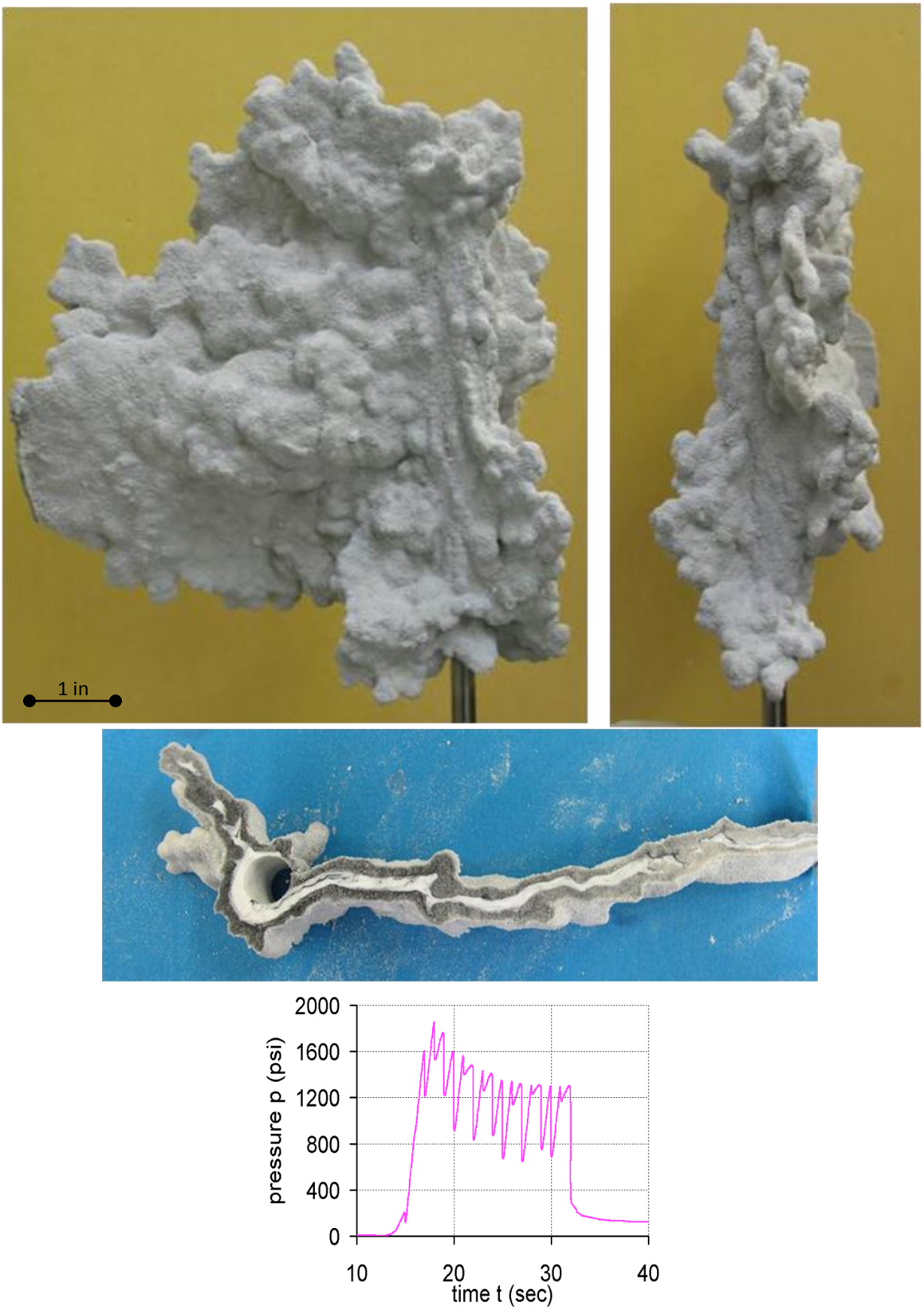

Figure A.27. Test 11-06-2008.

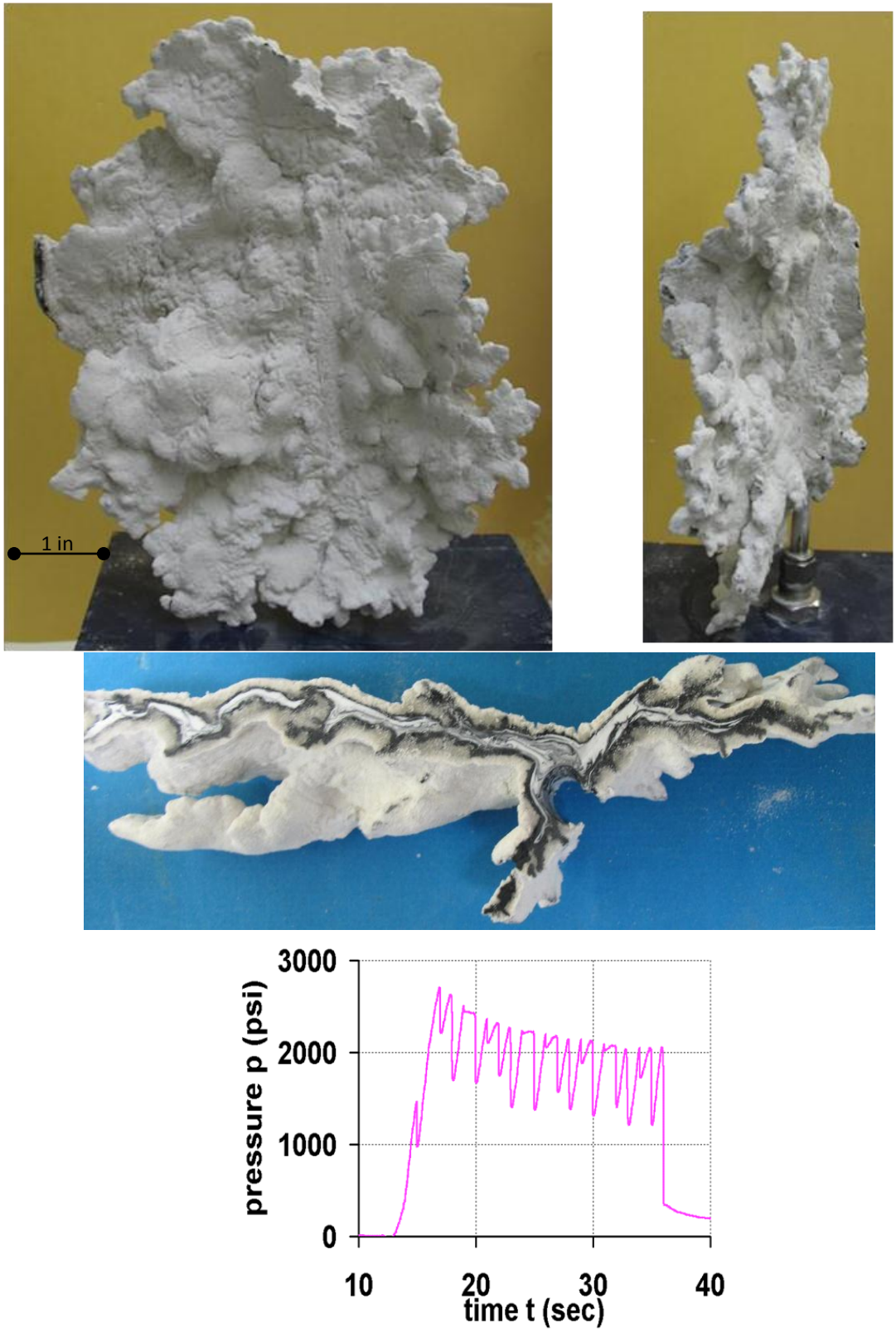

Figure A.28. Test 11-17-2008.

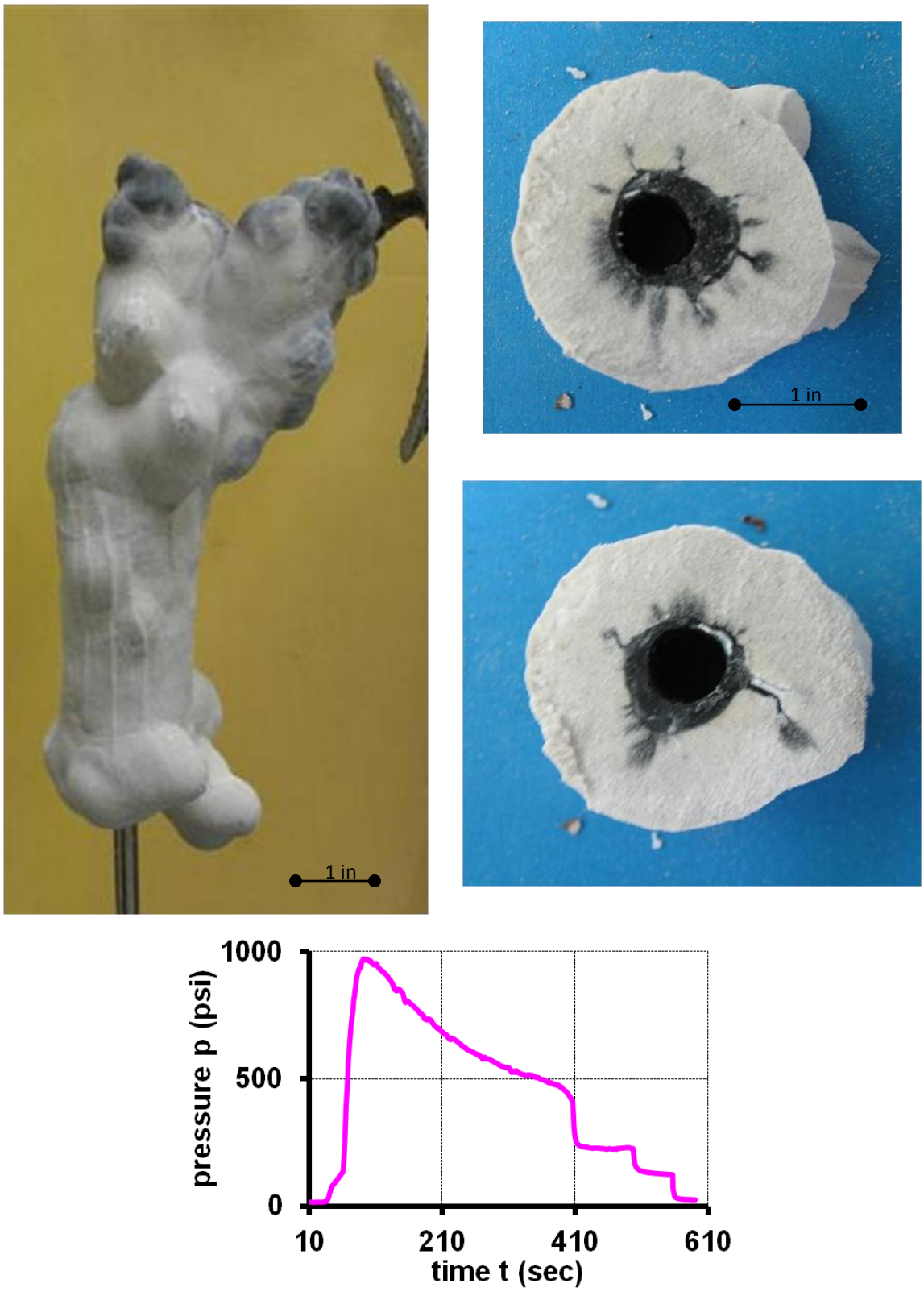

Figure A.29. Test 9-11-2009.

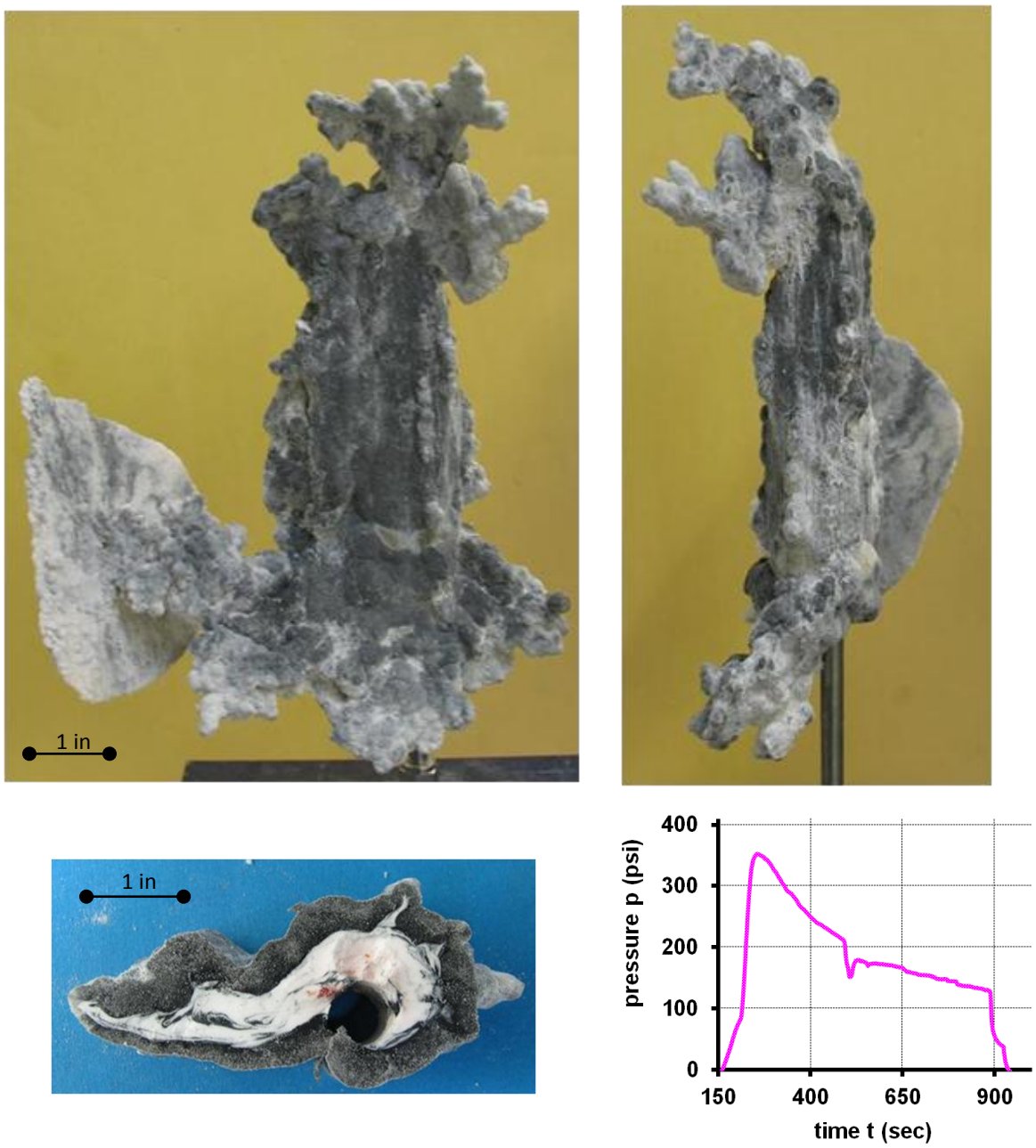

Figure A.30. Test 9-23-2009.

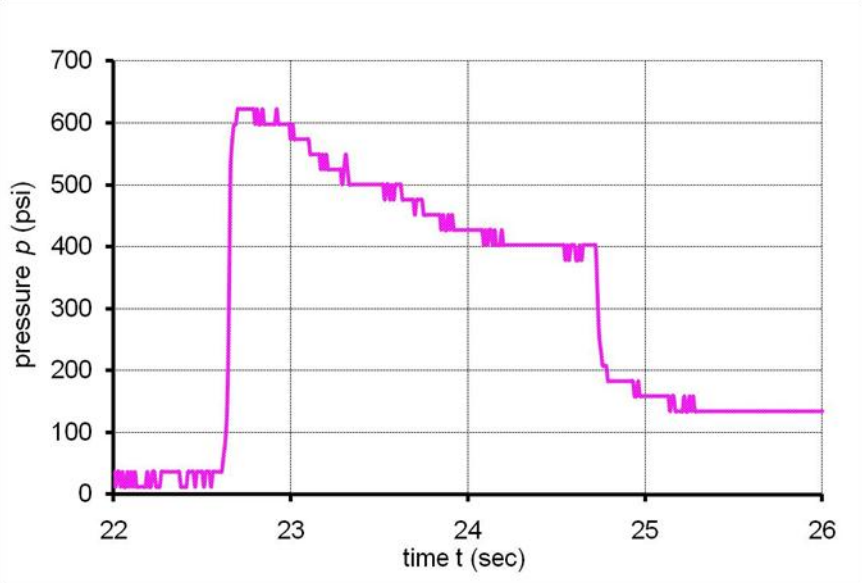

Figure A.31. Test 8-03-2010.

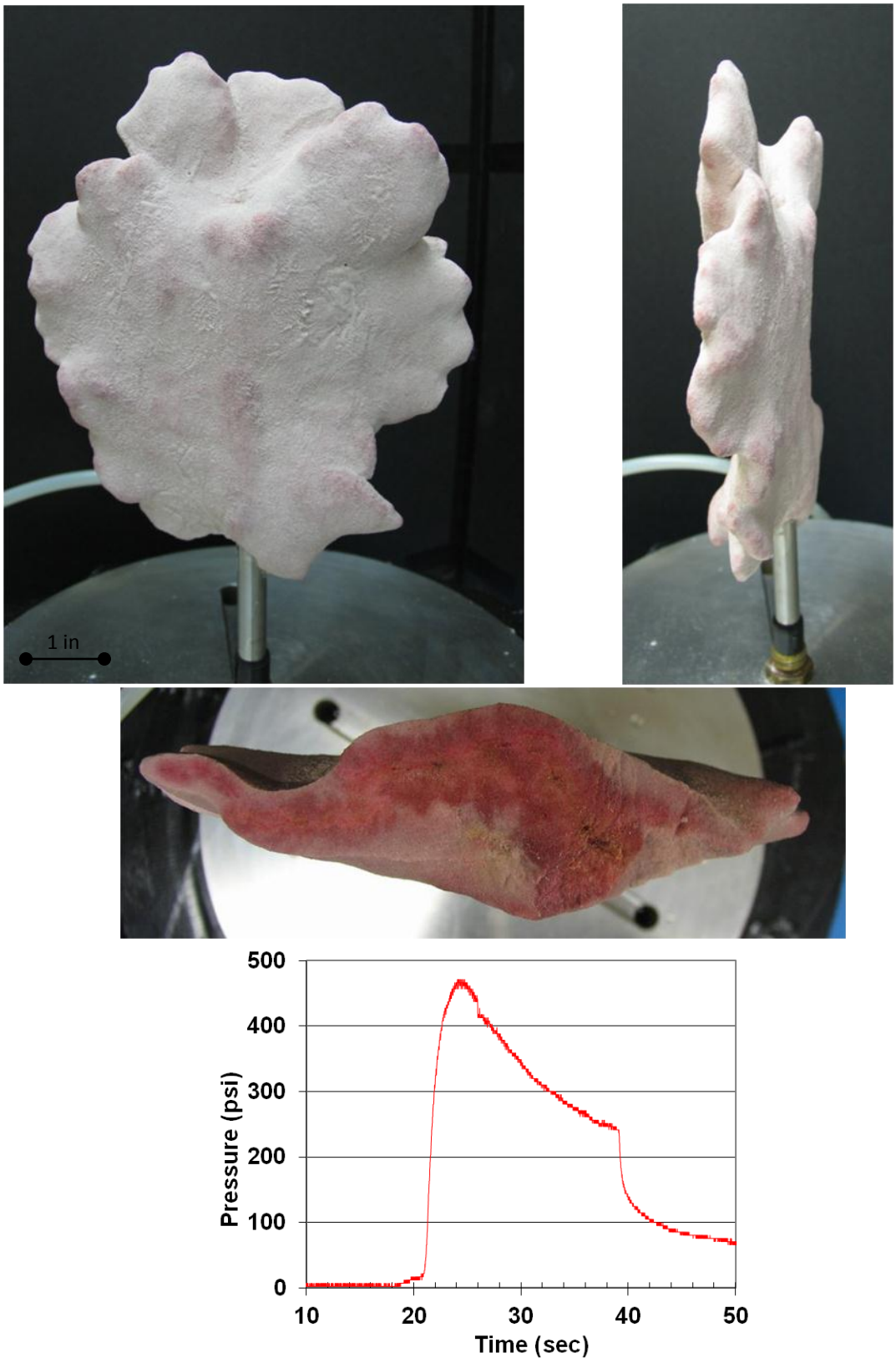

Figure A.32. Test 8-10-2010.

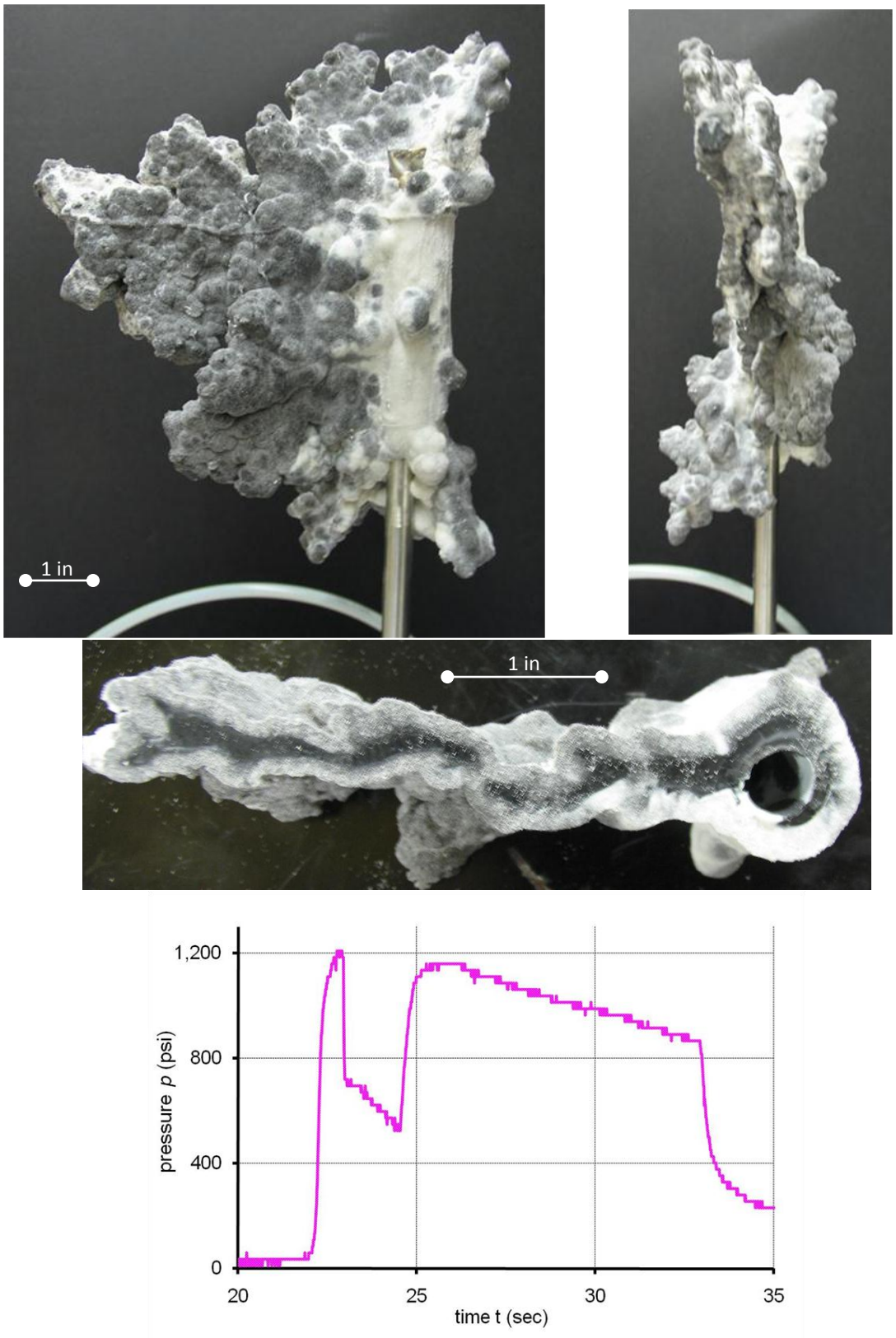

Figure A.33. Test 9-03-2010.

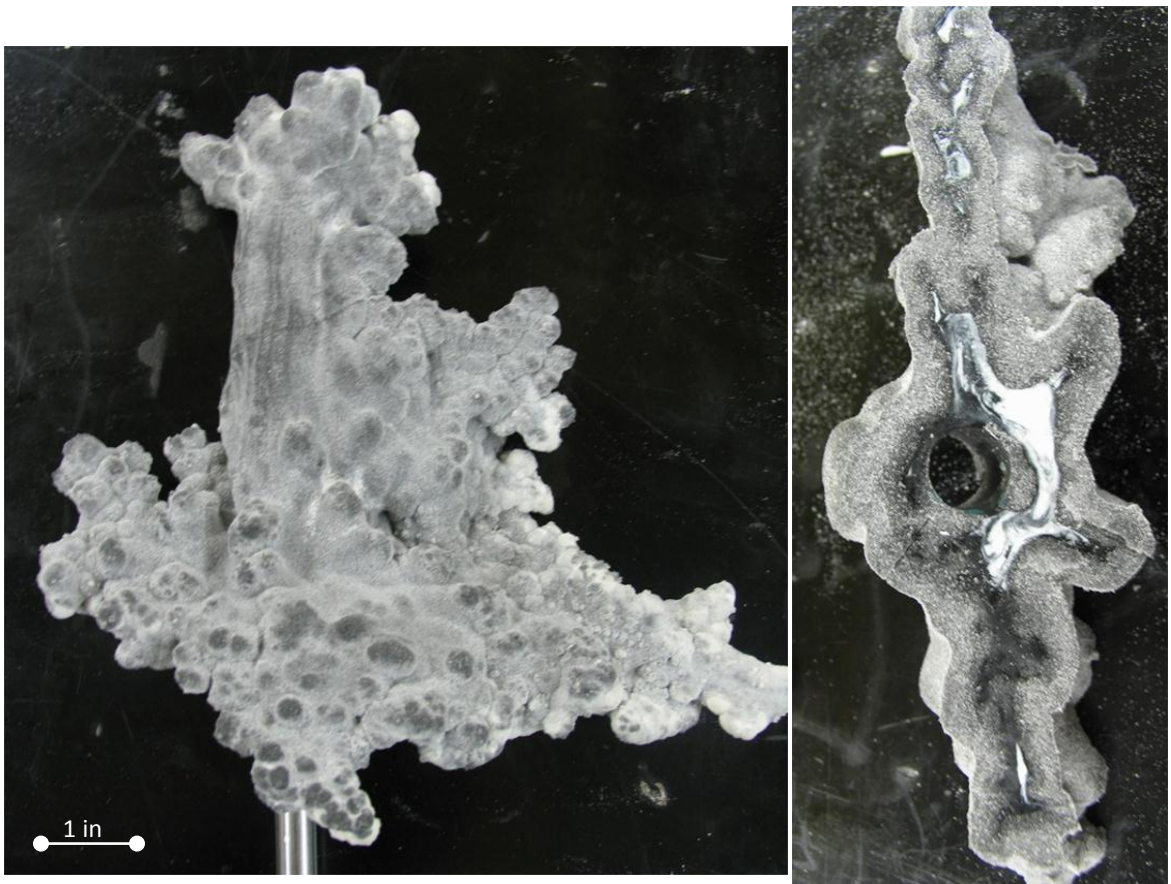

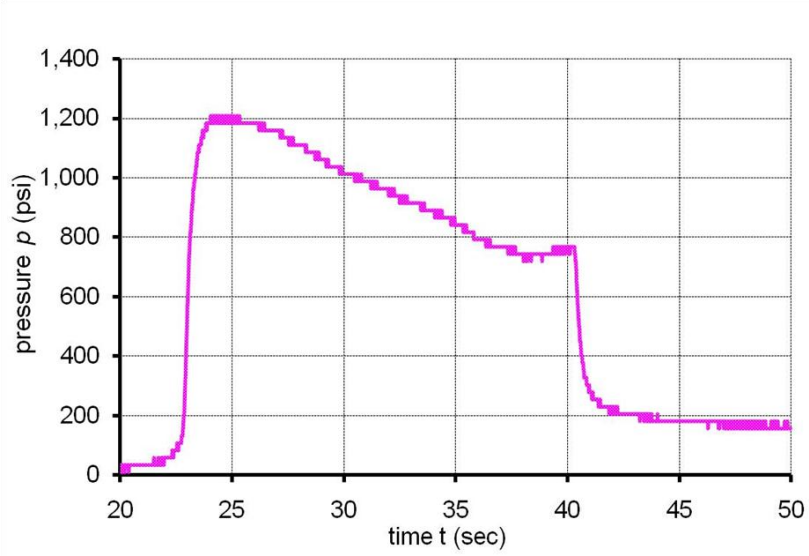

Figure A.34. Test 9-13-2010.

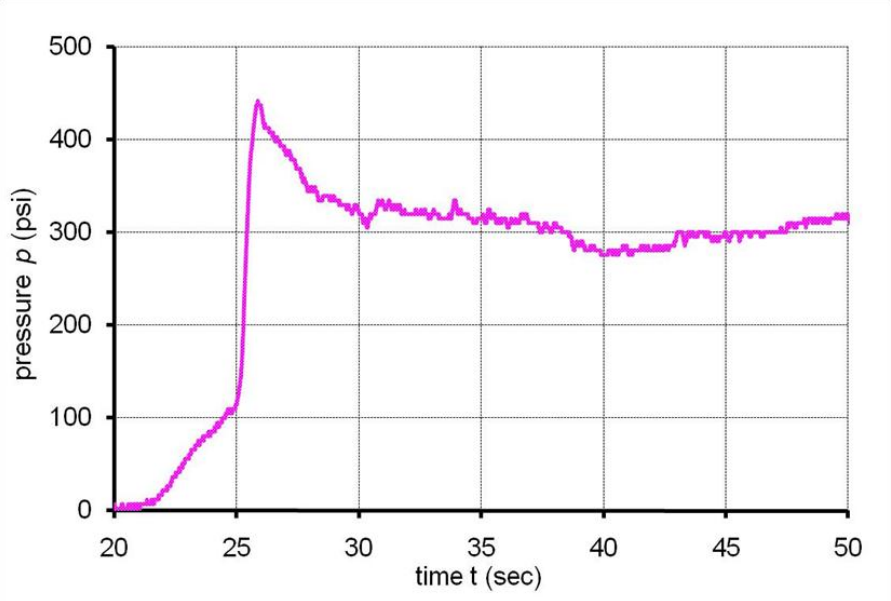

Figure A.35. Test 10-14-2010.

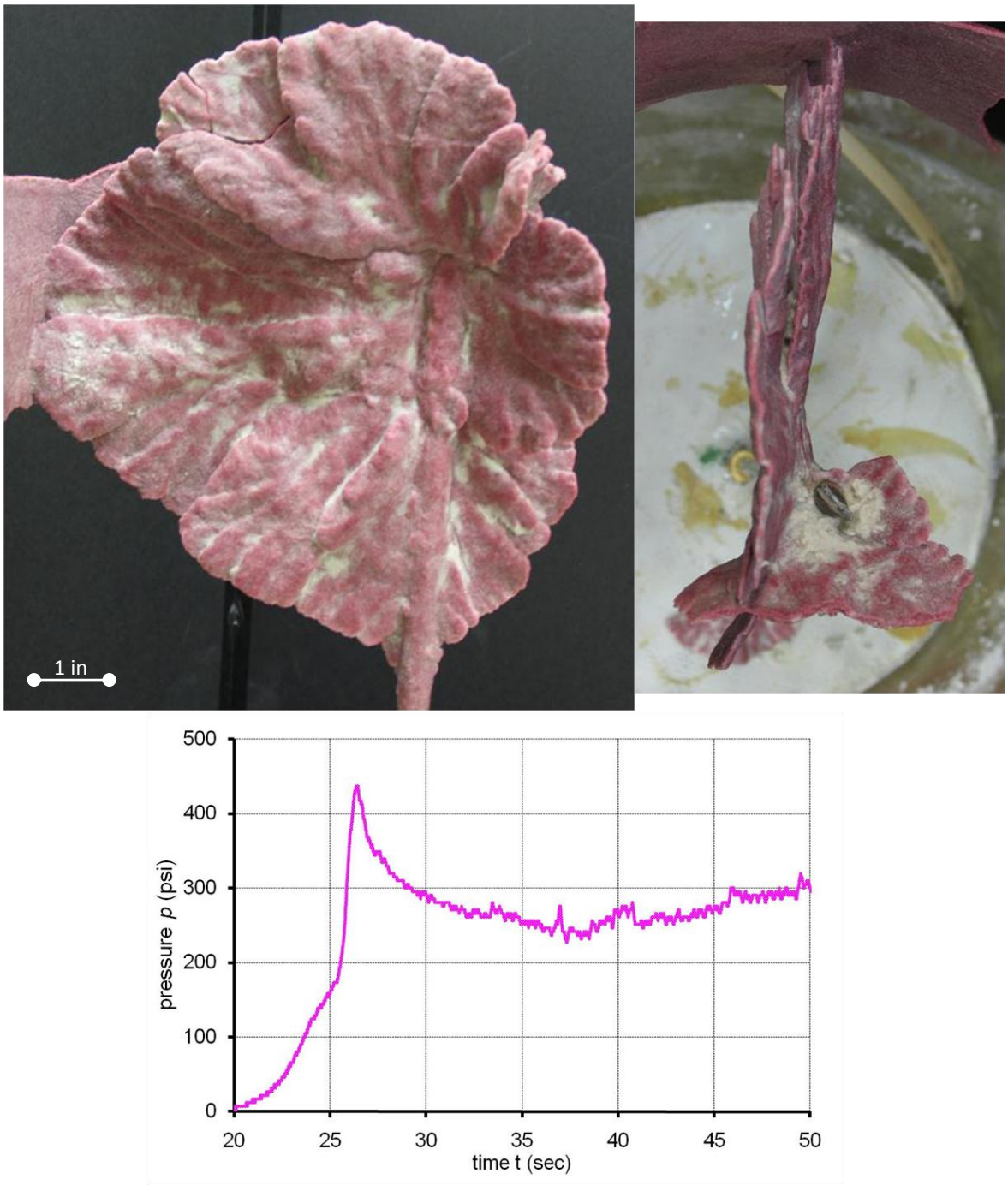

Figure A.36. Test 10-21-2010.

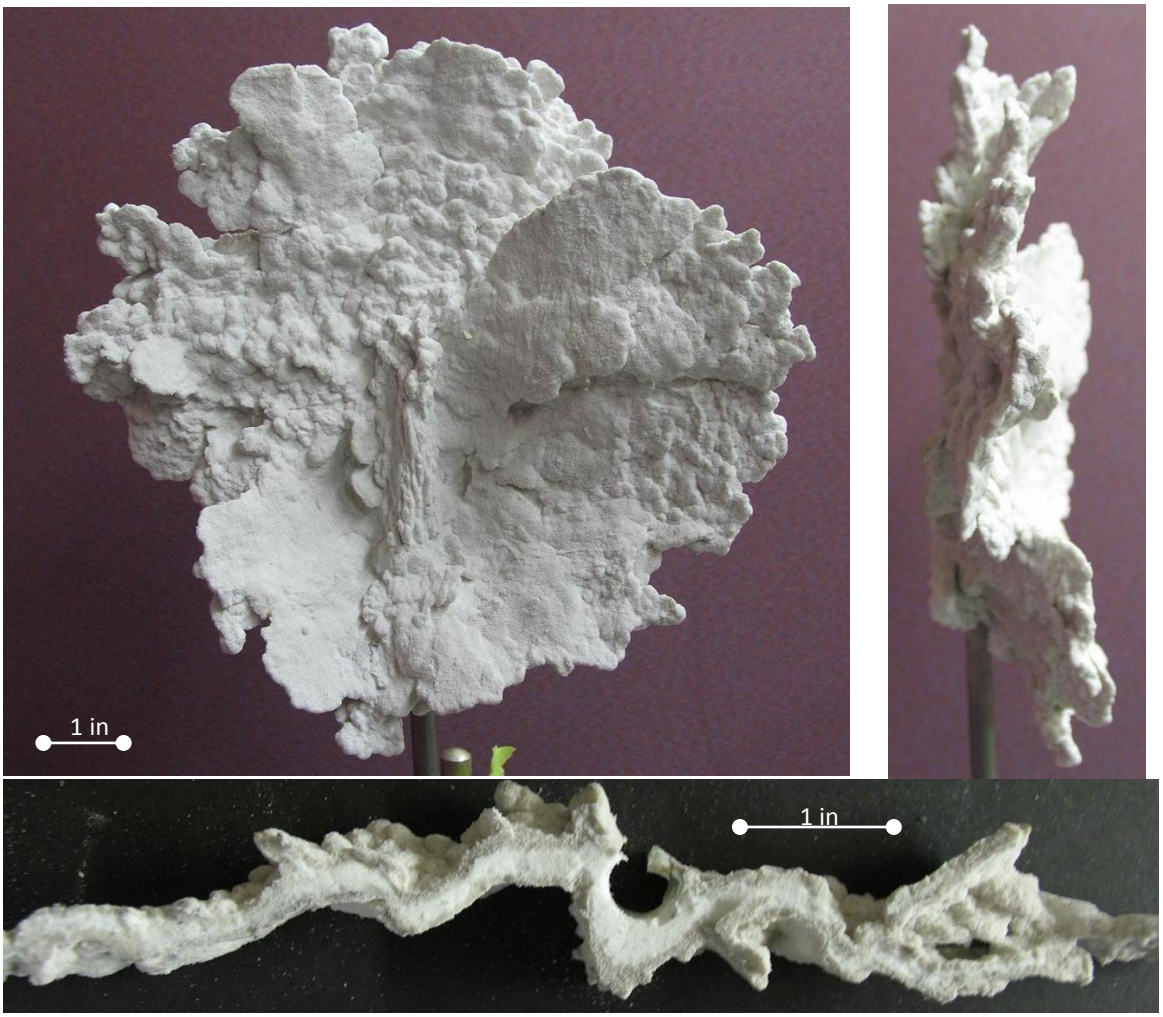

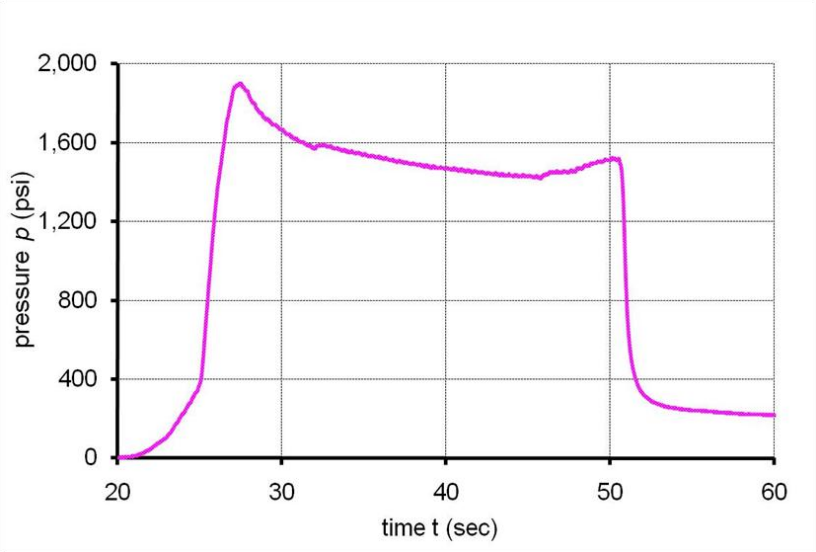

Figure A.37. Test 11-05-2010.

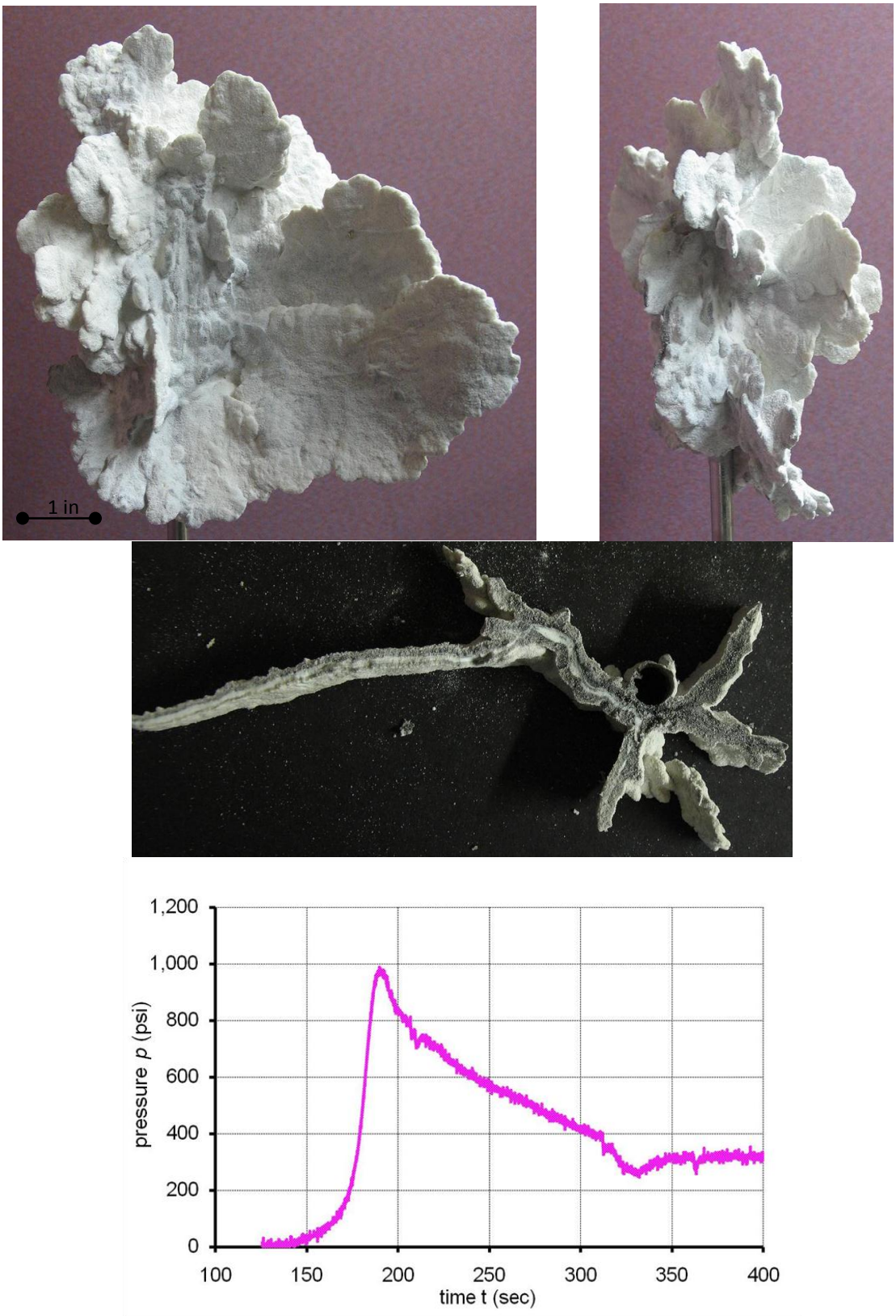

Figure A.38. Test 11-11-2010.

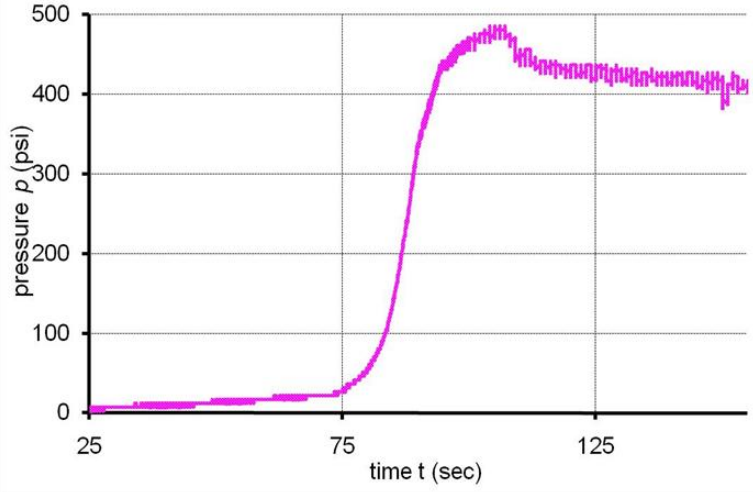

Figure A.39. Test 11-19-2010.

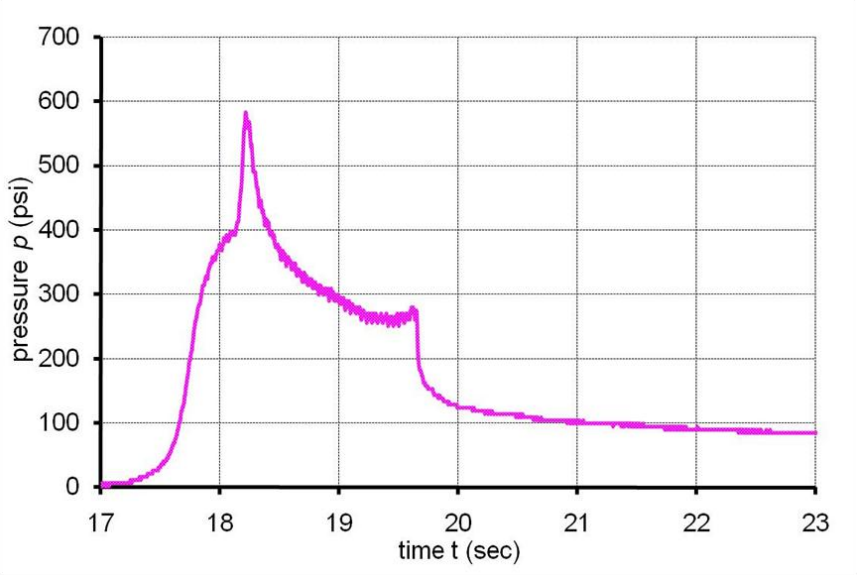

Figure A.40. Test 11-30-2010.

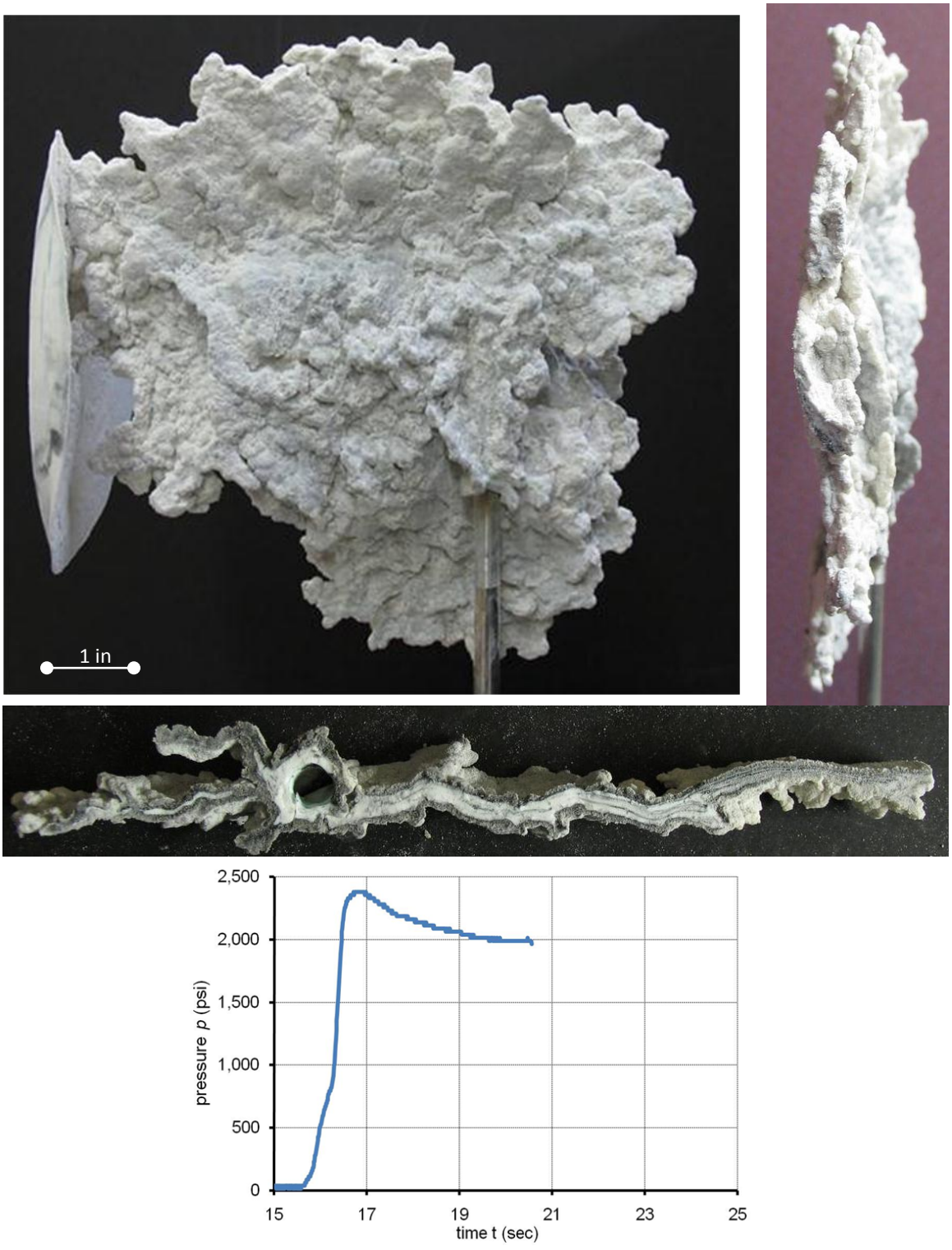

Figure A.41. Test 1-31-2011.

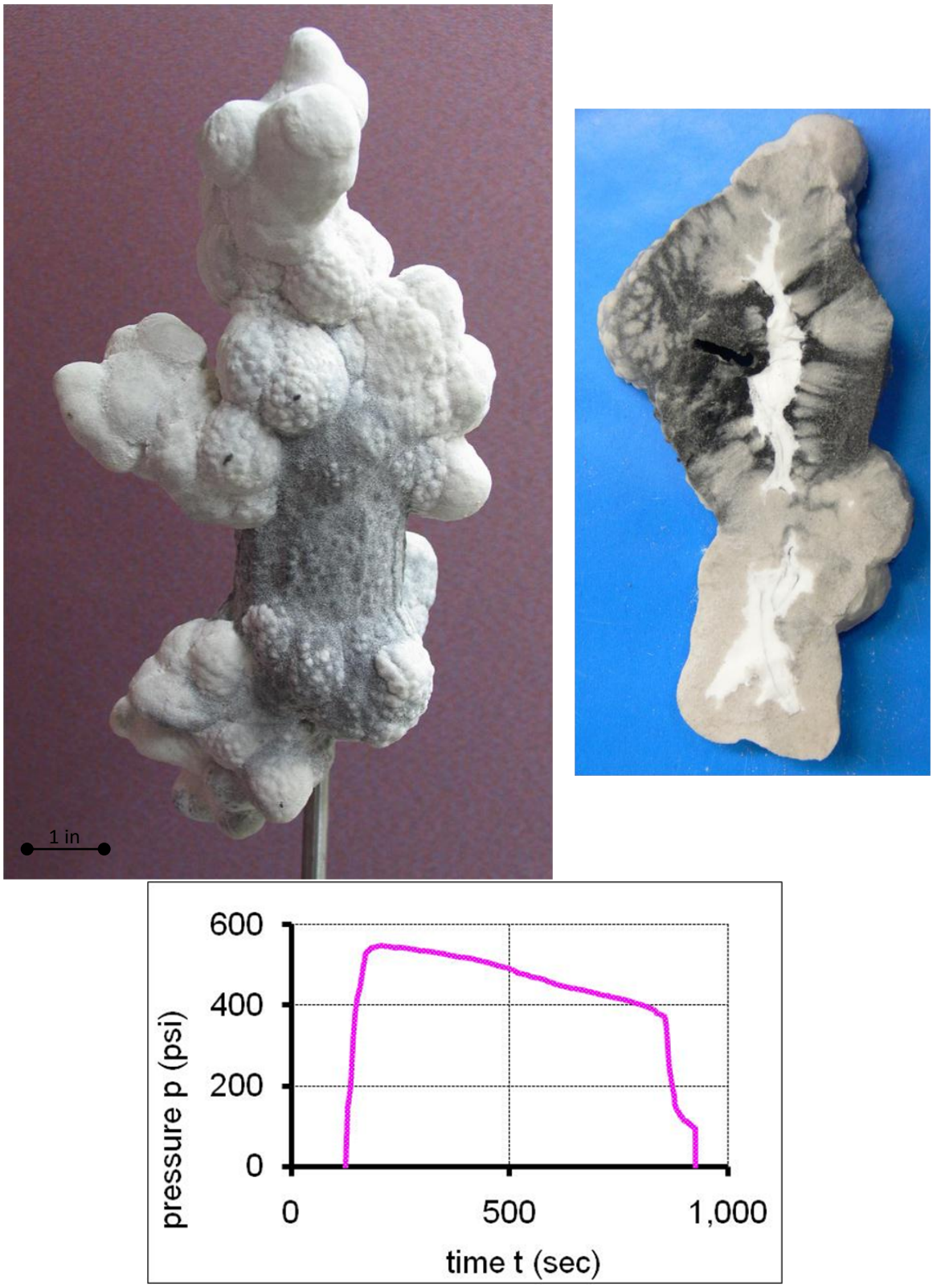

Figure A.42. Test 2-10-2011.

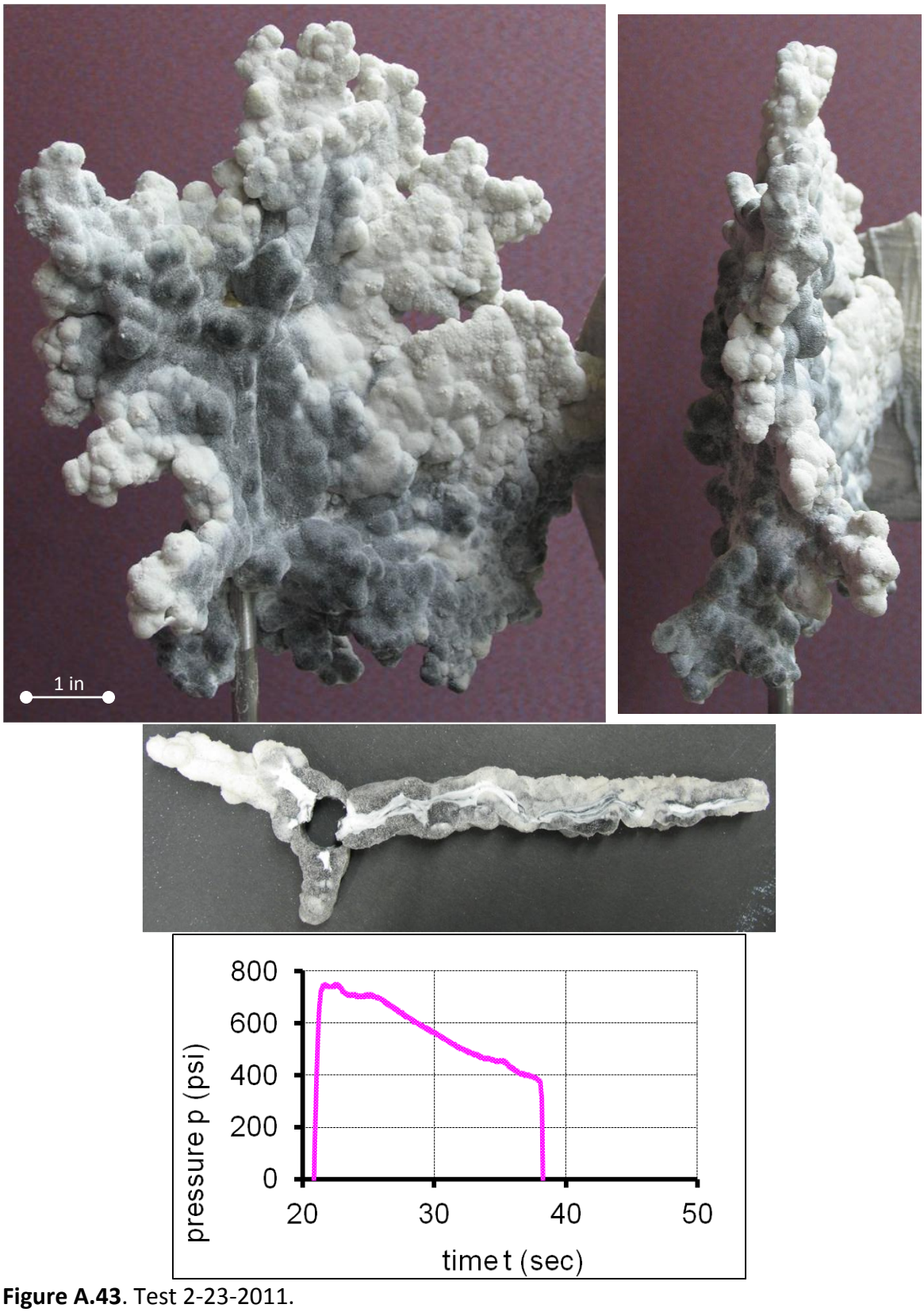

Figure A.43. Test 2-23-2011.

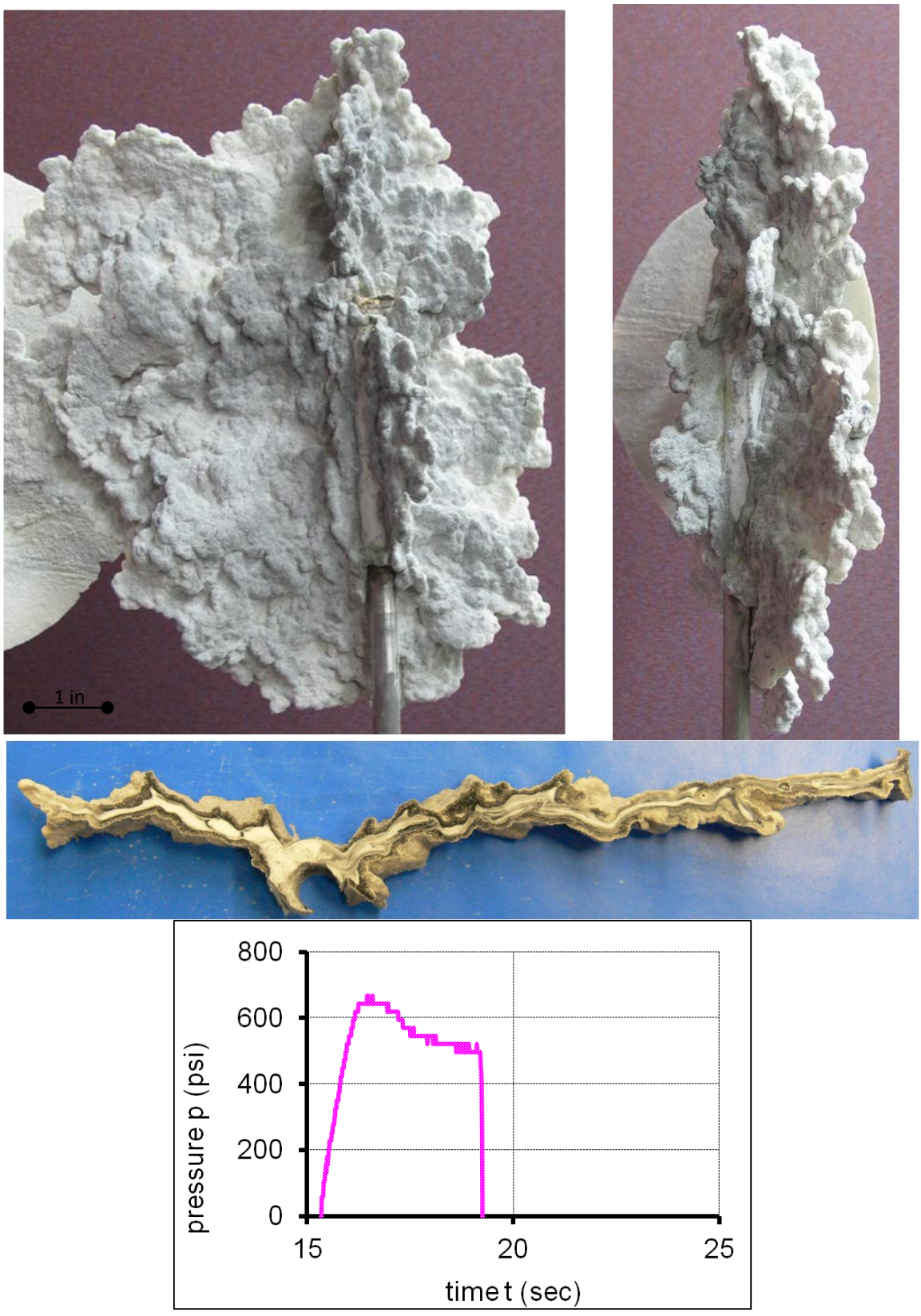

Figure A.44. Test 3-03-2011.

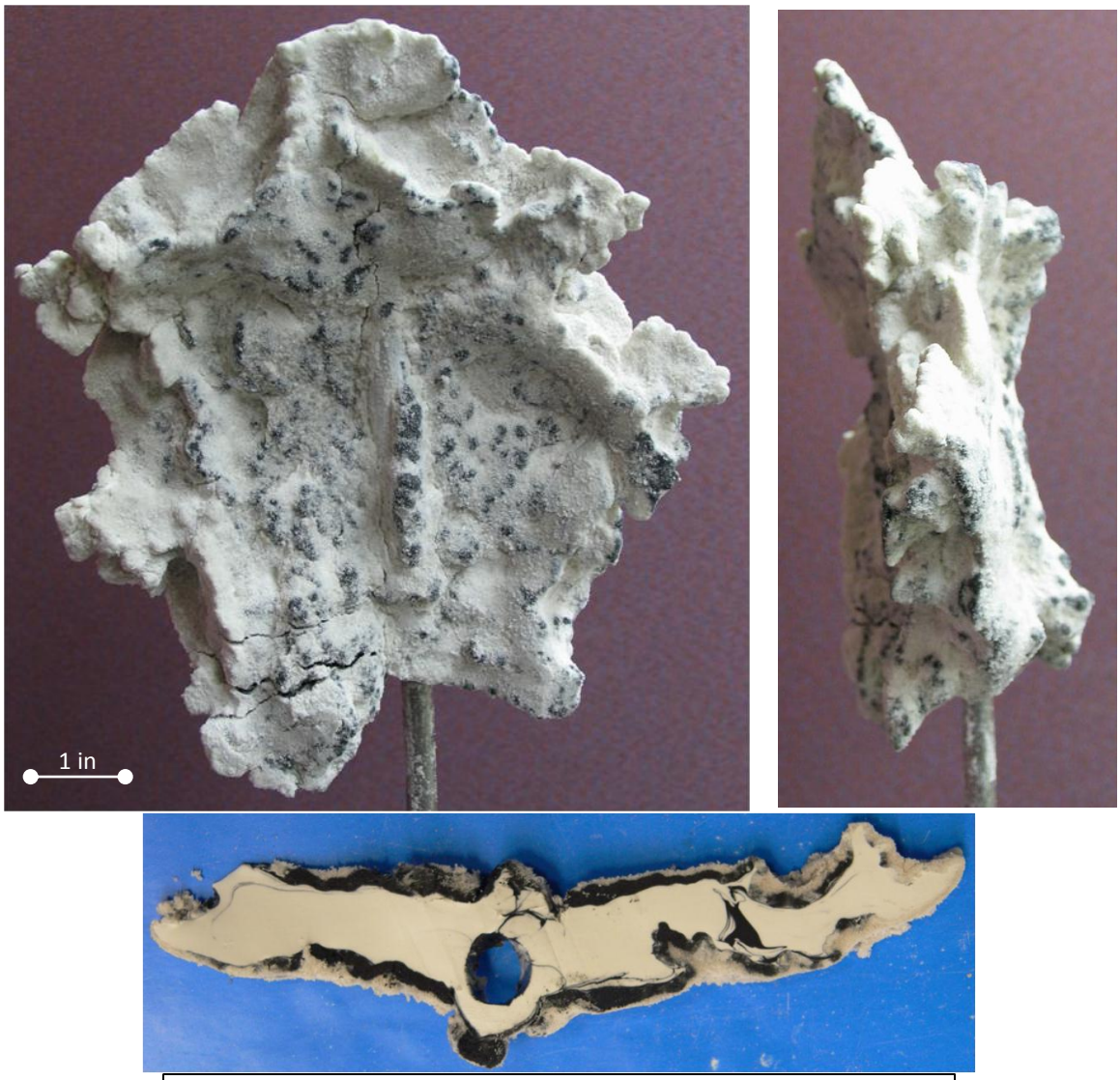

Figure A.45. Test 3-10-2011.

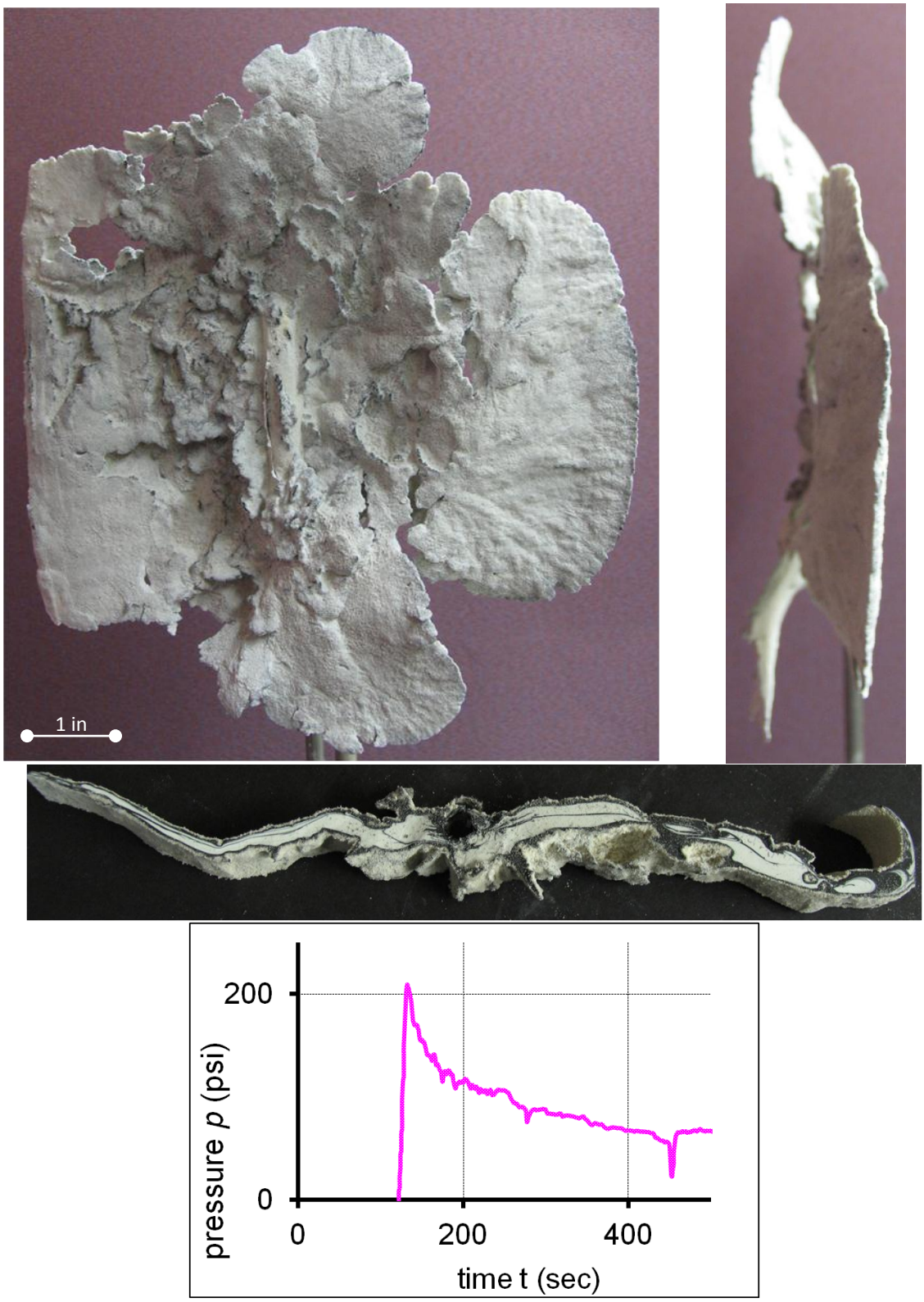

Figure A.46. Test 5-10-2005.

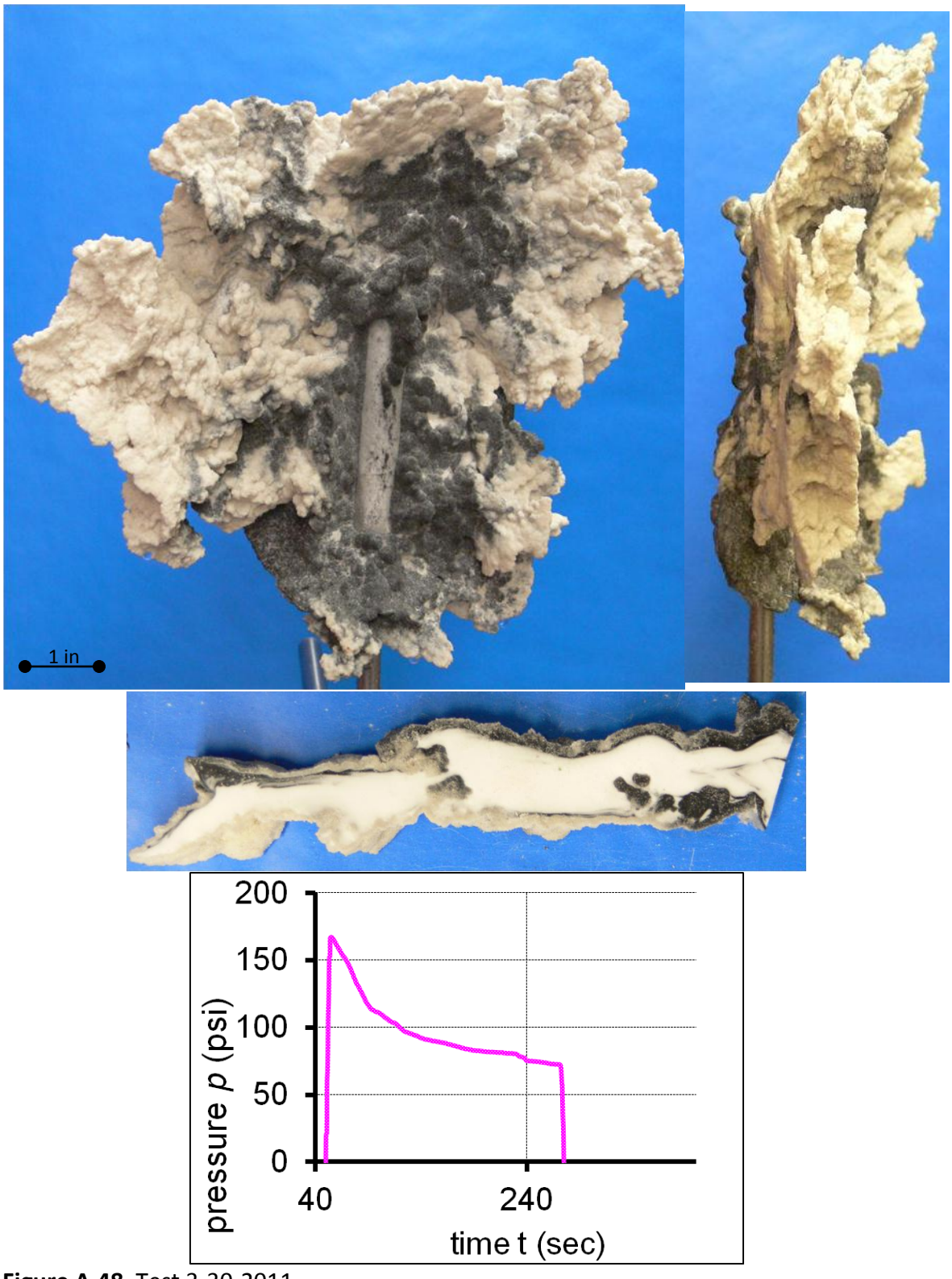

Figure A.48. Test 3-30-2011.

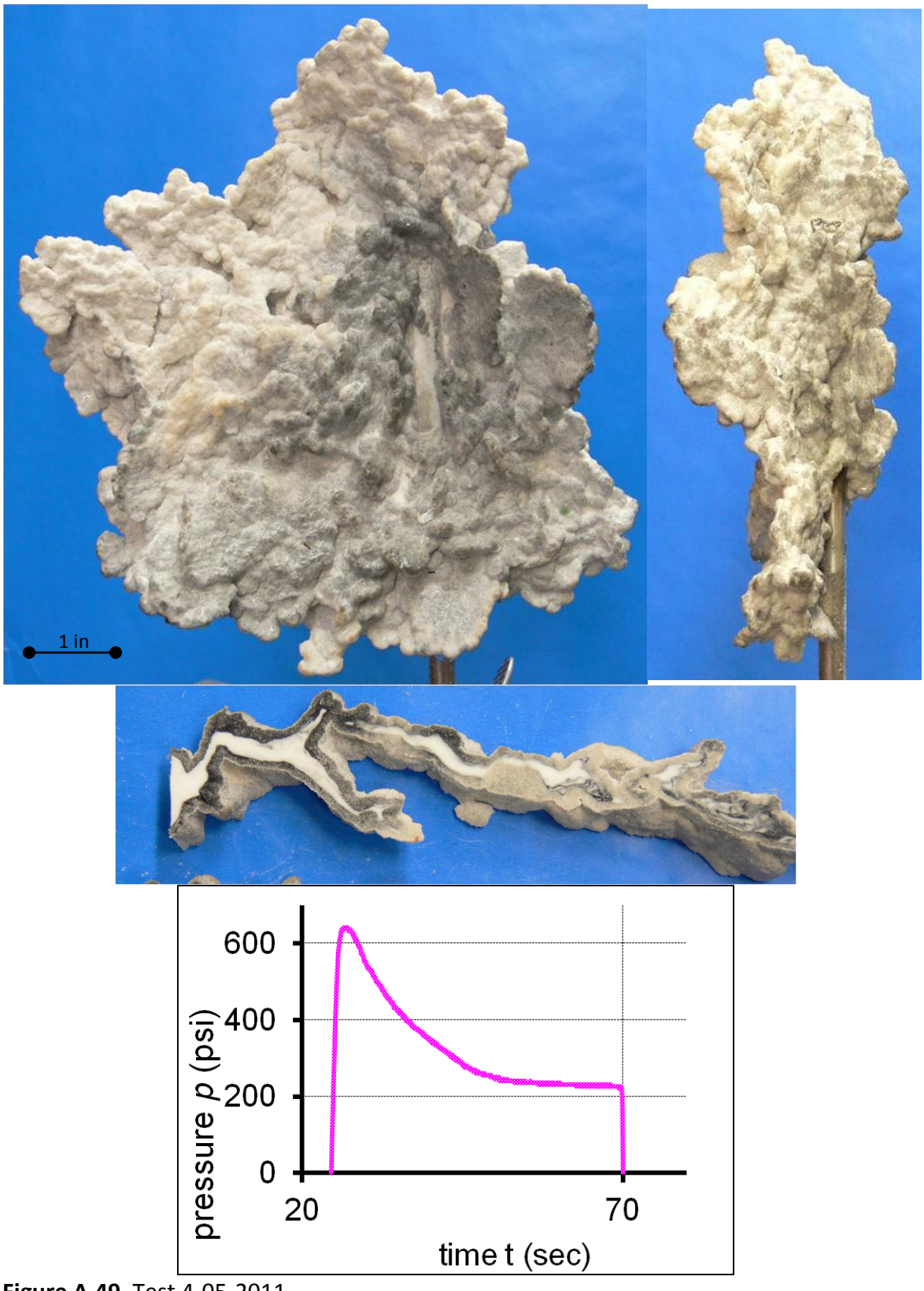

Figure A.49. Test 4-05-2011.

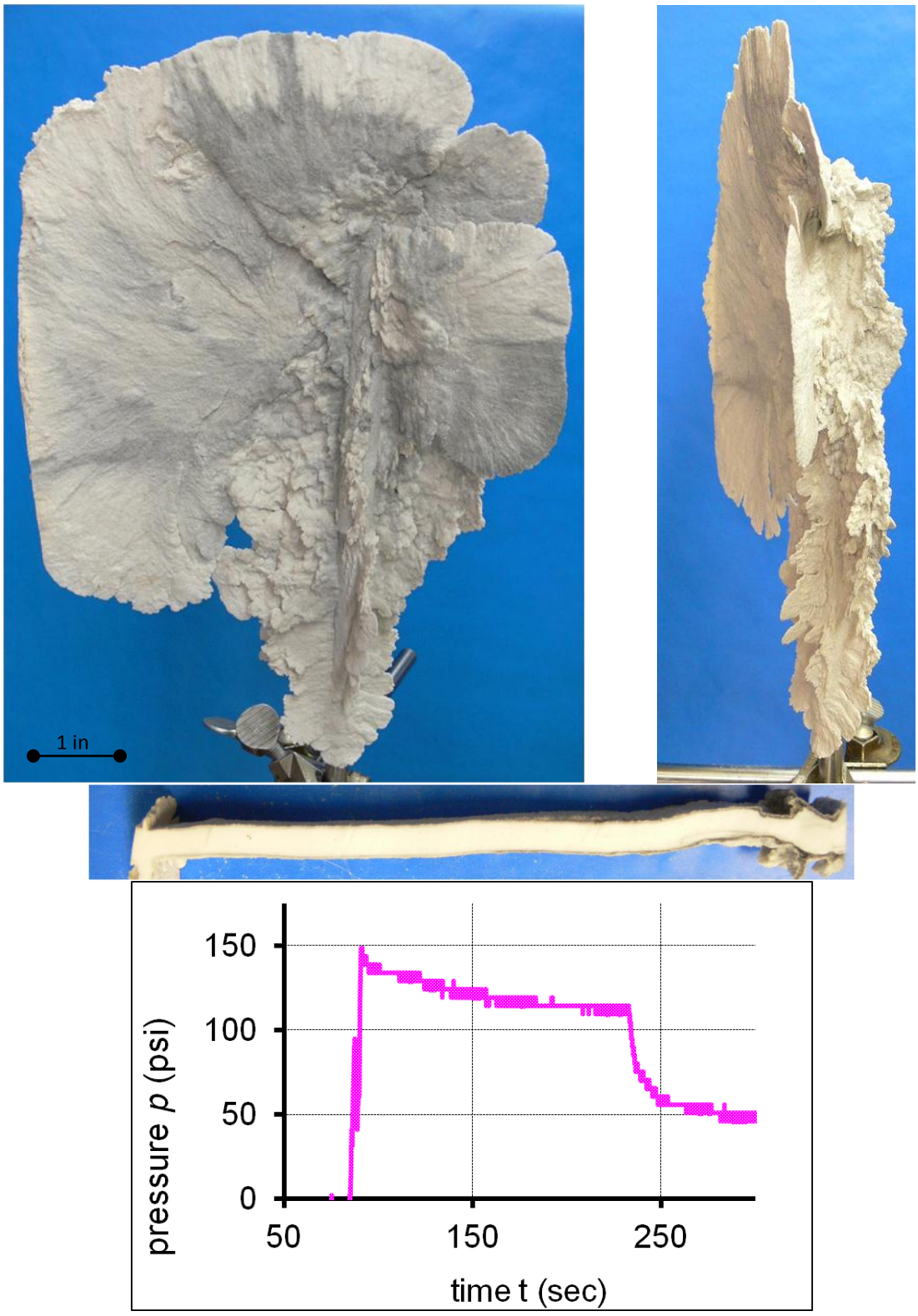

Figure A.50. Test 5-12-2011.

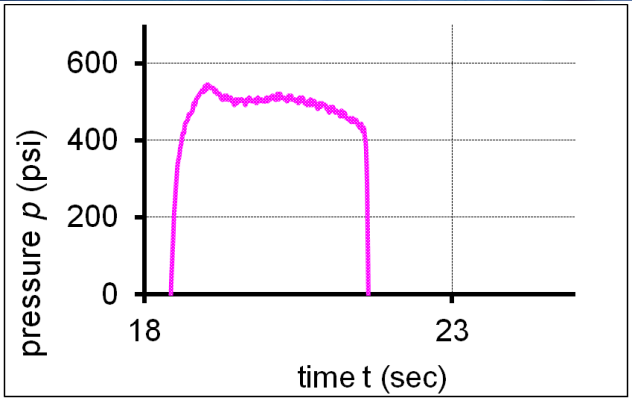

Figure A.51. Test 5-19-2011.

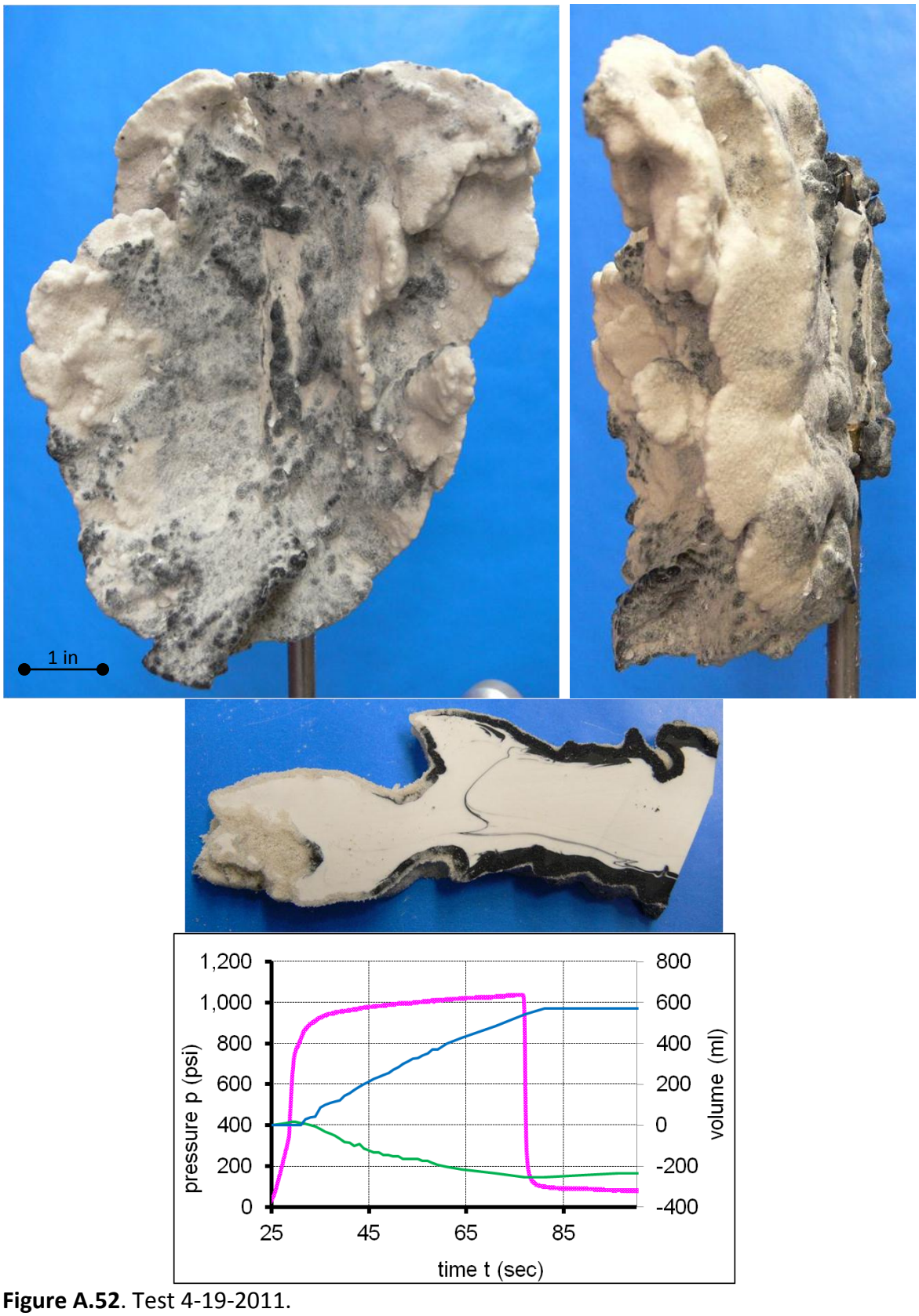

Figure A.52. Test 4-19-2011.

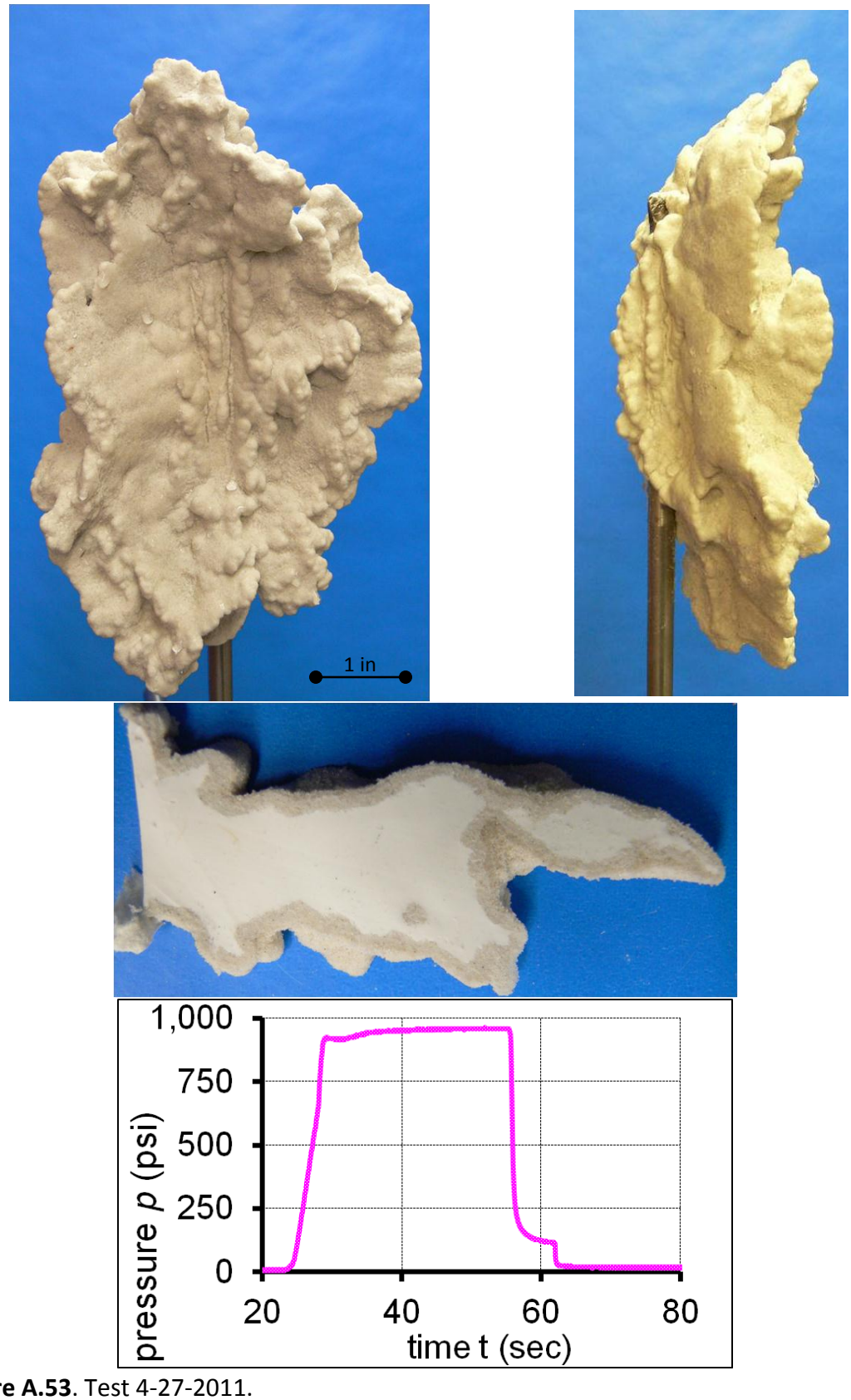

Figure A.53. Test 4-27-2011.

E. Other Equipment Cells

I. Small Triaxial Cell

The Small Triaxial Cell (STC) (**Figure A.54**) is of similar configuration and capacity as the Large Triaxial Cell (LTC) described in Chapter 3. However, the sample has a diameter of 4 in and a height of 8.25 in. This small sample size proved useful in testing the injection source and injection techniques. Additionally the STC allowed for a simple analysis of the effect of changes in pore fluid. The results are presented in Chapter 4. The injected volumes were limited due to the small sample size. This also limited the maximum flow rate that could be applied.

The results from the STC agree qualitatively with the results generated in the LTC. The fracture morphologies matched well and in general leakoff and fracture aperture values followed similar trends. Tests under similar conditions, pressure signatures were less consistent, however. We recorded lower peak pressures than large-scale tests under similar conditions. The magnitude of the reduction of peak pressures was typically $\sim 20\%$. Further, the small sample size tended to limit the reproducibility in the post peak injection pressure-time curves. The characteristic of the produced pressure curves were not consistent (along with peak pressures), though the fracture morphology remained similar.

The lower injection pressures in the STC could be attributed to the boundary affect. Many of our tests exhibited evidence of shear band development during the injection event. These shear bands were readily apparent in the membrane prior to

sample excavation**. Figure A.57** shows an example of the shear band development. The shear band development was not confined to the STC. In some limited instances the LTC did show similar shear band development. However, within the STC, shear bands were common. We consider the experimental results qualitative in nature.

II. Constrained Boundary Cells

A number of constrained boundary cells were utilized for initiation/leakoff characterization tests and for fracturing of consolidated materials tests. These cells were simply a constrained boundary within a loading frame that applied a vertical load. There was a large constrained cell (LCC) and a small constrained cell (SCC).

The SCC has a diameter of 6 in and a height of 6 in (**Figure A.57**). The injection tubing is fixed to the bottom of the cell and the injection source is a single hole drilled in the side of the tubing. A number of invasion tests were completed and the results are presented in the appendices of Chapter 4.

The LCC has a diameter of 11 in and a height of 18 in in height. It is basically a steel tube with a diameter of 12 in welded to a steel base plate with a thickness of ½ in. The injection source can be installed either through the base or through the top of the sample. Several tests were conducted to study various sample permeability along with layered samples and source geometry selections. The results are presented in the appendices of Chapter 4.

Figure A.54. Small Triaxial Cel (STC) and loading frame

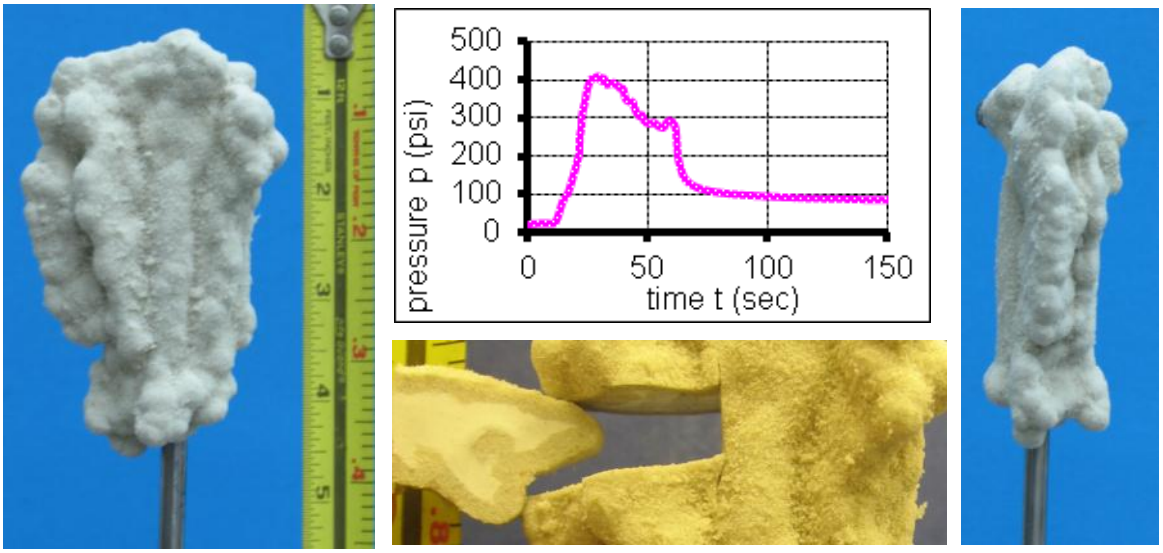

Figure A.55. Example test from STC.

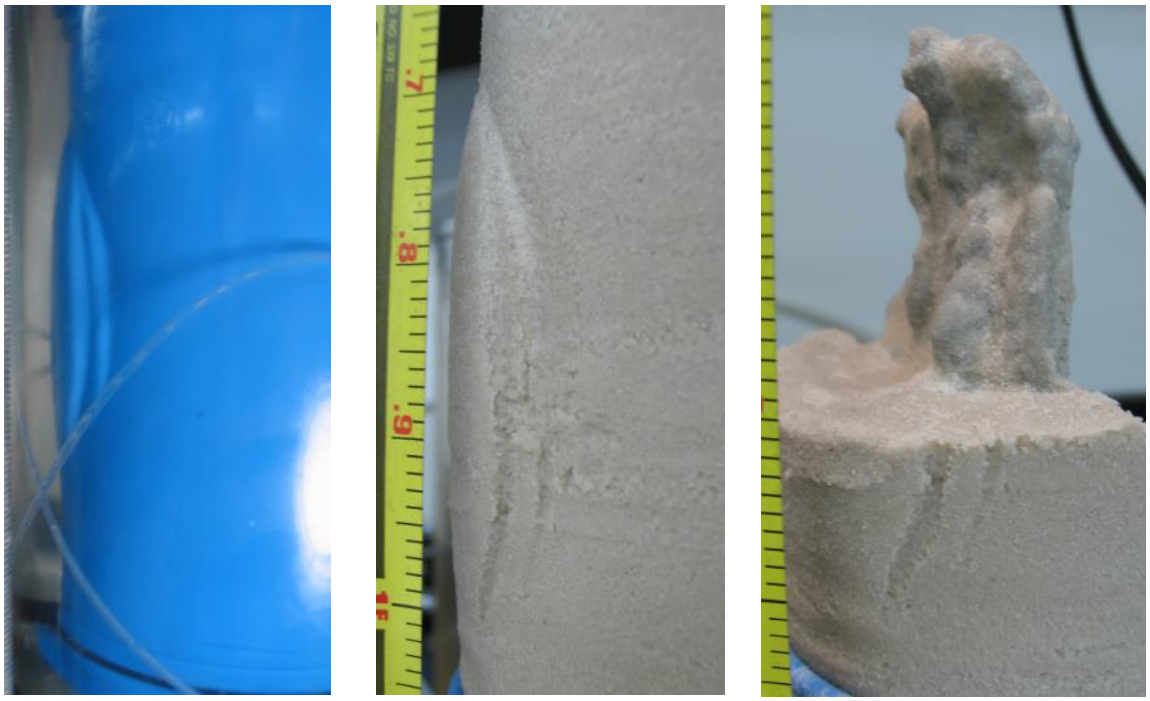

(a) **(b)** **(c)**

Figure A.56. Example of shear band propagation in STC (a) noticable dislocation in membrane under load (b) surface of sample after membrane removal (c) sample oreintation with shear band during excavation.

(a) **(b)** **(c)**

Figure A.57. SCC close up (a) and within loading frame (b) The LCC in loading frame (c).

F. Injection source

I. Point source

The point source geometry (shown in **Figure A.58**) was convenient from a manufacturing standpoint. In addition pre-filling of the injection source tube with fracturing fluid prior to the injection event was possible. Our experience showed point source geometry complicated the resulting fracture shape. In addition, peak and propagation pressure signatures were less uniform across multiple samples. The general fracture shape tended to be more arbitrary and less planar than other fractures generated from the linear or cylindrical sources (**Figure A.59**). In addition, any modeling attempt would benefit from the symmetry of cylindrical source geometry.

The inconstancies in the peak pressure can be attributed to the small point source. Failure of material can be expected to initiate at the weakest point in the formation. The initial fluid flow is exposed to a limited volume of the formation with a small point source. Therefore, we would not expect uniformity in initiation pressures across multiple samples given the inherent inhomogeneity at the scale of the point source.

The variability in the pressure signature during propagation can be attributed the fluid flow within the fracture. The cylindrical source (and linear source as well) generate fairly planer uniform fracture. The unique geometry generated from the point source complicates the fracture form, thus affects propagation pressures (illustrated by **Figure A.59**)

II. Linear source

The linear source in **Figure A.58** was the first iteration in the change from the point source geometry. Initially we attempted to direct the fracture plane by creating a slot in the injection tubing. However, over 10 separate fracture tests, the fracture always propagated in a planar shape perpendicular to the slot orientation. This could be a boundary affect due to the interface developed between the casing of the tubing and the initial fluid leakoff. Other researchers were successful in generating fracture in a prescribed plane by creating notches in the formation (e.g., [*Dong and De Pater*, 2008]). The linear source geometry was the most consistent in creating planar features, more so than even the cylindrical source. The manufacturing of the source, however, proved the most labor intensive.

III. Cylindrical source

The cylindrical source geometry was the final design and the source geometry used in the bulk of the presented work. A number of design iteration did take place but the in general the source remained the same.

Examples of the results, due to the change in source geometry, are shown in **Figure A.59**. This was a series of test conducted with the same conditions just three different injected volumes. This was to illustrate the stages of fracture development. Note the reproducibility of the fracture curves and the similarity in fracture morphologies.

One of the more noticeable features of these fractures is the end effects on the top and bottom of the developed fracture in **Figure A.61** (c). We initially attributed this to end effects of the source geometry and sample interaction. However, a closer inspection revealed a weakness in the manufacturing process creating the injection source. These end effects are more due to the failure of the bonding agent between the wire mesh and casing. Once recognized and corrected the geometry of the fracture was typically planar and more uniform as shown in **Figure A.59** (c) and (d).

Figure A.58. Examples of linear (right) and point (left) source geometry.

(a) (b) (c) (d)

Figure A.59. Illustration of the fracture geometry due to point source (a and b) and cylindrical source (c and d).

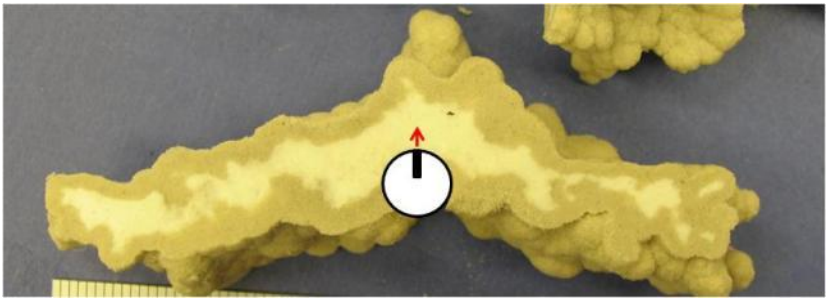

Figure A.60. Ilistration of the linear source and coresponding fracture red arrow indicates the direction of fluid flow out of the source. Fracture development is perpendicular to source outlet.

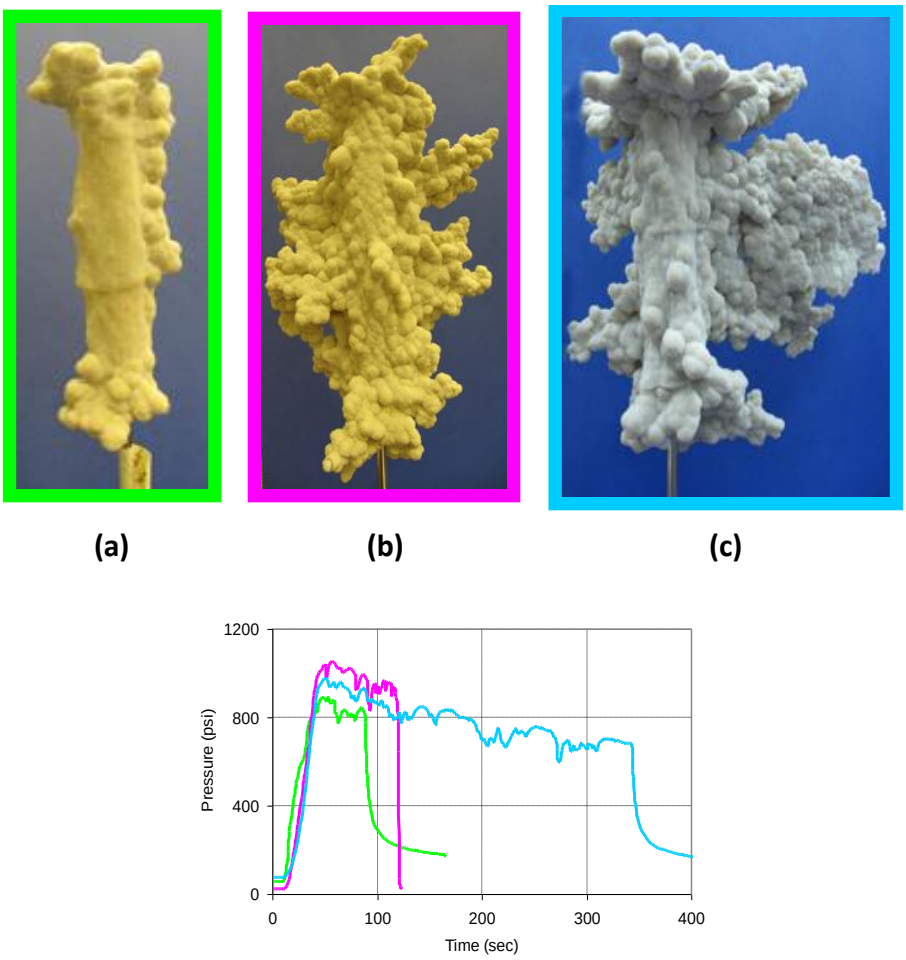

Figure A-61. Results of three cylindrical source geometry tests.

REFERENCES

Abass, H. H., A. H. Habbtar, and A. Shebatalhamd (2003), "Sand Control During Drilling, Perforation, Completion and Production," paper presented at Proceedings - 13th Middle East Oil and Gas Show and Conference, Technology Solution for the Oil and Gas Business: New Middle East Focus, MEOS 2003, June 9, 2003 - June 12, 2003, Society of Petroleum Engineers (SPE), Bahrain, Bahrain.

Adachi, J. I., and E. Detournay (2002), Self-Similar Solution of a Plane-Strain Fracture Driven by a Power-Law Fluid, *International Journal for Numerical and Analytical Methods in Geomechanics*, *26*, 579-604.

Al-Shaikh-Ali, M. M. H., A. G. Davis, and M. J. Lloyd (1981), In Situ Measurement of K0 in a Stiff Fissured Glacial Till by Hydraulic Fracturing, *Ground Engineering*, *14*, 19-22, 24-25.

Alonso, A., and M. Mingo (2010), The Expansion of "Non Conventional" Production of Natural Gas (Tight Gas, Gas Shale and Coal Bed Methane). A Silent Revolution, paper presented at 2010 7th International Conference on the European Energy Market, EEM 2010, June 23, 2010 - June 25, 2010, IEEE Computer Society, Madrid, Spain.

Alsiny, A., I. Vardoulakis, and A. Drescher (1992), Deformation Localization in Cavity Inflation Experiments on Dry Sand, *Geotechnique*, *42*, 395-410.

Anderson, T. L. (1995), *Fracture Mechanics: Fundamentals and Applications*, 2nd ed., CRC Pres, Boca Raton.

Au, S. K. A., K. Soga, and A. T. Yeung (2006), A New Laboratory Apparatus for Grout Injection Studies, *Geotechnical Testing Journal*, *29*, 95-101.

Barenblatt, G. I. (2003), *Scaling*, Cambridge University Press, Cambridge, 171 pp.

Bird, R.B.; Armstrong, R.C.; Hassager, O. (1987) Dynamics of polymeric liquids. Vol. 1, 2nd Ed, John Wiley and Sons Inc.,New York, NY, 784 pp.

Bjerrum, L., J. K. T. L. Nash, R. M. Kennard, and R. E. Gibson (1972), Hydraulic Fracturing in Field Permeability Testing. *Norwegian Geotechnical Institute*, 94, 1-10

Bohloli, B., and C. J. de Pater (2006), Experimental Study on Hydraulic Fracturing of Soft Rocks: Influence of Fluid Rheology and Confining Stress, *Journal of Petroleum Science and Engineering*, *53*(1-2), 1-12.

Bunger, A. P., E. Detournay, and D. I. Garagash (2005), Toughness-Dominated Hydraulic Fracture with Leak-Off, *International Journal of Fracture*, *134*(Copyright 2006, IEE), 175-190.

Bunger, A. P., E. Detournay, D. I. Garagash, and A. P. Peirce (2007), Numerical Simulation of Hydraulic Fracturing in the Viscosity-Dominated Regime, paper presented at SPE - Hydraulic Fracturing Technology Conference 2007, January 29, 2007 - January 31, 2007, Society of Petroleum Engineers, College Station, TX, United States.

Chang, H. (2004), Hydraulic Fracturing in Particulate Materials. Dissertation thesis, Georgia Institute of Technology, Atlanta GA.

Chang, H., L. N. Germanovich, R. Wu, J. C. Santamarina, and P. E. Dijk(2003), Hydraulic Fracturing in Cohesionless Particulate Materials, American Geophysical Union, Washington, DC, United States (USA), United States (USA), 2003 Dec 08.

Chilton, RA and R Stainsby, 1998, Pressure loss equations for laminar and turbulent non-Newtonian pipe flow, *Journal of Hydraulic Engineering* 124(5) pp. 522 ff

Chin, L. Y., and C. T. Montgomery (2004), A Numerical Model for Simulating Solid Waste Injection in Soft Rock Reservoirs, paper presented at 2004 SPE Annual Technical Conference and Exhibition, September 26, 2004 - September 29, 2004, Society of Petroleum Engineers (SPE), Houston, TX, United States.

De Pater, C. J., and Y. Dong (2007), Experimental Study of Hydraulic Fracturing in Sand as a Function of Stress and Fluid Rheology, paper presented at SPE - Hydraulic Fracturing Technology Conference 2007, January 29, 2007 - January 31, 2007, Society of Petroleum Engineers, College Station, TX, United States.

De Pater, C. J., and Y. Dong (2009), Fracture Containment in Soft Sands by Permeability or Strength Contrasts, paper presented at SPE Hydraulic Fracturing Technology Conference 2009, January 19, 2009 - January 21, 2009, Society of Petroleum Engineers, The Woodlands, TX, United States.

Desroches, J., E. Detournay, B. Lenoach, P. Papanastasiou, J. R. A. Pearson, M. Thiercelin, and A. Cheng (1994), The Crack-Tip Region in Hydraulic Fracturing, *P Roy Soc Lond a Mat*, *447*(1929), 39-48.

Detournay, E. (2004), Propagation Regimes of Fluid-Driven Fractures in Impermeable Rocks, *International Journal of Geomechanics*, *4*, 35-45.

Detournay, E., and D. I. Garagash (2003), The near-Tip Region of a Fluid-Driven Fracture Propagating in a Permeable Elastic Solid, *Journal of Fluid Mechanics*, *494*(Copyright 2004, IEE), 1-32.

Detournay, E., A. P. Peirce, and A. P. Bunger (2007), Viscosity-Dominated Hydraulic Fractures, paper presented at 1st Canada-US Rock Mechanics Symposium - Rock Mechanics Meeting Society's Challenges and Demands, May 27, 2007 - May 31, 2007, Taylor and Francis/Balkema, Vancouver, BC, Canada.

Dong, Y. (2010), Hydraulic Fracture Containment in Sand, Dissertation thesis, Delft University of Technology.

Dong, Y., and C. J. De Pater (2007a), Closure of Hydraulic Fractures Visualized by X-Ray Ct Technique in Sand, paper presented at 1st Canada-US Rock Mechanics Symposium - Rock Mechanics Meeting Society's Challenges and Demands, May 27, 2007 - May 31, 2007, Taylor and Francis/Balkema, Vancouver, BC, Canada.

Dong, Y., and C. J. de Pater (2007b), Closure of Hydraulic Fractures Visualized by X-Ray Ct Technique in Sand, *Proc Monogr Eng Wate*, 665-672 1728.

Dong, Y., and C. J. De Pater (2008), Observation and Modeling of the Hydraulic Fracture Tip in Sand, paper presented at 42nd U.S. Rock Mechanics - 2nd U.S.-Canada Rock Mechanics Symposium 2008, June 29, 2008 - July 2, 2008, Omnipress, San Francisco, CA, United States.

Economides, M. J., and K. G. Nolte (2000), *Reservoir Stimulation*, 3rd ed., J. Wiley, Chichester, England ; New York.

Elwood, D. E. Y. (2008), Hydraulic Fracture Experiments in a Frictional Material and Approximations for Maximum Allowable Mud Pressure, Dissertation thesis, Queen's University Kingston, Ontario, Canada

Flores-Berrones, R., M. Ramirez-Reynaga, and E. J. Macari (2010), Internal Erosion and Rehabilitation of an Earth-Rock Dam, *Journal of Geotechnical and Geoenvironmental Engineering*, *137*, 150-160.

Franquet, J. A. E., Michael J. (1999), Effect of Stress and Stress Path on Young's Modulus and Poisson Ratio of Unconsolidated Rocks: A New Idea for Hydraulic Fracturing in *Latin American and Caribbean Petroleum Engineering Conference*, Caracas, Venezuela.

Gafar, K., K. Soga, A. Bezuijen, M. P. M. Sanders, and A. F. Van Tol (2009), Fracturing of Sand in Compensation Grouting, paper presented at 6th International Symposium on Geotechnical Aspects of Underground Construction in Soft Ground, IS-SHANGHAI 2008, April 10, 2008 - April 12, 2008, CRC Press, Shanghai, China.

Garagash, D., and E. Detournay (2000), Tip Region of a Fluid-Driven Fracture in an Elastic Medium, *Journal of Applied Mechanics, Transactions ASME*, *67*, 183-192.

Garagash, D. I., and E. Detournay (2005), Plane-Strain Propagation of a Fluid-Driven Fracture: Small Toughness Solution, *Transactions of the ASME. Journal of Applied Mechanics*, *72*, 916-928.

Garagash, D. I., E. Detournay, and J. I. Adachi (2011), Multiscale Tip Asymptotics in Hydraulic Fracture with Leak-Off, *Journal of Fluid Mechanics*, *669*(Compendex), 260-297.

Geertsma, J., and F. D. Klerk (1969), A Rapid Method of Predicting Width and Extent of Hydraulically Induced Fractures, *Journal of Petroleum Technology*, *21*(DEC), 1571-&.

Germanovich, L. N., R. S. Hurt, and H. Huang (2007), Hydraulic Fracturing in Saturated Cohesionless Materials, paper presented at AGU Fall Meeting, Eos Trans, 25 Dec. 2007 San Fransisco, CA, USA.

Germanovich, L. N., and L. C. Murdoch (2010), Injection of Solids to Lift Coastal Areas, *Royal Society of London,* 6 Carlton House Terrace, London, SW1Y 5AG, United Kingdom.

Gil, I., and J.-C. Roegiers (2003), Coupled Elasto-Plastic Model for Hydraulic Fracturing of Unconsolidated Formations paper presented at *Technology Roadmap for Rock Mechanics (Proceedings of the 10th ISRM Congress, Johannesburg, September 2003) Johannesburg*

Golovin, E., H. Jasarevic, A. Chudnovsky, J. W. Dudley, and G. K. Wong (2010), Observation and Characterization of Hydraulic Fracture in Cohesionless Sand, paper presented at 44th US Rock Mechanics Symposium and the 5th US/Canada Rock Mechanics Symposium, June 27, 2010 - June 30, 2010, Omnipress, Salt Lake City, UT, United States.

Guo, Q., Q. Chen, and C. Wang (2006), Development of Hydraulic Fracturing in-Situ Stress Measurement Technology and Its Application, paper presented at International Symposium on In-situ Rock Stress - In-situ Rock Stress Measurement, Interpretation and Application, June 19, 2006 - June 21, 2006, Taylor and Francis/Balkema, Trondheim, Norway.

Hainey, B. W., and J. C. Troncoso (1992), Frac-Pack. An Innovative Stimulation and Sand Control Technique, paper presented at Proceedings of the International Symposium on Formation Damage Control, Febrary 26, 1992 - Febrary 27, 1992, Publ by Soc of Petroleum Engineers of AIME, Lafayette, LA, USA.

Harison, J. A., B. O. Hardin, and J. Mahboub (1994), Fracture Toughness of Compacted Cohesive Soils Using Ring Test, *Journal of geotechnical engineering*, *120*, 872-891.

Henderson, J. K., J. A. Harmon, and W. B. Harley (1954), Hydraulic Fracturing Improves Production, *Oil and Gas Journal*, *52*(42), 162-164.

Herschel, W.H.; Bulkley, R. (1926), "Konsistenzmessungen von Gummi-Benzollösungen", Kolloid Zeitschrift 39: 291–300,

Hocking, G. (1996), Soil Hydraulic Fracturing, *Water Well Journal*, *50*, 70-72.

Hocking, G. (2004), Deep Permeable Reaction Barriers, *Pollution Engineering*, *36*, 14-16.

Holditch, S. A., and H. A. Madani (2010), Global Unconventional Gas - It Is There, but Is It Profitable?, *JPT, Journal of Petroleum Technology*, *62*, 42-49.

Huang, H., and R. Wu (2008), Fluid Injection into Granular Media under Confinement, paper presented at The XVth International Congress on Rheology. The Society of Rheology 80th Annual Meeting, 3-8 Aug. 2008, AIP, USA.

Huang, H., F. Zhang, P. Callahan, and J. Ayoub (2011), Fluid Injection Experiments in Two-Dimensional Porous Media, in *SPE Hydraulic Fracturing Technology Conference*, edited by S. o. P. Engineers, Society of Petroleum Engineers The Woodlands, Texas, USA.

Hurt, R. S., R. Wu, L. Germanovich, H. Chang, and P. V. Dyke (2005), On Mechanisms of Hydraulic Fracturing in Cohesionless Materials, paper presented at AGU Fall Meeting, Eos Trans, San Francisco, CA.

Ito, T., A. Igarashi, and K. Yamamoto (2009), Laboratory Test of Hydraulic Fracturing in Unconsolidated Deformable Rocks, *Poro-Mechanics Iv*, 1001-1006 1151.

Ito, T., A. Igarashi, K. Suzuki, S. Nagakubo, M. Matsuzawa, and K. Yamamoto (2008), Laboratory Study of Hydraulic Fracturing Behavior in Unconsolidated Sands for Methane Hydrate Production, in *Offshore Technology Conference*, edited, Houston, Texas, USA.

Jasarevic, H., E. Golovin, A. Chudnovsky, J. W. Dudley, and G. K. Wong (2010), Observation and Modeling of Hydraulic Fracture Initiation in Cohesionless Sand, paper presented at 44th US Rock Mechanics Symposium and the 5th US/Canada Rock Mechanics Symposium, June 27, 2010 - June 30, 2010, Omnipress, Salt Lake City, UT, United States.

Ji, L., A. Settari, and R. B. Sullivan (2009), A Novel Hydraulic Fracturing Model Fully Coupled with Geomechanics and Reservoir Simulation, Society of Petroleum Engineers (SPE), P.O. Box 833836, Richardson, TX 75083-3836, United States.

Jones, J., and D. Soler (1999), Fracture Stimulation of Shallow, Unconsolidated Kern River Sands, paper presented at Proceedings of the 1999 SPE International Thermal Operations and Heavy Oil Symposium, March 17, 1999 - March 19, 1999, Soc Pet Eng (SPE), Bakersfield, CA, USA.

Jonk, R., A. Mazzini, D. Duranti, J. Parnell, B. Cronin, and A. Hurst (2003), Fluid Escape from Reservoirs: Implications from Cold Seeps, Fractures and Injected Sands Part Ii. The Fluids Involved, Elsevier, P.O. Box 211, Amsterdam, 1000 AE, Netherlands.

Khodaverdian, M., and P. McElfresh (2000), Hydraulic Fracturing Stimulation in Poorly Consolidated Sand: Mechanisms and Consequences, paper presented at Proceedings of the 2000 SPE Annual Technical COnference and Exhibition on Drilling and Completion, October 1, 2000 - October 4, 2000, Society of Petroleum Engineers (SPE), Dallas, TX, United States.

Khodaverdian, M., T. Sorop, S. Postif, and P. Van Den Hoek (2009), Polymer Flooding in Unconsolidated Sand Formations - Fracturing and Geomechanical Considerations (Spe-121840), paper presented at 71st European Association of Geoscientists and Engineers Conference and Exhibition 2009, June 8, 2009 - June 11, 2009, Society of Petroleum Engineers, Amsterdam, Netherlands.

Khodaverdian, M., T. Sorop, S. Postif, and P. Van Den Hoek (2010a), Polymer Flooding in Unconsolidated-Sand Formations: Fracturing and Geomechanical Considerations, Society of Petroleum Engineers (SPE), P.O. Box 833836, Richardson, TX 75083-3836, United States.

Khodaverdian, M., T. G. Sorop, P. J. Van Den Hoek, S. Sathyamoorthy, and E. Okoh (2010b), Injectivity and Fracturing in Unconsolidated Sand Reservoirs: Waterflooding Case Study, Offshore Nigeria, paper presented at 44th US Rock Mechanics Symposium and the 5th US/Canada Rock Mechanics Symposium, June 27, 2010 - June 30, 2010, Omnipress, Salt Lake City, UT, United States.

Kim, S. (2011), Mechanics of Catastrophic Failure, Dissertation thesis, Georgia Institute of Technology, Atlanta, GA.

Lambe, T. W. (1951), *Soil Testing for Engineers*, 165 p. pp., Wiley, New York,.

Lambe, T. W., and R. V. Whitman (1979), *Soil Mechanics, Si Version*, xiii, Wiley, New York, NY, 553 pp.

Lefebvre, G., M. Bozozuk, A. Philibert, and P. Hornych (1991), Evaluating Ko in Champlain Clays with Hydraulic Fracture Tests, *Canadian Geotechnical Journal*, *28*, 365-377.

Lenormand, R. (1989), Flow through Porous Media: Limits of Fractal Patterns, *Proceedings of the Royal Society of London, Series A (Mathematical and Physical Sciences)*, *423*, 159-168.

Leroueil, S., L. Samson, and M. Bozozuk (1983), Laboratory and Field Determination of Preconsolidation Pressures at Gloucester, *Canadian Geotechnical Journal*, *20*, 477-490.

Lullo, G. D., J. Curtis, and J. Gomez (2004), A Fresh Look at Stimulating Unconsolidated Sands with Proppant-Laden Fluids, paper presented at 2004 SPE Annual Technical Conference and Exhibition, September 26, 2004 - September 29, 2004, Society of Petroleum Engineers (SPE), Houston, TX, United States.

Lutenegger, A. J. (1990), Determination of in Situ Lateral Stresses in a Dense Glacial Till, *Transportation Research Record*, *1278*, 194-203.

Macosko, Christopher W. (1994). *Rheology: Principles, Measurements, and Applications*. Wiley-VCH.

Martin, A. N. (2000), Crack Tip Plasticity: A Different Approach to Modelling Fracture Propagation in Soft Formations, paper presented at Proceedings - SPE Asia Pacific Oil and Gas Conference and Exhibition, Winning Technology and Teamwork, APOGCE 2000, October 16, 2000 - October 18, 2000, Society of Petroleum Engineers (SPE), Brisbane, QLD, Australia.

Mitchell, J. K., K. i. Soga, and Knovel (2005), *Fundamentals of Soil Behavior*, edited, John Wiley & Sons, Hoboken, N.J. 600 pp.

Munson, B. R., D. F. Young, and T. H. Okiishi (2002), *Fundamentals of Fluid Mechanics*, 4th ed., Wiley, New York, NY. 810 pp.

Murdoch, L. C. (1993a), Hydraulic Fracturing of Soil During Laboratory Experiments .1. Methods and Observations, *Geotechnique*, *43*(2), 255-265.

Murdoch, L. C. (1993b), Hydraulic Fracturing of Soil During Laboratory Experiments .2. Propagation, *Geotechnique*, *43*(2), 267-276.

Murdoch, L. C. (1993c), Hydraulic Fracturing of Soil During Laboratory Experiments .3. Theoretical-Analysis, *Geotechnique*, *43*(2), 277-287.

Murdoch, L. C. (1995), Forms of Hydraulic Fractures Created During a Field-Test in Overconsolidated Glacial Drift, *Quarterly Journal of Engineering Geology*, *28*, 23-35.

Murdoch, L. C. (2002), Mechanical Analysis of Idealized Shallow Hydraulic Fracture, *Journal of Geotechnical and Geoenvironmental Engineering*, *128*, 488-495.

Murdoch, L. C., and J. L. Chen (1997), Effects of Conductive Fractures During in-Situ Electroosmosis, *J Hazard Mater*, *55*(1-3), 239-262.

Murdoch, L. C., and W. W. Slack (2002), Forms of Hydraulic Fractures in Shallow Fine-Grained Formations, *Journal of Geotechnical and Geoenvironmental Engineering*, *128*, 479-487.

Murdoch, L. C., J. R. Richardson, Q. Tan, S. C. Malin, and C. Fairbanks (2006a), Forms and Sand Transport in Shallow Hydraulic Fractures in Residual Soil, *Canadian Geotechnical Journal*, *43*, 1061-1073.

Nassir, M., A. Settari, and R. Wan (2010), Modeling Shear Dominated Hydraulic Fracturing as a Coupled Fluid-Solid Interaction, paper presented at International Oil and Gas Conference and Exhibition in China 2010: Opportunities and Challenges in a Volatile Environment, IOGCEC, June 8, 2010 - June 10, 2010, Society of Petroleum Engineers, Beijing, China.

Nilson, R. H. (1986), Integral Method for Predicting Hydraulic Fracture Propagation Driven by Gases or Liquids, *International Journal for Numerical and Analytical Methods in Geomechanics*, *10*, 191-211.

Nilson, R. H., and S. K. Griffiths (1986), Similarity Analysis of Energy Transport in Gas-Driven Fractures, *International Journal of Fracture*, *30*, 115-134.

Olson, J. E., J. Holder, and S. M. Hosseini (2011), Soft Rock Fracturing Geometry and Failure Mode in Lab Experiments, paper presented at SPE Hydraulic Fracturing Technology Conference 2011, January 24, 2011 - January 26, 2011, Society of Petroleum Engineers, The Woodlands, TX, United States.

Ostermeier, R. M., J. H. Pelletier, C. D. Winker, J. W. Nicholson, F. H. Rambow, and K. M. Cowan (2002), Dealing with Shallow-Water Flow in the Deepwater Gulf of Mexico, *Leading Edge (Tulsa, OK)*, *21*, 660+662-668.

Papanastasiou, P. (1997), The Influence of Plasticity in Hydraulic Fracturing, *International Journal of Fracture*, *84*(1), 61-79.

Prodanovic, M., J. Holder, and S. L. Bryant (2009), Coupling Capillarity-Controlled Fluid Displacement with Unconsolidated Sediment Mechanics: Grain Scale Fracture Opening, paper presented at SPE Annual Technical Conference and Exhibition 2009, ATCE 2009, October 4, 2009 - October 7, 2009, Society of Petroleum Engineers (SPE), New Orleans, LA, United States.

Rohler, H., D. Mooren, and K. Georgi (2002), Underground Gas Storage Project Breitbrunn/Eggstatt - Applied Geosciences in Planning, Steering, and Formation Evaluation of the Storage Wells

Santamarina, J. C., K. A. Klein, and M. A. Fam (2001), *Soils and Waves : [Particulate Materials Behavior, Characterization and Process Monitoring]*, J. Wiley & Sons, Chichester, England ; New York, 488 pp.

Savitski, A. A., and E. Detournay (2002), Propagation of a Penny-Shaped Fluid-Driven Fracture in an Impermeable Rock: Asymptotic Solutions, *International Journal of Solids and Structures*, *39*, 6311-6337.

Settari A., P. R. K., C. T. Yee (1989), Coupling of Fluid Flow and Soil Behaviour to Model Injection into Uncemented Oil Sands, *Journal of Canadian Petroleum Technology*, *28*(1).

Shin, H., and C. J. Santamarina (2010), Fluid-Driven Fractures in Uncemented Sediments: Underlying Particle-Level Processes, *Earth and Planetary Science Letters*, *299*, 180-189.

Soga, K., S. K. A. Au, M. R. Jafari, and M. D. Bolton (2005), Laboratory Investigation of Multiple Grout Injections into Clay, *Geotechnique*, *55*, 257-258.

Soga, K., K. O. Gafar, M. Y. A. Ng, and S. K. A. Au (2006a), Macro and Micro Behaviour of Soil Fracturing, *Proc Monogr Eng Wate*, 421-427 524.

Soga, K., K. O. Gafar, M. Y. A. Ng, and S. K. A. Au (2006b), Macro and Micro Behaviour of Soil Fracturing, paper presented at International Symposium on Geomechanics and Geotechnics of Particulate Media - Geomechanics and Geotechnics of Particulate Media, September 12, 2006 - September 14, 2006, Taylor and Francis/Balkema, Ube, Yamaguchi, Japan.

Staheli, K. P., Christopher G.; Wetter Laura , (2010), Effectiveness of Hydrofracture Prediction for Hdd Design, in *North American Society for Trenchless Technology (NASTT) No-Dig Show 2010*, edited, Chicago, Illinois.

Talbot, J. R. (1994), Mechanics of Cracking in Embankment Dams, paper presented at Proceedings of the ASCE National Convention, October 9, 1994 - October 13, 1994, ASCE, Atlanta, GA, USA.

Van den Hoek, P. J. (1993), New 3d Model for Optimised Design of Hydraulic Fractures and Simulation of Drill-Cutting Reinjection, paper presented at Offshore Europe 93; Proceedings, September 7, 1993 - September 10, 1993, Publ by Society of Petroleum Engineers (SPE), Aberdeen, Scotl.

Wang, J.-J., J.-G. Zhu, C. F. Chiu, and H. Zhang (2007), Experimental Study on Fracture Toughness and Tensile Strength of a Clay, *Engineering Geology*, *94*, 65-75.

Wedman, M. L., K. W. Lynch, and J. W. Spearman (1999), Hydraulic Fracturing for Sand Control in Unconsolidated Heavy-Oil Reservoirs in *SPE Western Regional Meeting*, edited, p. 12, Anchorage, Alaska.

Wilkinson, W. L. (1960) *Non-Newtonian Fluids*, Pergamon. London.

Wong, R. C. K., and M. C. Alfaro (2001), Fracturing in Low-Permeability Soils for Remediation of Contaminated Ground, *Canadian Geotechnical Journal*, *38*(2), 316-327.

Wu, R. (2006), Some Fundamental Mechanisms of Hydraulic Fracturing, Dissertation thesis, 301 pp, Georgia Institute of Technology, ATLANTA GA.

Wu, R., L. N. Germanovich, and R. S. Hurt (2009), Experimental and Theoretical Study of Mixed-Mode I+Iii Crack Propagation and Segmentation, paper presented at 43rd U.S. Rock Mechanics Symposium, June 28, 2009 - July 1, 2009, Asheville, NC, United States.

Xu, B., Y. Yuan, and R. C. K. Wong (2010), Modeling of the Hydraulic Fractures in Unconsolidated Oil Sands Reservoir, paper presented at 44th US Rock Mechanics Symposium and the 5th US/Canada Rock Mechanics Symposium, June 27, 2010 - June 30, 2010, Omnipress, Salt Lake City, UT, United States.

Yu, H.-S. (2000), *Cavity Expansion Methods in Geomechanics*, xvi, 385 p. pp., Kluwer Academic Publishers, Dordrecht ; Boston.

Zhai, Z., and M. M. Sharma (2005), A New Approach to Modeling Hydraulic Fractures in Unconsolidated Sands, paper presented at SPE Annual Technical Conference and Exhibition, ATCE 2005, October 9, 2005 - October 12, 2005, Society of Petroleum Engineers (SPE), Dallas, TX, United states.

Zhai, Z., and M. M. Sharma (2006), Modeling Hydraulic Fractures in Unconsolidated Sands, *JPT, Journal of Petroleum Technology*, *58*, 54-55.

Zhang, F., and H. Huang (2011), Coupled Dem-Cfd Modeling of Fluid Injection into Granular Media, in *45th US Rock Mechanics / Geomechanics Symposium*, edited, San Francisco, CA.

Zhou, J., Y. Dong, C. J. De Pater, and P. L. J. Zitha (2010), Experimental Study of the Impact of Shear Dilation and Fracture Behavior During Polymer Injection for Heavy Oil Recovery in Unconsolidated Reservoirs, paper presented at Canadian Unconventional Resources and International Petroleum Conference 2010, October 19, 2010 - October 21, 2010, Society of Petroleum Engineers, Calgary, AB, Canada.